

U. S. Army Research Office Final Progress Report  
for the period  
1 July 1998 to 30 June 2001

"Lasing and electro-optic properties of quantum-  
Confined structures grown on novel index surfaces"

Grant No:

Project Director:

Institution:

DAAG55-98-1-0436

Arthur L. Smirl

University of Iowa

20010725 027

**REPORT DOCUMENTATION PAGE**Form Approved  
OMB NO. 0704-0188

Public Reporting burden for this collection of information is estimated to average 1 hour per response, including the time for reviewing instructions, searching existing data sources, gathering and maintaining the data needed, and completing and reviewing the collection of information. Send comment regarding this burden estimates or any other aspect of this collection of information, including suggestions for reducing this burden, to Washington Headquarters Services, Directorate for Information Operations and Reports, 1215 Jefferson Davis Highway, Suite 1204, Arlington, VA 22202-4302, and to the Office of Management and Budget, Paperwork Reduction Project (0704-0188), Washington, DC 20503.

1. AGENCY USE ONLY (Leave Blank)		2. REPORT DATE 1 April 2001		3. REPORT TYPE AND DATES COVERED Final Progress Report: 7/1/98-6/30/01	
4. TITLE AND SUBTITLE  Lasing and electro-optic properties of quantum-confined structures grown on novel index surfaces				5. FUNDING NUMBERS  DAAG55-98-1-0436	
6. AUTHOR(S) Arthur L. Smirl					
7. PERFORMING ORGANIZATION NAME(S) AND ADDRESS(ES) University of Iowa				8. PERFORMING ORGANIZATION REPORT NUMBER	
9. SPONSORING / MONITORING AGENCY NAME(S) AND ADDRESS(ES)  U. S. Army Research Office P.O. Box 12211 Research Triangle Park, NC 27709-2211				10. SPONSORING / MONITORING AGENCY REPORT NUMBER  38888.11-EL	
11. SUPPLEMENTARY NOTES  The views, opinions and/or findings contained in this report are those of the author(s) and should not be construed as an official Department of the Army position, policy or decision, unless so designated by the documentation.					
12 a. DISTRIBUTION / AVAILABILITY STATEMENT Approved for public release; distribution unlimited.				12 b. DISTRIBUTION CODE	
13. ABSTRACT (Maximum 200 words) The broad objective on this project is to investigate the unique optical and optoelectronic properties of [110], [111] and [112]-oriented multiple quantum wells (MQW's) and to study the ways in which strain and external optical fields can introduce crystallographic dependences to the optical properties of otherwise isotropic materials. Toward this end, we have demonstrated that dual-channel spectral interferometric techniques can be used to measure the amplitude, phase and polarization state of extremely weak ultrafast coherent emission from MQW's. The vectorial dynamics of the coherent four-wave mixing emission are found to exhibit systematic variations with excitation fluence, time delay between incident pulses, the tuning of the laser wavelength, and the orientation of the input polarizations. This time-dependent polarization state indicates that the pump pulses have induced dynamic anisotropies in the sample. From these anisotropies, a self consistent picture of the excitonic and carrier dynamics is obtained that delineates the roles of the various many body effects. These studies demonstrate that time-resolved polarimetry is an extremely sensitive way to study many body effects and that the vectorial dynamics contain essential information about quantum interference and optical anisotropies that would be difficult to obtain in any other way. This should make these techniques extremely useful in probing strained MQW's and semiconductors grown in unconventional directions, such as quantum dots. In addition, we are now using the coherent anisotropies and many body vectorial dynamics studied here to make high-speed high-contrast polarization sensitive modulators.					
14. SUBJECT TERMS				15. NUMBER OF PAGES	
				16. PRICE CODE	
17. SECURITY CLASSIFICATION OR REPORT UNCLASSIFIED	18. SECURITY CLASSIFICATION ON THIS PAGE UNCLASSIFIED	19. SECURITY CLASSIFICATION OF ABSTRACT UNCLASSIFIED	20. LIMITATION OF ABSTRACT  UL		

## TABLE of CONTENTS

Table of Contents.....	i
Problem Statement.....	1
Summary of Major Accomplishments.....	1-5
An Intrinsically Anisotropic [110]-Oriented Quantum Well Polarization Modulator .....	1
Measurement of the Time-Resolved Phase and Polarization State of the Coherent Emission from Multiple Quantum Wells.....	2
Ultrafast Time-Resolved Heavy-Hole and Light-Hole Quantum Beats in the Polarization State of Coherent Emission from Quantum Wells .....	2
Heavy-Hole and Light-Hole Oscillations in the Coherent Emission from Quantum Wells as a Test for Exciton-Exciton Correlations .....	3
Use of Polarization Dynamics to Determine the Optical Selection Rules for Excitonic Transitions in Strained and Unstrained Quantum Wells .....	3
Differential Measurements of Dipole and Raman Coherences and of Exciton-Exciton Interactions in Quantum Wells.....	4
Polarization Dynamics of the Nonlinear Coherent Emission from Uniaxially-Strained Quantum Wells.....	4
Papers Published .....	6
Papers Given at Conferences .....	8
<b>Appendix A:</b> Electro-Optic Polarization Modulation in [110]-Oriented GaAs-InGaAs Multiple Quantum Wells	
<b>Appendix B:</b> The Vectorial Dynamics of Coherent Emission from Excitons	
<b>Appendix C:</b> Heavy-Hole and Light-Hole Oscillations in the Coherent Emission from Quantum Wells: Evidence for Exciton-Exciton Correlations	
<b>Appendix D:</b> Polarization Dynamics and Optical Selection Rules for Excitonic Transitions in Strained Quantum Wells	
<b>Appendix E:</b> Differential Measurements of Dipole and Raman Coherence and of Exciton- Exciton Interactions in Quantum Wells	
<b>Appendix F:</b> Polarization Dynamics of the Nonlinear Coherent Emission from Uniaxially- Strained Quantum Wells	

## **U.S. ARMY RESEARCH OFFICE FINAL PROGRESS REPORT for the period 1 July 1998 TO 30 June 2001**

**TITLE of PROJECT:** Lasing and electro-optic properties of quantum-confined structures grown on novel index surfaces

**GRANT NUMBER:** DAAG55-98-1-0436

**PERIOD COVERED BY REPORT:** 1 July 1998 to 30 June 2001

**INSTITUTION:** The University of Iowa

**PRINCIPAL INVESTIGATOR:** Arthur L. Smirl

**PROBLEM STATEMENT:** The majority of the heterostructures grown by molecular beam epitaxy (MBE) and metalorganic chemical vapor deposition (MOCVD) over the last thirty years have been grown on substrates oriented in the [001] crystallographic direction. By comparison, there has been very little work on growth on other crystallographic axes or on applications of such structures. However, theoretical considerations (and several recent experiments) would indicate that unique and useful properties can be realized by growth in other directions. For example, the effective mass, the optical matrix elements, nonlinear susceptibilities, piezoelectric effects and the effects of strain and of confinement are all expected to depend upon crystallographic direction. In addition, it is expected that the application of an external strain or the application an intense optical field will induce similar anisotropies in the optical properties of conventionally oriented materials. Here, we proposed to continue a fundamental investigation of the unique optical and optoelectronic properties of [110], [111] and [112]-oriented multiple quantum wells (MQWs) and of the optical anisotropies that could be introduced by strain and optical excitation in conventionally oriented materials. The latter should be particularly useful in, for example, constructing high-speed high-contrast spatial light modulators.

**MAJOR ACCOMPLISHMENTS:** The work performed during this contract period has resulted in 16 papers published (including 1 invited and 3 invited chapters in books) and 19 papers presented at conferences (6 invited). This work was also supported in part by ARO grant number: DAAG55-97-1-0306.

**An Intrinsically Anisotropic [110]-Oriented Quantum Well Polarization Modulator:** We have demonstrated that the optical anisotropy inherent in biaxially-strained [110]-oriented GaAs-In<sub>x</sub>Ga<sub>1-x</sub>As multiple quantum wells (MQWs) can be used to construct a prototype electro-optic modulator that is sensitive to the polarization state of the transmitted light. In this device, application of a voltage across a p-i-n region containing the MQWs is used to produce a change in the in-plane birefringence and dichroism. This, in turn, causes a change in the ellipticity and a rotation of a linearly polarized input beam. Subsequently, a phase retarder and a linear analyzer are used to convert this polarization modulation into an intensity modulation. Ellipsometric measurements, which directly determine the degree of dichroism and birefringence as a function



of wavelength and voltage, were systematically performed on this device and were used to optimize the operating wavelength, the alignment of the modulator and to predict the maximum contrast ratio. These results allow the design of future structures with an enhanced contrast ratio (1000:1), good bandwidth (4 nm), tunability (10 nm) and operating temperature range (35 C), but with a relatively low throughput (1%). Even larger contrast ratios and throughputs are predicted for MQW structures with narrower excitons, but with a degraded bandwidth, tunability, and hence, increased sensitivity to temperature. This approach to the construction of polarization modulators requires only elementary post-growth processing. It is applicable to systems that require high contrast modulation but can tolerate the larger insertion losses. [see Appendix A for details]

**Measurement of the Time-Resolved Phase and Polarization State of the Coherent Emission from Multiple Quantum Wells:** Time-integrated and time-resolved four-wave mixing (FWM) techniques have proven to be powerful tools for studying excitonic dynamics and coherent processes in both bulk and quantum confined semiconductor structures. Conventional techniques have provided considerable information about the temporal amplitude and the spectral amplitude of the emitted FWM signal, but they have provided no information about the temporal phase or the spectral phase. However, complete characterization of the emitted field requires the measurement of both! We have used both direct time-resolved ellipsometric and spectrally-resolved dual-beam interferometric techniques to study the dephasing dynamics of excitons and carriers in GaAs/AlGaAs multiple quantum wells by time resolving the *amplitude*, *phase* and *polarization state* of the weak coherent FWM emission from such nanostructures. Initially, we have focused on a single series of FWM experiments in a single multiple quantum well sample in which we excited only the heavy-hole transitions, thus eliminating the need to consider heavy-hole and light-hole beating phenomena. The spectral amplitudes and the spectral phases of the  $x$  and  $y$  components of the coherent FWM emission are found to exhibit systematic (but distinct) variations with excitation fluence, time delay between the two incident pulses, the detuning of the laser wavelength from the heavy hole exciton, and the orientation of the input polarizations. This time-dependent polarization state indicates that the pump pulses have induced dynamic anisotropies in the sample. From these anisotropies, a self consistent picture of the temporal dynamics of the amplitude, phase and polarization state is obtained that delineates the roles of many body effects, such as local field corrections (LFC), excitation-induced dephasing (EID) and biexcitons (BIF), in determining the excitonic dynamics. For example, under certain conditions, dramatic discontinuities are observed in the temporal evolutions of the phase and polarization state. We have shown that these are manifestations of many body and biexcitonic effects. As such, the latter can be used to estimate the relative strengths of these processes. These studies have established the sensitivity of polarization-based techniques for studying many body and biexcitonic processes. In fact, when only heavy-holes are excited, all of the polarization dynamics are associated with many-body effects--since without them the emitted polarization is expected to be linear and constant in time. [A detailed review of our extensive body of work in this area is provided for the readers convenience in Appendix B.]

**Ultrafast Time-Resolved Heavy-Hole and Light-Hole Quantum Beats in the Polarization State of Coherent Emission from Quantum Wells:** For the measurements described in the previous paragraph, the laser was purposefully tuned slightly below the heavy-hole (hh) exciton to ensure that we excited as few light holes (lh) as possible and to avoid the complication of

quantum beating between the lh and hh. Here, we have measured the dynamics of the amplitude, phase and polarization state of the emission from a GaAs-AlGaAs MQW when the excitation spectrum was tuned so that both hh and lh excitons were excited and quantum beats were observed. We find that all of the parameters that describe the polarization state (including the ellipticity, the orientation of the polarization ellipse, and the sense of rotation) oscillate in time at the hh-lh beat frequency. To our knowledge, this is the first observation of time-resolved quantum beats in the polarization state. When approximately equal numbers of hh and lh excitons are excited (i.e., in the strong quantum beat regime), some of the features can be qualitatively described without many-body effects; however, even in this regime, it is clear that the beats are "distorted" by other effects. In the weak quantum beating regime, it is clear that the quantum beating is superposed upon polarization dynamics that require the inclusion of many-body and biexcitonic effects. [see Appendix B]

**Heavy-Hole and Light-Hole Oscillations in the Coherent Emission from Quantum Wells as a Test for Exciton-Exciton Correlations :** We have used the polarization selection rules for four-wave mixing and a test that was originally designed to distinguish between quantum beats and polarization interference to demonstrate the presence of strong exciton-exciton correlations in GaAs-AlGaAs multiple quantum wells. We have shown that when the four-wave-mixing signal is produced by two pulses that have the same circular polarization the oscillations observed at the heavy-hole-light-hole frequency exhibit quantum-beat-like behavior. The latter observation is contrary to the predictions based on either the density matrix equations for two independent three-level systems or the conventional semiconductor Bloch equations (in the Hartree-Fock approximation), both of which predict that polarization interference, but not quantum beats, should be observed. (Note: these are the two most commonly used approaches to modeling excitonic interactions in quantum wells.) Consequently, the observation of quantum-beat-like behavior when exciting with two pulses having the same circular polarization provides clear evidence for exciton-exciton correlations and evidence that those correlations go beyond those contained in the semiconductor Bloch equations. The procedure that we use provides a simple effective test for such processes. In addition, we have shown that excitation-induced-dephasing (EID) is among those processes that can produce such correlations. A model based on the latter process predicts new dynamic features that are not characteristic of either quantum beating or polarization interference. We have demonstrated that such features are indeed observed, and we have used these new features to place quantitative limits on the magnitude of the density-dependent dephasing for the first time. [see Appendices B and C]

**The Use of Polarization Dynamics to Determine the Optical Selection Rules for Excitonic Transitions in Strained and Unstrained Quantum Wells:** The circularly polarized optical selection rules (CPOSr) for the heavy-hole (*hh*) and light-hole (*lh*) excitonic transitions have played an essential role in the interpretation of the detailed studies of dephasing processes in semiconductors that have been performed in recent years.. However, it is often impossible to avoid introducing stress and strain into the samples used in these experiments during growth and fabrication. For this reason, it is important to understand and to quantify the effects of stress and strain on the optical selection rules. Here, we have used the dual-beam spectral interferometric techniques described above to time-resolve the polarization state of the coherent emission from both intentionally and unintentionally strained GaAs/AlGaAs multiple quantum wells following irradiation with very weak femtosecond pulses. We have shown that any

anisotropy in the in-plane strain will result in dramatic oscillations in the intensity, the orientation, and the ellipticity of the coherent emission at the heavy-hole light-hole beat frequency. We have shown this behavior to be the result of replacing the circularly polarized optical selection rules with elliptically polarized selection rules in the uniaxially strained sample. When only the heavy-hole transition is excited with linearly polarized light, these elliptical selection rules lead to a linearly polarized coherent emission that is rotated with respect to incident orientation. We have used the degree of rotation of the coherent emission as a function of sample orientation to quantify the anisotropy in the strain. When the in-plane strain is uniform, no such rotation and no light-hole heavy-hole beats in the polarization state of the coherent emission are observed. [see Appendix D]

**Differential Measurements of Dipole and Raman Coherences and of Exciton-Exciton Interactions in Quantum Wells:** When light-hole (*lh*) and heavy-hole (*hh*) excitons are excited in semiconductors and multiple quantum wells (MQWs), the coherent superposition of electronic states produces oscillations (or quantum beats) in the third-order nonlinear optical emission. In order for quantum beats (as opposed to polarization interference) to be produced, the *hh* and *lh* excitons must be coupled in some way. If the two excited oscillators share a common energy level, then that level can provide the necessary coupling. However, recent experimental and theoretical work has demonstrated that the *lh-hh* excitonic coupling necessary for *lh-hh* quantum beating also can be produced by the many-body Coulomb interactions between excitons. Some of these Coulomb correlations are established on a time scale that is rapid compared to the pulsewidths used here and can be regarded as instantaneous. By comparison, others are initially weak, but they continue to act and to build-up over time; hence, they can be regarded as cumulative. In this work, we have investigated these *hh* and *lh* correlations by using a novel temporally-gated differential technique in concert with a conventional technique to measure the time-integrated quantum beats (TI-QBs) in the ultrafast coherent third-order emission from excitons in GaAs/AlGaAs quantum wells. We have demonstrated that, when the emitted signal is measured in the probe direction, the conventional technique approximately samples the third-order nonlinear polarization at its initial value (for optically thin samples), and as a consequence, tends to suppress the contributions of the *cumulative* many-body correlations to the emission. By contrast, the *gated* differential technique (described below) yields a signal that integrates over the emission time of the third-order nonlinear polarization, and therefore, this signal is dominated by these cumulative correlations between *hh* and *lh* excitons. We have then shown that these two complementary techniques can be used together with the polarization selection rules for the *hh* and *lh* excitonic transitions to isolate the contributions of the higher-order cumulative coupling between the excitons and to separately measure the conduction-to-valence band (interband) coherence and the coherence between the *hh* and *lh* valence bands (intervalence band coherence). [see Appendix E]

**Polarization Dynamics of the Nonlinear Coherent Emission from Uniaxially-Strained Quantum Wells:** Previously, all of our time-resolved ellipsometric experiments have been performed in conventional [001]-oriented unstrained GaAs/AlGaAs MQW's. Such MQW structures possess no intrinsic in-plane anisotropy in their linear absorptive or refractive properties. Even though quantum confinement breaks the symmetry along the growth direction, the in-plane linear optical properties remain isotropic. It has been shown, however, that the application of a uniaxial stress in the plane of the wells will reduce the in-plane symmetry by

mixing the heavy-hole and light-hole valence band states to produce large linear and nonlinear optical anisotropies. Here, we have performed the first measurements of the dynamics of the *amplitude*, *phase* and *polarization state* of the coherent nonlinear emission from an anisotropic uniaxially-strained GaAs-AlGaAs MQW. We find that the polarization state of the coherent emission varies dramatically with both sample orientation and with time. The variations in polarization state with sample orientation confirm the presence of an intrinsic static (strain-induced) anisotropy. By contrast, the time-varying ellipticity and orientation indicate the presence of a dynamic induced anisotropy and are definitive signatures of many body effects. Consequently, these results illustrate that the vectorial dynamics are determined by (and therefore contain information about) both intrinsic static and induced dynamic anisotropies. In order to interpret the experimental results further, we have extended the phenomenological model that we have previously used to include anisotropic optical matrix elements which correspond to the strain in our sample. This model reproduces many of the qualitative features displayed by the data. We anticipate that further refinements in the model will allow a more detailed analysis of the many body effects underlying the vectorial dynamics. Work on this project continues. [Appendix F]

## PAPERS PUBLISHED:

### Journals:

1. "Electro-Optic Polarization Modulation in [110]-Oriented GaAs-InGaAs Multiple Quantum Wells", M. J. Snelling, X. R. Huang, D. R. Harken, Arthur L. Smirl, and E. Towe, *IEEE J. Quantum Electron.* **33**, 1114 (1997).
2. "Electro-Optic Polarization Modulation in [110]-Oriented GaAs-InGaAs Multiple Quantum Wells", M. J. Snelling, X. R. Huang, D. R. Harken and Arthur L. Smirl, in *OSA Trends in Optics and Photonics Series (TOPS)*, vol. **14**, *Spatial Light Modulators 1997*, G. Burdge and S. C. Esener (eds.), (Optical Society of America, 1997), p.141.
3. "Characterization of the Polarization State of Weak Ultrashort Coherent Signals by Dual-Channel Spectral Interferometry", W. J. Walecki, David N. Fittinghoff, Arthur L. Smirl, and Rick Trebino, *Opt. Lett.* **22**, 81 (1997).
4. "Temporally and Spectrally-Resolved Amplitude and Phase of Coherent Four-Wave-Mixing Emission from GaAs Quantum Wells", X. Chen, Wojciech J. Walecki, O. Buccafusca, David N. Fittinghoff and Arthur L. Smirl, *Phys. Rev. B* **56**, 9738 (1997).
5. "Dynamics of the Amplitude, Phase and Polarization State of Coherent Emission from Quantum Wells", Arthur L. Smirl, Wojciech J. Walecki, Xiayuan Chen and Osvaldo Buccafusca, *Phys. Stat. Sol. (B)* **204**, 16 (1997).
6. "Measurement of the Ultrafast Polarization Dynamics of Weak Four-Wave-Mixing Signals Using Dual-Channel Femtosecond Spectral Interferometry", O. Buccafusca, X. Chen, Wojciech J. Walecki and Arthur L. Smirl, *J. Opt. Soc. Am. B* **15**, 1218 (1998).
7. "Ultrafast Time-Resolved Quantum Beats in the Polarization State of Coherent Emission from Quantum Wells," Arthur L. Smirl, X. Chen, and O. Buccafusca, *Opt. Lett.* **23**, 1120 (1998).
8. "Ultrafast Time-Resolved Quantum Beats in the Polarization State of Coherent Emission from Quantum Wells", A. L. Smirl, X. Chen and O. Buccafusca, in *Ultrafast Phenomena XI*, (Springer-Verlag, Berlin 1998), p. 221.
9. "Heavy-Hole and Light-Hole Oscillations in the Coherent Emission from Quantum Wells: Evidence for Exciton-Exciton Correlations," Arthur L. Smirl, Martin J. Stevens, X. Chen, and O. Buccafusca, *Phys. Rev. B* **60**, 8267 (1999).
10. "Interaction-Induced Effects in the Nonlinear Coherent Response of Quantum Well Excitons," H. P. Wagner, A. Schätz, W. Langbein, J. M. Hvam, Arthur L. Smirl, *Phys. Rev. B* **60**, 4454 (1999).

11. "Differential Measurements of Dipole and Raman Coherence and of Exciton-Exciton Interactions in Quantum Wells, Martin J. Stevens, Eric J. Gansen, Scot A. Hawkins, K. Jarasiunas, Arthur L. Smirl, and D. G. Steel, submitted to *Phys. Rev. B*.
12. "Polarization Dynamics and Optical Selection Rules for Excitonic Transitions in Strained Quantum Wells," Scot A. Hawkins, Martin J. Stevens, and Arthur L. Smirl, submitted to *Phys. Rev. B*.

**Invited Publications:**

13. "Heavy-Hole and Light-Hole Quantum Beats in the Polarization State of Coherent Emission from Quantum Wells," Arthur L. Smirl, X. Chen, and O. Buccafusca, *IEEE J. Quantum Electron.* **35**, 523-531 (1999).

**Invited Chapters in Books:**

14. "Coherent Exciton Dynamics: Time-Resolved Polarimetry," Arthur L. Smirl, in *Semiconductor Quantum Optoelectronics: From Quantum Physics to Smart Devices*, edited by A. Miller and D. M. Finlayson (Institute of Physics Publishing, Bristol, 1999), pp. 25-94.
15. "The Vectorial Dynamics of Coherent Emission from Excitons," Arthur L. Smirl, in *Ultrafast Phenomena in Semiconductors* edited by Frank Tsen (Springer Verlag, New York, 2000), pp. 443-507.
16. "Measuring Ultrafast Polarization Dynamics: POLLIWOG," Arthur L. Smirl, to be published in *Frequency-Resolved Optical Gating: The Measurement of Ultrashort Laser Pulses*, edited by Rick Trebino (Springer Verlag, New York, 2001), pp. .

**PAPERS PRESENTED at MEETINGS:**

1. **INVITED:** "Complete Characterization of Coherent Nonlinear Emission from GaAs Quantum Wells", Arthur L. Smirl, Novel Optical Materials and Applications (NOMA '97), Cetraro, Italy, 8-13 June 1997.
2. "Dynamics of the Amplitude, Phase and Polarization State of Coherent Emission from Quantum Wells", Arthur L. Smirl, Wojciech J. Walecki, Xiayuan Chen and Osvaldo Buccafusca, International Conference on Nonequilibrium Carrier Dynamics in Semiconductors (HCIS 10), Berlin, Germany, 28 July-1 August 1997.
3. "Complete Characterization of Coherent Emission from Quantum-Confined Semiconductors using Spectral Interferometry: Advantages and Limitations", Wojciech J. Walecki, X. Chen, O. Buccafusca, and Arthur L. Smirl, Optical Society of America Annual Meeting, Long Beach, CA, 12-17 October 1997.
4. **INVITED:** "Ultrafast Polarization Dynamics of Coherent Emission from Excitons in Quantum Wells", Arthur L. Smirl, Symposium on "Ultrafast Phenomena in Semiconductors" at SPIE's Optoelectronics/LASE, Photonics West, San Jose, CA, 24-30 January 1998.
5. "Discontinuities in the Time-Resolved Phase and Polarization State of Coherent Emission from Multiple Quantum Wells", O. Buccafusca, X. Chen, and Arthur L. Smirl, Conference on Radiative Processes and Dephasing in Semiconductors, Coeur d'Alene, Idaho, 2-4 February-1998.
6. **INVITED:** "Polarization Dynamics of Coherent Emission from Quantum Wells", Arthur L. Smirl, The 1998 March Meeting of the American Physical Society, Los Angeles, CA, 16-20 March 1998.
7. "Time-Resolved Quantum Beats in the Polarization State of Coherent Emission from Multiple Quantum Wells", X. Chen, O. Buccafusca, and Arthur L. Smirl, International Conference on Quantum Electronics (IQEC '98), San Francisco, CA, 3-8 May 1998.
8. **INVITED:** "Ultrafast Coherent Phenomena", Arthur L. Smirl, A series of 4 one-hour lectures at the 50<sup>th</sup> Scottish Universities Summer School on "Semiconductor Quantum Optoelectronics: From Quantum Physics to Smart Devices", St. Andrews, Scotland, 21 June-4 July 1998.
9. "Ultrafast Time-Resolved Quantum Beats in the Polarization State of Coherent Emission from Quantum Wells," Arthur L. Smirl, X. Chen, and O. Buccafusca, XI<sup>th</sup> International Conference on Ultrafast Phenomena, Garmisch-Partenkirchen, Germany, 12-17 July 1998.
10. **INVITED:** "The Effects of Crystallographic Orientation on the Nonlinear Optical Properties of Quantum Wells," Arthur L. Smirl, The International Conference on Novel Index Surfaces (NIS '98), San Rafael, Segovia, Spain, 6-9 October 1998.

11. "Polarization Dynamics of the Nonlinear Coherent Emission from Uniaxially-Strained Quantum Wells," Arthur L. Smirl, X. Chen, M. J. Stevens, O. Buccafusca, R. Binder and I. Rumyantsev, Quantum Optoelectronics Conference (QOE '99), Aspen, CO, 12-16 April 1999.
12. "Heavy-hole and Light-hole Oscillations in the Coherent Emission from Quantum Wells: Evidence for Exciton-Exciton Correlations," M. J. Stevens, Arthur L. Smirl, O. Buccafusca and X. Chen, Quantum Electronics and Laser Science Conference (QELS '99), Baltimore, MD, 23-28 May 1999.
13. **INVITED:** "Quantum Beating of Dynamically Interacting Excitons in Semiconductors: Vectorial Dynamics and Polarization Selection Rules," Arthur L. Smirl, 30<sup>th</sup> Winter Colloquium on the Physics of Quantum Electronics (PQE 00), Snowbird, Utah, 9-12 January 2000.
14. "Dipole Quantum Beats of Dynamically Interacting Excitons," Martin J. Stevens, Zetian Mi, Arthur L. Smirl and D. G. Steel, Quantum Electronics and Laser Science Conference (QELS '00), San Francisco, CA, 7-12 May 2000.
15. "Differential Measurements of Raman Coherence and of Dynamically Interacting Excitons in Quantum Wells," Arthur L. Smirl, Martin J. Stevens, Eric J. Gansen, K. Jarasiunas, and D. G. Steel, XII<sup>th</sup> International Conference on Ultrafast Phenomena, Charleston, SC, 9-13 July 2000.
16. "Differential Measurements of Interband and Intersubband Coherence and Exciton-Exciton Correlations in Quantum Wells," Scot A. Hawkins, Martin J. Stevens, Eric J. Gansen, K. Jarasiunas, Arthur L. Smirl and D. G. Steel, Conference on Nonlinear Optics: Materials, Fundamentals and Applications 2000, Kaua'i-Lihue, Hawaii, 6-10 August 2000.
17. "Coherent All-Optical Polarization Switching in Quantum Wells," Eric J. Gansen, K. Jarasiunas, Scot A. Hawkins, Martin J. Stevens, and Arthur L. Smirl, Conference on Nonlinear Optics: Materials, Fundamentals and Applications 2000, Kaua'i-Lihue, Hawaii, 6-10 August 2000.
18. "Heavy-Light Hole Beats and the Optical Selection Rules for Excitonic Transitions in Quantum Wells," Martin J. Stevens, Scot A. Hawkins and Arthur L. Smirl, Optical Society of America Annual Meeting, Providence, RI, 22-26 October 2000.
19. "Coherent All-Optical Polarization Switching Based on Exciton-Exciton Correlations in Quantum Wells," Martin J. Stevens, Scot A. Hawkins, Eric J. Gansen, K. Jarasiunas and Arthur L. Smirl, Optical Society of America Annual Meeting, Providence, RI, 22-26 October 2000.



# Electrooptic Polarization Modulation in [110]-Oriented GaAs-InGaAs Multiple Quantum Wells

M. J. Snelling, X. R. Huang, Dean R. Harken, *Member, IEEE*,  
Arthur L. Smirl, *Senior Member, IEEE*, and Elias Towe, *Member, IEEE*

**Abstract**—An electrooptic modulator that is sensitive to the polarization state of transmitted light is demonstrated by using the intrinsic optical anisotropy of biaxially strained [110]-oriented GaAs-In<sub>x</sub>Ga<sub>1-x</sub>As multiple quantum wells. The ellipticity and the direction of polarization of a linearly polarized input pulse are modulated by a change in the in-plane dichroism and birefringence produced by a change in the voltage applied across the p-i-n region containing the quantum wells. Sensitive ellipsometric measurements are used to directly measure the anisotropy in the complex index of refraction between the two principal in-plane axes of the sample as a function of wavelength for selected voltages. The latter information is then used to determine the operating wavelength, the contrast ratio, the optical bandwidth, and the tunability of the modulator. This structure requires only standard elementary post-growth processing.

**Index Terms**—Anisotropic media, birefringence, electrooptic materials/devices, optical polarization, quantum-confined Stark effect, quantum-well devices, spatial light modulators, strain.

## I. INTRODUCTION

**N**ORMAL incidence electrooptic modulators are needed for applications, for example, in computing, communications, displays, printing, and publishing. An ideal device would be capable of high-speed operation, have a large dynamic range, have a low insertion loss, and accommodate broad spectral bandwidths. It would also be insensitive to ambient and device temperature fluctuations, and it would have a low switching voltage that is compatible with (and it should be integrable with) detector and control electronics. Since these are often competing characteristics, it is usually necessary to trade one for another in order to satisfy the requirements for a given application.

For example, most research on semiconductor modulators to date has focused on amplitude modulation and has relied on the quantum-confined Stark effect (QCSE) [1] to produce the required change in absorption. In this type of device, a change in an applied voltage across the multiple-quantum-well (MQW) region causes a shift in wavelength for the

excitonic absorption resonance. However, restrictions on the desired operating voltage, acceptable insertion losses and growth considerations combine to limit the number of quantum wells (QW's) that realistically can be incorporated into MQW modulators. This limitation on the number of wells also restricts the maximum available change in absorbance and prevents the contrast ratio from exceeding  $\sim 10:1$ . In fact, this ratio is more typically  $\sim 4:1$  [2], [3]. The contrast ratio can be improved and the operating voltage can be reduced by incorporating the MQW structure in a Fabry-Perot cavity (values as high as  $100:1$  have been reported [4]), but typically at the expense of a reduction in optical bandwidth [4], [5] or an increase in insertion loss. In fact, it has been demonstrated that in Fabry-Perot reflective electroabsorptive modulators (REAM's) increased contrast ratio can be directly traded for an increased insertion loss [6].

The insertion loss of a QCSE modulator is directly related to the absorbance of the device (i.e., the product of the absorption coefficient and the total thickness of the QW material) in the on state and can be quite modest for a resonant device (e.g.  $\sim 1.5$ – $7$  dB). The requirement for low insertion loss and minimal contrast ratios ( $>3:1$ ) combine, however, to dictate higher operating voltages in current devices (typically  $>10$  V) than are optimal for integration with silicon integrated technology. This operating voltage, however, can be reduced by using a stack of interdigitated p-i(MQW)-n structures that are arranged to be optically in series and electrically in parallel [7]–[10]. The price paid for this reduction in switching voltage is an increase in capacitance and decrease in speed.

In addition, the on (or off) state for a QCSE amplitude modulator is determined by whether the operating wavelength is tuned off (or on) an excitonic resonance, and this excitonic resonance shifts with temperature at a rate of  $\sim 1$  nm/3.5 °C [7], [8]. Consequently, if this resonance is very narrow (typically,  $<2$  nm wide), then the QCSE modulator will have a relatively narrow optical bandwidth and will inherently have a narrow operating temperature range. It has been shown [7], [8], however, that the operating temperature range can be extended by using MQW's with broader excitonic features. This increased temperature range comes at the expense of contrast ratio or switching voltage (or some combination thereof).

By comparison, much higher contrast ratios can be obtained for modulators that are sensitive to the polarization state of

Manuscript received December 2, 1996; revised March 4, 1997. This work was supported by the Army Research Office, the Defense Advanced Research Projects Agency, and the National Science Foundation.

M. J. Snelling, X. R. Huang, D. R. Harken, and A. L. Smirl are with the Laboratory for Photonics & Quantum Electronics, University of Iowa, Iowa City, IA 52242 USA.

E. Towe is with the Laboratory for Optics & Quantum Electronics, University of Virginia, Charlottesville, VA 22903 USA.

Publisher Item Identifier S 0018-9197(97)04697-6.

the transmitted light, rather than its amplitude. A polarization-sensitive modulator may be fabricated from any material that is optically anisotropic, i.e., any material for which the absorption coefficient and/or refractive index are different for orthogonal axes. On passage through an anisotropic material, linearly polarized light is, in general, converted to elliptical polarization and the semi-major axis of the polarization ellipse is rotated from the input plane of polarization. To modulate the transmitted beam, it is necessary that the anisotropy, and hence the polarization state of the output beam, be altered either optically or electrically. For example, liquid crystal and magneto-optical devices have achieved contrast ratios  $>10^4:1$  by utilizing the birefringence and dichroism associated with their linear electro- or magneto-optical properties. Similarly, contrast ratios  $>10^4:1$  have been achieved in optically addressed III-V and II-VI semiconductor modulators (with the light propagating along the [001]-direction) by making use of the intrinsic anisotropies associated with the third-order nonlinear index of refraction and absorption coefficient in materials with zinc blende symmetry [11].

Unfortunately, conventional III-V MQW structures grown along the [001]-direction possess no intrinsic in-plane anisotropy in their linear absorptive or refractive properties which can be used to modulate the polarization state of transmitted light. Even though quantum confinement breaks the symmetry along the growth direction, the in-plane linear optical properties remain isotropic. It has been recently shown [12], [13], however, that the application of a uniaxial stress in the plane of the wells will reduce the in-plane symmetry by mixing the heavy hole ( $m_j = \pm 3/2$ ) and light hole ( $m_j = \pm 1/2$ ) valence band states to produce large optical anisotropies. In the latter studies [12], [13], the uniaxial in-plane strain was obtained following growth by bonding the MQW structure to a transparent uniaxial lithium tantalate ( $\text{LiTaO}_3$ ) substrate and subsequently removing the semiconductor substrate on which the sample was grown by epitaxial lift-off. The  $\text{LiTaO}_3$  substrate was cut such that the thermal expansion coefficient along one direction matched that of the MQW, but along the orthogonal direction it did not. A thermally induced uniaxial strain was then obtained by operating the device at a temperature different from the bonding temperature. An impressive contrast ratio of 5000:1 (corresponding to 37 dB of dynamic range) has been reported [14] for an electrically addressed modulator operating at 14 V containing 150 quantum wells at room temperature using the birefringence and dichroism induced by this uniaxial strain. From the data presented in [14], we estimate the insertion loss of this device to be of the order of 14 dB (corresponding to a transmission of  $\sim 4\%$ ), with 7 dB of this attributed to the additional insertion loss of the polarizer. This approach, however, requires considerable post-growth processing and the use of materials that are difficult to integrate into the semiconductor fabrication process.

Another approach to this problem would be to incorporate the strain and the anisotropy into the growth process by growing lattice-mismatched MQW's with an appropriate crystallographic orientation. To date, most light modulators manufactured from compound semiconductor MQW

heterostructures have been synthesized from GaAs-(Al,Ga)As or (In, Ga)As-GaAs grown on (100)-GaAs or InP substrates, primarily because of the ease of growth. Recent theoretical calculations [15]-[18] have predicted large optical anisotropies for MQW structures grown on substrates with orientations other than the conventional [001]. The largest anisotropies have been calculated [18] for the  $(\sqrt{3}10)$  and  $(1\sqrt{3}0)$  surfaces, however the appropriate materials for verifying these features have not yet been grown. Of more immediate interest are the (11 $\bar{1}$ ) family of planes, due to the relative ease of epitaxial growth in these orientations. Among this family, the largest in-plane optical anisotropy has been calculated for the [110] direction [17].

This intrinsic anisotropy (i.e., the difference between optical transition strengths for light polarized along the  $[\bar{1}10]$  and [001] directions) can arise either from quantum confinement or from strain. Even in the absence of strain, [110]-oriented QW's have an intrinsic anisotropy that is associated with the reduced symmetry of QW's grown on (110) surfaces compared with those on grown on (001) and (111) surfaces [18]. This optical anisotropy may be dramatically increased by incorporating a biaxial strain in the plane of the QW's [17]. The presence of this anisotropy has been experimentally verified [19], [20]. Furthermore, Sun *et al.* [21] have used the anisotropic gain associated with [110]-oriented biaxially strained MQW's to control the polarization direction of vertical-cavity surface-emitting laser structures. In addition, we have shown previously [22] that the intrinsic optical anisotropy can be exploited to construct an optically addressed polarization sensitive modulator. In this device, which contained only 50 wells, a 25:1 contrast ratio was achieved while operating at room temperature.

Here, we demonstrate that the intrinsic optical anisotropy of biaxially strained [110]-oriented GaAs- $\text{In}_x\text{Ga}_{1-x}\text{As}$  MQW's can be electrically addressed to produce a polarization-sensitive electrooptic modulator. In this proof-of-principle device, a change in the bias voltage produces a modulation of the dichroism and birefringence in the plane of the wells. This differential change in optical anisotropy, in turn, produces a modulation of the polarization state of a linearly polarized input pulse by changing its ellipticity and direction of polarization. This modulation of the polarization state is then converted into an amplitude modulation by using an appropriately oriented quarter-wave plate ( $\lambda/4$  plate) and an analyzer. The active mechanism for this device is the change in the in-plane anisotropy associated with the QCSE as a function of applied voltage. This is to be contrasted with the QCSE amplitude modulators discussed earlier, where the amplitude change is produced by an isotropic shift of the excitonic absorption with voltage. Nevertheless, both devices rely on the QCSE. Consequently, we expect to be able to make many of the same tradeoffs between design parameters as have been made for previous QCSE devices. For example, the presence of the  $\lambda/4$  plate and analyzer allows additional insertion loss to be exchanged for a higher contrast ratio. In this way, these polarization-rotation modulators extend the range of QCSE devices, and they have the potential for finding a niche in applications where extremely high contrast

ratios (on the order of  $10^4$ ) are needed and where additional insertion losses (of  $\sim 3$ – $20$  dB) can be tolerated.

We also report direct and detailed measurements of the anisotropy in both the real and imaginary parts of the complex index of refraction as a function of wavelength for selected voltages by using sensitive ellipsometric techniques. The latter measurements determine the differential anisotropy in the indices of refraction and the absorption coefficients between the on and off states, and they allow us to calculate the operating wavelength that maximizes the contrast ratio. To illustrate this predictive capability, we test and evaluate a unoptimized device containing only 50 6-nm-wide wells, and we show that the measured values for the contrast ratios, optical bandwidths, and tunability agree with expectations based on the ellipsometric measurements. Finally, we discuss device improvements and tradeoffs between the various design parameters. Specifically, we illustrate (as with QCSE amplitude modulators [7], [8]) that excitonic linewidth can be traded for tunability or operating temperature.

## II. EXPERIMENTAL

The device used here is the same one used in our previous nonlinear optical studies [22]. It is a p-i-(MQW)-n diode that was grown on a semi-insulating [110]-substrate which was tilted  $6^\circ$  toward the [111]B direction to ensure good layer quality [23]. Beginning with the substrate, the MBE growth consisted of: 1) a 1- $\mu\text{m}$ -thick  $n^+$ -GaAs buffer layer; 2) then a 100-nm-thick layer of n-type GaAs; 3) followed by the intrinsic MQW region; and finally, 4) a 100-nm-thick capping layer of p-type GaAs. The intrinsic MQW region consists of 50 periods of 6-nm-wide  $\text{In}_{0.13}\text{Ga}_{0.87}\text{As}$  QW's separated by 8-nm-thick GaAs barriers. The sample was processed into an array of mesas, each with electrical contacts which allowed the p-doped capping layer to be biased with respect to a common electrical connection to the n-doped layer. The current-voltage characteristics of the sample show it to be a good diode with a breakdown voltage of  $\sim 20$  V.

All of the optical measurements were performed using a synchronously modelocked styrl-13 dye laser that produced pulses with a 2-ps duration (FWHM). The repetition rate could be controlled between 147 kHz and 38 MHz using a cavity dumper and was selected to ensure complete recovery of the sample between pulses. For all measurements presented in this paper, the pulse fluence was reduced to  $< 0.2 \mu\text{Jcm}^{-2}$  to ensure that the sample transmission remained linear and to preclude any nonlinear effects.

The room-temperature anisotropy in the absorption of the device is illustrated in Fig. 1, which shows the measured linear absorption coefficients for incident light polarized parallel to the  $[\bar{1}10]$  and  $[001]$  axes. The assignment of these directions is slightly inaccurate due to the  $6^\circ$  tilt of the [110] GaAs substrate toward the [111]B direction. The small residual effects of the substrate were removed by subtracting the absorbance spectra measured with the beam passing through the entire device, including substrate, from the spectra measured with only the substrate in place. Notice that the heavy hole exciton resonances are clearly visible at room temperature, but are

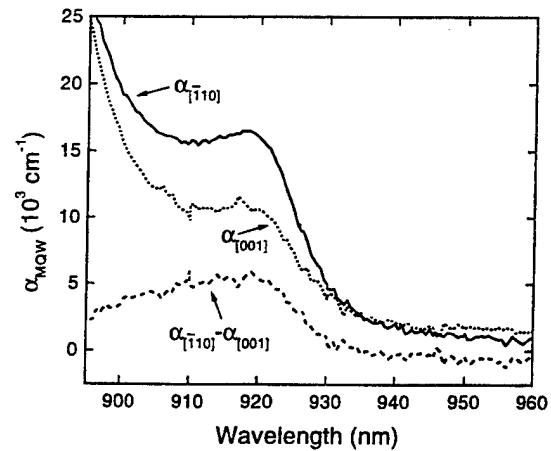


Fig. 1. The measured linear absorption coefficients of [110]-oriented  $\text{In}_{0.13}\text{Ga}_{0.87}\text{As}$ -GaAs MQW's as a function of wavelength for incident light polarized parallel to the  $[\bar{1}10]$  (solid line) and  $[001]$  (short dashed line) crystallographic axes of the [110]-oriented GaAs-InGaAs MQW's, and the difference in the two coefficients (long dashed line).

much broader in this particular sample than in high-quality GaAs-AlGaAs MQW's grown in the  $[001]$ -direction. As we will discuss, this feature can be used to an advantage to increase the tunability and optical bandwidth and to increase the operating temperature range (however, at the expense of a decrease in contrast ratio or an increase in switching voltage). The maximum change in absorption ( $\Delta\alpha$ ) is seen to be  $6.6 \times 10^3 \text{ cm}^{-1}$  at about 919 nm.

The prototype that we use to demonstrate electrooptic polarization modulation is shown schematically in Fig. 2. It consists of an initial polarizer  $P_1$  that is oriented to produce incident light that is linear and s-polarized (taken as the  $y$  direction). The sample is inserted with its two principal axes ( $[\bar{1}10]$  and  $[001]$ ) oriented at  $45^\circ$  with respect to the incident light, as shown in Fig. 2. Because of the dichroism (shown in Fig. 1) and the birefringence associated with these two axes, the signal light will emerge from the sample elliptically polarized and with its polarization direction rotated. A quarter-wave ( $\lambda/4$ ) plate and an analyzer  $P_2$  are then used to extinguish the light transmitted by the sample when it is in the off state. The  $\lambda/4$  plate is oriented with its fast axis at an angle  $\theta$  with respect to the polarization direction of the incident light. The angle  $\theta$  is chosen so as to compensate for the ellipticity introduced by the sample when it is in the off state (i.e.,  $V = 0$ ) and by the substrate. The analyzer is nominally crossed with respect to the incident light, and it is rotated through an angle  $\psi$  with respect to the  $x$  direction to compensate for the rotation of the signal polarization introduced by the sample (in its off state), the sample substrate and the  $\lambda/4$  plate.

## III. ELLIPSOMETRIC MEASUREMENTS

The dichroism and the birefringence of the MQW's

$$\Delta\alpha_{\text{MQW}}(\lambda, V) = \alpha_{[\bar{1}10]}^{\text{MQW}}(\lambda, V) - \alpha_{[001]}^{\text{MQW}}(\lambda, V) \quad (1)$$

and

$$\Delta n_{\text{MQW}}(\lambda, V) = n_{[\bar{1}10]}^{\text{MQW}}(\lambda, V) - n_{[001]}^{\text{MQW}}(\lambda, V) \quad (2)$$

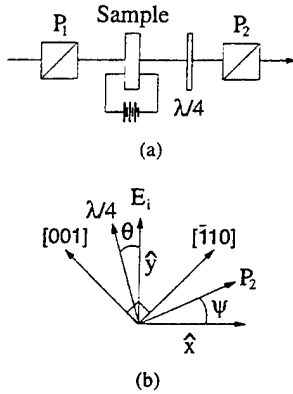


Fig. 2. Schematic of the geometry used to demonstrate electrooptic polarization modulation using  $[110]$ -oriented strained MQW's, where  $P_1$  and  $P_2$  denote polarizers,  $\lambda/4$  a quarter-wave plate,  $E_i$  the  $s$ -polarization of the incident field,  $\theta$  the orientation of the fast axis of the  $\lambda/4$  plate, and  $\psi$  the pass axis of the analyzer  $P_2$  and where  $[110]$  and  $[001]$  denote the orientation of the principal crystallographic axes. The same geometry, with the  $\lambda/4$  plate removed, was used for the ellipsometric measurements of the birefringence and dichroism of these samples as a function of voltage.

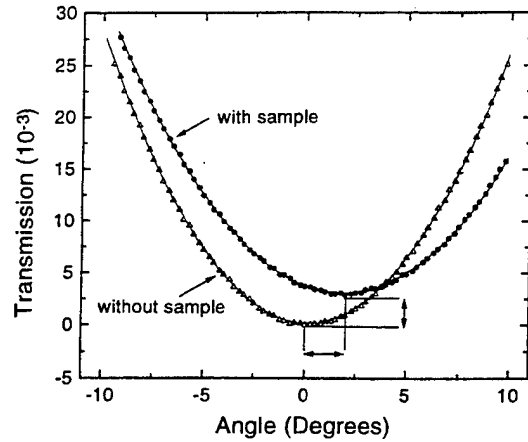


Fig. 3. A typical ellipsometric measurement of the birefringence and dichroism at a wavelength of 925 nm and a bias of 0 V. The transmission of the apparatus shown in Fig. 1 was measured as a function of the angle  $\psi$ , with the  $\lambda/4$  plate removed, with and without the sample in place. The solid lines are fits to the parabolic form given by (3) of the text. The horizontal displacement of the minimum is proportional to the anisotropy in the absorbance and the vertical displacement to the anisotropy in the birefringence.

respectively are functions of the wavelength  $\lambda$  and the bias voltage  $V$ , where  $\alpha_{[110]}^{\text{MQW}}$  ( $\alpha_{[001]}^{\text{MQW}}$ ) and  $n_{[110]}^{\text{MQW}}$  ( $n_{[001]}^{\text{MQW}}$ ) are the absorption coefficient and the refractive index of the wells, respectively, for light polarized along the  $[110]$  ( $[001]$ ) direction. Similarly, for wavelengths near the MQW heavy-hole exciton, the substrate has a birefringence  $\Delta n_s$ , and it has a weak anisotropic absorption  $\Delta \alpha_s$  that is associated with the band tail of GaAs. To deterministically optimize the modulator contrast ratio by choosing the correct operating wavelength, it is first necessary to determine the magnitude and dispersion associated with this anisotropy, and it is useful to separate the effects of the substrate from those of the MQW structure. In this section, we describe our measurement of these parameters using sensitive ellipsometric techniques.

The experimental geometry that we used for the ellipsometric measurements was identical to that shown in Fig. 2 for the modulator, except that the quarter-wave plate was removed. In this configuration, the transmission  $T$  of the crossed polarizer-analyzer pair (with the sample in place) can be written as a function of the orientation of the analyzer, for small analyzer angles  $\psi$ , as

$$T(\psi) = (1 - R)^2 \exp[-(\alpha_{\text{MQW}}d + \alpha_s l)] \cdot \left[ \left( \psi - \frac{\Delta \alpha_{\text{MQW}}d + \Delta \alpha_s l}{4} \right)^2 + \left( \frac{\pi(\Delta n_{\text{MQW}}d + \Delta n_s l)}{\lambda} \right)^2 \right] \quad (3)$$

where  $R$  is the reflection coefficient of the air-semiconductor interface and  $d(l)$  is the total thickness of the QW's (substrate) and where

$$\alpha_{\text{MQW}} = (\alpha_{[110]}^{\text{MQW}} + \alpha_{[001]}^{\text{MQW}})/2$$

and

$$\alpha_s = (\alpha_{[110]}^s + \alpha_{[001]}^s)/2$$

are the average absorption coefficients of the MQW's and the substrate, respectively. Notice that the analyzer transmission is a parabolic function of the angle  $\psi$ , that the minimum is displaced from  $\psi = 0$  by  $(\Delta \alpha_{\text{MQW}}d + \Delta \alpha_s l)/4$ , and that the transmission is offset from  $T = 0$  by an amount proportional to  $(\pi(\Delta n_{\text{MQW}}d + \Delta n_s l)/\lambda)^2$ .

Typical ellipsometric measurements are shown in Fig. 3 for a wavelength of 925 nm and a bias of 0 V. The location of  $\psi = 0$  was determined experimentally by locating the minimum in transmission with no sample in place. The results of such a calibration are shown as the open triangles in Fig. 3. The transmission was then measured as a function of analyzer angle  $\psi$  with the sample in place. Values for the total anisotropic absorbance  $\Delta \alpha_{\text{MQW}}d + \Delta \alpha_s l$  and the total anisotropic phase delay  $2\pi(\Delta n_{\text{MQW}}d + \Delta n_s l)/\lambda$  were then extracted using (3). This procedure was repeated as the wavelength of the laser was tuned across the excitonic absorption feature for each of several selected bias voltages.

Representative measurements of  $\Delta \alpha_{\text{MQW}}d + \Delta \alpha_s l$  and  $2\pi(\Delta n_{\text{MQW}}d + \Delta n_s l)/\lambda$  as a function of wavelength are summarized in Figs. 4 and 5, respectively, for bias voltages of 0 and 6 V. Also shown are the results of measurements of the anisotropy in the substrate absorbance  $\Delta \alpha_s l$  and phase delay  $2\pi(\Delta n_s l)/\lambda$ . The latter data are represented by the open squares in Figs. 4 and 5. The open squares were obtained with the sample in place but displaced slightly, so that the laser light passed through the substrate, but no longer passed through a mesa containing the MQW layers.

The contributions of the MQW region to the overall anisotropy,  $\Delta \alpha_{\text{MQW}}d$  and  $2\pi(\Delta n_{\text{MQW}}d)/\lambda$ , can be isolated by subtracting the measurements taken through only the substrate from those taken through both the substrate and the MQW region, since the laser pulses are very weak and the transmission has been experimentally verified to be linear. As shown in Fig. 4, both the absorbance and the dichroism of the substrate are negligible compared to those measured through

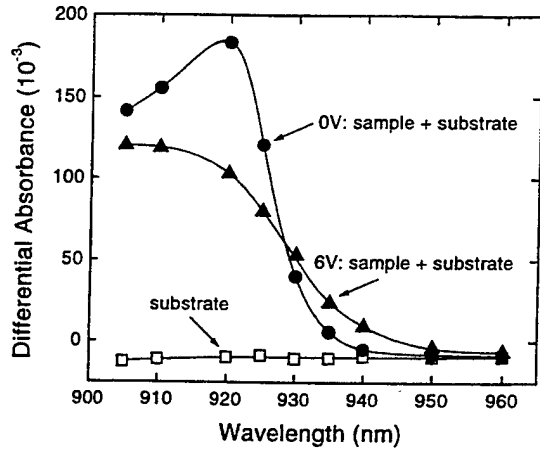


Fig. 4. Ellipsometric measurements of the differences in the absorbance of the MQW sample, including the substrate, for light polarized along the two principal crystallographic axes,  $\Delta\alpha_{MQWd} + \Delta\alpha_s l$ , for a bias of 0 V (solid circles) and 6 V (solid triangles) and of the substrate alone (open squares). The lines are guides to the eye.

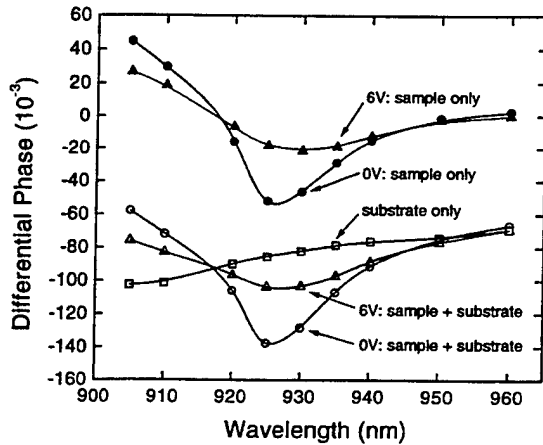


Fig. 5. Ellipsometric measurements of the differences in the phase delays of the MQW region for light polarized along the two principal crystallographic axes,  $2\pi(\Delta n_{MQWd})/\lambda$ , for a bias voltage of 0 V (solid circles) and 6 V (solid triangles). The results for the MQW region were obtained by subtracting the corresponding results for the MQW region plus substrate  $2\pi(\Delta n_{MQWd} + \Delta n_s l)/\lambda$  (open circles and triangles for 0 and 6 V, respectively) from those for the substrate alone  $2\pi(\Delta n_s l)/\lambda$  (open squares). The lines are guides to the eye.

the device plus substrate. Consequently, the solid circles and the solid triangles in Fig. 4 approximately give the anisotropy of the MQW region, i.e.,  $\Delta\alpha_{MQWd}$ . By comparison, as shown by the open squares in Fig. 5, the substrate exhibits significant birefringence, and this birefringence is found to be unaffected by the bias voltage applied across the p-i-(MQW)-n region (at least for the range of voltages studied here). When the birefringence of the substrate is eliminated, the contributions of the MQW region,  $2\pi(\Delta n_{MQWd})/\lambda$ , are given by the solid circles and the solid triangles for 0 and 6 V, respectively.

As a check on consistency and as assurance that we have successfully separated the effects of the substrate from those of the MQW's, we compare in Fig. 6 the measured values for the dichroism  $\Delta\alpha_{MQW}$  of the MQW's (at 0 V) as taken from the ellipsometric measurements of Fig. 4 with those taken from

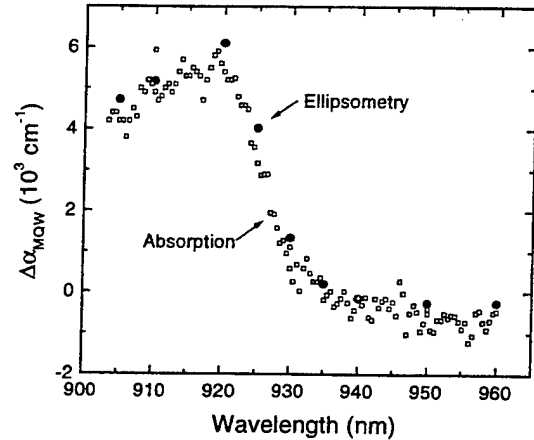


Fig. 6. Comparison of ellipsometric (Fig. 4) and transmission (Fig. 1) measurements of the difference in the absorption coefficients of the MQW region for light polarized along the two principal crystallographic axes,  $\Delta\alpha_{MQW}$ .

the anisotropic absorption measurements of Fig. 1. Notice that the two sets of data are in excellent qualitative and very good, but not perfect, quantitative agreement. The data for the absorption measurements (Fig. 1) and for the ellipsometric measurements (Fig. 4) were knowingly taken from different positions on a single mesa. We have separately determined that the absorption spectra vary slightly from position to position. The data in Fig. 6 give a good indication of the errors that can be introduced by day-to-day repositioning of the sample.

We make a similar comparison for the birefringence of the MQW's in Fig. 7. In this figure, we compare the values of  $\Delta n_{MQW}$  taken from the ellipsometric measurements of Fig. 5 to the values calculated by means of a Kramers-Kronig transformation of the anisotropic absorption measurements of Fig. 1. Again, as with the dichroism, there is excellent qualitative agreement and reasonable quantitative agreement between the two sets of measurements. In this case, the principal sources of error are believed to be the finite spectral range for the absorption data used for the Kramers-Kronig transformation and the spot-to-spot variations in well width, composition, and surface quality across the sample. The results shown in Figs. 6 and 7 clearly confirm that the anisotropy in the absorption displayed in Fig. 1 can be attributed entirely to the MQW region and that the effect of the substrate is to introduce a background birefringence, which we have now successfully quantified.

#### IV. DESIGN AND DEMONSTRATION OF MODULATOR

The principal factor to be chosen in order to optimize the contrast ratio of the polarization modulator shown in Fig. 2 is the operating wavelength. By using a quarter-wave plate and an analyzer, one can, in principle, always null the light that is transmitted by the sample when it is in its off state. In practice, the degree to which this light can be extinguished is limited by the extinction ratio of the polarizer pair and sample uniformity. Nevertheless, for all practical purposes, the degree to which the off-state transmission can be nulled is independent of operating wavelength. Consequently, the operating wavelength

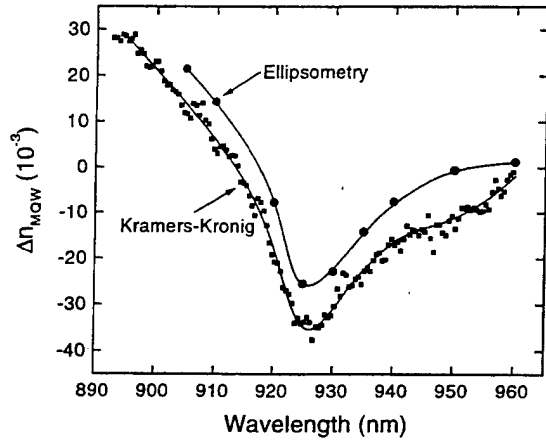


Fig. 7. Comparison of ellipsometric (Fig. 5) measurements of the difference in the indices of refraction of the MQW region for light polarized along the two principal crystallographic axes  $\Delta n_{MQW}$  with the same quantity obtained by performing a Kramers-Kronig transformation on the transmission measurements from Fig. 1. The lines are guides to the eye.

should be chosen to provide the combination of dichroism and birefringence that will maximize the transmission in the on state. Since the anisotropy associated with the substrate is independent of the operating voltage, the effect of the substrate can be negated at each wavelength by judiciously choosing the initial positions of the analyzer and  $\lambda/4$  wave plate. The transmission of the modulator in the on state can then be maximized simply by maximizing the combined changes in the birefringence and in the dichroism of the MQW's between the off and on states.

To make these comments more quantitative, we begin by noting that the transmission of the modulator with the  $\lambda/4$  wave plate in place can be written (for small angles  $\psi$  and  $\theta$ ) as

$$T(\psi) = (1 - R)^2 \exp[-(\alpha_{MQW}d + \alpha_s l)] \cdot \left[ \left( (\psi - \theta) - \frac{\pi(\Delta n_{MQW}d + \Delta n_s l)}{\lambda} \right)^2 + \left( \theta - \frac{\Delta \alpha_{MQW}d + \Delta \alpha_s l}{4} \right)^2 + X \right] \quad (4)$$

where  $X$  represents the extinction ratio of the polarizer-analyzer pair and the  $\lambda/4$  plate together with the sample in

place. Experimentally, the transmission of the modulator in its off state (0V) is minimized at each wavelength  $\lambda$  by arranging the analyzer and  $\lambda/4$  wave plate such that

$$(\psi - \theta) = \frac{\pi(\Delta n_{MQW}(\lambda, 0V)d + \Delta n_s(\lambda)l)}{\lambda} \quad (5)$$

and

$$\theta = \frac{\Delta \alpha_{MQW}(\lambda, 0V)d + \Delta \alpha_s(\lambda)l}{4} \quad (6)$$

When these conditions are used in (4), the transmission in the off state is given by

$$T(\lambda, 0V) = X(1 - R)^2 \exp[-(\alpha_{MQW}(\lambda, 0V)d)] \quad (7)$$

and the transmission in the on state, which determines the insertion loss, is given by (8), shown at the bottom of the page. The contrast ratio (CR) is then trivially obtained by taking the ratio of the two transmissions. The result is given by (9), shown at the bottom of the page.

The values for  $\Delta \alpha_{MQW}(\lambda, V)$  and  $\Delta n_{MQW}(\lambda, V)$  that were measured in the previous section can now be used in (9) to calculate the wavelength dependence of the contrast ratio and to determine the optimal operating wavelength. The results of such a calculation are shown by the open circles in Fig. 8. Notice that the contrast ratio is strongly peaked with a maximum value of  $\sim 10:1$  predicted near 923 nm and a width of approximately 10 nm (FWHM). The solid circles in Fig. 8 represent measurements of the CR as a function of wavelength which confirm these predictions. The measured values are seen to have a marginally narrower spectrum than those predicted theoretically. This is not the result of a fundamental difference between the calculated and measured values, but is an artifact of our measurement procedures. As inspection of (4)–(6) reveals, minimization of the modulator transmission in the off state (0 V) requires the optimization of the orientations of the  $\lambda/4$  wave plate and analyzer; unfortunately,  $\theta$  and  $\psi$  do not enter independently. Therefore, this optimization requires a tedious and laborious procedure consisting of choosing an orientation for  $\theta$ , subsequently rotating  $\psi$  until a relative minimum is obtained, and then repeating this procedure until an absolute minimum is definitively identified. Such a procedure was rigorously followed near 923 nm; however, away from this wavelength, a simpler and less precise technique was employed. Namely, the analyzer was optimized, but the  $\lambda/4$  wave plate was left unchanged. Consequently, the CR is

$$T(\lambda, 6V) = (1 - R)^2 \exp[-(\alpha_{MQW}(\lambda, 6V)d)] \cdot \left[ \left( \frac{\Delta \alpha_{MQW}(\lambda, 6V)d - \Delta \alpha_{MQW}(\lambda, 0V)d}{4} \right)^2 + \left( \frac{\pi(\Delta n_{MQW}(\lambda, 6V)d - \Delta n_{MQW}(\lambda, 0V)d)}{\lambda} \right)^2 + X \right] \quad (8)$$

$$CR(\lambda) = \frac{\exp[(\alpha_{MQW}(\lambda, 0V) - \alpha_{MQW}(\lambda, 6V)d)]}{X} \cdot \left[ \left( \frac{\Delta \alpha_{MQW}(\lambda, 6V)d - \Delta \alpha_{MQW}(\lambda, 0V)d}{4} \right)^2 + \left( \frac{\pi(\Delta n_{MQW}(\lambda, 6V)d - \Delta n_{MQW}(\lambda, 0V)d)}{\lambda} \right)^2 + X \right] \quad (9)$$

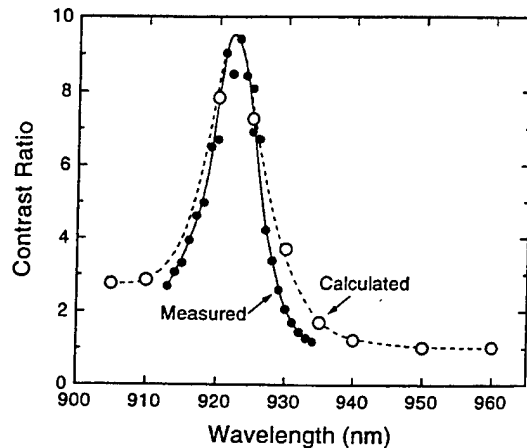


Fig. 8. Comparison of the measured (solid circles) and calculated (open circles) values for the contrast ratio of the [110]-oriented GaAs-InGaAs MQW electrooptic polarization modulator shown in Fig. 2. The calculated values were obtained using the differential absorbance and phase provided by the ellipsometric measurements of Figs. 4 and 5. The lines are guides to the eye.

expected to be increasingly less than ideal for wavelengths away from the peak.

The excitonic feature shown in Fig. 1 is much broader than that expected for high-quality [001]-oriented GaAs/AlGaAs MQW's (e.g.,  $<2$  nm); however, the broad exciton in the present sample has effectively allowed us to trade CR for optical bandwidth and tunability or, equivalently, for insensitivity to changes in ambient temperature. This tunability is evident in Fig. 8. Notice that the modulator maintains a contrast ratio of  $>4:1$  over a wavelength range of  $>10$  nm, which corresponds to an operating temperature range of  $>35$  °C. Consequently, this device is much less sensitive to temperature than typical GaAs-AlGaAs amplitude modulators that exhibit narrower excitons, have a smaller operating bandwidth, yet exhibit similar contrast ratios. Note that the approach of trading excitonic linewidth (i.e., CR) for insensitivity to temperature is similar to that used in [7] and [8] in extending the operating temperature range for QCSE amplitude modulators.

For the measurements shown in Fig. 8, the analyzer (but not the  $\lambda/4$  wave plate) orientation was optimized at each wavelength. In ordinary use, both would remain fixed. Consequently, the tunability and optical bandwidth of the modulator used here are illustrated in an alternative way in Fig. 9, where we show the measured CR as a function of wavelength for selected fixed orientations of the analyzer. For these measurements, the  $\lambda/4$  wave plate orientation was optimized for operation at 923 nm and held fixed thereafter. For the curve with the maximum contrast ratio at 923 nm, which has the analyzer set to  $4.6^\circ$ , the CR can be seen to be greater than  $5:1$  for an optical bandwidth of  $\sim 4$  nm. In addition, the modulator response is shown to be tunable over a range of  $\sim 10$  nm by changing the orientation of the analyzer, but not the  $\lambda/4$  wave plate. The latter is the same tunability that is evident in Fig. 8 and was discussed in the preceding paragraph.

The peak switching ratio at 923 nm is shown in Fig. 10 to increase as a function of voltage to a value of  $22:1$  at 13 V, corresponding to a field of  $\sim 188$  kV/cm. Most importantly, notice that contrast ratios in excess of  $4:1$  can be obtained with

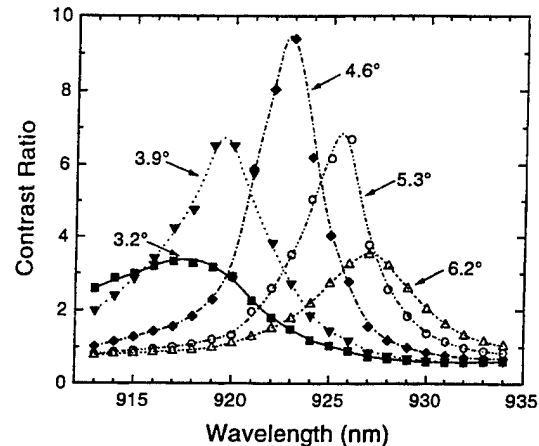


Fig. 9. Demonstration of the tunability of the polarization modulator. The contrast ratio is shown as a function of wavelength for selected fixed orientations of the analyzer angle  $\Psi$  with the orientation of the  $\lambda/4$  plate fixed.

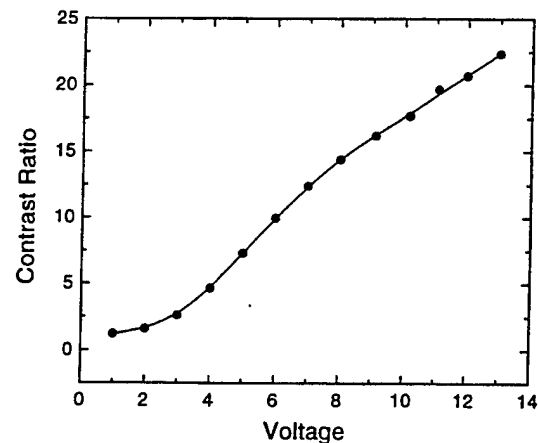


Fig. 10. The CR of the electrooptic polarization modulator at 923 nm as a function of the reverse bias voltage. The line is a guide to the eye.

switching voltages as low as 4 V (corresponding to a field of  $\sim 57$  kV/cm), even for devices with as few as 50 wells.

The results shown in Figs. 8–10 clearly demonstrate that the in-plane dichroism and birefringence of [110]-oriented MQW's can be used to construct a polarization-sensitive electrooptic modulator. Moreover, the tunability, optical bandwidth, switching voltage, and temperature range of the current device are impressive; however, the contrast ratio ( $10:1$ ) is disappointing and the insertion loss ( $\sim 33$  dB) is daunting. We wish to emphasize that these values are not indicative of what can be achieved, but are a consequence of the unoptimized sample used in this first proof-of-principle demonstration. We estimate that a more realistic design coupled with slight improvements in materials quality should result in typical contrast ratios in the range of  $10^3:1$ – $10^4:1$  (i.e., 30–40 dB of dynamic range) with overall device transmissions in the range of 1%–30% (insertion losses of 5–20 dB), depending on other device constraints.

In the current unoptimized device, the peak contrast ratio and the optical throughput are limited by a number of factors.

The most important is the thickness of the QW region,  $d$ . For our sample, this region has a thickness of 300 nm (i.e., 50 wells, each 6 nm thick). As indicated by (9), for a given set of material parameters, the CR (in the small signal limit) increases rapidly in direct proportion to  $d^2 \exp[(\alpha(0V) - \alpha(6V))d]$ . By comparison, inspection of (8) indicates that the device transmission in the on state increases and then decreases with thickness as dictated by the factor  $d^2 \exp[-\alpha(6V)d]$ . Consequently, if we use the materials values presented in Figs. 1, 4, and 5 (i.e., if we keep the same material), but we increase the thickness of the MQW region so as to optimize the throughput (i.e.,  $d = 2/(\alpha(6V))$ ), it is straightforward to show, using (8) and (9), that the CR can be increased to  $>1000:1$  (30 dB) and the optical throughput to 1% (20-dB insertion loss). Notice that, since in this analysis, we are keeping the same material, the optical bandwidth, tunability, and operating temperature range represented in Fig. 9 would be maintained. It should be recognized, however, that increasing the MQW thickness will increase the switching voltage proportionately. In this case, the price paid for a high CR, good optical bandwidth, tunability, and a wide operating temperature range will be a relatively high insertion loss and a high switching voltage.

In addition, a similar analysis indicates that improved MQW material with a narrower exciton should allow an improved throughput and an improved CR for a given thickness and switching voltage, but this would come at the loss of some of the optical bandwidth, tunability, and operating temperature range illustrated in Fig. 9.

## V. SUMMARY AND CONCLUSION

We have used an ellipsometric technique to determine the anisotropies of the refractive indices and absorption coefficients along the principal axes of a [110]-oriented GaAs-InGaAs p-i(MQW)-n diode structure as a function of wavelength for selected reverse bias voltages. We have also demonstrated that this intrinsic in-plane dichroism and birefringence, which are associated with the crystallographic orientation and biaxial strain, can be used to construct a polarization-sensitive electrooptic modulator. The measured differential changes in these anisotropies with voltage have then been used to choose the optimum operating wavelength and to predictably evaluate the performance of this device. As predicted, the unoptimized device used here exhibited a contrast ratio of 10:1 when biased at 6 V, had an insertion loss of  $\sim 33$  dB, had an optical spectral bandwidth of 4 nm and could be tuned over  $>10$  nm with a contrast ratio of  $>4:1$ . The latter translates into a useable operating temperature range of  $>35^\circ\text{C}$ .

This relatively low contrast ratio (by comparison to other polarization-sensitive devices) and the high insertion loss are not typical of [110]-oriented polarization modulators, but are primarily the result of a thin QW region (total well thickness of 300 nm) and a relatively broad excitonic linewidth in the unoptimized sample that happened to be available for this demonstration. We estimate that by simply increasing the thickness of the current material the CR could be increased to  $>1000:1$  and the insertion loss reduced to 20 dB, but at

the expense of an increased switching voltage. The use of improved MQW material with narrower excitonic features should further improve both CR and throughput, but at the expense of optical bandwidth and tunability (and therefore increased sensitivity to ambient and device temperature changes). The latter may or may not represent a desirable trade.

Typically, polarization-sensitive QCSE modulators are capable of higher contrast ratios than the equivalent amplitude modulators, but they have a higher insertion loss. Essentially, the presence of the polarizers restricts throughput, but boosts the modulation ratio without restricting bandwidth. Consequently, as a class, QCSE polarization modulators will be most useful for applications that require high dynamic range, but will tolerate higher insertion loss. A disadvantage of the polarization modulators described here is that they require growth in an unconventional direction. Nevertheless, they have an advantage over uniaxially strained polarization rotation modulators, which require bonding to a substrate and subsequent epitaxial lift off, in that they require less post-growth processing.

## REFERENCES

- [1] D. A. B. Miller, D. S. Chemla, T. C. Damen, A. C. Gossard, W. Wiegmann, T. H. Wood, and C. A. Burrus, "Electric field dependence of optical absorption near the band gap of quantum well structures," *Phys. Rev. B*, vol. 28, pp. 1043-1060, 1985.
- [2] K. W. Jelley, R. W. H. Engelman, K. Alavi, and H. Lee, "Well size related limitations on maximum electroabsorption in GaAs/AlGaAs multiple quantum well structures," *Appl. Phys. Lett.*, vol. 55, pp. 70-72, 1989.
- [3] D. A. B. Miller, "Quantum-well self-electro-optic effect devices," *Opt. Quantum Electron.*, vol. 22, pp. S61-S98, 1990.
- [4] K.-K. Law, R. H. Yan, L. A. Coldren and J. L. Merz, "Self-electro-optic devices based on a superlattice asymmetric Fabry-Perot modulator with an on-off ratio greater than 100:1," *Appl. Phys. Lett.*, vol. 57, pp. 1345-1347, 1990.
- [5] C.-H. Lin, K. W. Goossen, K. Sadra and J. M. Meese, "Normally-on GaAs/AlAs multiple quantum well Fabry-Perot reflection modulators for large 2-dimensional arrays," *Appl. Phys. Lett.*, vol. 65, pp. 1242-1244, 1994.
- [6] B. Pezeshki, D. Thomas, and J. S. Harris, "Optimization of modulation ratio and insertion loss in reflective electroabsorption modulators," *Appl. Phys. Lett.*, vol. 57, pp. 1491-1492, 1990.
- [7] K. W. Goosen, J. E. Cunningham, W. Y. Jan and D. A. B. Miller, "Interleaved contact electroabsorption modulator using doping selective contacts with  $25^\circ\text{C}$  to  $95^\circ\text{C}$  operating range," *IEEE Photon. Technol. Lett.*, vol. 5, pp. 181-183, 1993.
- [8] K. W. Goosen, J. E. Cunningham, W. Y. Jan, "Optical bandwidth considerations in p-i-n multiple quantum well modulators," *J. Lightwave Technol.*, vol. 13, pp. 461-464, 1995.
- [9] R. Windisch, M. Kneissl, P. Kiesel, B. Knüpfer, and G. H. Döhler, "Low voltage high-contrast n-i-p-i based waveguide modulators with alloyed selective contacts," *IEEE Photon. Technol. Lett.*, vol. 10, pp. 1325-1327, 1996.
- [10] X. R. Huang, S. K. Cheung, A. N. Cartwright, A. L. Smirl, W. F. Tseng, and J. G. Pellegrino, "An interdigitated stacked p-i-n multiple quantum well modulator," *IEEE Photon. Technol. Lett.*, vol. 8, pp. 1172-1174, 1996.
- [11] W. A. Schroeder, D. S. McCallum, D. R. Harken, M. D. Dvorak, D. R. Andersen, and A. L. Smirl, "Intrinsic and induced anisotropy of nonlinear absorption and refraction in zincblende semiconductors," *J. Opt. Soc. Amer. B*, vol. 12, pp. 401-415, 1995.
- [12] H. Shen, M. Wraback, J. Pamulapati, P. G. Newman, M. Dutta, Y. Lu and H. C. Kuo, "Optical anisotropy in GaAs/AlGaAs multiple quantum wells under thermally-induced uniaxial strain," *Phys. Rev.*, vol. 47, pp. 13933-13936, 1993.
- [13] H. Shen, M. Wraback, J. Pamulapati, M. Dutta, P. G. Newman, A. Ballato, and Y. Lu, "Normal incidence high contrast multiple quantum



- well light modulator based on polarization rotation," *Appl. Phys. Lett.*, vol. 62, pp. 2908-2910, 1993.
- [14] H. Shen, J. Pamulapati, M. Wraback, M. Taysing-Lara, M. Dutta, H. C. Kuo, and Y. Lu, "High contrast optical modulator based on electrically tunable polarization rotation and phase retardation in uniaxially strained (100) multiple quantum wells," *IEEE Photon. Technol. Lett.*, vol. 6, pp. 700-702, 1994.
  - [15] Y. Kajikawa, M. Hata, and T. Isu, "Optical matrix elements in (110)-oriented quantum wells," *Jpn. J. Appl. Phys.*, vol. 30, pp. 1944-45, 1991.
  - [16] Y. Kajikawa, "Anomaly in the in-plane polarization properties of (110)-oriented quantum wells under [110] uniaxial stress," *Phys. Rev. B*, vol. 47, pp. 3649-3660, 1993.
  - [17] R. H. Henderson and E. Towe, "Strain and crystallographic orientation effects on interband optical matrix elements and band gaps of [11 $\bar{1}$ ]-orientated III-V epilayers," *J. Appl. Phys.*, vol. 78, pp. 2447-2455, 1995.
  - [18] ———, "Effective mass theory for III-V semiconductors on arbitrary (*hkl*) surfaces," *J. Appl. Phys.*, vol. 79, pp. 2029-2037, 1995.
  - [19] Y. Kajikawa, M. Hata, T. Isu, and Y. Katayama, "Linear polarization effects in (110) quantum wells for light propagating perpendicular to the well planes," *Surf. Sci.*, vol. 267, pp. 501-504, 1992.
  - [20] D. Sun, E. Towe, M. J. Hayduk, and R. K. Boncek, "Observation of polarization-dependent electroabsorption in (In,Ga)As/GaAs modulator structures oriented in the [110] crystallographic direction," *Appl. Phys. Lett.*, vol. 63, pp. 2881-2883, 1993.
  - [21] D. Sun, E. Towe, P. H. Ostdiek, J. W. Grantham, and G. J. Vansuch, "Polarization control of vertical-cavity surface emitting lasers through the use of an anisotropy gain distribution in [110]-orientated strained quantum-well structures," *IEEE J. Select. Topics Quantum Electron.*, vol. 1, pp. 674-680, 1995.
  - [22] D. S. McCallum, X. R. Huang, A. L. Smirl, D. Sun, and E. Towe, "Polarization rotation modulator in a strained [110]-oriented multiple quantum well," *Appl. Phys. Lett.*, vol. 66, pp. 2885-2887, 1995.
  - [23] D. Sun and E. Towe, "Molecular beam epitaxial growth of (Al,Ga)AsGaAs heterostructures and Si doping characterization study on vicinal (110)-GaAs substrates," *J. Cryst. Growth*, vol. 132, pp. 166-172, 1993.
- M. J. Snelling**, photograph and biography not available at the time of publication.
- X. R. Huang**, photograph and biography not available at the time of publication.
- Dean R. Harken** (S'89-M'91), photograph and biography not available at the time of publication.
- Arthur L. Smirl** (S'73-M'75-SM'84), photograph and biography not available at the time of publication.
- Elias Towe** (S'84-M'87), photograph and biography not available at the time of publication.

## CHAPTER 9

# The Vectorial Dynamics of Coherent Emission from Excitons

Arthur L. Smirl

### 9.1 Introduction

Many nonlinear optical techniques based on ultrafast laser pulses have been used to investigate coherent effects and dephasing processes associated with nonequilibrium carriers and excitons in semiconductors and semiconductor heterostructures [1,2]. One of the techniques that has proven to be very powerful for monitoring the decay of the coherent macroscopic polarization, and the one that has been most frequently used, is four-wave mixing (FWM).

A common geometry for performing time-integrated four-wave mixing (TI-FWM) measurements is shown in Figure 9.1a (e.g., see [3–7]). Typically, each ultrashort pulse from a mode-locked laser is divided into two parts. One pulse with wave vector  $\mathbf{k}_2$  is time delayed by an amount  $\tau_{21} = \tau_2 - \tau_1$  with respect to the other with wave vector  $\mathbf{k}_1$  (where  $\tau_1$  ( $\tau_2$ ) is the time of arrival of the  $\mathbf{k}_1$ -pulse ( $\mathbf{k}_2$ -pulse) at the sample surface). This delay can be either positive or negative. The two pulses are spatially overlapped on the sample surface, and their interaction through the nonlinear material polarization produces an FWM signal in the  $2\mathbf{k}_2 - \mathbf{k}_1$  direction, as shown. Clearly, the material must maintain some degree of memory of the phase of the first pulse until the arrival of the second pulse if signal is to be obtained in the  $2\mathbf{k}_2 - \mathbf{k}_1$  direction for time delays greater than the width of the optical pulses. Consequently, some measure of the coherence time (or dephasing time) in the material can be obtained by simply using a slow detector to measure the FWM signal as a function of the time delay  $\tau_{21}$ , as indicated schematically in Figure 9.1a. Since the detector integrates over the ultrashort emission time, the quantity actually measured is the TI-FWM intensity, which is proportional to

$$I_{TI}(\tau_{21}) \propto \int_{-\infty}^{\infty} |\mathcal{P}_{2\mathbf{k}_2 - \mathbf{k}_1}(t, \tau_{21})|^2 dt, \quad (9.1)$$

where  $\mathcal{P}_{2\mathbf{k}_2 - \mathbf{k}_1}$  denotes the slowly varying amplitude of the material polarization that radiates in the  $2\mathbf{k}_2 - \mathbf{k}_1$  direction. (For thin samples, the field emitted in the  $2\mathbf{k}_2 - \mathbf{k}_1$  direction is proportional to this polarization amplitude.) Additional information can be obtained by using a spectrometer to obtain the TI-FWM spectral

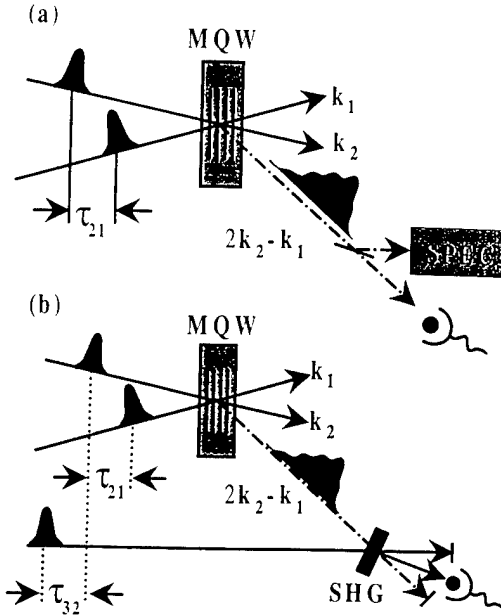


FIGURE 9.1. Conventional geometries for measuring (a) the TI-FWM intensity  $I_{TI}(\tau_{21})$  and the TI-FWM spectral intensity (or power spectrum)  $I_{PS}(\tau_{21}, \omega)$  of the FWM emission, and (b) the TR-FWM intensity  $I_{TR}(\tau_{32}, \tau_{21})$  by performing a cross correlation of the FWM signal with a reference pulse using a second-harmonic-generation crystal (SHG). SPEC denotes a spectrometer.

intensity of the FWM emission as a function of delay:

$$I_{PS}(\tau_{21}, \omega) \propto |\mathcal{P}_{2k_2-k_1}(\tau_{21}, \omega)|^2. \quad (9.2)$$

Typically, time resolution is obtained in conventional FWM experiments by using some variation of the geometry shown schematically in Figure 9.1b (e.g., see [3, 8–13]). In the latter geometry, the time-resolved four-wave mixing (TR-FWM) signal usually is obtained by cross correlating the FWM signal with an ultrashort laser reference pulse. In this case, it is the time-integrated up-converted signal that is measured:

$$I_{TR}(\tau_{32}, \tau_{21}) \propto \int_{-\infty}^{\infty} |\mathcal{P}_{2k_2-k_1}(\tau_{32} - t)|^2 |\mathbf{E}_R(t)|^2 dt, \quad (9.3)$$

where  $\mathbf{E}_R$  is the field of the reference pulse and  $\tau_{32}$  is the delay between the reference and the  $k_2$ -pulse. If the reference pulse is much shorter than the FWM emission, then  $I_{TR}(\tau_{32})$  will provide an accurate representation of the FWM intensity.

Conventional techniques, such as those shown in Figure 9.1, have provided an enormous amount of information about the excitonic dynamics in semiconductors. For example, two of the early observations that proved critical were (i) the existence of a TI-FWM signal at negative time delays [7] and (ii) the observation that

the peak in the TR-FWM emission occurs long after both pump pulses have exited the sample [14]. These two features were initially taken as evidence of the importance of an interaction-induced field (or so-called local field correction (LFC)) [15–18]. Subsequent experiments, in both bulk GaAs and GaAs/AlGaAs multiple quantum wells (MQWs), have indicated that the density-dependent dephasing of the excitonic states [or so-called excitation-induced dephasing (EID)] provides an additional contribution to the FWM signal and can also produce these two features [19–24]. Finally, excitonic molecules (biexcitons) also have been shown to contribute to the FWM signal and to produce TI-FWM signals at negative delays and delayed peaks in the TR-FWM signal (e.g., [25–32]). One of the techniques that has proved to be extremely useful in separating, identifying, and establishing the importance of these processes is to study the strength and evolution of the FWM signal as a function of the state of polarization of the incident pulses. A pronounced dependence on the state of polarization of the incident pulses has been observed in these studies, and this polarization dependence has been used to extract information concerning both coherent and incoherent exciton–exciton interactions.

While there have been a large number of studies (e.g., [8, 9, 11, 20, 22, 29–37]) that have addressed the dependence of the strength of the FWM signal (or its spectrum) on input polarization, there have been few attempts to monitor the polarization state of the emitted FWM signal itself. The first of the latter studies [38, 39] measured, in effect, the orientation of the polarization ellipse associated with the TI-FWM signal, but the degree to which the FWM signal was elliptically (or linearly) polarized and the degree to which the signal was unpolarized were not reported. Even though the state of polarization was only partially determined and the polarization state was not time resolved, these measurements provided significant new information by revealing a previously unexpected dependence of the polarization of the TI-FWM signal on the polarizations of the two input pulses, which was later interpreted in terms of EID. These two early studies stimulated our own interest and work in this area.

Even though conventional TI-FWM and TR-FWM techniques (such as those shown in Figure 9.1) have been very useful, nevertheless, the information that they provide is incomplete. Because such conventional techniques measure either the spectral or the temporal intensity, they provide considerable information about the temporal amplitudes and the spectral amplitudes of the emitted FWM signals, but they provide no information about the temporal phases or the spectral phases. Moreover, such measurements are scalar. That is, they either integrate over all polarization directions or select a single polarization component. Consequently, they provide little or no information about the vectorial nature of the emission. In this chapter the main objective is to demonstrate and describe techniques that fully characterize the emission. That is, they measure the spectral and temporal phases as well as the spectral and temporal amplitudes of the FWM signal, and thus they determine the vectorial dynamics. We hope to convince the reader that the vectorial dynamics contain essential information about the FWM emission and that time-resolved polarization spectroscopy is an extremely sensitive way to

study many-body effects, quantum interference, and material anisotropies—both intrinsic and induced.

The organization of this chapter is as follows. We begin by describing techniques that can be used to directly measure the polarization state of extremely weak coherent emission from quantum wells. In Section 9.2 we describe a femtosecond time-resolved technique that allows the polarization state to be measured directly in the time domain, and in Section 9.3 we describe a spectral interferometric spectroscopic technique that provides the same information by measuring the amplitudes and phases of two orthogonal components of the radiation in the spectral domain. Both of these techniques allow the complete characterization of the emitted FWM signal, including its vectorial dynamics. In Section 9.4 we describe the use of these techniques to measure the polarization state of the time-resolved four-wave mixing signal when only heavy-hole excitons are excited. In the latter section we show that the orientation of the polarization ellipse and the ellipticity vary dramatically and systematically in time during a single FWM emission. In the following section (Section 9.5) we then compare these experimental findings to predictions based on a two-level model for the heavy-hole exciton that does not include many-body effects. The latter model predicts a linear polarization state for the FWM signal that remains constant during the emission. Consequently, taken together, Sections 9.4 and 9.5 suggest that the vectorial dynamics are a direct reflection of the exciton–exciton interactions and dynamics, since without such interactions the polarization state would be linear and constant. In Section 9.6 we show how the simple two-level model of Section 9.5 (based on the optical Bloch equations) can be phenomenologically modified to include such effects as local fields, a density-dependence to the dephasing, and biexcitons, and we show that such a modification produces qualitative agreement with all of the observed tendencies in the data of Section 9.4.

In Section 9.7 we extend our results to include the situation where the laser is tuned to excite both light and heavy holes. In this regime, the ellipticity and orientation of the polarization ellipse (as well as the FWM amplitude) are observed to oscillate dramatically at the heavy-hole–light-hole beat frequency. These studies demonstrate that time-resolve polarimetry is also sensitive to (and can be used to study) quantum interference effects. Finally, in Section 9.8 we describe the use of the polarization selection rules for four-wave mixing and a test that was originally designed to distinguish between quantum beats and polarization interference to demonstrate the presence of strong exciton–exciton correlations and to place quantitative limits on the magnitude of the density-dependent dephasing used in the phenomenological model described in Section 9.6.

## 9.2 Femtosecond Time-Resolved Ellipsometry

One way to time-resolve the polarization state of the FWM emission is to incorporate a quarter-wave ( $\lambda/4$ ) plate, a half-wave ( $\lambda/2$ ) plate, and an analyzing polarizer

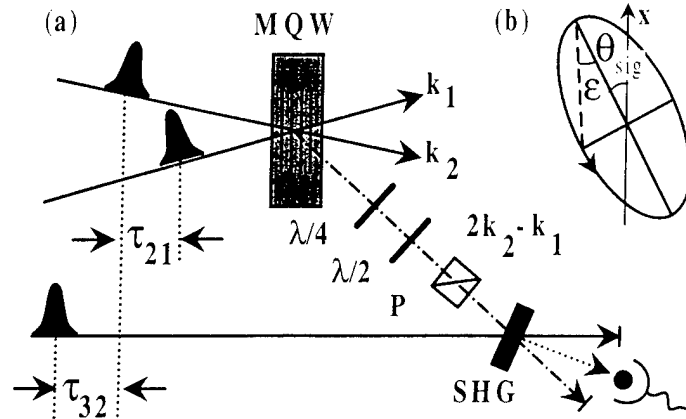


FIGURE 9.2. (a) Schematic of the time-resolved ellipsometric (TRE) apparatus for directly time resolving the polarization state of the emitted FWM signal, where  $\lambda/4$  denotes a quarter-wave plate;  $\lambda/2$ , a half-wave plate; P, a polarizer; and SHG, a second-harmonic-generation crystal. (b) The nomenclature and conventions used to define the polarization ellipse.

(P) into the TR-FWM setup shown in Figure 9.1b, as indicated in Figure 9.2. The complete polarization state in the direction  $2\mathbf{k}_2 - \mathbf{k}_1$  can then be determined by performing measurements using the following (or similar) procedure. With the quarter-wave plate removed, the analyzer is oriented to pass *s*-polarized light. With the analyzer held stationary, the half-wave plate then is rotated through angles ranging from  $0^\circ$  to  $90^\circ$ . For each orientation of the half-wave plate, the TR-FWM signal transmitted by these components is measured by cross correlating it with a reference pulse in a second harmonic generation (SHG) crystal. The quarter-wave plate is then inserted and is oriented with its fast axis along the *x* direction (parallel to the incident *s*-polarized  $\mathbf{E}_2$  field). With the quarter-wave plate and analyzer held stationary, the half-wave plate is again rotated through angles ranging from  $0^\circ$  to  $90^\circ$ , and for each angle, the signal is again cross correlated with the reference pulse. This entire procedure is necessary for obtaining the time-resolved polarization state for a single FWM configuration. It must be repeated for each change in input polarization state, time delay, or excitation fluence.

One can readily show that the intensities transmitted by the analyzer without  $I_{wo}$  and with  $I_w$  the quarter-wave plate present are given by

$$I_{wo}(\varphi) = \frac{1}{2} [S_0 + S_1 \cos(4\varphi) + S_2 \sin(4\varphi)] \quad (9.4)$$

and

$$I_w(\varphi) = \frac{1}{2} [S_0 + S_1 \cos(4\varphi) - S_2 \sin(4\varphi)], \quad (9.5)$$

respectively, where  $\varphi$  is the angle between the *x* axis and the fast axis of the half-wave plate and where the  $S_i$  represent the four Stokes parameters that are sufficient to completely determine the degree and state of polarization of the FWM signal [40]. These Stokes parameters are conventionally defined as [40]  $S_0 = I_x + I_y =$

$I_{+45} + I_{-45} = I_+ + I_-$ ,  $S_1 = I_x - I_y$ ,  $S_2 = I_{+45} - I_{-45}$ , and  $S_3 = I_+ - I_-$ , where  $I_x$ ,  $I_y$ ,  $I_{+45}$ , and  $I_{-45}$  denote the four linear components of the intensity along the  $x$  axis,  $y$  axis, and at  $\pm 45^\circ$  with respect to the  $x$  axis, respectively, and where  $I_+$  and  $I_-$  denote the right and left circularly polarized components.

Inspection of (9.4) and (9.5) indicates that all four Stokes parameters can be determined from measurements of the FWM signal for four orientations of the half-wave plate [e.g.,  $I_{wo}(0^\circ)$ ,  $I_{wo}(22.5^\circ)$ ,  $I_{wo}(45^\circ)$ , and  $I_w(-22.5^\circ)$ ]. To check internal consistency, however, we always make six measurements as a function of reference delay  $\tau_{32}$ :  $I_{wo}(0^\circ)$ ,  $I_{wo}(45^\circ)$ ,  $I_{wo}(\pm 22.5^\circ)$ , and  $I_w(\pm 22.5^\circ)$ , and we check that the intensities  $S_0 = I_{wo}(0^\circ) + I_{wo}(45^\circ) = I_{wo}(22.5^\circ) + I_{wo}(-22.5^\circ) = I_w(22.5^\circ) + I_w(-22.5^\circ)$  give identical results in both magnitude and time dependence.

Once the Stokes parameters are extracted, the extent to which the TR-FWM signal has a well-determined polarization state is determined by calculating the degree of polarization  $P$  from the expression [40]:

$$P = (S_1^2 + S_2^2 + S_3^2)^{1/2} / S_0. \quad (9.6)$$

For the polarized component of the signal, the parameters that determine the polarization ellipse can also be directly determined from the Stokes parameters. The notation and conventions that we use for the polarization ellipse are shown in Figure 9.2b. The azimuthal angle  $\theta_{\text{sig}}$  indicates the orientation of the ellipse, the ellipticity angle  $\varepsilon$  is determined by the ratio of the minor to major axis, and  $S_0 = I_x + I_y$  denotes the total intensity. The azimuthal angle and the ellipticity angle are then calculated from the expressions

$$\tan(2\theta_{\text{sig}}) = S_2 / S_1 \quad (9.7)$$

and

$$\sin(2\varepsilon) = S_3 / (S_1^2 + S_2^2 + S_3^2)^{1/2}. \quad (9.8)$$

The roles of the various optical components shown in Figure 9.2 are now more readily apparent. On the one hand, a high-contrast linear polarizer is needed that is capable of selecting the various polarization components that determine the Stokes parameters. On the other, the transmitted FWM signal is required to have a constant linear polarization because of the phase matching requirements of the nonlinear up-conversion process used for time resolution. The combination of the half-wave plate and polarizer satisfies both requirements. The half-wave plate rotates the desired linear polarization component into coincidence with the pass axis of the polarizer, which is stationary and always oriented to provide the appropriate polarization for SHG. The insertion of the quarter-wave plate effectively converts the components of circular polarization to linear so that they can then be passed by the half-wave plate-analyzer combination.

The time-averaged polarization state of the TI-FWM signal also can be measured using this same geometry by removing the SHG crystal and collecting the

transmitted signal on a photomultiplier. We always perform such measurements for comparison. We emphasize that when the TI-FWM polarization measurements are performed it is the time-integrated intensities  $I_w(\varphi)$  and  $I_{wo}(\varphi)$  and therefore the time-integrated Stokes parameters  $S_i$  that are measured. The time-averaged values for the degree of polarization  $P$ , the azimuthal angle  $\theta_{\text{sig}}$ , and the ellipticity angle  $\varepsilon$  are then obtained from (9.6–9.8) using these time-integrated Stokes parameters. We caution that it is necessary to keep this procedure in mind when comparing the time-integrated and time-resolved measurements of the polarization state. Specifically, one should not directly numerically integrate the time-resolved ellipticity angle, azimuthal angle, and degree of polarization for comparison with the measured time-averaged values; rather, one should first numerically integrate the time-resolved Stokes parameters, then use these in (9.6–9.8) to obtain time-averaged values for  $\varepsilon$ ,  $\theta_{\text{sig}}$ , and  $P$ .

Also, because the TI-FWM polarization measurements are less tedious to perform, we typically introduce an even larger degree of redundancy into the time-integrated measurements. That is, we collect data for a continuous range of angles between  $0^\circ$  and  $90^\circ$  with, and without, the quarter-wave plate in place. Such a procedure produces two sinusoidal curves of TI-FWM intensity versus  $\varphi$ , which can then be fitted to extract the four time-integrated Stokes parameters. Also notice that the half-wave plate is not entirely necessary when time-integrated measurements are performed. The half-wave plate can be removed, and the TI-FWM measurements can be obtained by simply rotating the polarizer (and of course repeating the measurements with and without the quarter-wave plate in place). If this is done, one must take care to modify (9.4) and (9.5) to account for the factor of 2 difference in the angular dependence when one rotates a polarizer, rather than a half-wave plate followed by an analyzer. We prefer to use the combination of half-wave plate and analyzer, even when performing TI-FWM measurements, because it significantly reduces our experimental uncertainty by allowing us to rotate a zero-order wave plate rather than a thick Glan-Thompson polarizer.

All of the measurements using this technique were performed with a 2.5 MHz train of transform-limited 100 fs pulses from a self-modelocked Ti:sapphire laser. The  $\mathbf{k}_1$ -pulse was focused onto the sample with a spot size of  $80 \mu\text{m}$  ( $1/e$  radius), and the other, with wave vector  $\mathbf{k}_2$ , was spatially overlapped with the first and focused to a radius of  $40 \mu\text{m}$ . The external angle between  $\mathbf{k}_1$  and  $\mathbf{k}_2$  was  $\approx 15^\circ$ . The two incident pump beams were modulated at two separate frequencies by using a dual channel mechanical chopper, and the FWM signal was synchronously detected at the sum frequency using a lock-in amplifier. The time delay  $\tau_{21}$  between the two pulses was calibrated by using the autocorrelation signal from second-harmonic generation in a 1-mm-thick  $\text{LiIO}_3$  crystal, and for the measurements to be reviewed here, the time delay was set either to a positive delay of  $\tau_{21} = 300$  fs or a negative delay of  $\tau_{21} = -300$  fs to avoid temporal overlap of the two pump pulses. The  $\mathbf{k}_2$ -pulse was arranged to be linearly and s-polarized, and its polarization was typically held constant throughout the experiments, with the polarization vector  $\mathbf{E}_2$  defining the  $x$  axis. The polarization of the  $\mathbf{k}_1$ -pulse was also linear (with a polarization contrast ratio of better than 100:1), but the linear polarization  $\mathbf{E}_1$



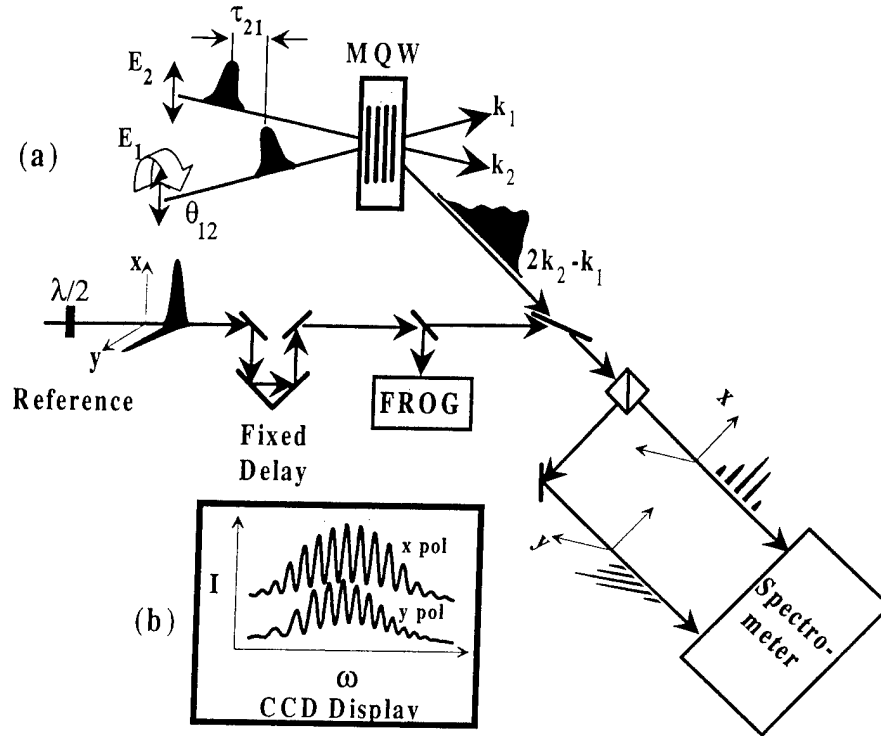


FIGURE 9.3. (a) Spectral interferometric geometry for the dual-channel (POLLIWOG) measurement of the amplitude, phase, and polarization state of the FWM signal; (b) schematic of spectral interferograms for the  $x$  and  $y$  components as displayed on the CCD array attached to the spectrometer. FROG denotes the setup for the characterization of the reference pulse by frequency-resolved optical gating.

was continuously rotated counterclockwise through an angle  $\theta_{12}$  with respect to the fixed  $E_2$ -polarization by using a zero-order half-wave plate, as described in more detail in the next section. In our experiments, the reference pulse was a 100 fs transform-limited pulse taken directly from the Ti:sapphire laser (without bandwidth restriction).

### 9.3 Dual-Channel Spectral Interferometry: POLLIWOG

We also can determine the vectorial nature of our FWM signal by using the dual-beam spectral interferometric geometry shown in Figure 9.3. As before, each  $\approx 100$  fs pulse from our mode-locked Ti:sapphire laser is divided into three parts. Two of the pulses, with wave vectors  $k_1$  and  $k_2$ , are used to generate the FWM signal in the direction  $2k_2 - k_1$ . In this case, the third (reference) pulse is linearly polarized at  $45^\circ$ , so that it has equal  $x$  and  $y$  components. A single fixed time delay  $\tau$  is introduced between the reference pulse and the FWM signal, and the amplitude and the phase of the reference are carefully measured. Any one of several techniques

can be used to provide a fully characterized reference pulse (e.g., [41–43]). In our case, we chose to use second-harmonic frequency-resolved optical gating (SHG-FROG) [44]. The signal and the reference are allowed to interfere by combining them collinearly. The combined signal is then separated into  $x$  and  $y$  components, and each component is separately dispersed by a spectrometer. Typical spectral interferograms for the  $x$  and  $y$  components as recorded on a CCD array are shown in the inset of Figure 9.3. Each interferogram has the form

$$I_{\text{SI}}^i(\omega) = I_{\text{FWM}}^i(\omega) + I_{\text{ref}}^i(\omega) + 2\sqrt{I_{\text{FWM}}^i(\omega)}\sqrt{I_{\text{ref}}^i(\omega)}\cos(\phi_{\text{FWM}}^i(\omega) - \phi_{\text{ref}}^i(\omega) - \omega\tau), \quad (9.9)$$

where  $I_{\text{FWM}}^i(\omega)$  and  $I_{\text{ref}}^i(\omega)$  are the spectral intensities and  $\phi_{\text{FWM}}^i(\omega)$  and  $\phi_{\text{ref}}^i(\omega)$  are the spectral phases of the FWM signal and reference pulses, respectively, and where  $i$  takes on the values  $x$  and  $y$  for the two orthogonal components. The delay  $\tau$  (typically a few ps) is chosen to yield fringes of a convenient spacing.

Since the spectral intensity and spectral phase of the  $x$  component ( $y$  component) of the reference pulse are fully known (in this case, from the FROG characterization) and since the spectral intensity of the  $x$  component ( $y$  component) of the FWM signal can be separately measured by blocking the reference and measuring it with the spectrometer, then the amplitude and phase of the  $x$  component ( $y$  component) of the signal and the delay  $\tau$  can be retrieved from the corresponding spectral interferograms using fringe inversion techniques that have been discussed previously [45–47]. The temporal intensities and phases are then obtained by inverse Fourier transformation.

The technique used here [48] can be readily recognized as an extension of the dual-quadrature spectral interferometry discussed by Lepetit et al. [45], except that in [45] the reference pulse was circularly polarized, rather than linearly polarized as it is here, and the orthogonal components of the reference were used to obtain quadrature in the spectral interferograms to improve signal-to-noise rather than to measure the polarization state. Our technique should also be readily recognized as a dual-beam version of the TADPOLE (acronym for Temporal Analysis by Dispersing a Pair Of Light E-fields) technique described in [46], with FROG providing the fully characterized reference pulse. Consequently, in the spirit that led to the acronyms FROG and TADPOLE, it has been suggested that we refer to this technique as POLLIWOG for POLarization Labeled Interference versus Wavelength of Only a Glint, and we often find it convenient to do so. While it has been suggested that spectral interferometry (SI) might be used to determine the polarization state of the unknown signal pulse (see footnote 22 of [45]), to our knowledge, this is the first actual use of SI for this purpose.

While POLLIWOG is a straightforward extension of existing SI techniques, it is nevertheless a useful one, which has many advantages over previously used techniques for determining the polarization state. As we discussed in Section 9.2, the temporal amplitudes, phases, and polarization state of FWM signals can also be measured by using the time-resolved ellipsometric (TRE) techniques described there. TRE has the advantage of directly measuring the temporal amplitudes and

phase differences, rather than indirectly obtaining them by inverse Fourier transformation of the spectral amplitudes and phases as required by SI. TRE does not require interferometric stability. It also relaxes the requirements for characterizing the reference pulse, since it is usually sufficient to characterize it with an autocorrelation trace. Because of the use of lock-in techniques and because of the temporal gating associated with the cross correlation process, TRE has excellent discrimination against scattered light, and it requires very little data reduction. However, TRE is labor intensive, requiring the tedious manipulation of waveplates to isolate the various components of the field that determine the polarization state and the scanning of delay stages to perform the cross correlations necessary for obtaining the time resolution. Most importantly, these cross correlations require the use of a nonlinear process (e.g., up-conversion), which limits the sensitivity, making them unsuitable for measuring very weak FWM signals. This limited sensitivity of TRE has, for example, previously restricted the investigations of coherent effects in semiconductors to relatively large carrier densities.

By comparison, SI directly measures the spectral amplitudes and phases. The temporal amplitudes and phases are obtained indirectly by inverse transformation. In this sense SI and TRE techniques are complementary. SI requires more complete characterization of the reference pulse, and short-term interferometric stability, but SI is simpler in the sense that it does not require the tedious scanning of delay stages or the manipulation of waveplates. Consequently, it requires less effort in laboratory; however, SI requires more processing of the data once it is acquired. Fortunately, this processing can be easily automated. In addition, POLLIWOG provides additional information not provided by TRE. From TRE measurements one can directly extract the temporal evolution of the total intensity,  $I_x(t) + I_y(t)$ , and the state of polarization, i.e., the azimuthal angle  $\theta_{\text{sig}}(t)$  and the ellipticity angle  $\epsilon(t)$ . Put another way, TRE directly provides the individual intensities,  $I_x(t)$  and  $I_y(t)$ , and the phase difference  $\phi_x(t) - \phi_y(t)$ ; but the individual phases,  $\phi_x(t)$  and  $\phi_y(t)$ , are not obtained.

Notice that a single, simpler linear SI measurement provides *all* of this information with a sensitivity that has been shown to extend into the zeptojoule ( $10^{-21}$  J) regime [46]! In fact, this sensitivity is arguably the most important advantage of SI. To date, the minimum usable SI signal levels in our FWM experiments have been limited to  $\approx 1$  aJ because of the randomly scattered coherent light from the semiconductor surface and the dewar windows and because of the background photoluminescence from the sample. The latter level is still more than an order of magnitude better than we have achieved using time-resolved FWM correlation techniques. This ( $\approx 1$  aJ) should not be regarded as a fundamental limit, but is merely a reflection of the limitations of our current apparatus.

Finally, the reader should be aware that there has been another previous measurement (before the SI and TRE measurements described here) of the temporal amplitude and phase of FWM signals, but the measurements were scalar and the polarization state was not explicitly investigated. In this very impressive set of measurements [49, 50], five complementary quantities were measured. Chemla et al. [50] measured all of the quantities suggested in Figure 9.1, namely, the power

spectrum, the TI-FWM signal, and the TR-FWM signal. In addition, they measured the first-order interferometric auto and cross correlations. Like TRE, this approach has the advantage of directly measuring the temporal amplitude and phase, rather than indirectly obtaining them by inverse transform from the spectral amplitude and phase. However, it also requires the use of nonlinear processes, which again limits the sensitivity. In addition, such correlations require interferometric stability, tedious scanning of time delays, and considerable experimental dexterity; for example,  $\approx 20$  points per optical period were acquired in the previous measurements [50].

## 9.4 Complete Characterization of the Coherent Emission from the Heavy Hole

In this section we demonstrate that the time-resolved polarization state of the coherent FWM emission from MQWs contains essential information about many-body effects that would be difficult to obtain in any other way. In this demonstration we will focus on measurements that can be most easily understood and interpreted. That is, we will focus on a single set of FWM experiments in a single MQW sample in which we excite only the hh transitions, thus eliminating the need to consider hh-lh beating phenomena. Furthermore, we will concentrate on a single polarization scheme for the incident radiation. Namely, we will measure the amplitude, phase, and polarization state of the FWM emission as the linearly polarized field  $\mathbf{E}_1$  of the  $\mathbf{k}_1$ -pulse is rotated through an angle  $\theta_{12}$  with respect to the fixed linearly polarized field  $\mathbf{E}_2$  of the  $\mathbf{k}_2$ -pulse, as indicated in Figure 9.3. And finally, we will fix the time delay between the two pump pulses at  $\tau_{21} = +300$  fs. We have performed an extensive set of such measurements (at both positive and negative delays) using both the direct time-resolved techniques (TRE) of Section 9.2 [51, 52] and the spectral interferometric techniques (POLLIWOG) of Section 9.3 [53, 54]. In our presentation here we will feature the POLLIWOG results.

### 9.4.1 POLLIWOG Measurements of hh Emission

All of the measurements of the hh emission that we have reported to date have been performed on one of two samples prepared from the same MQW wafer. That wafer consists of 10 periods of 14-nm-wide GaAs wells separated by 17-nm-wide  $\text{Al}_{0.3}\text{Ga}_{0.7}\text{As}$  barriers. Each sample was processed by mounting it onto a glass flat, by removing the substrate with a selective etch to permit transmission measurements, and by applying an antireflection coating to the exposed semiconductor-air interface to reduce Fabry-Perot effects. The excitonic line width for each sample at 8 K was determined to be 0.75 meV (as measured with a tunable cw Ti:sapphire laser attenuated to produce an areal carrier density of  $< 10^7 \text{ cm}^{-2}$ ).

The measurements reported here were performed at 80 K to ensure that the hh exciton was homogeneously broadened. At this temperature, the hh exciton for

each sample has a line width of  $\approx 1.3$  meV. The splitting between the heavy-hole (hh) and light-hole (lh) excitons is 7.3 meV for one sample and  $\approx 12$  meV for the other. All of the TRE measurements described in [24, 51, 52] were performed with the 7.3 meV sample, and the POLLIWOG measurements described in this chapter and in [53–58] used the  $\approx 12$  meV sample. This difference in the hh-lh splittings is the only measurable distinction between the two samples that we have observed, and it is most likely the result of differing in-plane strains introduced when the samples are cooled. This strain is caused by the differing thermal expansion coefficients of the materials that form the semiconductor–glue–glass interfaces. The peak absorption coefficient of each sample is  $\approx 9 \times 10^4 \text{ cm}^{-1}$ , corresponding to a peak absorbance of  $\approx 1.3$ . The small number of wells was chosen as a compromise between maintaining FWM signal, minimizing nonlinear propagation effects, and reducing the contributions of well-width fluctuations to the inhomogeneous broadening. Comparison between the 8 K and 80 K line widths (0.75 vs. 1.3 meV) suggests that the homogeneous broadening of the exciton by phonon scattering is significant at the latter temperature. Moreover, at the fluences used here, one would expect additional homogeneous broadening from the excitonic and free carrier collisions. To quantify the latter expectation, we performed the three-pulse test for homogeneous broadening described in [59] for several excitation fluences. The ratio of the homogeneous to inhomogeneous line widths  $\Delta\omega_{\text{homo}}/\Delta\omega_{\text{inhomo}}$  extracted from these measurements ranged from  $\approx 4$  for  $0.5 \mu\text{J}/\text{cm}^2$  to  $> 6$  for  $2.3 \mu\text{J}/\text{cm}^2$ . Consequently, it is reasonable to assume that the broadening is predominately homogeneous for this sample at 80 K at an excitation level of  $1 \mu\text{J}/\text{cm}^2$ . Finally, the assertion of homogeneous broadening at this temperature and excitation level was further verified by the absence of echo-like behavior in the TR-FWM signal as a function of time delay  $\tau_{21}$ .

To reduce the number of lh and free carriers that were generated, the bandwidth of the two pump pulses was restricted to  $\approx 12$  meV, which resulted in a measured pulse width of 150 fs, and the laser was tuned  $\approx 6$  meV below the hh exciton, as shown schematically in the inset of Figure 9.4. For the sample with the 7.3 meV hh-lh splitting, with this bandwidth and this detuning, we estimate the initial lh exciton and free-carrier populations to be less than 5% of the hh population, and at the fluence reported here ( $1 \mu\text{J}/\text{cm}^2$ ), we estimate the hh areal density to be  $\approx 4 \times 10^9 \text{ cm}^{-2}$  (corresponding to  $\approx 3 \times 10^{15} \text{ cm}^{-3}$ ). For the sample with the 12 meV hh-lh splitting, the fraction of lh and free carriers excited was significantly smaller.

Typical spectral amplitudes and spectral phases for both the  $x$  and  $y$  components of the FWM signal that are extracted from the corresponding spectral interferograms are shown in Figure 9.4 for selected angles  $\theta_{12}$  between the two input polarizations. Notice that the  $x$  and  $y$  responses are very different. It is not sufficient to measure a single component or to perform a scalar measurement that integrates over all polarization directions. The vectorial nature is important! Specifically, for each  $\theta_{12}$ , notice that the emission for the  $y$  component is different in magnitude from the  $x$  component, that it is spectrally broader, and that it is slightly red-shifted with respect to the  $x$  component. In fact, this shift ( $\approx 1.5$  meV) is comparable to

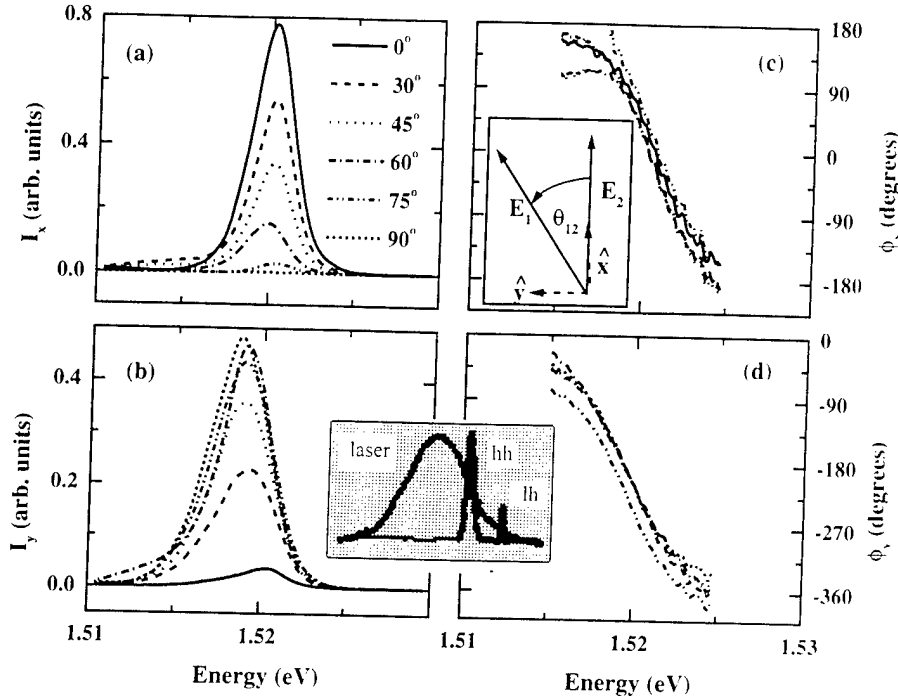


FIGURE 9.4. Measured spectral intensities, (a)  $I_x(\omega)$  and (b)  $I_y(\omega)$ , and spectral phases, (c)  $\phi_x(\omega)$  and (d)  $\phi_y(\omega)$ , for the  $x$  component and the  $y$  component, respectively, of the FWM signal for selected angles  $\theta_{12}$  between the two linear input polarizations and for a time delay  $\tau_{21} = +300$  fs. The top inset schematically shows the geometry and the nomenclature used for the two input polarizations: The linear  $s$ -polarization of  $E_2$  was fixed along the  $x$  direction, and the linear  $E_1$ -polarization was systematically rotated counterclockwise. The bottom inset shows the positions of the heavy-hole (hh) and the light-hole (lh) emission spectra with respect to the laser spectrum.

the expected biexcitonic binding energy. Also, notice that the  $x$  phases  $\phi_x$  and the  $y$  phases  $\phi_y$  are virtually independent of  $\theta_{12}$ . In addition,  $\phi_x$  and  $\phi_y$  are similar in shape; however, they are dramatically different in absolute magnitude, and their phase difference ( $\phi_x - \phi_y$ ) varies with wavelength. The second major point is the importance of measuring the spectral phases as well as the amplitudes. This phase information is not provided by conventional techniques, such as that shown in Figure 9.1a. If we had failed to measure the spectral phases, then the spectral amplitudes shown in Figure 9.4 could correspond to any number of temporal responses, depending on the shape and magnitude assumed for the spectral phases.

The corresponding temporal responses that are obtained by inverse Fourier transformation of the data in Figure 9.4—including the measured spectral phases  $\phi_x(\omega)$  and  $\phi_y(\omega)$ —are shown in Figure 9.5. The time origin is taken to coincide with the center of the  $E_2$ -pulse ( $t_2 \equiv 0$ ). In order to simplify the presentation and facilitate comparison with later theoretical calculations, we avoid the complications

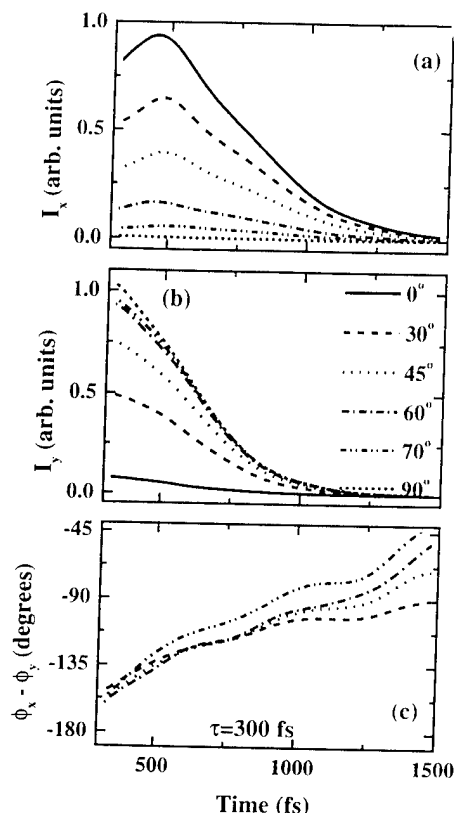


FIGURE 9.5. Measurements of (a) the  $x$  component of the intensity  $I_x(t)$ , (b) the  $y$  component of the intensity  $I_y(t)$ , and (c) the difference between the temporal phases  $\phi_x(t) - \phi_y(t)$  for selected angles  $\theta_{12}$  between the two linear input polarizations and for a time delay  $\tau_{21} = +300$  fs. The data are obtained by inverse Fourier transformation of the spectral data of Figure 9.4.

associated with the finite width of our pump pulses by plotting only the data for times  $t > 300$  fs. In this way, we ensure that there is no overlap of the two pump pulses and that all emission shown occurs after both pulses have completely exited the sample. As in the spectral domain (see Figure 9.4), notice that (for each  $\theta_{12}$ ) the  $x$  component of the emitted field has a distinctly different temporal behavior than the  $y$  component and that the difference in their temporal phases  $\phi_x(t) - \phi_y(t)$  varies dramatically in time. In particular,  $I_x(t)$  continues to grow long after the two pump pulses have exited the sample. This behavior is a consequence of many-body effects, and it suggests that such effects must, in general, be included. By comparison,  $I_y(t)$  decays more or less monotonically once the pump pulses have exited the sample. I want to emphasize that if we had performed a single scalar measurement, then we would have simply obtained the total intensity  $S_o$ , and the information about the differences in the  $x$  and  $y$  amplitudes and phases would

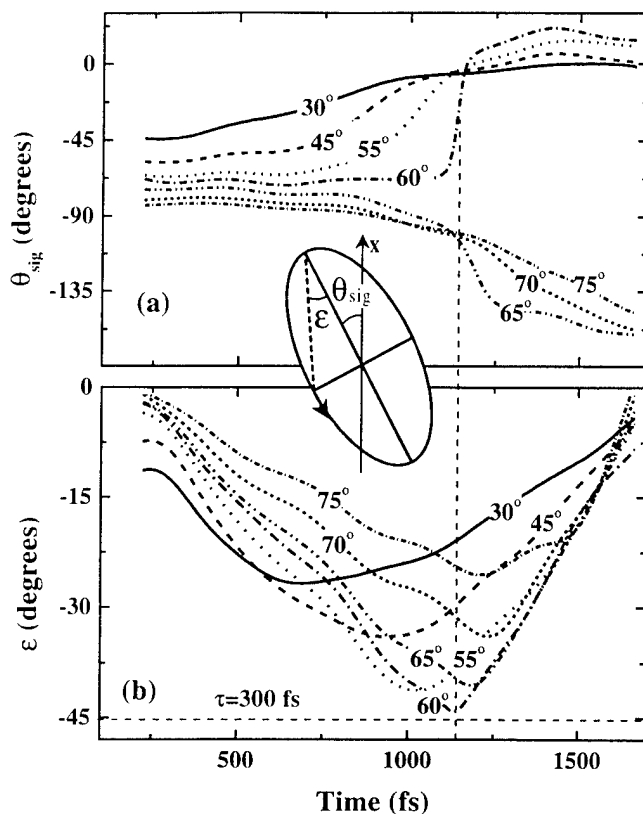


FIGURE 9.6. Measurements of (a) the azimuthal angle  $\theta_{\text{sig}}(t)$  and (b) the ellipticity angle  $\varepsilon(t)$  for selected angles  $\theta_{12}$  between the two input polarizations. The time delay was fixed at  $\tau_{21} = +300$  fs. For convenience, the notation used for the polarization ellipse is repeated in the inset. The dashed vertical line indicates the time at which  $\theta_{\text{sig}}$  undergoes a  $\pm 90^\circ$  discontinuity in orientation and the light is roughly circularly polarized ( $|\varepsilon| \approx 45^\circ$ ) for  $\theta_{12} \approx 60^\circ$ .

have been lost. Finally, of course, time-varying differences in amplitude and phase imply that the polarization state of the emitted radiation is varying in time.

#### 9.4.2 Discontinuity in the Polarization Direction

The dynamics of the polarization state are perhaps more evident if the data are displayed in terms of the parameters that directly define the polarization ellipse, as shown in Figure 9.6. Clearly, both the orientation and the ellipticity of the emitted FWM signal vary dramatically and systematically with time and with  $\theta_{12}$ . This figure contains a great deal of information, and it illustrates the rich variety and complexity of the information that can be obtained. The feature that I want to emphasize here is the distinct discontinuity in the temporal evolution of  $\theta_{\text{sig}}$ . Consequently, we have chosen the values of  $\theta_{12}$  displayed in Figure 9.6



to emphasize this feature. Specifically, for  $\theta_{12}$  less than some critical angle (in this case  $\theta_{12} < \approx 60^\circ$ ), the azimuthal angle  $\theta_{\text{sig}}$  rotates in the counterclockwise direction toward more positive (less negative) angles with increasing time. When  $\theta_{12}$  reaches the critical angle,  $\theta_{\text{sig}}$  abruptly undergoes a  $90^\circ$  jump or discontinuity at a particular time, indicated by the dotted line in Figure 9.6. For  $\theta_{12}$  larger than the critical angle,  $\theta_{\text{sig}}$  reverses direction and rotates in the clockwise direction, toward larger negative values, with increasing time. Also, notice that the magnitude of the ellipticity tends to increase then decrease with time for a given angle  $\theta_{12}$  between the two input polarizations, and finally, that  $\varepsilon$  tends to increase then decrease in magnitude with increasing  $\theta_{12}$  for a fixed time  $t$ . This discontinuity in rotation direction occurs at  $\approx 1140$  fs when the angle between the two input polarizations is  $\approx 60^\circ$  for the excitation conditions used to acquire the data shown in Figure 9.6. At this same moment and for this  $\theta_{12}$ , notice that the light is almost exactly circularly polarized (i.e.,  $|\varepsilon| \approx 45^\circ$ ).

The latter observations suggest the following phenomenological explanation of this discontinuity in the rotation direction of the polarization ellipse. The degree of ellipticity and the orientation of the polarization ellipse are related to the intensities and phases of the  $x$  and  $y$  components of the field by the following expressions:

$$\tan(2\theta_{\text{sig}}) = \frac{2\sqrt{I_x I_y}}{I_x - I_y} \cos(\phi_x - \phi_y), \quad (9.10)$$

$$\sin(2\varepsilon) = \frac{2\sqrt{I_x I_y}}{I_x + I_y} \sin(\phi_x - \phi_y). \quad (9.11)$$

Inspection of these two expressions reveals that  $\tan(2\theta_{\text{sig}})$  is undefined and  $\sin(2\varepsilon)$  is unity at the moment when  $I_x = I_y$  and  $(\phi_x - \phi_y) = \pm\pi/2$ . In terms of the polarization ellipse, this means that the light is circularly polarized and that the polarization cannot be specified. Consequently, we should expect to see a polarization discontinuity any time the polarization state becomes circularly polarized, i.e., the  $x$  and  $y$  components of the fields are equal and their phases differ by  $\pi/2$ .

To demonstrate that this qualitative explanation is consistent with the conditions under which we observe the discontinuity in the rotation direction of the polarization ellipse in Figure 9.6, we replot the data for  $\theta_{12} = 60^\circ$  (which is very near the discontinuity) in terms of  $I_x$ ,  $I_y$  (on a logarithmic scale) and the difference between their phases in Figure 9.7. Notice that for an angle between the input polarizations of  $\theta_{12} \approx 60^\circ$  the phase difference is  $90^\circ$  at  $\approx 1140$  fs. At that moment,  $I_x = I_y$ . This angle and this time are exactly the conditions under which we observed the discontinuity in Figure 9.6. Careful inspection of the data in Figure 9.5 reveals that these circumstances are not reproduced for any other angle or at any other time.

The behavior of the polarization ellipse near this  $90^\circ$  discontinuity in  $\theta_{\text{sig}}$  is illustrated qualitatively in Figure 9.8. In this figure we have sketched the ellipses corresponding to the data in Figure 9.7 for  $\theta_{12} = 60^\circ$  for selected times. Notice that the ellipse is initially (at  $t = 300$  fs) oriented with its major axis at  $\theta_{\text{sig}} \approx -70^\circ$ , and the ellipticity is small. As time progresses, the orientation of the ellipse remains

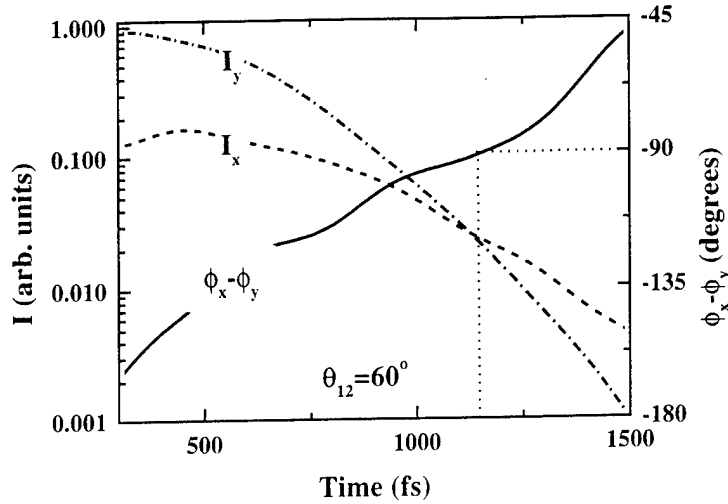


FIGURE 9.7. Measurements of the  $x$  component of the intensity  $I_x(t)$  (dashed line), the  $y$  component of the intensity  $I_y(t)$  (dashed-dotted line), and the difference between the temporal phases  $\phi_x(t) - \phi_y(t)$  (solid line) for  $\theta_{12} = 60^\circ$  and for a time delay  $\tau_{21} = +300$  fs. These are the same data as the  $\theta_{12} = 60^\circ$  curves plotted in Figure 9.5, except for the change in scale. The dotted lines indicate the time at which  $I_x = I_y$  and  $\phi_x(t) - \phi_y(t) = -90^\circ$ .

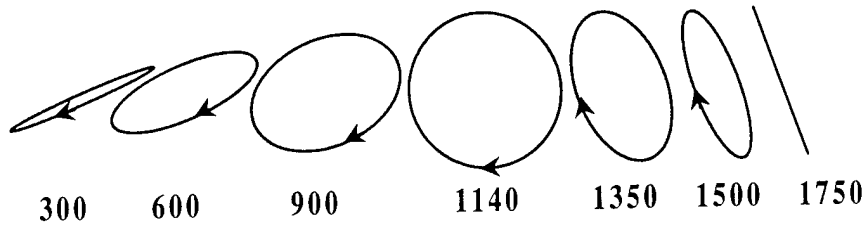


FIGURE 9.8. Schematic drawings of the polarization ellipses corresponding to the data in Figure 9.7 for selected time delays that illustrate the origin of the discontinuity in the orientation of the polarization ellipse shown in Figure 9.6.

roughly constant, but the ellipticity increases, until at  $t \approx 1140$  fs, the ellipse is approximately circularly polarized. At this moment, the orientation is clearly undefined. A moment later, the major axis has become the minor axis, and the ellipse has abruptly flipped its orientation by  $90^\circ$ . For times longer than 1140 fs the ellipticity begins to gradually decrease, but the orientation of the major axis remains at  $\theta_{\text{sig}} \approx 20^\circ$ . Eventually, the polarization approaches linear, but the orientation remains orthogonal to the initial orientation.

In terms of the azimuthal angle, a dramatic discontinuity has occurred at  $t \approx 1125$  fs; however, we can see that nothing unusual has happened to the overall polarization ellipse at that time. In fact, from another point of view, the orientation has not changed at all. From this alternative point of view, the orientation of the

ellipse has remained fixed, while one axis of the ellipse (which we initially called the minor axis) has continuously increased in magnitude with respect to the other (major) axis. At some moment ( $\approx 1140$  fs in this case), the two axes become equal, and eventually, the "minor" axis becomes larger than the "major" axis. This trend continues until the light approaches linear again. The discontinuity arises because we have chosen to change the labels on the two axes once the "minor" axis becomes larger than the "major" axis. Consequently, this is a mathematical discontinuity, not a physical one. The physical processes are continuous. Nevertheless, this discontinuity in the azimuthal angle is a useful feature because it serves as a dramatic indication of the time at which  $I_x = I_y$  and the  $x$  and  $y$  phases differ by  $\pi/2$ . This discontinuity in the polarization state is seen over a wide variety of excitation levels, detunings, and time delays; however, the angle and time at which this discontinuity occurs are very sensitive to each of these parameters.

### 9.4.3 Importance of Measuring the Phase

To illustrate the importance of accurately measuring the phases as well as the amplitudes, suppose that in the present measurements we had time-resolved both  $I_x(t)$  and  $I_y(t)$ , but we had failed to measure the phases  $\phi_x(t)$  and  $\phi_y(t)$ . This would have been the case, for example, if we had performed two time-resolved measurements (one for  $x$  and one for  $y$ ) using the conventional nonlinear cross correlation technique shown in Figure 9.1b. Furthermore, suppose that in the absence of any information about the phases we assume that the  $x$  and  $y$  phases are the same, i.e., we assume that the phase difference is zero. Figure 9.9 shows the results of reanalyzing the data of Figure 9.5 by keeping the measured values for  $I_x(t)$  and  $I_y(t)$ , but assuming  $\phi_x(t) - \phi_y(t) = 0$ . Notice that the initial orientations of the ellipses in Figure 9.9 are at positive angles, when the actual polarizations (Figure 9.6) are initially oriented in the opposite direction at roughly the same negative angle. Also, notice that each polarization ellipse in Figure 9.9 rotates clockwise (toward more negative  $\theta_{\text{sig}}$ ). Consequently, there is no discontinuity in  $\theta_{\text{sig}}$  of the type shown in Figure 9.6 (and discussed in the preceding paragraphs). As a result, the direction of rotation is incorrect for all  $\theta_{12}$  less than the critical angle. Most importantly, under these circumstances, we obtain a time-varying, but linear, polarization for each  $\theta_{12}$ . Therefore, not only are the initial positions and directions of rotation of the polarizations incorrect, but the information about the ellipticity has been entirely lost. As we will discuss in Section 9.6, this information is essential to identifying the various many-body contributions to the nonlinear response.

### 9.4.4 Complex Plane Representation

There is another way to represent the polarization data, and that is to display the polarization state in the complex plane (e.g., [40]). In this representation, every possible polarization state is mapped into the complex plane by defining a parameter  $\chi$  as the ratio of the amplitude and phase of the  $y$  component of the

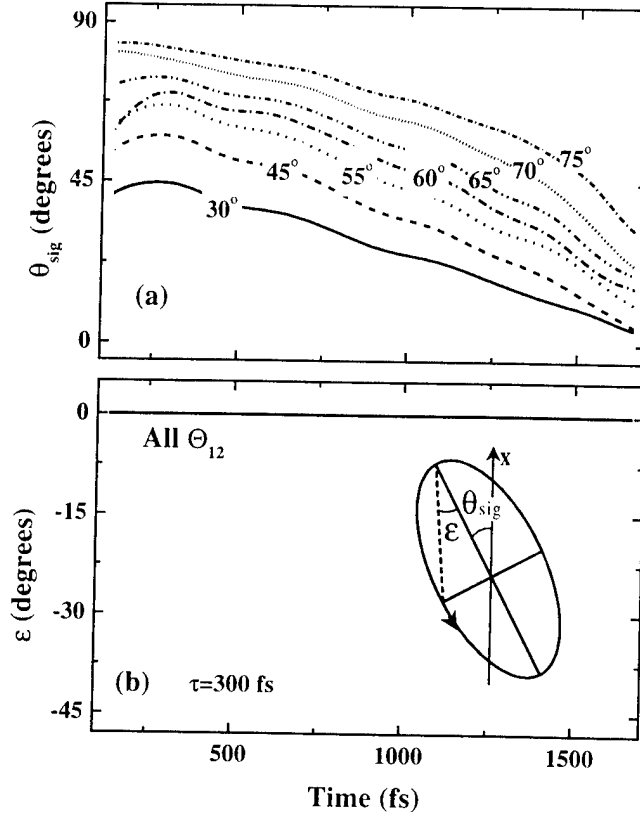


FIGURE 9.9. Simulated values for (a) the azimuthal angle  $\theta_{\text{sig}}(t)$  and (b) the ellipticity angle  $\epsilon(t)$  of the FWM emission for selected angles  $\theta_{12}$  between the two input polarizations. The simulations were performed using the measured  $x$  and  $y$  components of the intensity,  $I_x(t)$  and  $I_y(t)$ , given in Figure 9.5, but assuming a constant phase difference,  $\phi_x(t) - \phi_y(t) = 0$ .

FWM signal to that of the  $x$  component:

$$\chi = \sqrt{\frac{I_y}{I_x}} \exp[i(\phi_x - \phi_y)] = \frac{\sin \theta_{\text{sig}} \cos \epsilon + i \cos \theta_{\text{sig}} \sin \epsilon}{\cos \theta_{\text{sig}} \cos \epsilon - i \sin \theta_{\text{sig}} \sin \epsilon}. \quad (9.12)$$

Our notation and conventions (which are slightly different from those of [40]) are illustrated in Figure 9.10. As indicated, all linear polarizations fall along the real axis, with  $x$ -linear polarization at the origin and  $y$ -linear at  $\pm\infty$ . Right circularly polarized light is located at  $+i$  and left circularly polarized at  $-i$ .

One feature to notice for comparison with the data in Figure 9.11 is that a discontinuity in the orientation of the ellipse is expected any time a trajectory crosses the points  $\pm i$ . For example, notice that the imaginary axis represents a line where the difference in the  $x$  and  $y$  phases is constant and equal to  $90^\circ$ . Moreover, at  $-i$  the amplitudes are equal and the phases differ by  $90^\circ$ , i.e., the light is left circularly polarized. Consequently, if one begins at the origin and travels down the

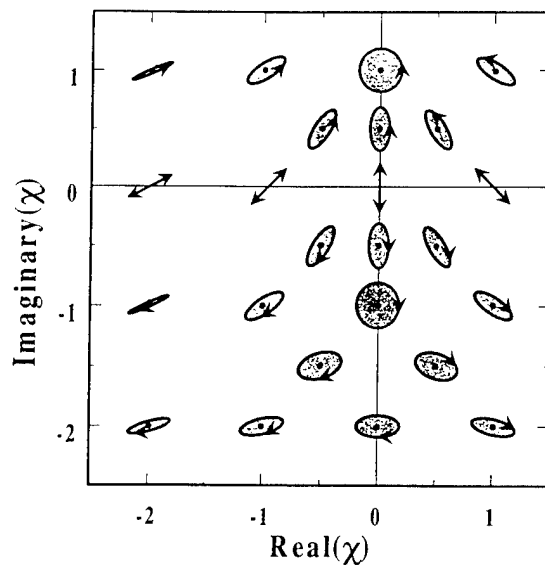


FIGURE 9.10. Schematic illustration of the notation used to map all possible polarization states onto the complex plane.

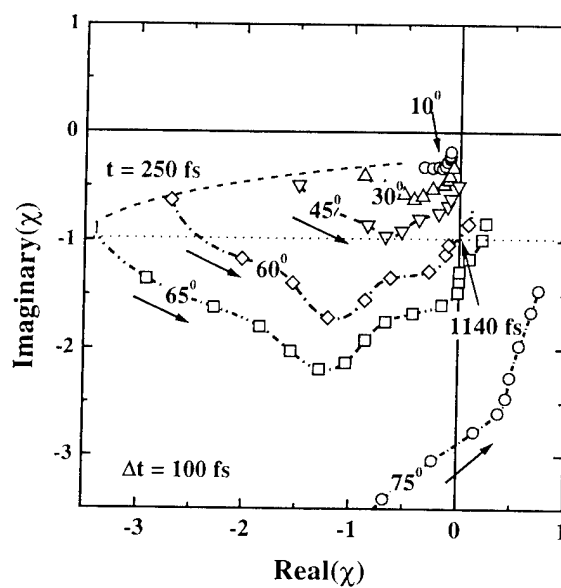


FIGURE 9.11. The polarization data of Figure 9.6 plotted as trajectories in the complex plane. The distance between symbols marks equal increments in time of 100 fs, and the arrows indicate the direction of increasing time. The curves begin at  $t = 250$  fs.

imaginary axis, the polarization is initially linearly polarized and oriented along the  $x$  direction. The ellipticity increases until the light is circularly polarized, at which point there is a sudden and abrupt change in orientation. Similar behavior is observed as one traverses the point  $-i$  from left to right. In fact, a discontinuous jump of  $90^\circ$  is encountered regardless of the direction of approach. This  $\pi/2$  discontinuity in the azimuthal angle when the point  $+i$  (or  $-i$ ) in the complex plane is crossed is well known (e.g., see [40], p. 42).

Figure 9.11 shows the polarization data of Figure 9.6 for selected angles  $\theta_{12}$  between the input polarizations replotted as trajectories in the complex plane. The arrows indicate the direction of increasing time, and the symbols mark equal increments in time of 100 fs. Each trajectory begins at  $t = 250$  fs. Notice that the trajectory that corresponds to an angle between the input polarizations of  $\theta_{12} = 60^\circ$  passes through the point  $-i$  at  $\approx 1140$  fs. At this moment the orientation of the polarization ellipse is undefined, a  $90^\circ$  jump in  $\theta_{\text{sig}}$  occurs, and the direction of rotation for the ellipse reverses. This is the same angle and the same time at which the same behavior was observed in Figure 9.6. Thus, Figs. 9.6 and 9.11 provide equivalent representations of the same mathematical discontinuity.

## 9.5 Comparison with Predictions for Two Independent Two-Level Systems

One dramatic way to demonstrate the sensitivity of time-resolved polarimetry to the contributions of many-body effects is to compare the experimental results described in the previous section to the predictions of a theoretical model that does not include these effects. The simplest such approach is to view the ultrafast dephasing of the coherent hh excitonic states in MQWs as a solid state analogue of an atomic two-level system [60]. The initial hope that excitons in semiconductors could be treated as a simple two-level system was based on their crude similarities to atoms. In very limited circumstances, the exciton can be regarded as an "atom" consisting of an electron and hole that are bound together by Coulombic attraction. As such, the exciton exhibits well-defined discrete energy levels. Thus, when a laser is tuned so that it excites only the hh transition (as it was for the data in the previous section), the light is essentially coupled to two isolated energy levels, much as if it were tuned to an atomic resonance.

In this section we will review the expected FWM response of excitons in semiconductors when the hh-to-conduction-band transition is treated as a two-level system. Because of spin degeneracy, the hh-to-conduction-band transition actually consists of two degenerate transitions: one for each spin state. If the spin relaxation times are long compared to the dephasing times of interest for the coherent effects, then these two systems can be regarded as independent. For this reason, we will actually consider the response of two independent two-level ( $2 \times 2$ ) systems, as depicted in Figure 9.12a, rather than a single system. As shown,  $\gamma_e$  accounts for the decay of carriers from the upper excitonic level. This level decay could be by

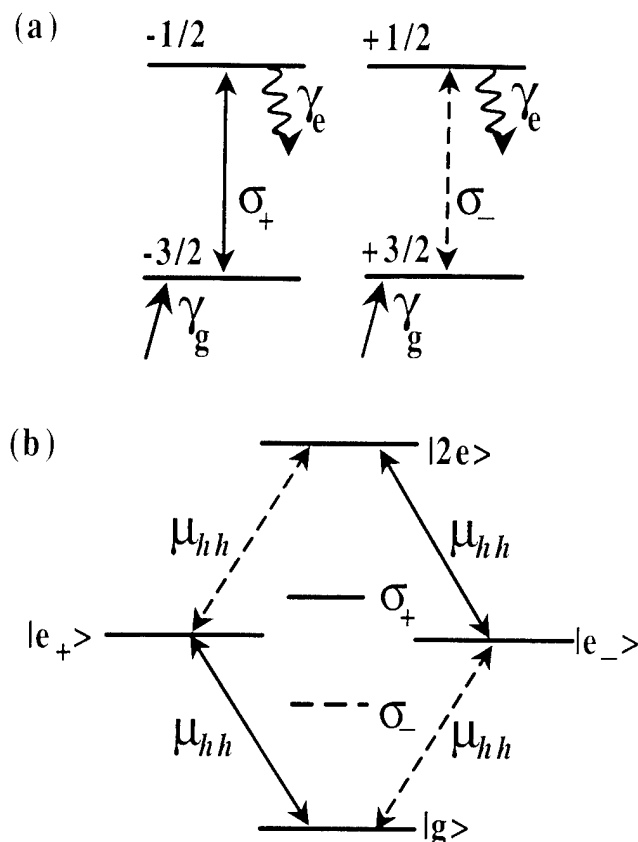


FIGURE 9.12. (a) Schematic of the two independent two-level ( $2 \times 2$ ) systems used to represent the hh transitions in the absence of many-body effects. (b) Schematic of the two-particle four-level energy diagram that is the equivalent of (a), where  $|g\rangle$  represents the ground state (neither spin system excited);  $|e_+\rangle$  denotes the state with the spin  $-\frac{1}{2}$  particle excited but the spin  $+\frac{1}{2}$  not;  $|e_-\rangle$ , the state with the spin  $+\frac{1}{2}$  system excited but the spin  $-\frac{1}{2}$  not; and  $|2e\rangle$ , the state with both particles excited. The solid (dashed) arrows represent transitions coupled by  $\sigma_+$  ( $\sigma_-$ ) polarized light, and  $\mu_{hh}$  corresponds to the hh exciton dipole matrix element.

recombination or by promotion into the conduction band continuum by carrier-carrier or carrier-phonon collisions. And  $\gamma_g$  represents the rate at which the lower level is repopulated by electrons from occupied states within the valence band.

Several excellent treatments of the interaction of electromagnetic radiation with a two-level system are available [61–63]. Elsewhere [58], we have presented a detailed review of the  $2 \times 2$  system in which we have made the formalism specific to four-wave mixing and have emphasized the vectorial nature of the emission. Here, we will review only those aspects that are needed to provide a direct comparison with experimental results presented in Section 9.4.

In general, the density matrix equations that describe the  $2 \times 2$  system shown in Figure 9.12a must be solved numerically. However, analytic solutions to these

equations can be obtained by using delta function excitation pulses and by expanding the solutions to third order using time-dependent perturbation theory. Specifically, we take the total incident field to consist of two delta function pulses with vector amplitudes  $\mathcal{E}_1$  and  $\mathcal{E}_2$  and propagation wave vectors  $\mathbf{k}_1$  and  $\mathbf{k}_2$ , which arrive at the sample at times  $t_1$  and  $t_2$ , respectively:

$$\begin{aligned} \mathbf{E} = & 1/2 [\mathcal{E}_1 \delta(t - t_1) \exp[-i(\nu t - \mathbf{k}_1 \cdot \mathbf{r})] + \text{c.c.}] \\ & + 1/2 [\mathcal{E}_2 \delta(t - t_2) \exp[-i(\nu t - \mathbf{k}_2 \cdot \mathbf{r})] + \text{c.c.}] \end{aligned} \quad (9.13)$$

In writing the field in this form, we have implicitly made use of the fact that the optical thickness of the active region of the sample ( $\approx 1 \mu\text{m}$ ) is much smaller than the spatial width of the  $\approx 150$  fs optical pulses ( $\approx 45 \mu\text{m}$ ), and we have assumed that the spot to which the pulses are focused and the angle between the two beams are sufficiently small to avoid beam walk-off.

For the experimental geometry used for the measurements in Section 9.4, the linear s-polarization of the  $\mathcal{E}_2$  pulse was held constant and the linear polarization of  $\mathcal{E}_1$  was systematically rotated through an angle  $\theta_{12}$  with respect to the fixed polarization of  $\mathcal{E}_2$ , as shown in Figure 9.3. If the  $x$  axis is taken to be parallel to the fixed  $\mathcal{E}_2$  field and  $z$  is taken along the direction of light propagation, the vector amplitudes of the two incident fields can be written as

$$\mathcal{E}_2 = \mathcal{E}_2 \hat{\mathbf{x}} = \mathcal{E}_2 (\hat{\sigma}_+ + \hat{\sigma}_-) / \sqrt{2} \quad (9.14a)$$

and

$$\begin{aligned} \mathcal{E}_1 &= \mathcal{E}_1 (\cos \theta_{12} \hat{\mathbf{x}} + \sin \theta_{12} \hat{\mathbf{y}}) \\ &= \mathcal{E}_1 [(\cos \theta_{12} - i \sin \theta_{12}) \hat{\sigma}_+ + (\cos \theta_{12} + i \sin \theta_{12}) \hat{\sigma}_-] / \sqrt{2}, \end{aligned} \quad (9.14b)$$

where  $\hat{\sigma}_+ = (\hat{\mathbf{x}} + i\hat{\mathbf{y}})/\sqrt{2}$  and  $\hat{\sigma}_- = (\hat{\mathbf{x}} - i\hat{\mathbf{y}})/\sqrt{2}$  are the complex unit polarization vectors for right and left circularly polarized light, respectively.

Using this notation and the selection rules shown schematically in Figure 9.12a, it is a straightforward task to solve the density matrix equations for the  $2 \times 2$  system to obtain the total polarization that propagates in the  $2\mathbf{k}_2 - \mathbf{k}_1$  direction as

$$\mathbf{P}(\mathbf{t})|_{2\mathbf{k}_2 - \mathbf{k}_1} = \frac{1}{2} [\mathcal{P}(t) \exp[-i\omega_{hh}t] \exp[i(2\mathbf{k}_2 - \mathbf{k}_1) \cdot \mathbf{r}] + \text{c.c.}], \quad (9.15)$$

where the slowly varying polarization amplitude is given by

$$\begin{aligned} \mathcal{P}(t, \tau_{21}) &= \kappa \Theta(t) \Theta(\tau_{21}) \exp[-\gamma(t + \tau_{21})] \exp[i\delta\tau_{21}] \{\cos \theta_{12} \hat{\mathbf{x}} - \sin \theta_{12} \hat{\mathbf{y}}\} \\ &= \kappa \Theta(t) \Theta(\tau_{21}) \exp[-\gamma(t + \tau_{21})] \exp[i\delta\tau_{21}] \\ &\quad \times \{[\cos \theta_{12} + i \sin \theta_{12}] \hat{\sigma}_+ + [\cos \theta_{12} - i \sin \theta_{12}] \hat{\sigma}_-\} / \sqrt{2}. \end{aligned} \quad (9.16)$$

In (9.16)  $\hbar\omega_{hh}$  is the hh transition energy,  $\gamma$  is the dephasing rate for the hh exciton,  $\delta = \omega_{hh} - \nu$ ,  $\Theta$  denotes the Heaviside step function, and

$$\kappa = \left( \frac{-i N \mu_{hh}^4 \mathcal{E}_2^2 \mathcal{E}_1^*}{8 \hbar^3} \right), \quad (9.17)$$



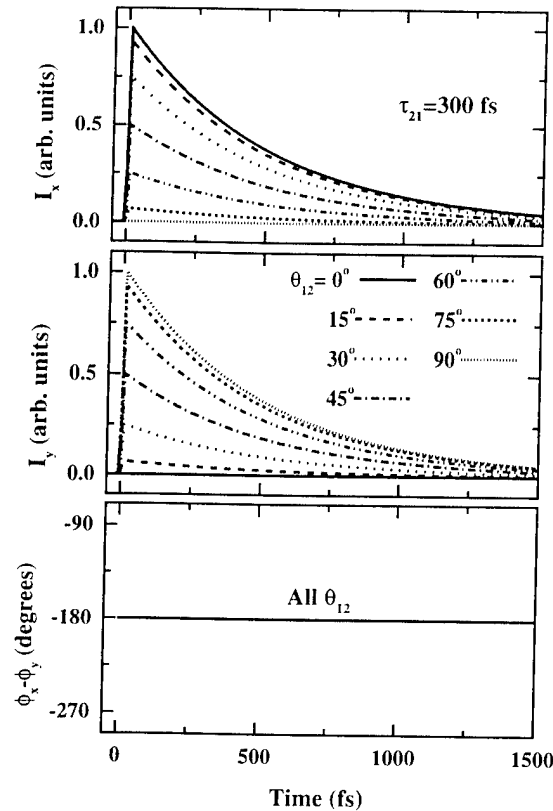


FIGURE 9.13. The  $x$  component  $I_x(t)$  and  $y$  component  $I_y(t)$  of the TR-FWM intensity and the temporal phase difference  $\phi_x(t) - \phi_y(t)$  between the  $x$  and  $y$  components of the field for selected angles  $\theta_{12}$  between the two linear input polarizations and for  $\tau_{21} = 300$  fs, as calculated from the  $2 \times 2$  model of Section 9.5 (without many-body effects).

where  $N$  is the number of oscillators of each spin type and  $\mu_{hh}$  is the hh transition matrix element, which is assumed to be the same for both spin states.

In writing (9.16), we have substituted  $\tau_{21}$  for  $(t_2 - t_1)$  and have taken our origin to coincide with the arrival of the  $\mathbf{k}_2$ -pulse (i.e.,  $t_2 \equiv 0$ ), and we have assumed that the population decays are long compared to the dephasing times. As we have already stated, the polarization given by (9.16) will act as a source in Maxwell's equations to produce the FWM field. If the sample is optically thin and the system is homogeneously broadened, then the FWM field will be directly proportional to the polarization given by (9.16).

The simulated temporal intensities  $I_x(t, \tau_{21})$  and  $I_y(t, \tau_{21})$  and temporal phase differences  $\phi_x(t, \tau_{21}) - \phi_y(t, \tau_{21})$  produced by (9.16) are shown in Figure 9.13 for selected angles  $\theta_{12}$  between the two input polarizations using a dephasing time of  $\gamma^{-1} = 1$  ps. These numerical solutions should be compared to the actual data shown in Figure 9.5. In contrast to the data, the calculated shape of the temporal intensity for the  $x$  component is exactly the same as for the  $y$  component, and

this shape does not change as the linear polarization of  $\mathcal{E}_1$  is rotated through an angle  $\theta_{12}$ . In addition, the numerical simulations produce no delayed rise in the  $x$  component of the FWM intensity, as required by the data. Rather, for a fixed  $\tau_{21}$ , both  $x$  and  $y$  intensities promptly decay in time at the same rate:  $2\gamma$ . Moreover, the phase difference between the  $x$  and  $y$  components is a constant  $180^\circ$ , independent of time  $t$ , time delay  $\tau_{21}$ , and angle  $\theta_{12}$ . By comparison, the measured phase difference shown in Figure 9.5c exhibits a monotonic increase with time, but also is not strongly dependent on  $\theta_{12}$ . Inspection of (9.16) and Figure 9.13 also indicates that no FWM signal is emitted before the arrival of the  $\mathcal{E}_2$ -pulse (recall that we have taken  $t_2 = 0$ ), that the initial intensity  $I_i(t = 0, \tau_{21})$ , for  $i = x, y$ , decreases exponentially at a rate of  $2\gamma$  as a function of time delay  $\tau_{21}$ , and that the ratio of  $I_y(t, \tau_{21})$  to  $I_x(t, \tau_{21})$  is independent of  $\tau_{21}$  and is proportional to the square of  $\tan \theta_{12}$ . The constant phase difference of  $180^\circ$  and the change in the relative magnitudes of the  $x$  and  $y$  intensities with  $\theta_{12}$  determine the vectorial nature of the FWM emission for the  $2 \times 2$  system.

These polarization properties can be more readily visualized by replotting the simulations of Figure 9.13 in terms of the parameters that determine the polarization ellipse, as we have done in Figure 9.14. The notation that we use for the polarization ellipse is repeated in the inset for the reader's convenience. The peak magnitude of the total intensity  $S_0$  is independent of the orientation of the two incident polarizations (i.e., independent of  $\theta_{12}$ ), and  $S_0$  decays in time at the rate  $2\gamma$ . In direct contrast to the time-resolved polarization data shown in Figure 9.6, the emitted FWM signal is always linearly polarized ( $\varepsilon = 0$ ), and the orientation of the polarization ellipse  $\theta_{\text{sig}}$  is constant in time for each  $\theta_{12}$ . As  $\mathcal{E}_1$  is rotated through an angle of  $+\theta_{12}$  in the counterclockwise direction (see inset Figure 9.4), the orientation of the FWM polarization rotates through an equal, but opposite, angle in the clockwise direction (i.e.,  $\theta_{\text{sig}} = -\theta_{12}$ ). Because the simulated polarization is linear and independent of time, it displays no discontinuity in the orientation of  $\theta_{\text{sig}}$  of the type observed in the data shown in Figure 9.6.

The static nature of the emission from the  $2 \times 2$  system is more clearly illustrated by plotting the simulations of Figs. 9.13 and 9.14 as trajectories in the complex plane, as shown in Figure 9.15. Notice that static points along the real axis mark the constant linear polarizations that would be expected for the FWM emission from the  $2 \times 2$  system in the absence of many-body effects. When compared directly to Figure 9.11, this representation in the complex plane provides a dramatic visualization of the power of femtosecond time-resolved polarization spectroscopy for studying many-body effects. In the absence of such effects, one would expect to observe stationary points in the plane. Instead, we see the wonderfully complicated trajectories shown in Figure 9.11 that cannot be explained without many-body effects and that contain a wealth of information about them.

Finally, it will prove useful when we include biexcitons in the next section to recognize that the two independent single-particle two-level diagrams of Figure 9.12a are equivalent to the two-particle four-level system shown in Figure 9.12b. In this two-particle energy level diagram, the ground state corresponds to two unexcited excitons: one for each spin system. The excited state  $|e_+\rangle$  corresponds to having

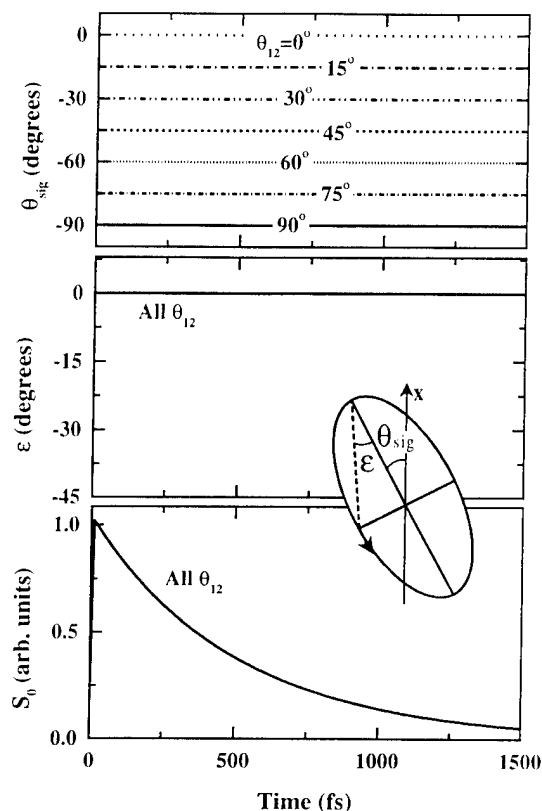


FIGURE 9.14. The temporal evolution of the azimuthal angle  $\theta_{\text{sig}}(t)$ , the ellipticity angle  $\epsilon(t)$ , and the total intensity  $S_0(t)$  of the TR-FWM emission for selected angles  $\theta_{12}$  between the two input polarizations, as calculated from the  $2 \times 2$  model of Section 9.5. This is an alternative representation of the TR-FWM simulations shown in Figure 9.13. For convenience the inset again shows the nomenclature and conventions that we adopt for defining the polarization ellipse.

the  $\sigma_+$  exciton in the excited state, but the  $\sigma_-$  exciton in the ground state. Similarly,  $|e_- \rangle$  corresponds to having  $\sigma_-$  excited and  $\sigma_+$  not. The state  $|2e \rangle$  represents two excited excitons, but unbound. It is a straightforward exercise to show that the density matrix equations for the four-level two-particle system of Figure 9.12b are the same as those for Figure 9.12a.

## 9.6 Phenomenological Inclusion of Many-Body Contributions

The simple two-level picture of FWM presented in Section 9.5 has been very successful in describing coherent interactions in atomic and molecular systems,

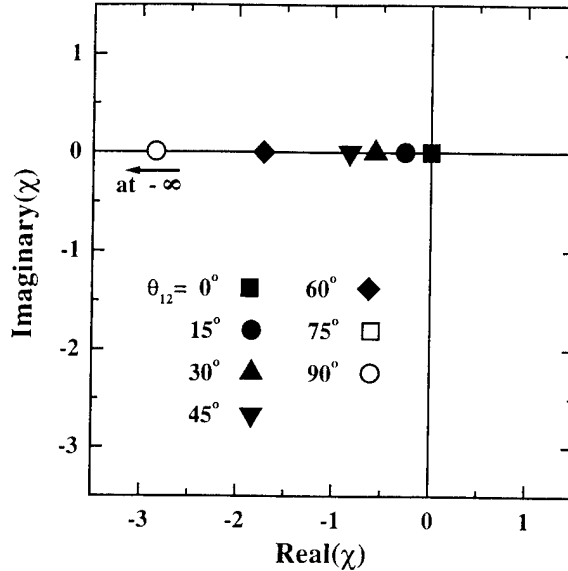


FIGURE 9.15. The polarization state as calculated from the  $2 \times 2$  model of Section 9.5 plotted in the complex plane. This is an alternative representation of the simulations shown in Figure 9.14, which illustrates that the polarization state for the FWM emission from a  $2 \times 2$  system is linear and independent of time.

and it has sometimes been used to gain qualitative information about coherent and incoherent FWM emission from semiconductors (e.g., [33, 60]). However, it is clear from the experimental results described in Section 9.4 that this approach does not account for many of the characteristics of coherent FWM emission from hh excitons in semiconductors. For example, it does not describe the observed vectorial dynamics of the FWM emission. It should not be surprising that this simple picture fails to adequately describe coherent interactions in semiconductors. The approach presented in Section 9.5 treats the electron-hole states as an ensemble of independent two-level systems. This is appropriate for a dilute medium, such as an atomic gas at low pressures, but is not expected to be accurate for a dense medium, such as semiconductors, where many-body effects are known to be important. In fact, as we have already mentioned in Section 9.1, a complete description of the behavior of the FWM signal has been shown to require the inclusion of various exciton-exciton interaction phenomena [24, 51–54], such as local field corrections (LFC) [4, 7, 15–18], excitation-induced dephasing (EID) [19–24], and biexciton formation (BIF) [25–32, 39]. In particular, each has been shown to produce TI-FWM signals at negative delays and delayed peaks in the TR-FWM signal, as required by experiment.

Various procedures have been developed for including these Coulomb-induced many-body effects in a microscopic theory. One approach is to use nonequilibrium Green's function methods to derive the most general form of the semiconductor Bloch equations (SBE) that include contributions of dynamical correlations and

quantum-kinetic processes [64–68]. Early numerical solutions have concentrated on effects such as dynamical screening within the screened Hartree–Fock approximation [69, 70], whereas the strong excitation and ultrafast regime (in which excitonic phase space filling is the leading nonlinearity) have been investigated extensively in the unscreened Hartree–Fock approximation. More recently, the influence of dynamical correlations in the screened Hartree–Fock approximation (and modifications thereof) on the ultrafast nonlinearities has been investigated [71]. On the other hand, correlations within the  $\chi^{(3)}$  regime, such as biexcitonic effects, have been found to be described within the dynamics-controlled truncation scheme [72–74]. In general, these approaches require lengthy numerical solutions, and analytic solutions are not possible. In order to minimize the formalism and to obtain closed-form solutions, we choose to include these processes phenomenologically by extending and modifying the density matrix approach that we began in the previous section.

Within this context, the simplest description of BIF in a homogeneously broadened MQW is to write the density matrix equations for the  $\sigma_+$  and  $\sigma_-$  transitions depicted by the two-particle five-level system shown in Figure 9.16 and to include LFC and EID effects phenomenologically. The five-level system of Figure 9.16 is readily recognized as the four-level system of Figure 9.12b to which we have added a level for the biexciton. Consequently, just as in Figure 9.12b, the ground state  $|g\rangle$  corresponds to having two unexcited excitons (one for each spin). The excited state  $|e_+\rangle$  corresponds to having the  $\sigma_+$  exciton in the excited state, but the  $\sigma_-$

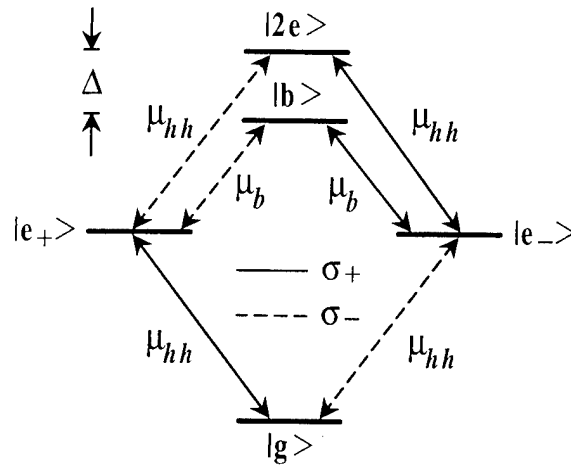


FIGURE 9.16. Schematic of the two-particle five-level energy diagram describing both spin systems and allowing for biexciton formation, where  $|g\rangle$  represents the ground state (neither spin system excited);  $|e_+\rangle$  denotes the state with the spin  $-\frac{1}{2}$  particle excited but the spin  $+\frac{1}{2}$  not;  $|e_-\rangle$ , the state with the spin  $+\frac{1}{2}$  system excited but the spin  $-\frac{1}{2}$  not;  $|b\rangle$ , the state with both particles excited and bound to form a biexciton; and  $|2e\rangle$ , the state with both particles excited but not bound to form a biexciton. The solid (dashed) lines represent transitions coupled by  $\sigma_+$  ( $\sigma_-$ ) polarized light,  $\hbar\Delta$  is the biexciton binding energy, and  $\mu_{hh}$  and  $\mu_b$  correspond to the hh exciton and the biexciton dipole matrix elements, respectively.

exciton in the ground state, and similarly,  $|e_- \rangle$  corresponds to having  $\sigma_-$  excited and  $\sigma_+$  not. The state  $|b \rangle$  indicates that both excitons of opposite spin are excited and bound to form a biexciton. The state  $|2e \rangle$  represents two excited excitons, but unbound. The latter state is actually a continuum state; however, since the light couples states near  $k = 0$  and since both excitonic and biexcitonic peaks appear as sharp lines in the MQW spectrum, this is a distinction that we will largely ignore (e.g., see [75] for a more complete discussion of this point).

The LFC is included by adding to the incident field a "local field" that is proportional to the total material polarization [15, 17]:

$$\mathbf{E}_{\text{local}} = \mathbf{E} + \mathbf{L}\mathbf{P}, \quad (9.18)$$

where  $\mathbf{P}$  is the total material polarization and  $\mathbf{L}$  is a local field parameter. The EID can be introduced by assuming that the dephasing rate is density-dependent  $\gamma(n)$  and by expanding it in a Taylor series and keeping the first two terms [20, 21]:

$$\gamma(n) = \gamma_0 + \frac{\partial \gamma}{\partial n} n = \gamma_0 + N \frac{\partial \gamma}{\partial n} (\rho_{ee}^+ + \rho_{ee}^-), \quad (9.19)$$

where  $\gamma_0$  is the low-density dephasing rate at the operating lattice temperature and  $n = N(\rho_{ee}^+ + \rho_{ee}^-)$  is the total density of excited excitons, regardless of spin. Here,  $N$  denotes the total density of oscillators of each spin system and  $\rho_{ee}^+$  ( $\rho_{ee}^-$ ) denotes the upper-level population matrix element for the spin  $-\frac{1}{2}$  ( $+\frac{1}{2}$ ) system. Because it is the total population that determines the dephasing rate, this term provides a coupling between the two spin systems. These two equations can now be substituted into the density matrix equations for the two-particle five-level system of Figure 9.16.

As in Section 9.5, in order to obtain a closed-form solution (to third order), we assume that the pulses  $\mathbf{E}_1$  and  $\mathbf{E}_2$  have delta-function time dependences, and we assume that the two fields are linearly polarized and that  $\mathbf{E}_1$  has been rotated counterclockwise by an angle  $\theta_{12}$  with respect to  $\mathbf{E}_2$ , as depicted in Figure 9.3 (and the inset to Figure 9.4). Under these circumstances, it is a tedious yet straightforward task to solve the density matrix equations in closed form to third order. For positive time delays at time  $t$ , the resulting third-order polarization in the  $2\mathbf{k}_2 - \mathbf{k}_1$  direction is given by

$$\begin{aligned} \mathcal{P}_{2\mathbf{k}_2 - \mathbf{k}_1}(t) = & \kappa \Theta(t) \Theta(\tau_{21}) \exp(i\delta' \tau_{21}) \exp(-\gamma(t + \tau_{21})) \\ & \times \left\{ 1 \begin{bmatrix} \cos \theta_{12} \hat{\mathbf{x}} \\ -\sin \theta_{12} \hat{\mathbf{y}} \end{bmatrix} + \left( \eta \begin{bmatrix} \cos \theta_{12} \hat{\mathbf{x}} \\ 0 \hat{\mathbf{y}} \end{bmatrix} + i\xi \begin{bmatrix} \cos \theta_{12} \hat{\mathbf{x}} \\ -\sin \theta_{12} \hat{\mathbf{y}} \end{bmatrix} \right) \frac{(1 - \exp(-\gamma_e t))}{\hbar \gamma_e} \right. \\ & \left. + B^2 [G(t) - \exp(\gamma t) \exp((i\Delta - \gamma_b)t) (1 + F(t))] \begin{bmatrix} \cos \theta_{12} \hat{\mathbf{x}} \\ \sin \theta_{12} \hat{\mathbf{y}} \end{bmatrix} \right\}, \quad (9.20) \end{aligned}$$

where

$$G(t) = \frac{-i\xi (1 - \exp((i\Delta - \gamma_{bg})t))}{\hbar (\gamma_{bg} - i\Delta)}$$

$$+ \frac{\xi^2}{\hbar^2 (\Gamma_1 + i\Delta)} \left( \frac{(1 - \exp((i\Delta - \gamma_{bg})t))}{\gamma_{bg} - i\Delta} - \frac{(1 - \exp(-2\gamma t))}{2\gamma} \right), \quad (9.21)$$

$$F(t) = \frac{i\xi (1 - \exp(-(i\Delta + \Gamma_4)t))}{\hbar (\Gamma_4 + i\Delta)} - \frac{i\xi (1 - \exp(-\Gamma_2 t))}{\hbar \Gamma_2} \\ + \frac{\xi^2}{\hbar^2 (\Gamma_1 + i\Delta)} \left( \frac{(1 - \exp(-\Gamma_2 t))}{\Gamma_2} - \frac{(1 - \exp(-(i\Delta + \Gamma_3)t))}{\Gamma_3 + i\Delta} \right), \quad (9.22)$$

where we have found it convenient to define the EID parameter  $\eta = 2\hbar N(\partial\gamma/\partial n)$  and the LFC parameter  $\xi = 2|\mu_{hh}|^2 NL$ , where (as in Section 9.5)  $N$  is the total number of oscillators that can be excited in each spin state and  $\mu_{hh}$  is the  $hh$  dipole matrix element. Both the EID parameter and LFC parameter as defined here have the dimensions of energy. In (9.20)–(9.22),  $\hbar\Delta$  is the biexciton binding energy,  $B^2 = |\mu_b/\mu_{hh}|^2$ , where  $\mu_b$  is the dipole matrix element for the exciton-to-biexciton transition and  $\Gamma_1 = 2\gamma - \gamma_{bg}$ ,  $\Gamma_2 = \gamma + \gamma_{bg} - \gamma_b$ ,  $\Gamma_3 = 3\gamma - \gamma_b$ , and  $\Gamma_4 = \gamma - \gamma_b + \gamma_e$ , where  $\gamma_b$  is the dephasing rate of the biexciton-to-exciton transition,  $\gamma_{bg}$  is the dephasing rate associated with the biexciton-to-ground-state coherence, and  $\delta' = \omega_{hh} - \nu - \xi/2\hbar$ .

In addition,  $\mathcal{P}$  is now the slowly varying amplitude that is associated with a total polarization that oscillates at the frequency  $\omega = \omega_{hh} - \xi/2\hbar$  where  $\hbar\omega_{hh}$  is the transition energy of the  $hh$  exciton and  $\xi/2\hbar$  is the static Lorentz shift caused by the local field:

$$\mathbf{P}(\mathbf{r}) \Big|_{2\mathbf{k}_2 - \mathbf{k}_1} = \frac{1}{2} [\mathcal{P}(t) \exp[-i\omega t] \exp[i(2\mathbf{k}_2 - \mathbf{k}_1) \cdot \mathbf{r}] + \text{c.c.}]. \quad (9.23)$$

Notice that (9.15) and (9.16) for the polarization of the  $2 \times 2$  system are recovered when  $B = 0$ ,  $\eta = 0$ , and  $\xi = 0$ .

To obtain this solution, one must include all of the possible transitions shown in Figure 9.16 in the polarization  $\mathbf{P}$  that appears in the local field (see (9.18)). Only by including all possible transitions does the resulting FWM polarization reduce to the correct  $2 \times 2$  expression in the limit of vanishing biexcitonic contributions. Furthermore, we have made two assumptions regarding the unbound two-exciton state. We have assumed that the dephasing rates and the dipole matrix elements between the  $|2e\rangle$  and single-exciton states  $|e_{\pm}\rangle$  are the same as those for the exciton-to-ground-state transitions, i.e., equal to  $\gamma$  and  $\mu_{hh}$ , respectively.

Equation (9.20) would seem to be a formidable result. However, by setting  $\eta = \xi = B = 0$ , the term multiplied by 1 is readily recognized as the solution to the  $2 \times 2$  system of Section 9.5 (see (9.16)). Similarly, by setting  $\xi = B = 0$ , the term multiplied by  $\eta$  is seen to give the contribution of EID when acting alone. Likewise, by first taking  $\eta = B = 0$  and then  $\eta = \xi = 0$ , the term multiplied by  $\xi$  can be identified as the LFC response, and the  $B^2$  term multiplied by 1 as the BIF response, respectively. The terms that involve either  $G(t)$  or  $F(t)$  are cross terms that disappear if either  $\xi$  or  $B$  vanishes. Elsewhere [58], we provide a detailed discussion of (9.20) and consider the physical origin of each of these terms. In that presentation [58], we introduce the independent  $2 \times 2$  system of Section 9.4 and

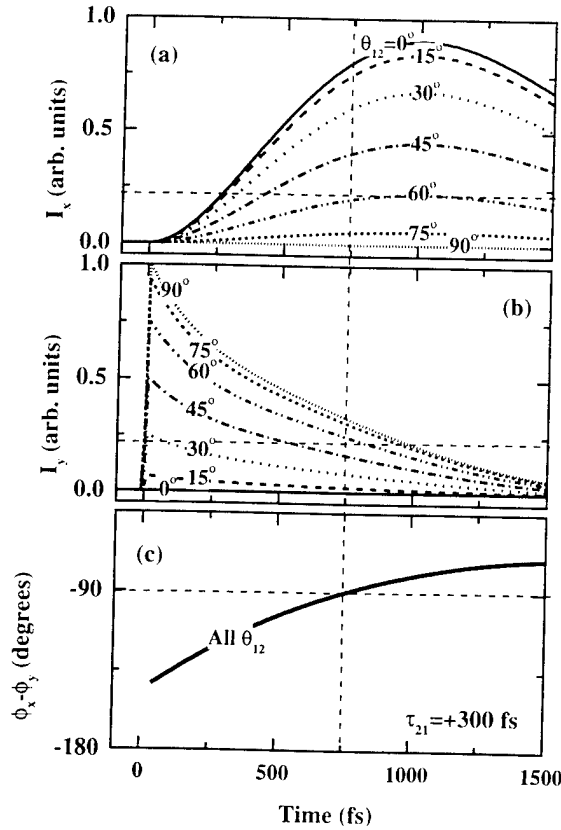


FIGURE 9.17. (a) The  $x$  component  $I_x(t)$  and (b) the  $y$  component  $I_y(t)$  of the TR-FWM intensity and (c) the phase difference,  $\phi_x(t) - \phi_y(t)$ , for selected angles  $\theta_{12}$  between the two input polarizations as calculated from the  $2 \times 2$  model modified to include EID, LFC, and BIF (i.e., calculated from the density matrix equations for the two-particle 5-level energy diagram of Figure 9.16 with EID and LFC included; see (9.20)). The time delay was fixed at  $\tau_{21} = +300$  fs.

each of the many-body effects one at a time in order to develop an intuitive feel for each contribution.

The  $x$  component  $I_x$  and the  $y$  component  $I_y$  of the TR-FWM intensity and the phase difference  $\phi_x - \phi_y$  between the  $x$  and  $y$  components of the field as calculated from (9.20) for  $\tau_{21} = 300$  fs are shown in Figure 9.17 for comparison with the data in Figure 9.5. In making this comparison one should remember that the simulated curves shown in Figure 9.17 should be "smoothed" by the finite width of the 150-fs excitation pulses for direct comparison with the experimental data. If this is kept in mind, the qualitative features depicted in these two figures are similar. The maximum value for  $I_y$  occurs at a significantly earlier time than that for  $I_x$ , and the maximum of  $I_x$  at an angle of  $\theta_{12} = 0^\circ$  is comparable to the maximum of  $I_y$  at an angle  $\theta_{12} = 90^\circ$ . In addition, notice that the temporal evolution of  $\phi_x - \phi_y$  is roughly the same for both simulation and experiment. In particular, notice that



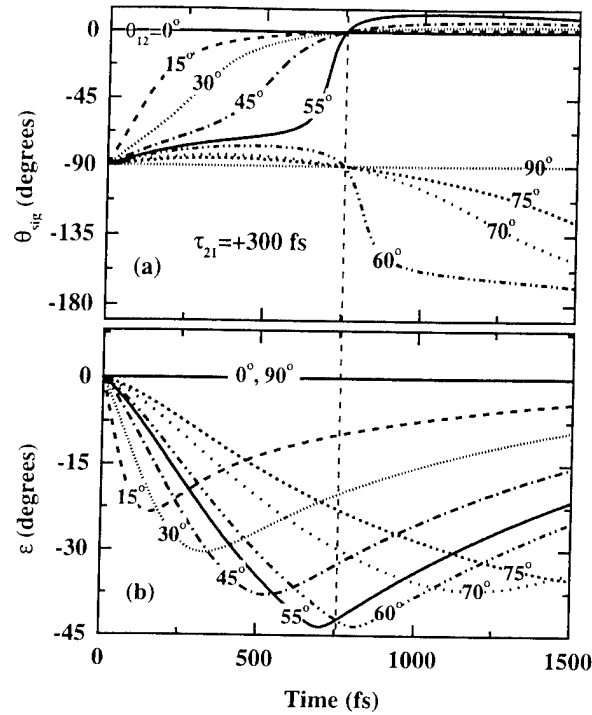


FIGURE 9.18. (a) The azimuthal angle  $\theta_{\text{sig}}(t)$  and (b) the ellipticity angle  $\varepsilon(t)$  for selected angles  $\theta_{12}$  between the two input polarizations as calculated from the  $2 \times 2$  model modified to include EID, LFC, and BIF (see (9.20)). The time delay was fixed at  $\tau_{21} = +300$  fs.

this phase difference is completely independent of  $\theta_{12}$  for our model and that it shows only a weak dependence in the data of Figure 9.5. Also notice that the phase difference  $\phi_x - \phi_y$  increases monotonically with time, and most importantly, at some moment its magnitude becomes equal to  $90^\circ$ .

The time-resolved azimuthal angle  $\theta_{\text{sig}}(t)$  and the ellipticity angle  $\varepsilon(t)$  corresponding to the calculated  $I_x(t)$ ,  $I_y(t)$ , and  $\phi_x - \phi_y$  of Figure 9.17 are plotted in Figure 9.18. (We have added a curve for  $\theta_{12} = 55^\circ$  to Figure 9.18 to emphasize the discontinuity in the azimuthal angle.) Again, when EID, LFC, and BIF are all included, the major features observed in the TR-FWM polarization data shown in Figure 9.6 are also present in the corresponding numerical simulations. The magnitude of the ellipticity increases then decreases with time. The azimuthal angle exhibits a distinct discontinuity. That is, the azimuthal angle moves toward more positive values (with increasing time) for small  $\theta_{12}$  and toward larger negative values for larger  $\theta_{12}$ . This discontinuity is present in the simulations only if all three

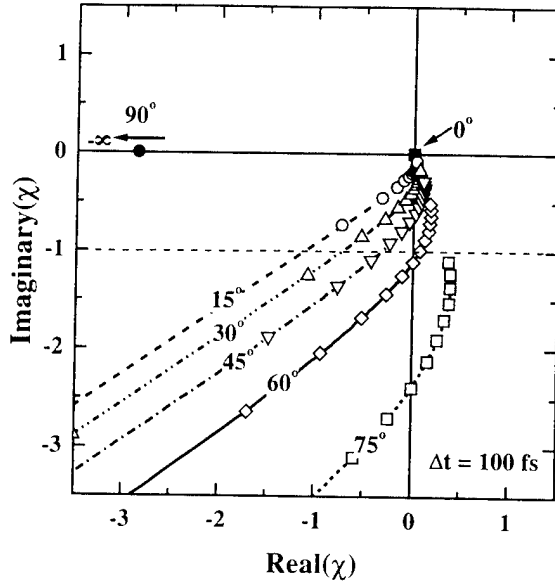


FIGURE 9.19. The TR-FWM polarization state as calculated from the  $2 \times 2$  model modified to include EID, LFC, and BIF (see (9.20)) plotted as trajectories in the complex plane. The time delay was fixed at  $\tau_{21} = +300$  fs.

processes are included, and it disappears if any of the processes is omitted (e.g., see Figure 26, 30, 32, or 38 of [58]).

Finally, the time-resolved polarization simulations of Figure 9.18 are replotted in the complex plane in Figure 9.19 for direct comparison with the data in Figure 9.11. Notice that the simulated trajectories in the complex plane are similar to those produced by the data. Specifically, notice that for an angle  $\theta_{12}$  between  $55^\circ$  and  $60^\circ$  the trajectory passes through  $-i$  at  $t \approx 750$  fs in Figure 9.19. These are the same time and the same angle at which the discontinuity in the orientation occurs for the simulations shown in Figure 9.18. The discontinuity in the orientation that is observed in the data (Figure 9.6) occurs at a slightly different angle and time, but under identical circumstances.

For purposes of producing the simulations shown in Figs. 9.17–9.19, the following values were assigned to the parameters appearing in (9.20)–(9.23):  $\gamma^{-1} = 1$  ps,  $\gamma_b^{-1} = \gamma_{bg}^{-1} = 720$  fs,  $\hbar\Delta = 1.5$  meV, and  $\gamma_e^{-1}$  was taken to be long compared to the dephasing times. In addition, the LFC parameter  $\xi$  equals 0.7 meV, the EID parameter  $\eta$  equals 2 meV, and  $\mu_{hh}/\mu_b = 1$ . We wish to point out that the numerical results presented in this section are most certainly sensitive to the particular choices of  $\xi$ ,  $\eta$ , and  $\mu_b$  as well as to the dephasing times. Nevertheless, we have performed extensive parametric studies, in which these parameters were varied over a considerable range (consistent with experimental conditions). We want to emphasize that while the quantitative position of a given feature depends on the choice of parameters, the qualitative features discussed here are surprisingly robust. In

particular, the discontinuity in the azimuthal angle shown in Figure 9.18 persisted over the entire range of parameters that we investigated when all three processes were included, but was not present for any other combination of processes.

Furthermore, it should be pointed out that this simple phenomenological model produces good qualitative agreement with a large number of features in the TR-FWM and TI-FWM signal that are not discussed in this chapter (see [51, 52, 58] for a discussion of some of these). Specifically, we note that the density matrix equations for the 5-level system of Figure 9.16 also can be solved to obtain a closed-form solution for the third-order polarization in the  $2\mathbf{k}_2 - \mathbf{k}_1$  direction at negative delays (including EID and LFC). This expression can be found in [58]. Such a phenomenological model produces good agreement with the corresponding time-resolved polarization state measured at negative delays (see [52] for a detailed comparison of the data at a negative delay and this model).

## 9.7 Heavy-Hole and Light-Hole Quantum Beats in the Polarization State

To this point, our experiments have been limited to investigations of the coherent emission from the heavy hole (hh). That is, the laser was purposefully tuned below the hh exciton sufficiently to ensure that we excited as few light holes (lh) as possible and to avoid the complication of quantum beating between the lh and hh. In this section we describe measurements of the dynamics of the amplitude, phase, and polarization state of the emission from the same GaAs-AlGaAs MQW when the excitation spectrum is tuned so that both hh and lh excitons are excited and quantum beats are observed. Oscillations in both the time-integrated (e.g., [16, 76–78]) and time-resolved [79] FWM signals have been studied previously when both hh and lh excitonic transitions are excited. For example, both the spectral behavior of the time-integrated signal [80] and the temporal behavior of the time-resolved signal [79] have been used to distinguish quantum beating (which is associated with two coupled oscillators that share a common level) from polarization interference (which is associated with two independent oscillators).

In addition, there have been several studies of quantum beating that have addressed the dependence of the FWM signal (or its spectrum) on the input polarization. For example, it has been demonstrated that the amplitudes of quantum beats produced by incident pulses with parallel polarizations are exactly out of phase with the beats produced by orthogonally polarized pulses [33, 81]. However, conventional techniques were used for these measurements, and the polarization state of the emitted FWM signal was not measured. In fact, to the best of our knowledge, there has been only one previous study [82] that monitored the polarization state of the emitted FWM radiation in semiconductors in the quantum beat regime. This study [82] measured the time-integrated orientation of the polarization ellipse associated with the emitted FWM signal in ZnSe epilayers, but the degree to which the FWM signal was elliptically polarized was not measured, and the polarization

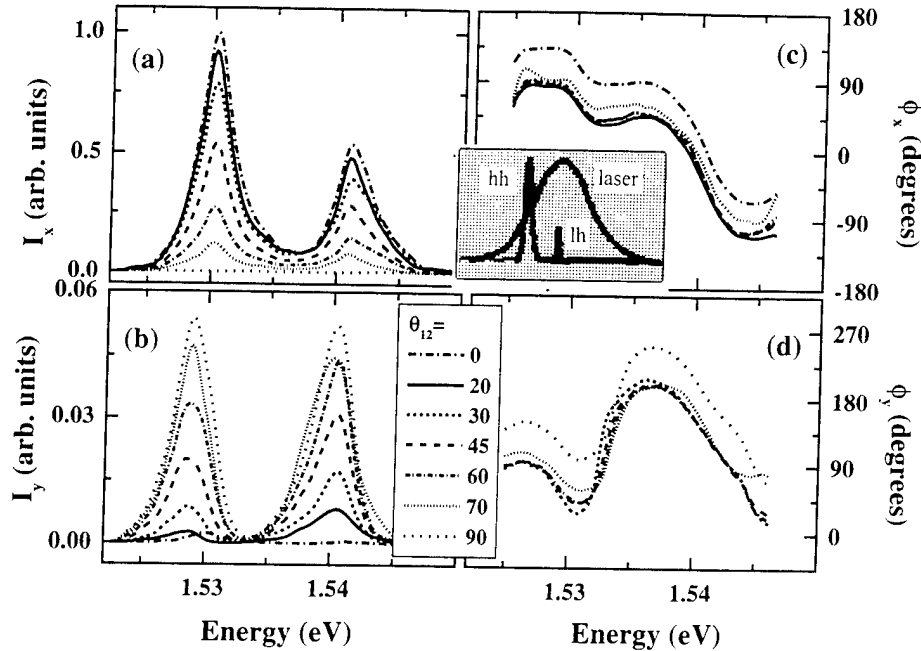


FIGURE 9.20. Measurements of the (a)  $x$  component,  $I_x(\omega)$ , and (b)  $y$  component,  $I_y(\omega)$ , of the spectral intensity and the (c)  $x$  component,  $\phi_x(\omega)$ , and (d)  $y$  component,  $\phi_y(\omega)$ , of the spectral phase of the FWM signal for selected angles  $\theta_{12}$  between the two linear input polarizations in the strong quantum beat regime. The top inset shows the positions of the heavy-hole (hh) and the light-hole (lh) emission spectra with respect to the laser spectrum.

state was not time resolved. Even so, these measurements [82] revealed a dramatic beating in the time-integrated orientational angle, which required the inclusion of EID. (BIF contributions were experimentally eliminated, and LFC effects were not included.) Typically, in such cases, the lh-hh beating behavior has been explained by solving the density matrix equations for two independent three-level systems without including many-body or biexcitonic effects [33].

### 9.7.1 Strong Quantum Beat Regime

Initially, we review measurements [55, 56] in which the laser was tuned onto the lh exciton so that both the hh and lh were strongly excited, as shown schematically in the inset to Figure 9.20. Typical spectral amplitudes and spectral phases for both the  $x$  and  $y$  components of the FWM signal, which were extracted from spectral interferograms taken under these circumstances, are shown in Figure 9.20. Results are shown for selected angles  $\theta_{12}$  between the two input polarizations. Clearly, strong emission is observed from both lh and hh excitons. Most importantly, notice that the  $x$  and the  $y$  spectral responses are again very different. As in Section 9.4 (when we excited only the hh), the emission for the  $y$  component of the FWM spectral intensity  $I_y(\omega)$  is red-shifted slightly with respect to the  $x$  com-

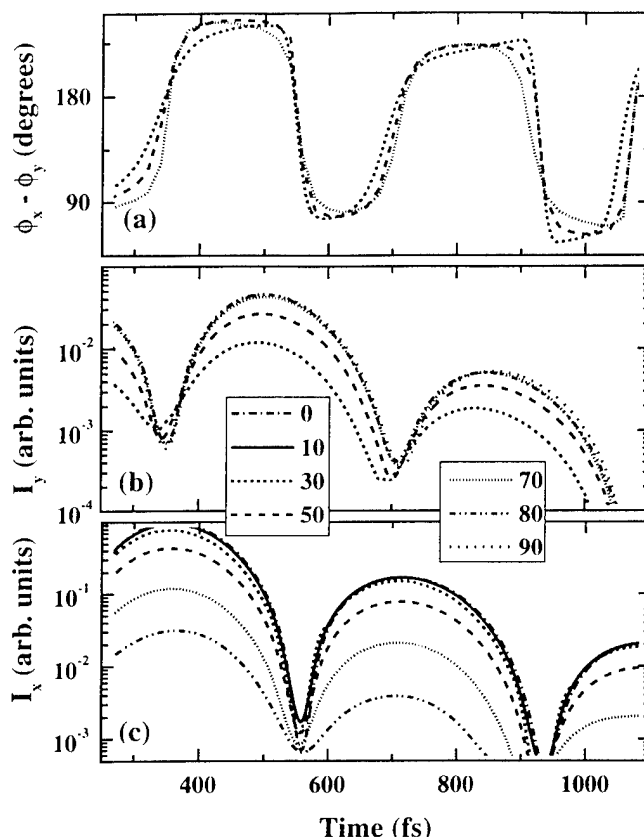


FIGURE 9.21. The measured (a) difference between the  $x$  and  $y$  components of the temporal phase,  $\phi_x(t) - \phi_y(t)$ , and the (b)  $y$  component,  $I_y(t)$ , and (c)  $x$  component,  $I_x(t)$ , of the temporal intensity of the FWM signal for selected angles,  $\theta_{\text{sig}}$ , between the two input polarizations in the strong quantum beat regime, which are obtained by inverse Fourier transformation of the measured spectral phases and amplitudes (see Figure 9.20).

ponent  $I_x(\omega)$ , and the emission gradually changes from being  $x$ -polarized to being  $y$ -polarized as the angle between the two input polarizations increases. In addition, the  $x$  and  $y$  spectral phases,  $\phi_x(\omega)$  and  $\phi_y(\omega)$ , have dramatically different magnitudes and slopes. Consequently, the spectral phase difference  $\phi_x(\omega) - \phi_y(\omega)$  varies significantly with wavelength. These differences in the amplitudes and phases of the  $x$  and  $y$  components of the FWM signal again illustrate why it is important to determine the vectorial nature of the emission.

The corresponding temporal amplitudes and phases that are obtained by inverse Fourier transformation of the data in Figure 9.20, including the measured spectral phases, are shown in Figure 9.21. Strong beats are observed in both the  $x$  and  $y$  intensities, and the oscillations in  $I_x(t)$  and  $I_y(t)$  are exactly out of phase, in agreement with measurements by other groups using conventional time-resolved FWM techniques [33, 81]. However, the temporal phase information is not provided by conventional techniques. Notice that the phase difference  $\phi_x(t) - \phi_y(t)$  also oscil-

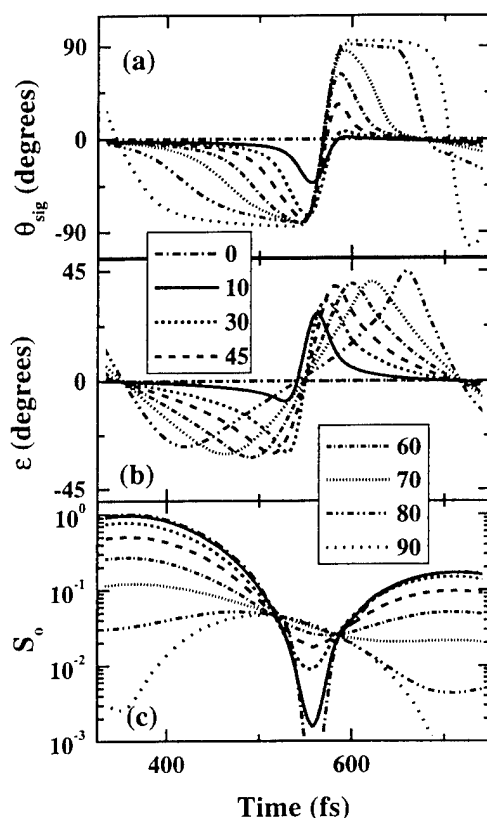


FIGURE 9.22. The measured time-resolved polarization state of the emitted FWM signal for roughly one beat period for selected angles between the two linear input polarizations  $\theta_{12}$  in the strong quantum beat regime, plotted in terms of the (a) azimuthal angle  $\theta_{\text{sig}}$ , (b) ellipticity angle  $\varepsilon$ , and (c) total intensity  $S_0$ .

lates at the hh-lh beat frequency, and in this strong quantum beat regime, abrupt phase jumps (approaching  $\pi$  in magnitude) are observed in the phase difference at each minimum in either  $I_x(t)$  or  $I_y(t)$ . Clearly, the time-varying differences in  $x$  and  $y$  amplitudes and phases shown in Figure 9.21 imply that the polarization state of the emitted radiation is varying in time.

In Figure 9.22, the dynamics of the polarization state corresponding to the data in Figure 9.21 are displayed explicitly in terms of the parameters that directly define the polarization ellipse for approximately one beat period ( $\approx 377$  fs). Clearly, each of these parameters oscillates at the hh-lh beat frequency. The corresponding temporal behavior of the polarization ellipse is sketched in Figure 9.23 for an angle between the two input polarizations of  $\theta_{12} = 60^\circ$ . Notice that the orientation of the ellipse rotates through a full  $180^\circ$  in one beat period. The ellipticity goes from linear to highly elliptical and then back to linear twice per beat period. And finally, the sense of rotation changes from clockwise (left circular) to counterclockwise

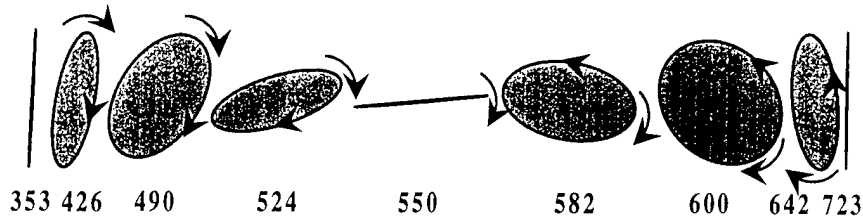


FIGURE 9.23. Schematic of the temporal evolution of the polarization ellipse for one beat period corresponding to the data in Figure 9.22 for  $\theta_{12} = 60^\circ$ .

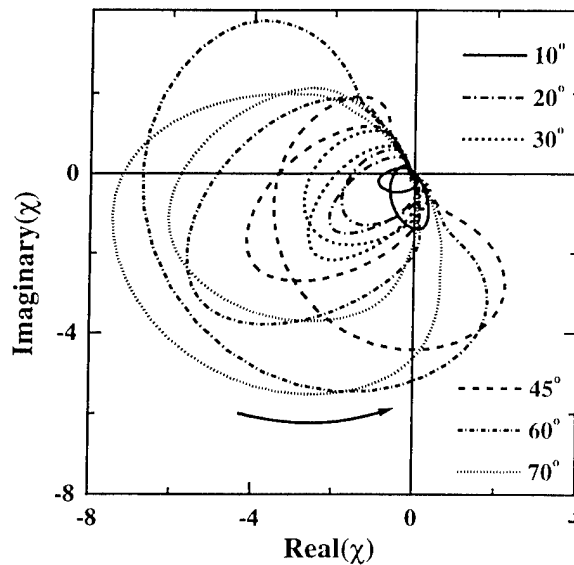


FIGURE 9.24. The measured time-resolved polarization state of the emitted FWM signal for selected angles between the two linear input polarizations  $\theta_{12}$  in the strong quantum beat regime plotted as trajectories in the complex plane.

(right circular) each period.

Figure 9.24 shows the data in the strong quantum beat regime (i.e., corresponding Figs. 9.21 and 9.22) when the polarization dynamics are replotted as trajectories in the complex plane. When plotted in this way, it is clear that the polarization state is not a perfectly periodic function of the hh-lh beat frequency, but only approximately so. In addition, the “radii” of the “oscillations” in the complex plane systematically increase with increasing  $\theta_{12}$ .

The results shown in Figs. 9.21–9.24 emphasize once again the importance of determining the vectorial dynamics. If a single time-resolved scalar measurement had been performed, then we would have simply obtained the total intensity  $S_0$ . All of the information about the differences in the  $x$  and  $y$  intensities and the

phase differences shown in Figure 9.21 and all of the information concerning the ellipticity and azimuthal angle shown in Figs. 9.22 and 9.23 would have been lost. Furthermore, without a knowledge of  $\phi_x(t) - \phi_y(t)$  or  $\varepsilon$ , we cannot determine the parameter  $\chi$  (see (9.12)). Consequently, we would lose all of the information about the trajectories shown in Figure 9.24. Finally, to verify that the oscillations described here were quantum beats, and not the result of polarization interference, we performed the tests described in [79].

### 9.7.2 A Qualitative Three-Level Description

As we have stated in the introduction to this section, lh-hh quantum beating behavior has often been explained by using a simple model based on the density matrix equations for two independent three-level systems [33], which does not include many-body or biexcitonic effects. In fact, as we will show in this subsection, many of the features in the polarization beating shown in Figs. 9.21–9.24 of Section 9.7.1 can also be qualitatively reproduced by this model without including many-body effects. In subsequent subsections we will show that many-body and biexcitonic effects are nevertheless clearly important.

In the simplest picture, the hh and lh excitons can be represented by two independent three-level ( $2 \times 3$ ) systems that satisfy the selection rules shown in Figure 9.25. The FWM emission from such a system, when it is excited by  $\delta$ -function input pulses, can be shown [33] to be proportional to

$$\begin{aligned} \mathcal{E}_{\text{FWM}} \propto & \Theta(t)\Theta(\tau_{21})\mathcal{E}_2^2\mathcal{E}_1^* \exp[-\gamma(t + \tau_{21})] \\ & \{ (1 + A \exp[-i\Omega t])(1 + A \exp[i\Omega\tau_{21}]) \cos\theta_{12}\hat{x} \\ & - (1 - A \exp[-i\Omega t])(1 - A \exp[i\Omega\tau_{21}]) \sin\theta_{12}\hat{y} \}, \quad (9.24) \end{aligned}$$

where  $\hbar\Omega$  is the difference between the hh and lh energies, and  $A$  is a phenomenological constant that reflects the relative strength of the lh FWM emission. In our case, the latter constant is the product of the square of the ratio of the lh and hh optical transition matrix elements ( $\approx \frac{1}{3}$ ) and a spectral weighting factor ( $\approx 2$ ) to account for the detuning of the excitation wavelength with respect to the hh and lh excitons. We emphasize that this description does not phenomenologically include EID, LFC, or BIF.

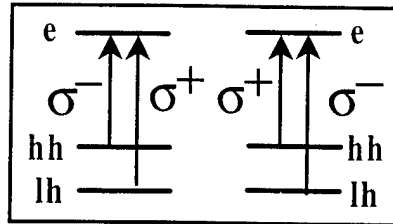


FIGURE 9.25. Schematic of the two independent three-level ( $2 \times 3$ ) systems used to represent the hh and lh transitions in the absence of many-body effects.



Inspection of (9.24) reveals that aside from an overall exponential decay, the time-dependent part of the  $x$  component,  $(1 + A \exp[-i\Omega t])$ , has the form of the sum of two vectors: a stationary hh unit vector and an lh vector of magnitude  $A$  that precesses about it at the lh-hh beat frequency  $\Omega$ . The  $y$  component  $(1 - A \exp[-i\Omega t])$  has a similar form, except that the temporal phase of the lh vector differs by  $180^\circ$ . The relative strengths of the  $x$  and  $y$  components are determined by the angle  $\theta_{12}$  between the linear polarizations of the two input pulses. In addition, for nonzero values of  $A$ , the amplitude and phase of the  $x$  and  $y$  components will be changed by the time delay between pump and probe  $\tau_{21}$  through the factors  $(1 \pm A \exp[i\Omega \tau_{21}])$ . For this reason, the time-resolved quantum beating behavior changes dramatically as a function of time delay.

The intensities  $I_x(t)$  and  $I_y(t)$  and the phase difference  $\phi_x(t) - \phi_y(t)$  that are calculated from (9.24) (using values of  $\tau_{21} = 390$  fs and  $A = 0.75$ ) are shown in Figure 9.26 for selected angles  $\theta_{12}$  between the input polarizations. The corresponding orientation of the polarization ellipse  $\theta_{\text{sig}}$ , its ellipticity angle  $\varepsilon$ , and the total intensity  $S_0$  are displayed in Figure 9.27 for roughly one beat period. The qualitative agreement with the data shown in Figs. 9.21 and 9.22 is apparent. The behavior illustrated in Figs. 9.21 and 9.22 and simulated in Figs. 9.26 and 9.27 is typical of that observed at this time delay for strong quantum beats (i.e., for comparable FWM emission from the hh and lh excitons). These tendencies vary dramatically for other time delays, for reasons discussed in the previous paragraph.

We caution that one should not conclude that many-body and biexcitonic effects are unimportant simply because many features in the strong quantum beat regime can be qualitatively described without them. Many-body effects are still present, and this can be seen most easily by comparing the data and the simulations for the independent  $2 \times 3$  system in the complex plane. Figure 9.28 shows the  $2 \times 3$  simulations (without many-body effects) in the strong quantum beat regime (i.e., corresponding to Figs. 9.26 and 9.27) when they are replotted in the complex plane. As suggested by Figure 9.28, quantum beating in the absence of many-body effects (i.e., (9.24)) can be readily shown to produce perfectly circular trajectories when plotted in the complex plane. The radius and the center of the circle are determined by  $A$ ,  $\theta_{\text{sig}}$ , and  $\tau_{21}$ . By comparison, the data (Figure 9.24) produce trajectories that are far from circular, and the "radius" changes significantly from one period to the next. These distortions suggest the importance of many-body effects, even in the presence of strong quantum beating. In the following section we provide additional evidence for the presence of these effects.

### 9.7.3 Weak Quantum Beat Regime

One way to see that many-body and biexcitonic effects are present is to gradually tune the laser to lower energies, so that fewer lh excitons are excited and the amplitude of the quantum beating is greatly reduced. Figure 9.29 shows the  $x$  and  $y$  components of the spectral amplitudes and phases that were measured for selected angles between the two input polarizations when the excitation wavelength was tuned so that the ratio of the hh emission peak to the lh peak was  $\approx 50 : 1$ . As in the

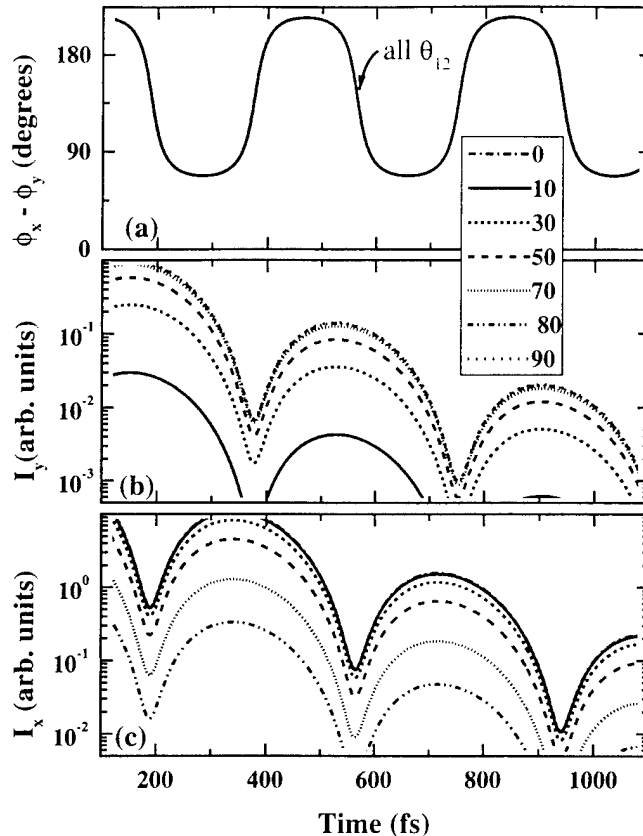


FIGURE 9.26. Simulated strong quantum beats in the  $x$  and  $y$  intensities and phase difference as calculated from the density matrix equations for the two independent three-level systems shown in Figure 9.25 (without the inclusion of many-body effects).

strong quantum beat regime (see Figure 9.20), notice that the  $x$  and  $y$  responses are very different. The emission for the  $y$  component is spectrally broader and is again red-shifted slightly with respect to the  $x$  component by an amount ( $\approx 1.5$  meV) roughly equal to the expected biexcitonic binding energy. Also, the  $x$  and  $y$  phases are similar in shape, but they have dramatically different absolute magnitudes and slopes.

The corresponding temporal intensities  $I_x(t)$  and  $I_y(t)$  and the phase difference  $\phi_x(t) - \phi_y(t)$  that are obtained by inverse transformation of the data in Figure 9.29 are shown in Figure 9.30. Notice that weak quantum beats are evident in both the amplitudes and phase difference. The data in Figure 9.30 are replotted in Figure 9.31 in terms of the orientation of the polarization ellipse  $\theta_{\text{sig}}(t)$ , the ellipticity angle  $\varepsilon(t)$ , and the total intensity  $S_0(t)$ . Clearly, each of these parameters oscillates at the hh-lh beat frequency; however, in this case, the quantum beats are superposed on a more complicated structure. For example, the orientation of the polarization ellipse  $\theta_{\text{sig}}(t)$  rotates toward more positive angles (counterclockwise)

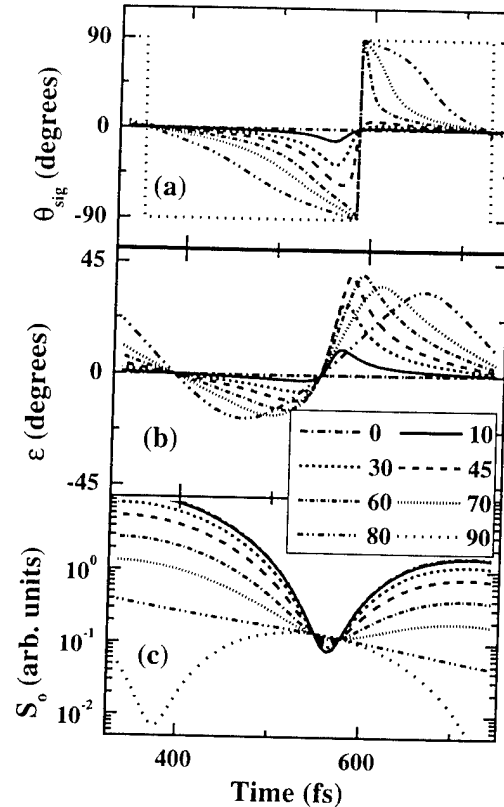


FIGURE 9.27. Simulations of the time-resolved (a) azimuthal angle  $\theta_{\text{sig}}$ , (b) ellipticity angle  $\varepsilon$ , and (c) total intensity  $S_0$  of the emitted FWM signal for roughly one beat period for selected angles between the two linear input polarizations  $\theta_{12}$  in the strong quantum beat regime, as calculated from the two independent three-level model shown in Figure 9.25.

for small angles  $\theta_{12}$  between the two incident linear polarizations, but reverses direction and rotates in the opposite direction (clockwise) for larger  $\theta_{12}$ . In addition, the ellipticity, on the average, increases and then decreases with time. We have discussed this behavior previously in Section 9.4 in connection with Figure 9.6, and we have argued in Section 9.6 that it requires the inclusion of many-body and biexcitonic effects. In addition, in Figure 9.30, it is evident that  $I_x(t)$  continues to grow long after the two pump pulses have exited the sample, which has also been taken to be a consequence of many-body effects.

To further illustrate that the quantum beats are superposed on a polarization dominated by many-body and biexcitonic effects, we show the corresponding independent  $2 \times 3$  simulations without many-body effects in Figure 9.32. These were calculated from (9.24) using  $A = 0.07$  and  $\tau_{21} = 300$  fs. While the beating phenomena shown in Figure 9.31 are well reproduced, the features that we have associated with many-body and biexcitonic effects are not. This is consistent with our conclusion that the latter features are associated with many-body effects and

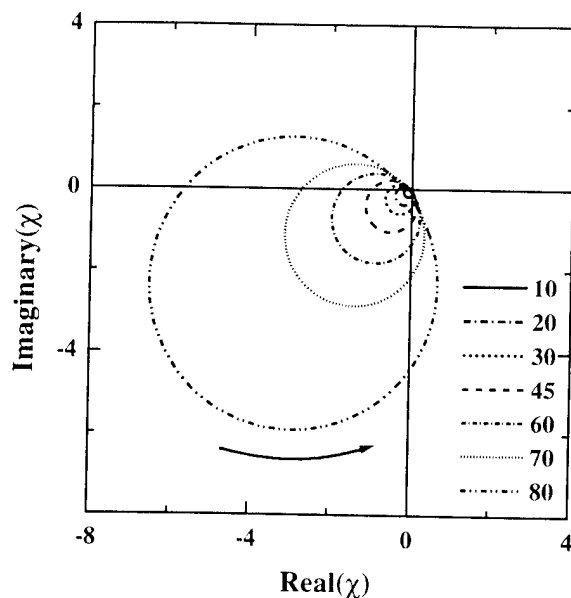


FIGURE 9.28. Simulations of the polarization state of the TR-FWM signal for selected angles between the two linear input polarizations  $\theta_{12}$  in the strong quantum beat regime, as calculated from the two independent three-level model shown in Figure 9.25, plotted as trajectories in the complex plane. The arrow indicates the direction of increasing time.

emphasizes the importance of including such effects. Consequently, Figs. 9.30 and 9.31 illustrate that time-resolved polarimetry is extremely sensitive both to quantum interference effects (in this case, lh and hh quantum beating) and to many-body effects.

The separate contributions of exciton–exciton interactions and simple quantum beating are more apparent if we compare both the data and the simulations in the complex plane. Figure 9.33 shows the data and the simulations (without many-body effects) in the weak quantum beat regime (i.e., corresponding to Figs. 9.31 and 9.32, respectively) when they are replotted in the complex plane. Clearly, this representation provides a dramatic visualization of the power of fs time-resolved polarization spectroscopy for studying both quantum beats and exciton–exciton correlations. In the absence of many-body effects, again one would expect quantum beating to produce trajectories that are perfect circles. Instead, the data show that the quantum beats appear as loops superposed on dramatic trajectories that cannot be explained without many-body effects. Finally, we note that when the laser excitation energy is tuned even further below the hh resonance, so that a negligible number of lh are excited, the beats (loops) are no longer visible. In the latter regime, our previous data shown in Section 9.4 are recovered.

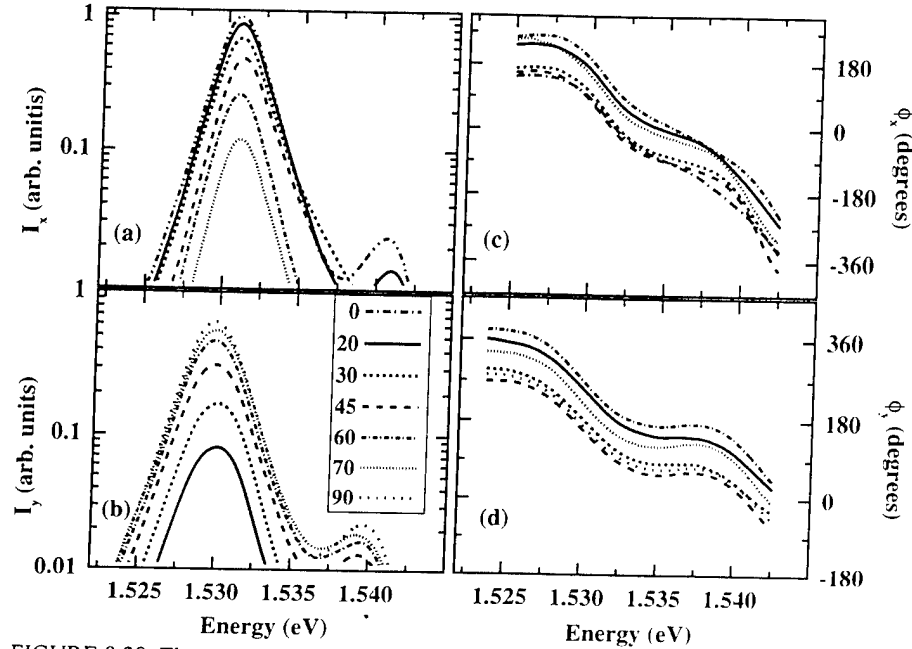


FIGURE 9.29. The measured (a)  $x$  component,  $I_x(\omega)$ , and (b)  $y$  component,  $I_y(\omega)$ , of the spectral intensity and the (c)  $x$  component,  $\phi_x(\omega)$ , and (d)  $y$  component,  $\phi_y(\omega)$ , of the spectral phase of the FWM signal for selected angles  $\theta_{12}$  between the two linear input polarizations in the weak quantum beat regime.

## 9.8 Heavy- and Light-Hole Oscillations: A Test for Exciton-Exciton Correlations

In the previous section we have shown that oscillations (or beats) are observed in the FWM signal when both hh and lh excitons are excited [16, 55, 56, 76–79, 83]. Similar beats have been observed between excitons in quantum wells of different widths [79, 80]. In one such study [79], which is of particular interest here, the behavior of the time-resolved FWM signal has been used to distinguish between quantum beating and polarization interference. In the context of [79], the oscillations are classified as quantum beats if the interference occurs within the material. For example, such oscillations might arise from two oscillators that share a common level. By comparison, the oscillations are classified as polarization interference if the interference occurs external to the material. For example, oscillations arising from the interference of light from two independent oscillators in a detector would be considered polarization interference. The definitions for quantum beating are actually more problematic than this (e.g., see [84, 85]), and we shall return to this discussion later.

Here, we describe time-resolved FWM measurements on a GaAs-AlGaAs MQW when the laser spectrum is tuned so that both hh and lh excitons are

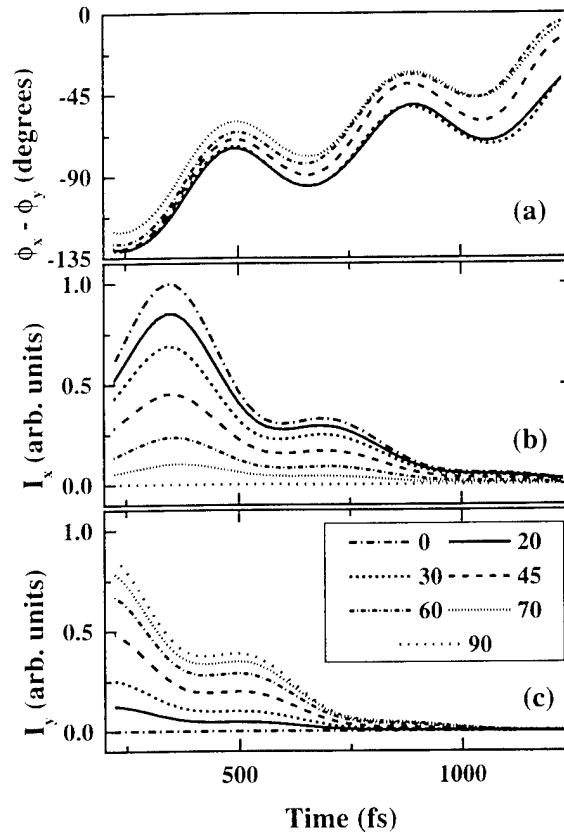


FIGURE 9.30. The measured (a) difference between the  $x$  and  $y$  components of the temporal phase,  $\phi_x(t) - \phi_y(t)$ , and the (b)  $x$  component,  $I_x(t)$ , and the (c)  $y$  component,  $I_y(t)$ , of the temporal intensity of the FWM signal for selected angles  $\theta_{sig}$  between the two input polarizations in the weak quantum beat regime, which are obtained by inverse Fourier transformation of the measured spectral phases and amplitudes shown in Figure 9.29.

excited and both excitation pulses have the same circular polarization. Under these excitation conditions, the hh and lh excitonic transitions share no common upper or lower states. Nevertheless, we demonstrate that strong oscillations at the hh-lh beat frequency are observed, and we use the test described in [79] to demonstrate that these oscillations behave like quantum beats, rather than polarization interference. Calculations based on the density matrix equations for two independent three-level ( $2 \times 3$ ) systems indicate that polarization interference, but not quantum beats, should be observed. Similar results are expected for the SBE in the Hartree-Fock limit. Consequently, this simple test provides an elegant demonstration of the importance of including many-body effects in any description of the excitonic dynamics and, more importantly, illustrates the necessity of including exciton-exciton correlations beyond the Hartree-Fock contributions. Additionally, we show that the observed quantum beating behavior can be reproduced by including a density-dependent dephasing term (i.e., by including EID).

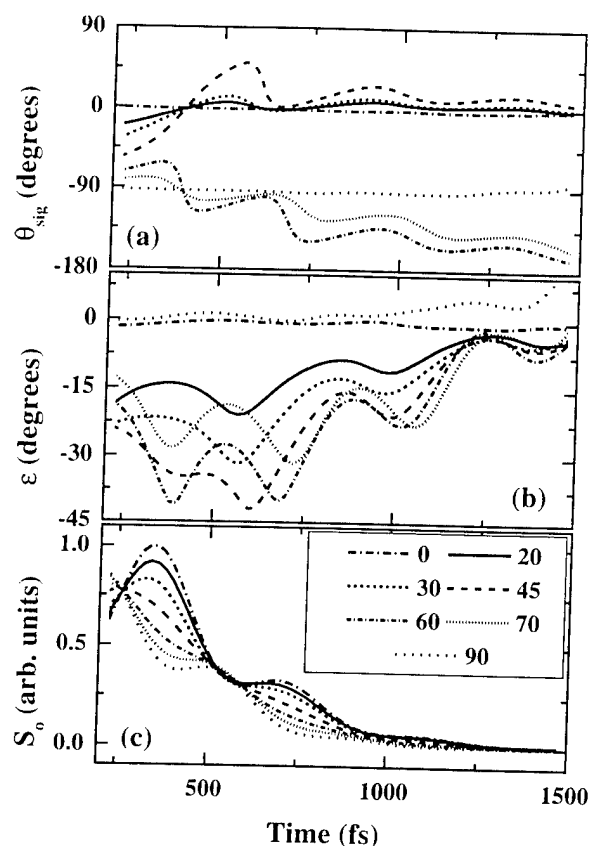


FIGURE 9.31. The measured time-resolved (a) azimuthal angle  $\theta_{\text{sig}}$ , (b) ellipticity angle  $\varepsilon$ , and (c) total intensity  $S_0$  in the weak quantum beat regime, corresponding to the data of Figure 9.30.

A simple phenomenological model based on EID predicts new features in the lh-hh oscillations that are quite distinct from those expected for purely quantum beating or for polarization interference. We demonstrate that these features are observed experimentally, and we use them to place limits on the magnitude of the density-dependent dephasing.

### 9.8.1 Distinguishing Quantum Beats from Polarization Interference

As stated above, in this section we will use a modified version of the test developed by Koch et al. [79] to distinguish between quantum beats and polarization interference to investigate exciton-exciton correlations. Consequently, in this subsection we will begin by reviewing the fundamentals of this test, and we will use it to demonstrate that we were justified in classifying the beats described in Section 9.7 as quantum beats.

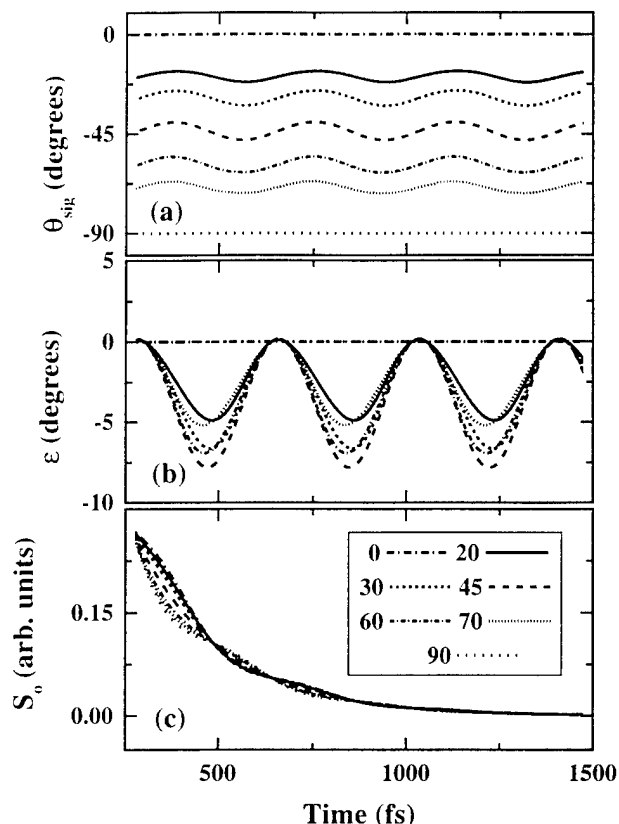


FIGURE 9.32. The two-independent-three-level-system ( $2 \times 3$ ) simulations (without many-body effects) of the (a) azimuthal angle  $\theta_{\text{sig}}$ , (b) ellipticity angle  $\epsilon$ , and (c) total intensity  $S_0$  in the weak quantum beat regime for comparison with Figure 9.31.

Basically, Koch et al. [79] recognized that the temporal FWM response of a system that consists of two nonresonant transitions that share a common level (e.g., either three-level system shown in Figure 9.25) has a different dependence on the time delay  $\tau_{21}$  than a system consisting of two nonresonant transitions that do not share a common level (e.g., the two-level systems shown in Figure 9.34). They [79] then used this difference in the temporal behavior as a function of time delay to classify the oscillations into one of two categories: quantum beats or polarization interference. We will first review the theoretical basis for this test, then illustrate its use experimentally. Our theoretical presentation will very closely parallel that of [79], but we will put the formalism into our context and notation for the reader's convenience. The models presented in this subsection will provide a useful comparison for later subsections.

In illustrating the procedure used to distinguish quantum beats from polarization interference, we will contrast the response of the two three-level ( $2 \times 3$ ) systems of Figure 9.25 with the response of the four uncoupled two-level systems shown in



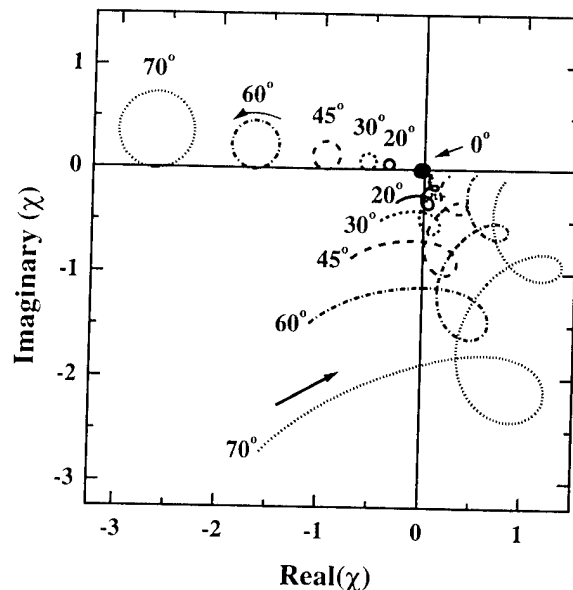


FIGURE 9.33. Comparison between the  $(2 \times 3)$  simulations (without many-body effects) and the data for selected  $\theta_{12}$  in the weak quantum beat regime when plotted as trajectories in the complex plane. The perfect circles represent the simulations, and the more complicated curves containing multiple loops the data. The arrows indicate the direction of increasing time.

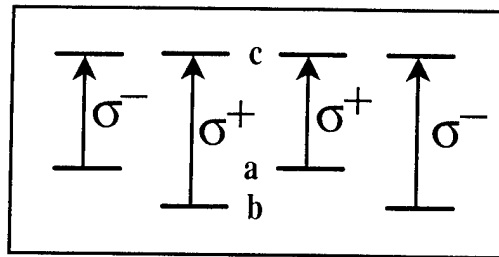


FIGURE 9.34. Schematic of four independent two-level systems for producing polarization interference.

Figure 9.34. Notice that many-body effects are not included in the analysis at this point. In order to obtain the simplest description of our experiments and in order to obtain a closed form solution, we again assume that the pulses in the  $\mathbf{k}_2$  and  $\mathbf{k}_1$  directions have delta function time dependencies given by  $\delta(t)$  and  $\delta(t + \tau_{21})$ , respectively. In addition, we assume that each is linearly ( $x$ ) polarized and that the dephasing is much faster than the population decay. Under these conditions, one can readily solve the density matrix equations for the four uncoupled systems shown in Figure 9.34 to third order. The FWM polarization that propagates in the

$2\mathbf{k}_2 - \mathbf{k}_1$  direction is found to be proportional to

$$\mathcal{P}_{PI} = \kappa \Theta(t) \Theta(\tau_{21}) \exp(-i\delta\tau_{21}) \exp(-\gamma(t + \tau_{21})) [1 + A^2 \exp(-i\Omega(t - \tau_{21}))] \hat{\mathbf{x}}, \quad (9.25)$$

where all of the constants and symbols have similar meanings as in previous sections. In particular,  $A$  in this case takes into account the strength of the emission from the  $c$ -to- $b$  transitions relative to that from the  $c$ -to- $a$  transitions, and  $\Omega = \omega_{cb} - \omega_{ca}$ . However, if for direct comparison with our expressions involving hh's and lh's we take the resonance frequencies to be  $\omega_{ca} = \omega_{hh}$ ,  $\omega_{cb} = \omega_{lh}$ , and the transition matrix elements to be  $\mu_{ca} = \mu_{hh}$  and  $\mu_{cb} = \mu_{lh}$ , then the meanings are precisely the same as in previous expressions. This slowly varying polarization amplitude is written from the frame of reference of the "hh" exciton. Thus, (9.25) is the sum of two independent oscillators: The first represents the polarization oscillating at the hh frequency and the second at the lh frequency. The magnitude of the total polarization (and therefore of the net emitted field) oscillates at the beat frequency  $\Omega$  with the phase determined by  $\tau_{21}$ , but there is no interaction (or interference) between the two polarizations within the material. Each propagates and oscillates independently. In this sense, the beating does not originate within the material.

The signal generated in the detector is proportional to the intensity and is proportional to

$$S_0 \propto |\mathcal{P}_{PI}|^2 \propto \Theta(t) \Theta(\tau_{21}) I_2^2 I_1 \exp[-2\gamma(t + \tau_{21})] \{1 + A^4 + 2A^2 \cos[\Omega(t - \tau_{21})]\}. \quad (9.26)$$

Thus, we see that the oscillations are a consequence of the nature of the detection process. Such oscillations were classified as polarization interference by [79]. It is also evident from this expression that the peak of each oscillation occurs at a time given by

$$t_p = \tau_{21} + m \left( \frac{2\pi}{\Omega} \right), \quad (9.27)$$

where  $m$  is an integer that labels the peak. Thus, one would expect to observe a linear relationship between each peak and the time delay  $\tau_{21}$  for polarization interference.

By comparison, if the two independent three-level systems of Figure 9.25 are excited with  $x$ -polarized pump pulses, both lh and hh states that share a common level will be excited (since  $x$ -polarized light is composed of equal parts left- and right-circular polarizations). In this case, the FWM polarization can be written as

$$\begin{aligned} \mathcal{P}_{QB} = & \kappa \Theta(t) \Theta(\tau_{21}) \exp(i\delta\tau_{21}) \exp(-\gamma(t + \tau_{21})) \\ & \times [(1 + A \exp(i\Omega\tau_{21}))(1 + A \exp(-i\Omega t))] \hat{\mathbf{x}}. \end{aligned} \quad (9.28)$$

Because of the shared level for each of the three-level systems, this polarization does not have the form of the sum of two independent oscillators or emitters. This is a consequence of the interference between polarizations within the material. The

detected intensity in this case takes the form

$$\begin{aligned}
 S_0 \propto |\mathcal{P}_{\text{QB}}|^2 \propto \Theta(t)\Theta(\tau_{21})I_2^2 I_1 \exp[-2\gamma(t + \tau_{21})] \\
 \times \{1 + 2A^2 + A^4 + 2(A + A^3) \cos \Omega\tau_{21} \\
 + 2(A + A^3 + 2A^2 \cos \Omega\tau_{21}) \cos \Omega t\}.
 \end{aligned} \tag{9.29}$$

Notice that the only time dependence is in the last term, which is proportional to  $\cos \Omega t$ . Now the peaks in the oscillations occur at times  $t_p$  given by  $t_p = m(2\pi/\Omega)$ . There is no dependence on  $\tau_{21}$ . The slope of the  $t_p$  versus  $\tau_{21}$  curve is 0. The oscillations in this case were classified by [79] as quantum beats.

Based on a similar analysis, Koch et al. [79] suggested that one could distinguish quantum beats from polarization interference by simply plotting the position of each peak  $t_p$  in the TR-FWM signal as a function of the time delay  $\tau_{21}$ . The result should be a straight line. The slope of the line will be zero if the time-resolved oscillations are the result of quantum beating, and the slope will be unity if they originate from polarization interference. (Note that we have taken our origin to coincide with the  $\mathcal{E}_2$  pulse. If the origin is taken to coincide with the  $\mathcal{E}_1$  pulse, as was done in the original paper [79], then a slope of 1 will be obtained for quantum beating and a slope of 2 for polarization interference.)

To illustrate this procedure and to test whether or not the hh-lh oscillations of Section 9.7 were the result of quantum beats or polarization interference, we performed this test on the FWM emission from our sample. Specifically, the laser wavelength was tuned onto the lh exciton so that both hh's and lh's were strongly excited. We then used the POLLIWOG geometry shown in Figure 9.3 to completely time resolve the FWM emission (including the polarization dynamics) as a function of time delay  $\tau_{21} (\equiv t_2 - t_1)$  between the pump and probe pulses. For this initial test, POLLIWOG measurements were performed for  $\mathbf{E}_1$  and  $\mathbf{E}_2$  having the same linear ( $x$ ) polarization state.

In Figure 9.35a, we show the total intensity  $S_0$  of the time-resolved FWM signal for various time delays  $\tau_{21}$  between the pump and probe pulses when the sample was excited with two  $x$ -polarized pump pulses. The ellipticity angle and the orientation of the polarization ellipse were also time resolved. To within our experimental accuracy, the FWM signal was found to be linearly and  $x$ -polarized for all times and all time delays. For this reason, we plot only the total intensity in Figure 9.35. Clearly, oscillations at the hh-lh beat frequency are observed at each delay shown. In Figure 9.35b we plot the position of each peak  $t_p$  in the time-resolved FWM signal (indicated by the arrows in Figure 9.35a) as a function of the time delay  $\tau_{21}$ , for a more complete set of time delays. Clearly, the slope is zero. Consequently, the oscillations shown in Figure 9.35 behave like quantum beats and not polarization interference. This is exactly the behavior that we would have expected from a simple density matrix model for the  $2 \times 3$  system shown in Figure 9.25 (without many-body effects) based on (9.29).

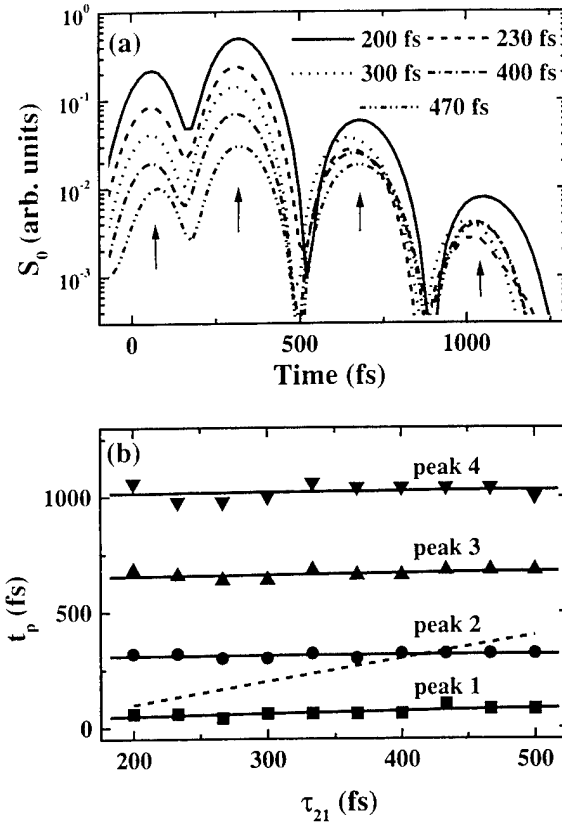


FIGURE 9.35. Results of measurements to distinguish quantum beating from polarization interference using two linearly  $x$ -polarized incident pump pulses: (a) Time-resolved measurements of the total intensity  $S_0$  of the FWM signal for selected time delays  $\tau_{21}$  between two incident pulses, and (b) the time  $t_p$  at which each peak (indicated by an arrow in Figure 9.35(a)) occurs as a function of  $\tau_{21}$ , for a more complete set of time delays. The dotted line indicates a slope of unity.

### 9.8.2 A Test for Exciton–Exciton Correlations

By contrast, if the two independent three-level systems shown in Figure 9.25 were excited with two right circularly polarized pulses, only the lh transition on the left and the hh transition on the right would be excited. In this case, on the basis of the arguments presented in Section 9.8.1, one would expect to observe lh–hh oscillations as the result of the interference of light emitted by each independent oscillator (i.e., polarization interference), but one would not expect to observe quantum beating. And in fact, the FWM polarization under these excitation conditions is given by

$$\begin{aligned} \mathcal{P}_{cir} = & 2\kappa \Theta(t) \Theta(\tau_{21}) \exp(-i\delta\tau_{21}) \exp(-\gamma(t + \tau_{21})) \\ & \times [1 + A^2 \exp(-i\Omega(t - \tau_{21}))] \hat{\sigma}_+, \end{aligned} \quad (9.30)$$

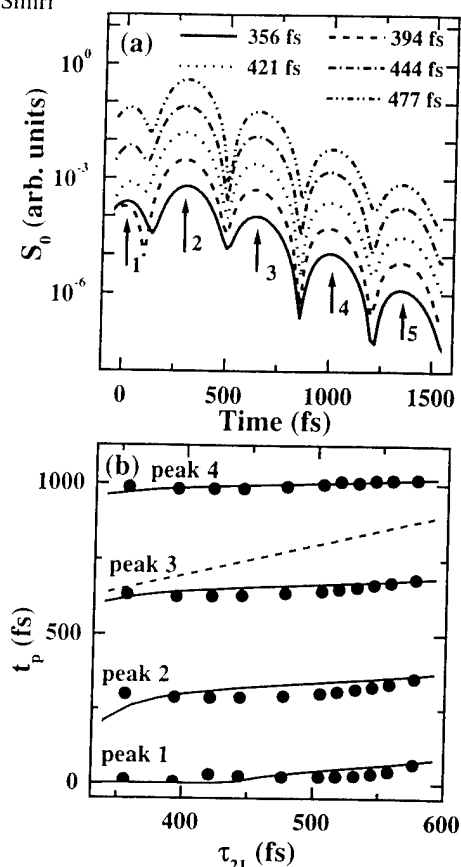


FIGURE 9.36. Results of measurements to distinguish quantum beating from polarization interference using two right circularly polarized pump pulses: (a) Time-resolved measurements of the total intensity  $S_0$  of the FWM signal for selected time delays  $\tau_{21}$  between the two incident pulses in the range between 350 and 600 fs, and (b) the time  $t_p$  at which each peak (indicated by one of the first four arrows in (a)) occurs as a function of  $\tau_{21}$ , for a more complete set of time delays. The dotted line indicates a slope of unity, and the solid lines are the result of simulations based on (9.31).

which has identically the same form as (9.25), except that the emission is circularly polarized. As a result, the measured time-resolved intensity has the same form as (9.26).

The results of performing the test to distinguish quantum beats from polarization interference when the sample is excited with two pulses that have the same (right) circular polarization are shown in Figure 9.36. In Figure 9.36a, the results of measuring the time-resolved FWM signal for selected time delays  $\tau_{21}$  between the pump and probe pulses are shown. Again, the polarization state was also measured, and the FWM signal was found to be right circularly polarized for all times and all time delays. As for the linear excitation pulses (i.e., Figure 9.35), pronounced oscillations at lh-hh beat frequency are evident. In Figure 9.36b, the position of each peak in the time-resolved FWM signal (indicated by the arrows in Figure 9.36a)

is plotted as a function of the time delay  $\tau_{21}$ , again for a more complete set of delays. The slope of each curve is approximately zero, not unity. Consequently, the oscillations produced when the sample is excited by two right circularly polarized pulses satisfy the criterion for quantum beats, not polarization interference. Since quantum beats would not be expected for two independent three-level systems without many-body effects (see (9.30)), this result suggests that the two excitonic systems are not independent, but are coupled and correlated. It should also be noted that the SBE, in their original form (i.e., in the Hartree-Fock limit, without EID or BIF included), also predict polarization interference, but no quantum beating when two right circularly polarized pulses are used. Consequently, the observation of quantum-beat-like behavior suggests a correlation beyond the Hartree-Fock limit. Our measurements are consistent with other [56, 74, 83] recent observations.

### 9.8.3 Coupling by Excitation-Induced Dephasing

The quantum-beating-like behavior shown in Figure 9.36 requires the inclusion of a process that strongly couples the two spin systems shown in Figure 9.25. One such process, which has been invoked previously, is EID [20]. EID can be phenomenologically included in the SBE [20], but analytical solutions to the full SBE are not possible, and in general, the SBE require lengthy numerical solution. The simplest approach is to solve the density matrix equations for the two three-level systems shown in Figure 9.25 and to again include EID phenomenologically by expanding the dephasing rate in a Taylor series, as given by (9.19). As we have stated previously, because it is the total population (regardless of spin) that determines the dephasing rate, EID provides a coupling between the two three-level systems. One can readily obtain a closed-form solution to these modified density matrix equations for right circular excitation pulses by making the same approximations that we have made throughout (namely, by assuming delta function time dependences for the excitation pulses and by assuming that the dephasing is much faster than the population decay). Under these circumstances, the FWM polarization that propagates in the  $2\mathbf{k}_2 - \mathbf{k}_1$  direction is found to be proportional to

$$\begin{aligned} \mathcal{P}_{\text{EID}} \propto & \Theta(t)\Theta(\tau_{21})\mathcal{E}_2^2\mathcal{E}_1^*\exp(-\gamma(t+\tau_{21})) \\ & \times \left\{ \left[ 1 + A^2 \exp(-i\Omega(t-\tau_{21})) \right] + \left( \frac{\eta t}{2\hbar} \right) \right. \\ & \times \left. \left[ (1 + A \exp(i\Omega\tau_{21}))(1 + A \exp(-i\Omega t)) \right] \right\} \hat{\sigma}^+. \quad (9.31) \end{aligned}$$

In writing (9.31), we have assumed that the carrier densities are sufficiently small that we may neglect the density dependence of the dephasing rate in determining the overall exponential decay. This density dependence is readily included. We neglect it for reasons of simplicity and self-consistency. This approximation in no way affects the conclusions discussed here. Equation (31) basically consists of two terms (each enclosed in square brackets). The first term (in square brackets) has

the same form as the FWM polarization that we have associated with polarization interference (see (9.25)), and the second term, which is multiplied by  $\eta t/2\hbar$ , has the same form as the FWM polarization that we have associated with quantum beats (see (9.28)).

There are two limits of immediate interest:  $\eta t/2\hbar \ll 1$  and  $\eta t/2\hbar \gg 1$ . When  $\eta t/2\hbar \ll 1$  for all times of interest, (9.31) reduces to the result that would be obtained for the two independent, uncoupled three-level systems shown in Figure 9.25 (i.e., to (9.30)). As we have already stated, in this case, the lh transition is excited in the system on the left and the hh transition in the system on the right. Under these conditions, the optically excited transitions share no common level, and there is no coupling between the excited states in the two independent systems. The latter conditions clearly correspond to polarization interference. In this limit, the detected intensity is given by (9.26) for polarization interference, and thus there is a linear relationship between the peak of one of the oscillations in time  $t_p$  and the time delay  $\tau_{21}$ , as predicted by (9.27). This limit ( $\eta = 0$ ) is represented by the dotted line in Figure 9.36b.

By comparison, if  $\eta t/2\hbar \gg 1$ , the light is still directly coupled only to the lh transition on the left and the hh transition on the right. That is, the optically excited transitions still technically share no common level, but now the upper levels are strongly coupled through the density-dependent dephasing given by (9.19). In this case, using (9.31), we find the total FWM intensity to be proportional to

$$\begin{aligned} S_0 \propto |\mathcal{P}_{\text{EID}}|^2 \propto \Theta(t)\Theta(\tau_{21})I_2^2 I_1 (\eta t/2\hbar)^2 \exp[-2\gamma(t + \tau_{21})] \\ \times \left\{ 1 + 2A^2 + A^4 + 2(A + A^3) \cos \Omega \tau_{21} \right. \\ \left. + 2(A + A^3 + 2A^2 \cos \Omega \tau_{21}) \cos \Omega t \right\}. \end{aligned} \quad (9.32)$$

Except for the multiplicative factor of  $(\eta t/2\hbar)^2$ , (9.32) is mathematically equivalent to (9.29) that one obtains for quantum beating when one excites the two independent three-level systems shown in Figure 9.25 with linearly polarized light (without including many-body effects). Thus, we see that in the strong coupling limit the effects of EID are mathematically equivalent to sharing a common level, even though there is clearly a physical difference. In this limit, as with (9.29), the slope of the  $t_p$  versus  $\tau_{21}$  curve is 0, which is identical to the slope exhibited by the data shown in Figure 9.36. This is the type of behavior that previously has been attributed to quantum beating.

The solid curves in Figure 9.36b are the results of simulations using the full FWM polarization given by (9.31) with  $\eta = 4$  meV and  $\Omega = 2\pi/340$  fs<sup>-1</sup>, and they demonstrate that this model produces qualitative and quantitative agreement with the data presented to this point. However, (9.31) predicts new features in the hh-lh oscillations that are not characteristic either of pure quantum beating or of polarization interference. For example, as we explained earlier, the first term in square brackets in (9.31) produces a response that is characteristic of polarization interference, and the second term in square brackets (which is multiplied by  $\eta t/2\hbar$ ) produces a response that resembles quantum beating. Since the second term is proportional to time, one expects it to be negligible for times  $t \ll 2\hbar/\eta$  and dom-

inant for  $t \gg 2\hbar/\eta$ . In other words, for the parameters given here, (9.31) predicts a transition from polarization-interference-like behavior to quantum-beating-like behavior on a characteristic time scale of  $2\hbar/\eta \approx 330$  fs (for  $\eta = 4$  meV). It is very difficult to unambiguously distinguish a transition of this duration occurring near  $t = 0$  because of the finite widths of our pulses (which are not currently taken into account in our model).

Equation (9.31) also predicts a dynamic periodic competition between the two types of oscillations as a function of time delay  $\tau_{21}$ , with a period equal to the lh-hh beat frequency. Inspection of (9.31) reveals that the “quantum beating” term is not only multiplied by  $\eta t/2\hbar$ , but is proportional to  $(1 + A \exp(i\Omega\tau_{21}))$ . Consequently, the contribution of the term that we have associated with “quantum beating” will be periodically reduced with respect to the term that we have associated with “polarization interference.” A minimum in the “quantum beating” term will occur each time  $\tau_{21}$  is an odd multiple of  $\pi/\Omega$ . The consequences of this behavior are illustrated in Figure 9.37, where the simulated time-resolved FWM signals (calculated using (9.31)) are shown for equally spaced time delays between 300 and 667 fs. Notice that for time delays  $\tau_{21}$  near 510 fs ( $\approx 3\pi/\Omega$ ) the positions of the peaks in the FWM signal are shifted, the oscillations are distorted, and their amplitudes are dramatically reduced at early times  $t$ . At longer times  $t$  (as  $\eta t/2\hbar$  becomes larger and the “quantum beating” term increases in strength), the

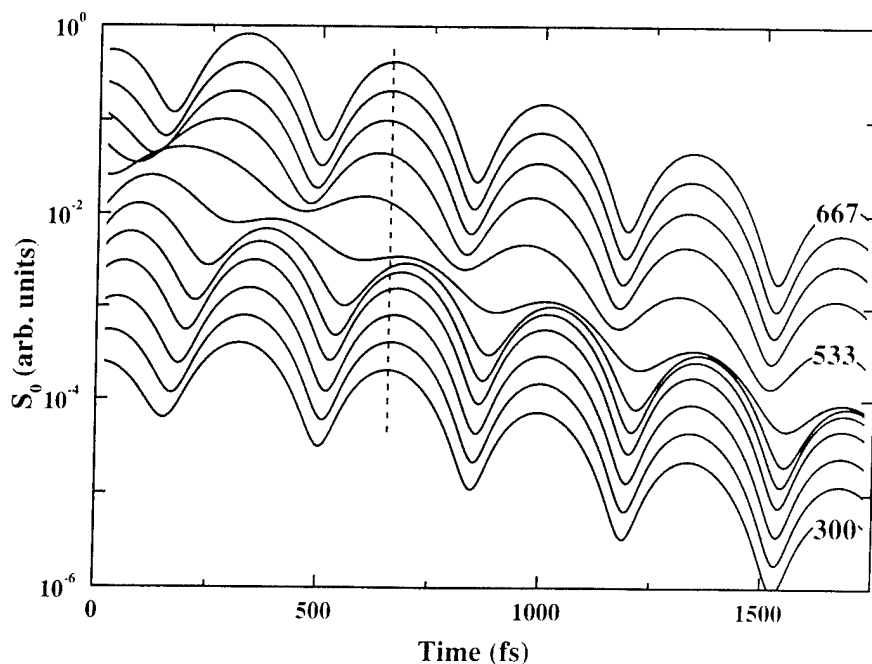


FIGURE 9.37. Calculations (using 9.31) of the total intensity  $S_0$  of the FWM signal as a function of time for equally spaced time delays  $\tau_{21}$  between the two incident pulses in the range between 300 and 667 fs.



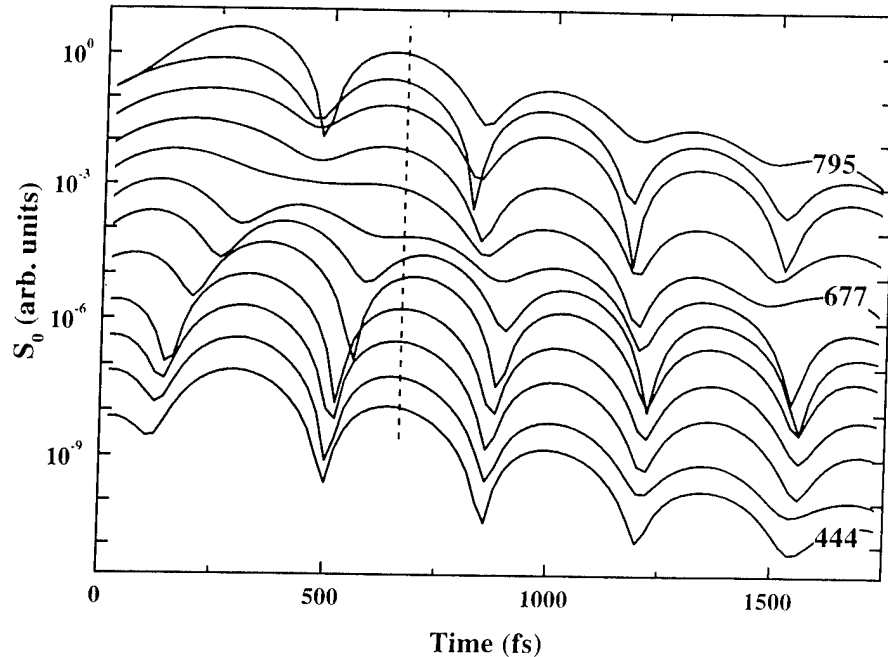


FIGURE 9.38. Measurements of the total intensity  $S_0$  of the FWM signal as a function of time for equally spaced time delays  $\tau_{21}$  between the two incident pulses in the range between 444 and 795 fs.

oscillations become stronger, their periods more regular, and the positions of the beat maxima more quantum-beat-like. Similar behavior is consistently observed in the data, as illustrated in Figure 9.38.

Careful comparison of Figure 9.37 and Figure 9.38 shows that the minimum in the “quantum beating” contribution in the data occurs at a time delay that is shifted by  $\approx 140$  fs compared to the minimum in the simulations. We do not know the origin of this shift, and it is the subject of ongoing investigation; however, we speculate that it is a consequence of our assuming delta function excitation pulses. The actual excitation pulses are each  $\approx 150$  fs in duration, and the frequencies that are resonant with the hh exciton have been determined to have phases that are slightly different from those that are resonant with the lh. Consequently, with the exception of the simulations shown in Figure 9.37, the time delays for all simulations have been shifted by 140 fs to facilitate a direct comparison with the data.

The new features described above, which are not characteristic of quantum beating or polarization interference, and the excellent agreement between the data and the simulations based on (9.31) are also apparent if both data and simulation are plotted in the conventional format used to discriminate quantum beats from polarization interference (e.g., see Figure 9.35 or 9.36). Figure 9.39 shows a plot of the temporal position of the peak in the lh-hh oscillations as a function of delay between the two pump pulses. This figure differs from Figure 9.36 in that

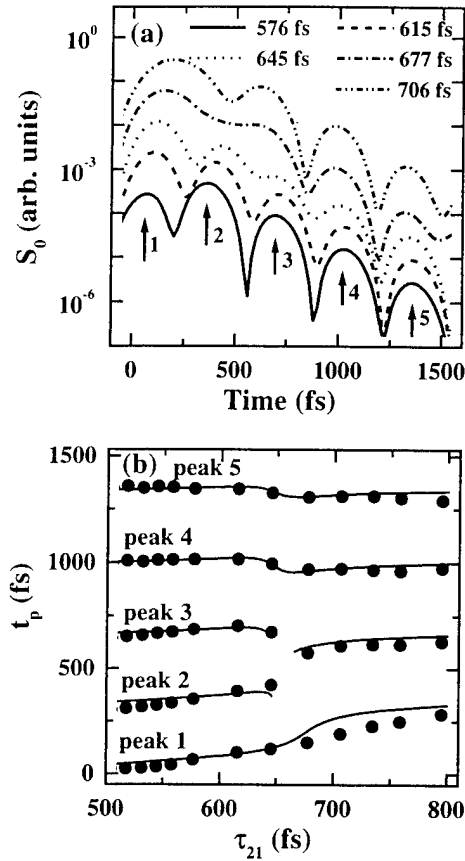


FIGURE 9.39. (a) Time-resolved measurements of the total intensity  $S_0$  of the FWM signal for selected time delays  $\tau_{21}$  between the two incident pulses in the range between 500 and 800 fs, and (b) the time  $t_p$  at which each peak (indicated by an arrow in (a)) occurs as a function of  $\tau_{21}$ , for a more complete set of time delays. The solid lines are the result of simulations based on (9.31).

it focuses on the behavior at longer time delays in the vicinity of a minimum in the quantum beating term. Clearly, the data in this region cannot be described by a straight line with slope of either 0 or 1 as required by quantum beating or polarization interference, respectively, acting individually. Simulations based on (9.31) do, however, produce good agreement with the data.

We recognize the crudeness of the calculation presented here. Our principal point is not that EID is responsible for the quantum-beating-like behavior shown in Figs. 9.36–9.40, although we have shown that our results are consistent with this possibility. What this calculation and the data of Figs. 9.36–9.40 demonstrate is that when excitation pulses with the same circular polarizations are used, the test that was originally designed to distinguish quantum beats from polarization interference becomes an effective test for excitonic correlations beyond local field

effects and beyond those contained in the original SBE in the Hartree–Fock limit. In fact, the data presented here suggest that such effects are not only important, but that they dominate the FWM response under these excitation conditions. Finally, the features observed here make it clear that the coupling between the spin systems is dynamic, rather than static. While hh-lh mixing of the valence band states (e.g., as the result of strain or quantum confinement) can conceptually provide a coupling between the two spin systems, such a mixing would produce a static coupling and can not explain the dynamic results discussed here.

A secondary point to be made concerning the results presented in this section is that the classification of lh-hh oscillations as quantum beats or polarization interference is problematic and perhaps overly simplistic. If one accepts the definition that oscillations arising from interference within the sample are quantum beats, then in this sense, the oscillations arising from the exciton–exciton correlations are quantum beats. However, the beats arising from the exciton–exciton correlations are clearly fundamentally different from the beats arising from lh and hh transitions that share a common level. The coupling is dynamic in the case of the former, and the sharing is a static condition for the latter. Finally, it can be argued that the term “quantum beats” should be reserved for measuring oscillations that directly monitor the Raman coherence terms. In the latter sense, all of the phenomena that we have discussed here must be classified as polarization interference, since two-pulse self-diffraction FWM geometries do not monitor the Raman coherence directly (see [84] for a discussion of this latter point).

#### 9.8.4 *Estimate of the EID Coupling Strength*

We emphasize that this technique isolates, and is particularly sensitive to, the strength of the Coulomb-induced coupling between the excitons. We now illustrate this sensitivity by using the simple model that we have described in Section 9.6. That model phenomenologically includes EID, LFC, and BIF. The LFC will not provide a resonant coupling between the two spin systems, and therefore, they can be neglected. Moreover, the technique described here prevents the formation of pure biexcitons involving either two hh excitons or two lh excitons of opposite spin by using two excitation pulses with the same circular polarizations. However, under these excitation conditions, mixed biexcitons can be formed from one hh exciton and one lh exciton having opposite spins. Mixed hh-lh biexcitons have been observed in ZnSe quantum wells, but their contribution to the FWM signal was found to be roughly an order of magnitude weaker than that of hh biexcitons [86]. We have examined our FWM spectra for evidence of mixed lh-hh biexciton formation when we excite with two right circularly polarized pulses, and we find no resolvable signal at the expected mixed biexciton frequency (to within our experimental accuracy under our excitation conditions). For these reasons, we neglect the contributions of mixed lh-hh biexcitons here. Consequently, within the context of this phenomenological model, only EID can provide the needed coupling. Therefore, when the sample is excited with two pulses having the same

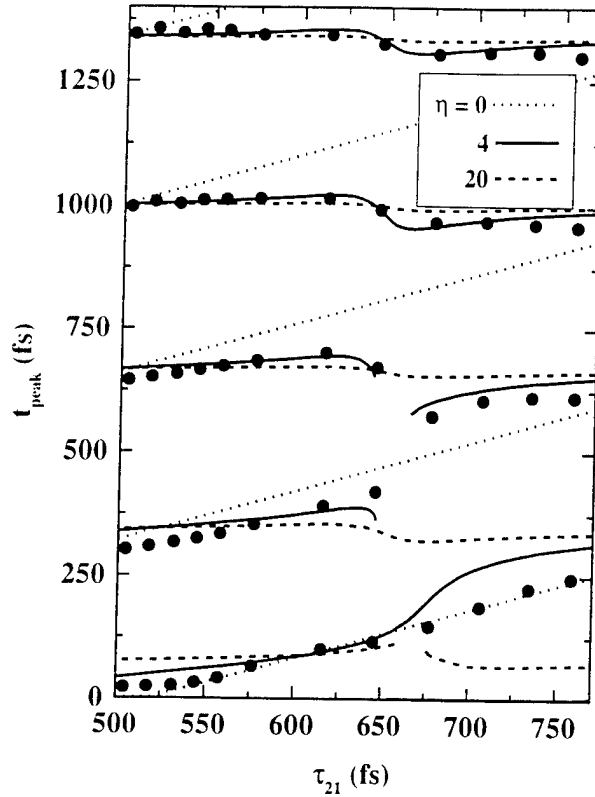


FIGURE 9.40. Comparison between the measured (solid dots) and the simulated time  $t_p$  at which each peak in the lh-hh oscillations occurs as a function of  $\tau_{21}$  for three values of the EID parameter:  $\eta = 0$  (dotted line), 4 (solid line), and 20 meV (dashed line).

circular polarization, the model that we have used in Section 9.6 reduces to the one used in Section 9.8.3.

In fact, the features displayed in Figs. 9.36–9.39 allow a rough quantitative estimate of the strength of the coupling between the two spin systems, again, within the context of the model presented here. Figure 9.40 illustrates the sensitivity of this technique to the EID parameter. This figure shows a comparison between the data and simulations using three values of the EID parameter:  $\eta = 0$ , 4, and 20 meV. Notice that  $\eta = 0$  produces reasonable agreement for all time delays  $\tau_{21}$  for early times  $t$ , when EID effects are expected to be negligible (i.e.,  $t \ll 2\hbar/\eta$ ), but poor agreement at later times (when  $t > 2\hbar/\eta$ ). By comparison,  $\eta = 20$  produces acceptable agreement with the data at later times when EID effects are expected to dominate, but poor agreement for earlier times. Of the three values shown here, only  $\eta = 4$  produces acceptable agreement at all times. The simulated solid curves

shown in Figures. 9.36, 9.37, and 9.39 were all produced using this value for the EID parameter. From a comparison with the data presented in this work only, we estimate the EID parameter to be  $4 \pm 2$  meV.

## 9.9 Summary

In this chapter we have demonstrated that sensitive techniques exist that allow one to measure the amplitude, phase, and polarization state of extremely weak, ultrafast coherent emission from MQWs, and that the vectorial dynamics contain useful information about many-body effects, quantum interference, and optical anisotropies that would be difficult to obtain in any other way. In fact, as we have illustrated here, when only hh excitons are excited, all of the polarization dynamics are associated with many-body effects. Under these excitation conditions, the amplitudes and the phases of the  $x$  and  $y$  components of the coherent FWM emission are found to exhibit systematic (but distinct) variations with the orientation of the input polarizations. From these, a self-consistent picture of the temporal dynamics of the amplitude, phase, and polarization state is obtained that delineates the roles of many-body effects, such as local field corrections, excitation-induced dephasing, and biexcitons, in determining the excitonic dynamics. Consequently, this is an extremely sensitive geometry for studying such effects, one that we have only begun to exploit!

In addition, we have shown that the polarization state is extremely sensitive to the differences in phase associated with various quantum beating phenomena. For example, when both hh and lh excitons are excited, we have shown that the ellipticity, the orientation, and the sense of rotation of the polarization ellipse (as well as the FWM emission amplitude) oscillate dramatically at the hh-lh quantum beat frequency. In the strong quantum beat regime, some of the features can be qualitatively described without many-body effects; however, even in this regime, it is clear, when the data are replotted in the complex plane, that the beats are "distorted" by other effects. In the weak quantum beating regime, it is clear that the quantum beating is superposed upon polarization dynamics that require the inclusion of many-body and biexcitonic effects.

We have also shown that the polarization selection rules for FWM can be used to modify a test that was originally designed to distinguish between quantum beats and polarization interference to demonstrate the presence of strong exciton-exciton correlations in MQWs. Specifically, we have demonstrated that the oscillations at the hh-lh frequency exhibit quantum-beat-like behavior even when the FWM signal is produced by two pulses that have the same circular polarization. The latter observation is contrary to the predictions based on either the density matrix equations for two independent three-level systems or the conventional semiconductor Bloch equations, both of which predict that polarization interference, but not quantum beats, should be observed. Consequently, the observation of quantum-beat-like behavior when exciting with two pulses having the same circular polarization pro-

vides clear evidence for exciton–exciton correlations and provides evidence that those correlations go beyond those contained in the semiconductor Bloch equations in the Hartree–Fock limit. The procedure that we have described provides a simple effective test for such processes. In addition, we have shown that excitation-induced dephasing is among those processes that can produce such correlations. A model based on the latter process predicts new features that are not characteristic of either quantum beating or polarization interference. We have demonstrated that such features are indeed observed, and we have used these to place quantitative limits on the magnitude of the density-dependent dephasing in the context of a simple phenomenological model.

Finally, we remark that the studies reviewed here demonstrate that the polarization state is very sensitive to all sorts of induced and intrinsic anisotropies—in both the index of refraction and the absorption coefficient. This should also make these techniques extremely useful in probing the band structure of strained MQWs and MQWs grown in unconventional directions.

*Acknowledgments:* This work was supported in part by the U.S. Army Research Office and the National Science Foundation. The work presented in this chapter is part of an extended effort by several current and former students, postdoctoral fellows, and research scientists. I want to thank each for his contributions, which I have tried to acknowledge through the various referenced publications. I explicitly thank Jeremy Bolger, Osvaldo Buccafusca, Xiaoyuan Chen, Shekar Patkar, Andy Paul, Weijian Sha, and Martin Stevens. I also would like to acknowledge numerous insightful conversations with Duncan Steel, Hailin Wang, and Rolf Binder and to thank Joe Pellegrino for providing the sample used throughout many of our experiments. Special acknowledgment goes to Rick Trebino, who is the coinventor of the POLLIWOG technique.

## 9.10 References

- [1] R.T. Phillips (ed.), *Coherent Optical Interactions in Semiconductors*, NATO ASI Series B:Physics, Vol. 30 (Plenum, New York, 1994).
- [2] J. Shah, *Ultrafast Spectroscopy of Semiconductors and Nanostructures*, (Springer-Verlag, Heidelberg, 1996).
- [3] L. Schultheis, M.D. Sturge, J. Hegarty: *Appl. Phys. Lett.* **47**, 995 (1985).
- [4] L. Schultheis, J. Kuhl, A. Honold, C.W. Tu: *Phys. Rev. Lett.* **57**, 1635 (1986).
- [5] L. Schultheis, J. Kuhl, A. Honold, C.W. Tu: *Phys. Rev. Lett.* **57**, 1797 (1986).
- [6] L. Schultheis, A. Honold, J. Kuhl, K. Köhler, C.W. Tu: *Phys. Rev. B* **34**, 9027 (1986).

- [7] K. Leo, M. Wegner, J. Shah, D.S. Chemla, E.O. Göbel, T.C. Damen, S. Schmitt-Rink, W. Schäfer: *Phys. Rev. Lett.* **65**, 1340 (1990).
- [8] S.T. Cundiff, H. Wang, D.G. Steel: *Phys. Rev. B* **46**, 7248 (1992).
- [9] S.T. Cundiff, D.G. Steel: *IEEE J. Quantum Electron.* **28**, 2423 (1992).
- [10] D.S. Kim, J. Shah, T.C. Damen, W. Schäfer, F. Jahnke, S. Schmitt-Rink, K. Köhler: *Phys. Rev. Lett.* **69**, 2725 (1992).
- [11] D.S. Kim, J. Shah, J.E. Cunningham, T.C. Damen, S. Schmitt-Rink, W. Schäfer: *Phys. Rev. Lett.* **68**, 2838 (1992).
- [12] A. Lohner, K. Rick, P. Leisching, A. Leitenstorfer, T. Elsaesser, T. Kuhn, F. Rossi, W. Stolz: *Phys. Rev. Lett.* **71**, 77 (1993).
- [13] M.D. Webb, S.T. Cundiff, D.G. Steel: *Phys. Rev. Lett.* **66**, 934 (1991).
- [14] S. Weiss, M.A. Mycek, J.-Y. Bigot, S. Schmitt-Rink, D.S. Chemla: *Phys. Rev. Lett.* **69**, 2685 (1992).
- [15] M. Wegener, D.S. Chemla, S. Schmitt-Rink, W. Schäfer: *Phys. Rev. A* **42**, 5675 (1990).
- [16] K. Leo, E.O. Göbel, T.C. Damen, J. Shah, S. Schmitt-Rink, W. Schäfer, J.F. Müller, K. Köhler, P. Ganser: *Phys. Rev. B* **44**, 5726 (1991).
- [17] S. Schmitt-Rink, S. Mukamel, K. Leo, J. Shah, D.S. Chemla: *Phys. Rev. A* **44**, 2124 (1991).
- [18] W. Schäfer, F. Jahnke, S. Schmitt-Rink: *Phys. Rev. B* **47**, 1217 (1993).
- [19] A. Honold, L. Schultheis, J. Kuhl, C.W. Tu: *Phys. Rev. B* **40**, 6442 (1989).
- [20] H. Wang, K. Ferrio, D.G. Steel, Y.Z. Hu, R. Binder, S.W. Koch: *Phys. Rev. Lett.* **71**, 1261 (1993).
- [21] Y.Z. Hu, R. Binder, S.W. Koch, S.T. Cundiff, H. Wang, D.G. Steel: *Phys. Rev. B* **49**, 14382 (1994).
- [22] T. Rappen, U.G. Peter, M. Wegener, W. Schäfer: *Phys. Rev. B* **49**, 10774 (1994).
- [23] D.G. Steel, H. Wang, M. Jiang, K. Ferrio, S.T. Cundiff: In *Coherent Optical Interactions in Semiconductors*, edited by R. T. Phillips (Plenum, New York, 1994), pp. 157–179.
- [24] S. Patkar, A.E. Paul, W. Sha, J.A. Bolger, A.L. Smirl: *Phys. Rev. B* **51**, 10789 (1995).
- [25] B.F. Feuerbacher, J. Kuhl, K. Ploog: *Phys. Rev. B* **43**, 2439 (1991).
- [26] S. Bar-Ad, I. Bar-Joseph: *Phys. Rev. Lett.* **68**, 349 (1992).

- [27] D.J. Lovering, R.T. Phillips, G.J. Denton, G.W. Smith: *Phys. Rev. Lett.* **68**, 1880 (1992).
- [28] K.-H. Pantke, D. Oberhauser, V. G. Lyssenko, J.M. Hvam, G. Weimann: *Phys. Rev. B* **47**, 2413 (1993).
- [29] H.H. Yaffe, Y. Prior, J.P. Harbison, L.T. Florez: *J. Opt. Soc. Am. B* **10**, 578 (1993).
- [30] H. Wang, J. Shah, T.C. Damen, L.N. Pfeiffer: *Solid State Commun.* **91**, 869 (1994).
- [31] T. Saiki, M. Kuwata-Gonokami, T. Matsusue, H. Sakaki: *Phys. Rev. B* **49**, 7817 (1994).
- [32] E.J. Mayer, G.O. Smith, V. Heuckeroth, J. Kuhl, K. Bott, A. Schulze, T. Meier, D. Bennhardt, S.W. Koch, P. Thomas, R. Hey, K. Ploog: *Phys. Rev. B* **50**, 14730 (1994).
- [33] S. Schmitt-Rink, D. Bennhardt, V. Heuckeroth, P. Thomas, P. Haring, G. Maidorn, H. Bakker, K. Leo, D.S. Kim, J. Shah, K. Köhler: *Phys. Rev. B* **46**, 10460 (1992).
- [34] D. Bennhardt, P. Thomas, R. Eccleston, E.J. Mayer, J. Kuhl: *Phys. Rev. B* **47**, 13485 (1993).
- [35] D.S. Kim, J. Shah, T.C. Damen, L.N. Pfeiffer, W. Schäfer: *Phys. Rev. B* **50**, 5775 (1994).
- [36] H. Schneider, K. Ploog: *Phys. Rev. B* **49**, 17050 (1994).
- [37] E.J. Mayer, G.O. Smith, V. Heuckeroth, J. Kuhl, K. Bott, A. Schulze, T. Meier, S.W. Koch, P. Thomas, R. Hey, K. Ploog: *Phys. Rev. B* **51**, 10909 (1995).
- [38] R. Eccleston, J. Kuhl, D. Bennhardt, P. Thomas: *Solid State Commun.* **86**, 93 (1993).
- [39] K. Bott, O. Heller, D. Bennhardt, S.T. Cundiff, P. Thomas, E.J. Mayer, G.O. Smith, R. Eccleston, J. Kuhl and K. Ploog: *Phys. Rev. B* **48**, 17418 (1993).
- [40] R.M.A. Azzam, N.M. Bashara: *Ellipsometry and Polarized Light* (North-Holland, Amsterdam, 1988).
- [41] K.W. DeLong, R. Trebino, D.J. Kane: *J. Opt. Soc. Am. B* **11**, 1595 (1994) and references therein.
- [42] J.L.A. Chilla, O.E. Martinez: *Opt. Lett.* **16**, 39 (1991).
- [43] K.C. Chu, J.P. Heritage, R.S. Grant, K.X. Liu, A. Dienes, W.E. White, A. Sullivan: *Opt. Lett.* **20**, 904 (1991).
- [44] K.W. DeLong, R. Trebino, J. Hunter, W.E. White: *J. Opt. Am. B* **11**, 2206 (1994) and references therein.



- [45] L. Lepetit, G. Chériaux, M. Joffré: *J. Opt. Soc. Am. B* **12**, 2467 (1995).
- [46] D.N. Fittinghoff, J.L. Bowie, J.N. Sweetser, R.T. Jennings, M.A. Krumbügel, K.W. DeLong, R. Trebino, I.A. Walmsley: *Opt. Lett.* **21**, 884 (1996).
- [47] M. Kujawinska: In *Interferogram Analysis*, Robinson D W and Reid G T. eds. (Institute of Physics, Bristol, UK, 1993), pp. 141–193.
- [48] W.J. Walecki, D.N. Fittinghoff, A.L. Smirl, R. Trebino: *Opt. Lett.* **22**, 81 (1997).
- [49] J.-Y. Bigot, M.-A. Mycek, S. Weiss, R. G. Ulbrich, D.S. Chemla: *Phys. Rev. Lett.* **70**, 3307 (1993).
- [50] D.S. Chemla, J.Y. Bigot, M.-A. Mycek, S. Weiss, W. Schäfer: *Phys. Rev. B* **50**, 8439 (1994).
- [51] A.E. Paul, J.A. Bolger, A.L. Smirl, J.G. Pelligrino: *J. Opt. Soc. Am. B* **13**, 1016 (1996).
- [52] J.A. Bolger, A.E. Paul, A.L. Smirl: *Phys. Rev. B* **54**, 11666 (1996).
- [53] X. Chen, W.J. Walecki, O. Buccafusca, D.N. Fittinghoff, A.L. Smirl: *Phys. Rev. B* **56**, 9738 (1997).
- [54] O. Buccafusca, X. Chen, W. Walecki, A.L. Smirl: *J. Opt. Soc. Am. B* **15**, 1218 (1998).
- [55] A.L. Smirl, X. Chen, O. Buccafusca: *Opt. Lett.* **23**, 1120 (1998).
- [56] A.L. Smirl, X. Chen, O. Buccafusca: *IEEE J. Quantum Electron.* **35**, 523 (1999).
- [57] A.L. Smirl, M.J. Stevens, X. Chen, O. Buccafusca: *Phys. Rev. B* **60**, 8267 (1999).
- [58] A.L. Smirl: In *Semiconductor Quantum Optoelectronics: From Quantum Physics to Smart Devices*, edited by A. Miller, M. Ebrahimzadeh and D. M. Finlayson (Institute of Physics Publishing, London, 1999), pp. 25–94.
- [59] A.M. Weiner, S. De Silvestri, E.P. Ippen: *J. Opt. Soc. Am. B* **2**, 654 (1985).
- [60] T. Yajima, Y. Taira: *J. Phys. Soc. Japan* **47**, 1620 (1979).
- [61] L. Allen, J.H. Eberly: *Optical Resonance and Two-Level Atoms*, (Interscience, New York, 1975).
- [62] M. Sargent, M.O. Scully, W.E. Lamb.: *Laser Physics* (Addison-Wesley, New York, 1977).
- [63] P. Meystre, M. Sargent: *Elements of Quantum Optics* (Springer-Verlag, Berlin, 1991).
- [64] W. Schäfer and J. Treusch, *Z. Phys. B* **63**, 407 (1986).

- [65] R. Zimmermann, *Many-Particle Theory of Highly Excited Semiconductors*. (Teubner, Leipzig, 1988).
- [66] H. Haug, S.W. Koch: *Quantum Theory of the Optical and Electronic Properties of Semiconductors*, (World Scientific, Singapore, 1993).
- [67] R. Binder and S.W. Koch, *Prog. Quant. Electr.* **19**, 307 (1995).
- [68] H. Haug and A. P. Jauho, *Quantum Kinetics in Transport and Optics of Semiconductors*, (Springer, Berlin, 1996).
- [69] R. Zimmermann, K. Kilimann, W.D. Kraeft, D. Kremp, G. Röpke, *Phys. Stat. Sol. (b)* **90**, 175 (1978).
- [70] W. Schäfer, K. H. Schuldt and R. Binder, *Phys. Stat. Sol. (b)* **150**, 407 (1988).
- [71] C. Sieh, T. Meier, F. Jahnke, A. Knorr, S. W. Koch, P. Brick, M. Hübner, C. Ell, J. Prineas, G. Kitrova and H. M. Gibbs, *Phys. Rev. Lett.* **82**, 3112 (1999).
- [72] V. M Axt and A. Stahl, *Z. Phys. B* **93**, 195 (1994); *ibid*, 205 (1994).
- [73] M. Z. Maialle and L. J. Sham, *Phys. Rev. Lett.* **73**, 3310 (1994).
- [74] P. Kner, S. Bar-Ad, M.V. Marquezini, D.S. Chemla, W. Schäfer: *Phys. Rev. Lett.* **78**, 1319 (1997).
- [75] T. Östreich, K. Schönhammer, L.J. Sham: *Phys. Rev. Lett.* **74**, 4698 (1995).
- [76] K. Leo, T.C. Damen, J. Shah, E.O. Göbel, K. Köhler: *Appl. Phys. Lett.* **57**, 19 (1990).
- [77] K. Leo, T.C. Damen, J. Shah, K. Köhler: *Phys. Rev. B* **42**, 11359 (1990).
- [78] E.O. Göbel, K. Leo, J. Damen, J. Shah, S. Schmitt-Rink, W. Schäfer, J.F. Muller, K. Köhler: *Phys. Rev. Lett.* **64**, 1801 (1990).
- [79] M. Koch, J. Feldmann, G. von Plessen, E.O. Göbel, P. Thomas, K. Köhler: *Phys. Rev. Lett.* **69**, 3631 (1992).
- [80] V.G. Lyssenko, J. Erland, I. Balslev, K.-H. Pantke, B.S. Razbirin, J.M. Hvam: *Phys. Rev. B* **48**, 5720 (1993).
- [81] J. Kuhl, E.J. Mayer, G. Smith, R. Eccleston, D. Bennhardt, P. Thomas, K. Bott, O. Heller: In *Coherent Optical Interactions in Semiconductors*, edited by R. T. Phillips (Plenum, New York, 1994), pp. 1–31, and references therein.
- [82] A. Tookey, D.J. Bain, I.J. Blewett, I. Galbraith, A.K. Kar, B.S. Wherrett, B. Vögele, K.A. Prior, B.C. Cavenett: *J. Opt. Soc. Am. B* **15**, 64 (1998).
- [83] A.E. Paul, W. Sha, S. Patkar, A.L. Smirl: *Phys. Rev. B* **51**, 4242 (1995).
- [84] K.B. Ferrio, D.G. Steel: *Phys. Rev. Lett.* **80**, 786 (1998).
- [85] M. Phillips and H. Wang, *Solid State Commun.* **111**, 317 (1999).
- [86] H. P. Wagner, W. Langbein and J. M. Hvam, *Phys. Rev. B* **59**, 4584 (1999).

# Heavy-hole and light-hole oscillations in the coherent emission from quantum wells: Evidence for exciton-exciton correlations

Arthur L. Smirl,\* Martin J. Stevens, X. Chen, and O. Buccafusca

*Laboratory for Photonics & Quantum Electronics, 138 IATL, University of Iowa, Iowa City, Iowa 52242*

(Received 15 January 1999)

We demonstrate the presence of strong exciton-exciton correlations in GaAs-AlGaAs multiple quantum wells by using the polarization selection rules for four-wave mixing and a test that was originally designed to distinguish between quantum beats and polarization interference. We show that, when the four-wave-mixing signal is produced by two pulses that have the same circular polarization, dynamic beating behavior is observed at the heavy-hole-light-hole frequency that provides evidence of Coulomb-induced correlations that go beyond those expected from the semiconductor Bloch equations in the Hartree-Fock approximation and beyond the local field corrections used in simple phenomenological models. Moreover, this behavior cannot be explained by invoking biexcitonic effects. We demonstrate that this dynamic excitonic coupling can be explained in terms of a competition between quantum-beat-like and polarization-interference-like behavior, and we show that such behavior can be used to place quantitative limits on the coupling strength. In addition, we use a simple phenomenological model to show that excitation-induced-dephasing can produce such correlations. [S0163-1829(99)06435-8]

## I. INTRODUCTION

In recent years, dephasing processes associated with non-equilibrium carriers in semiconductors and semiconductor heterostructures often have been investigated by using four-wave-mixing (FWM) techniques to monitor the decay of the coherent macroscopic polarization.<sup>1,2</sup> Initially, the dephasing was studied by measuring the temporally-integrated intensity or spectrum of the diffracted FWM signal.<sup>3-7</sup> Later, the FWM intensity was time-resolved by cross correlating it with an ultrashort laser pulse via frequency up conversion in a nonlinear crystal.<sup>8-12</sup> When excitons of different energies are excited, oscillations (or beats) are observed both in the time-integrated and time-resolved FWM signal. Such beats have been observed, for example, between light-hole (lh) and heavy-hole (hh) excitons<sup>13-20</sup> and between excitons in quantum wells of different widths.<sup>17,21</sup> In one such study,<sup>17</sup> which is of particular interest here, the behavior of the time-resolved FWM signal was used to distinguish quantum beating (which is associated with two coupled oscillators that share a common level) from polarization interference (which is associated with two independent oscillators).

Often, the beating behavior has been explained by using the single-particle density matrix equations for two independent three-level systems.<sup>22</sup> However, a complete description of the behavior of the FWM signal has been shown to require the inclusion of various exciton-exciton interaction phenomena,<sup>23-27</sup> such as local field corrections,<sup>7,15,28-31</sup> excitation-induced dephasing,<sup>32-35</sup> and biexcitons.<sup>36-43</sup> Various procedures have been developed for including these Coulomb-induced many-body effects in a microscopic theory. One approach is to use nonequilibrium Green's functions methods to derive the most general form of the semiconductor Bloch equations (SBE's) that include contributions of dynamical correlations and quantum kinetic processes.<sup>44-48</sup> Early numerical solutions have concentrated

on effects such as dynamical screening within the screened Hartree-Fock approximation,<sup>49,50</sup> whereas the strong and ultrafast regime, in which excitonic phase space filling is the leading nonlinearity, has been investigated extensively in the unscreened Hartree-Fock approximation. More recently, the influence of dynamical correlations in the screened Hartree-Fock approximation (and modifications thereof) on the ultrafast nonlinearities has been investigated.<sup>51</sup> On the other hand, correlations within the  $\chi^{(3)}$  regime, such as biexcitonic effects, have been found to be described within the dynamics controlled truncation scheme.<sup>52-54</sup>

Here, we perform time-resolved FWM measurements on a GaAs-AlGaAs multiple quantum well when the excitation spectrum is tuned so that both hh and lh excitons are excited, and we demonstrate that strong oscillations at the hh-lh beat frequency are observed when the two pump pulses have the same circular polarizations. Moreover, we use the test described in Ref. 17 to demonstrate that these oscillations behave as quantum beats, rather than polarization interference. Calculations based on the density matrix equations for two independent three-level systems indicate that polarization interference, but not quantum beats, should be observed. Similar results are expected for the SBE in the Hartree-Fock limit. Consequently, this simple test provides an elegant demonstration of the importance of including many body effects in any description of the excitonic dynamics and, more importantly, illustrates the necessity of including exciton-exciton correlations beyond the Hartree-Fock contributions. Additionally, we show that the observed quantum beating behavior can be reproduced by including a density-dependent dephasing term (so-called excitation-induced dephasing or EID). A simple phenomenological model based on EID predicts new features in the lh-hh oscillations that are quite distinct from those expected for purely quantum beating or for polarization interference. We demonstrate that these features are observed experimentally, and we use them

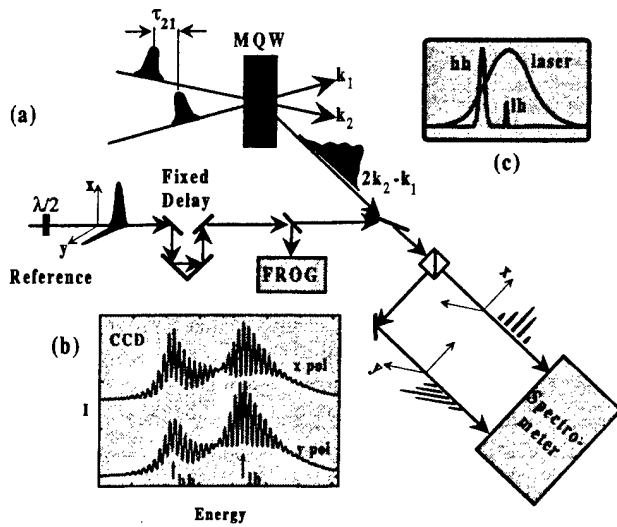


FIG. 1. (a) Spectral interferometric geometry for the dual-channel measurement of the amplitude, phase, and polarization state of the FWM signal, (b) typical spectral interferograms for the  $x$  and  $y$  components as displayed on the CCD array attached to the spectrometer, and (c) schematic showing the laser detuning with respect to the FWM power spectrum.

to place limits on the magnitude of the density-dependent dephasing.

## II. DUAL-CHANNEL SPECTRAL INTERFEROMETRY

Our measurements were performed using the dual-channel spectral interferometric technique shown schematically in Fig. 1. This technique, which we have described previously,<sup>26,27,55</sup> allows the complete characterization of the FWM emission, including its amplitude, phase and vectorial dynamics. As shown, each pulse from our mode-locked Ti:sapphire laser was divided into three parts. Two of the pulses [ $\sim 150$  fs full-width at half maximum of the intensity (FWHM)], with fields  $E_1$  and  $E_2$  and wave vectors  $\mathbf{k}_1$  and  $\mathbf{k}_2$ , were used to generate the FWM signal in the direction  $2\mathbf{k}_2 - \mathbf{k}_1$  in the conventional manner. The third (reference) pulse was linearly polarized at  $45^\circ$ , so that it had equal  $x$  and  $y$  components. A fixed time delay was introduced between the reference pulse and the FWM signal, and the amplitude and the phase of the reference pulse were carefully measured using second-harmonic frequency-resolved optical gating (SHG-FROG).<sup>56</sup> The FWM signal then was allowed to interfere with the fully characterized time-delayed reference pulse by combining them collinearly. The combined signal was subsequently separated into  $x$  and  $y$  components, and each component was separately dispersed by a spectrometer. Typical spectral interferograms for the  $x$  and  $y$  components as recorded on a CCD array are shown in Fig. 1(b). They each have the form

$$I_{SI}^i(\omega) = I_{FWM}^i(\omega) + I_{ref}^i(\omega) + 2\sqrt{I_{FWM}^i(\omega)}\sqrt{I_{ref}^i(\omega)} \times \cos[\phi_{FWM}^i(\omega) - \phi_{ref}^i(\omega) - \omega\tau], \quad (1)$$

where  $I_{FWM}^i(\omega)$  and  $I_{ref}^i(\omega)$  are the spectral intensities and  $\phi_{FWM}^i(\omega)$  and  $\phi_{ref}^i(\omega)$  are the spectral phases of the FWM signal and reference pulse, respectively, and where  $i$  takes on

the values  $x$  and  $y$  for the two polarization directions. The delay  $\tau$  (typically  $\sim 5$  ps) was chosen to yield fringes of a convenient spacing.

If the spectral intensity  $I_{ref}^i(\omega)$  and spectral phase  $\phi_{ref}^i(\omega)$  of each component of the reference are known, then the spectral intensity  $I_{FWM}^i(\omega)$  and spectral phase  $\phi_{FWM}^i(\omega)$  of each component of the FWM signal and the reference time delay  $\tau$  can be retrieved from the corresponding spectral interferograms with a high degree of accuracy using fringe inversion techniques<sup>57,58</sup> that have been discussed previously. For our measurements, the spectral intensity  $I_{ref}^i(\omega)$  and the spectral phase  $\phi_{ref}^i(\omega)$  of each component of the reference pulse were independently determined from the FROG characterization. A degree of redundancy was achieved by separately measuring the spectral intensity  $I_{FWM}^i(\omega)$  of each component of the FWM signal by blocking the reference and measuring it with the spectrometer. Similarly, each component of the spectral intensity  $I_{ref}^i(\omega)$  of the reference was determined by blocking the signal and measuring it with the spectrometer. The delay  $\tau$  was also confirmed using a separate calibration procedure.

The temporal amplitude  $I_{FWM}^i(t)$  and the temporal phase  $\phi_{FWM}^i(t)$  of each component were subsequently obtained by inverse Fourier transformation of the corresponding spectral amplitude and phase. In this way, the complete time-resolved vectorial dynamics, as well as the overall amplitude and phase, were measured. We emphasize that conventional time-resolved FWM techniques measure the temporal intensity, and therefore, they provide no phase information. Moreover, such techniques are scalar in nature. That is, either they monitor a single selected polarization component of the FWM signal, or they integrate over all polarization directions. In either case, conventional techniques provide little or no information about the vectorial dynamics which occur during a FWM emission process. Previously, we have shown that the vectorial dynamics contain essential information about many-body and quantum-interference effects that would be difficult to obtain using conventional techniques.<sup>19,20,23-27</sup>

Here, we completely time resolve the FWM emission (including the polarization dynamics) as a function of the time delay  $\tau_{21} (\equiv t_2 - t_1)$  between the two pump pulses for two input polarization configurations: (i)  $E_1$  and  $E_2$  having the same linear ( $x$ ) polarization and (ii)  $E_1$  and  $E_2$  having the same (right) circular polarization. The measurements were performed on a sample consisting of 10 periods of  $\sim 14$ -nm-wide GaAs wells alternating with 17-nm-thick  $\text{Al}_{0.3}\text{Ga}_{0.7}\text{As}$  barriers, which was grown on a (001)-oriented GaAs substrate. The sample was mounted onto a glass flat, the GaAs substrate was removed by selective etching to permit transmission measurements, and an antireflection coating was applied to the exposed air-semiconductor interface to reduce Fabry-Perot effects. The measurements were performed at 80 K. At this temperature, the sample had a hh linewidth of  $\sim 1.3$  meV, and a hh-lh energy separation of 12 meV. The bandwidth of the excitation pulses was restricted to  $\sim 15$  meV, which resulted in a measured pulsewidth of  $\sim 150$  fs (FWHM). Given the hh-lh splitting, this spectral width was sufficiently broad to allow the simultaneous excitation of both lh's and hh's, yet was narrow enough to allow the ratio

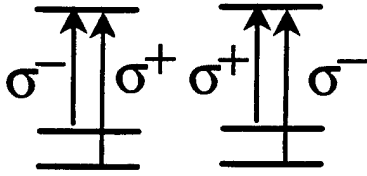


FIG. 2. Schematic of the two independent three-level ( $2 \times 3$ ) systems used to represent the hh and lh electronic transitions in the absence of many body effects, where  $\sigma^+$  denotes right circularly polarized light and  $\sigma^-$  denotes left circular polarization.

of hh-to-lh emission to be varied over a wide range as the laser wavelength was tuned. At the fluence used here ( $\sim 1 \mu\text{J}/\text{cm}^2$ ), the estimated carrier density is  $\sim 1.5 \times 10^{16} \text{ cm}^{-3}$  ( $\sim 2 \times 10^{10} \text{ cm}^{-2}$ ), and the hh linewidth is further broadened to  $\sim 3.7 \text{ meV}$ . At this operating temperature and carrier density, this sample has been separately shown to be homogeneously broadened.

### III. DISTINGUISHING QUANTUM BEATS FROM POLARIZATION INTERFERENCE

As stated in the introduction, we will use a modified version of the test developed by Koch *et al.*<sup>17</sup> to distinguish between quantum beats and polarization interference to investigate exciton-exciton correlations. Basically, Koch *et al.*<sup>17</sup> recognized that the temporal FWM response of a system that consists of two nonresonant transitions that share a common level has a different dependence on the time delay  $\tau_{21}$  than a system that consists of two nonresonant transitions that do not share a common level. They<sup>17</sup> then used this difference in the temporal behavior as a function of time delay to classify the oscillations into one of two categories: quantum beats or polarization interference. In this section, we begin by first reviewing the fundamentals of this test, then illustrate its use experimentally. Our theoretical presentation will closely parallel that of Ref. 17, but we will put the formalism into our context and notation for the reader's convenience. The results reviewed in this section then will provide a useful direct comparison for the results presented in later sections.

We will illustrate the procedure used to distinguish quantum beats from polarization interference by contrasting the FWM response of the two three-level ( $2 \times 3$ ) systems of Fig. 2 when they are excited with two pump pulses having the same linear polarization with the response of the same systems when they are excited with two pump pulses having the same circular polarization. In the simplest picture (and in the absence of many body effects), the  $2 \times 3$  system and the selection rules shown in Fig. 2 can be used to represent the electronic states associated with the hh and lh transitions for the two spin states in a quantum well.

We initially assume that each pulse is linearly ( $x$ ) polarized. In addition, in order to obtain the simplest description of our experiments and in order to obtain a closed form solution, we assume that the pulses in the  $\mathbf{k}_2$  and  $\mathbf{k}_1$  directions have delta function time dependencies given by  $\delta(t)$  and  $\delta(t + \tau_{21})$ , respectively. Under these excitation conditions, both lh and hh transitions that share a common level in each of the  $2 \times 3$  systems shown in Fig. 2 will be excited (since  $x$ -polarized light is composed of equal parts left- and right-

circular polarizations). In this case, one can readily solve the density matrix equations for the two three-level systems shown in Fig. 2 to third-order. The polarization that propagates in the  $2\mathbf{k}_2 - \mathbf{k}_1$  direction is found to be proportional to

$$\mathcal{P}_{\text{QB}} \propto \Theta(t) \Theta(\tau_{21}) \mathcal{E}_2^2 \mathcal{E}_1^* \exp[-\gamma(t + \tau_{21})] \times \{ [1 + A \exp(i\Omega\tau_{21})] [1 + A \exp(-i\Omega t)] \} \hat{x}, \quad (2)$$

where  $\Theta$  denotes the Heaviside step function,  $\mathcal{E}_1$  and  $\mathcal{E}_2$  are the slowly varying electric field amplitudes of the two pump pulses,  $\gamma$  is the dephasing rate,  $\hbar\Omega$  is the difference between the hh and lh energies, and  $A$  is a phenomenological constant that reflects the relative strength of the lh FWM emission. In our case,  $A$  is the product of the square of the ratio of the lh and hh optical transition matrix elements ( $\sim \frac{1}{3}$ ) and a spectral weighting factor ( $\sim 2$ ) to account for the detuning of the excitation wavelength with respect to the hh and lh excitons, as shown schematically in Fig. 1(c). Furthermore, we have assumed that the dephasing is much faster than the population decay.

The slowly varying polarization amplitude given by Eq. (2) is written from the frame of reference of the hh exciton. Thus, the term  $[1 + A \exp(-i\Omega t)]$  in Eq. (2) is the sum of two oscillators: The first represents the polarization oscillating at the hh frequency, and the second at the lh frequency. However, these oscillators are not independent. The initial (at  $t=0$ ) relative phases and amplitudes of the two oscillators are fixed at a value determined by the factor  $[1 + A \exp(i\Omega\tau_{21})]$  which multiplies both oscillators. This coupling is a consequence of the shared level, and in this sense, the "interference" or beating takes place within the material. The magnitude of the total polarization (and therefore of the net emitted field) oscillates at the beat frequency  $\Omega$  with a phase that is independent of  $\tau_{21}$ .

The signal generated in the detector is proportional to the intensity and, therefore, it is proportional to

$$S_0 \propto |\mathcal{P}_{\text{QB}}|^2 \propto \Theta(t) \Theta(\tau_{21}) I_2^2 I_1 \exp[-2\gamma(t - \tau_{21})] \times \{ 1 + 2A^2 + A^4 + 2(A + A^3) \cos \Omega \tau_{21} + 2(A + A^3 + 2A^2 \cos \Omega \tau_{21}) \cos \Omega t \}. \quad (3)$$

Notice that the only term that oscillates in time is the last one, which is proportional to  $\cos \Omega t$ . Consequently, it is evident that the peaks of this oscillation occur at times  $t_p$  given by

$$t_p = m(2\pi/\Omega), \quad (4)$$

where  $m$  is an integer which labels successive peaks. Thus, the position of a given peak does not depend on  $\tau_{21}$ . The slope of the  $t_p$  versus  $\tau_{21}$  curve is 0. Such oscillations were classified in Ref. 17 as quantum beats.

By contrast, if the two independent three-level systems shown in Fig. 2 are excited with two right-circularly polarized pulses, only the lh transition on the left and the hh transition on the right will be excited. In this case, the two excited oscillators share no common level, and the FWM polarization that propagates in the  $2\mathbf{k}_2 - \mathbf{k}_1$  direction is proportional to

$$\mathcal{P}_{PI} \propto \Theta(t) \Theta(\tau_{21}) \mathcal{E}_2^* \mathcal{E}_1^* \exp[-\gamma(t + \tau_{21})] \times \{1 + A^2 \exp[-i\Omega(t - \tau_{21})]\} \hat{\sigma}_+, \quad (5)$$

where  $\hat{\sigma}_+$  denotes right circularly polarized light. The slowly varying polarization amplitude given by Eq. (5) again is written from the frame of reference of the "hh" exciton. In this case, Eq. (5) is the sum of two independent oscillators: The first represents the polarization oscillating at the hh frequency, and the second the polarization oscillating at the lh frequency with an independent phase determined by  $\tau_{21}$ . The magnitude of the total polarization (and therefore of the net emitted field) oscillates at the beat frequency  $\Omega$  with the phase determined by  $\tau_{21}$ , but there is no interaction (or interference) between the two polarizations within the material. Each propagates and oscillates independently. In this sense, the beating does not originate within the material.

Again, the signal generated in the detector is proportional to the intensity and is proportional to

$$S_0 \propto |\mathcal{P}_{PI}|^2 \propto \Theta(t) \Theta(\tau_{21}) I_2^2 I_1 \exp[-2\gamma(t + \tau_{21})] \times \{1 + A^4 + 2A^2 \cos[\Omega(t - \tau_{21})]\}. \quad (6)$$

In this case, we see that the oscillations are a consequence of the nature of the detection process. Such oscillations were classified as polarization interference in Ref. 17. It is also evident from this expression that the peak of each oscillation occurs at a time given by

$$t_p = \tau_{21} + m \left( \frac{2\pi}{\Omega} \right). \quad (7)$$

Thus, one would expect to observe a linear relationship between each peak and the time delay  $\tau_{21}$  for polarization interference.

Based on a similar analysis, Koch *et al.*<sup>17</sup> suggested that one could distinguish quantum beats from polarization interference by simply plotting the position of each peak  $t_p$  in the time-resolved FWM signal as a function of the time delay  $\tau_{21}$ . The result should be a straight line. The slope of the line will be zero if the time-resolved oscillations are the result of quantum beating, and the slope will be unity if they originate from polarization interference. (Note that we have taken our origin to coincide with the  $\mathcal{E}_2$  pulse. If the origin is taken to coincide with the  $\mathcal{E}_1$  pulse, as was done in the original paper,<sup>17</sup> then a slope of 1 will be obtained for quantum beating and a slope of 2 for polarization interference.) We emphasize that many body effects are not included in the analysis to this point.

To illustrate this procedure and to test whether the hh-lh oscillations in our previous publication<sup>20</sup> were the result of quantum beats or polarization interference, we performed this test on the FWM emission from our sample. Specifically, the laser wavelength was tuned onto the lh exciton so that both hh's and lh's were strongly excited. We used the geometry shown in Fig. 1 to completely time resolve the FWM emission (including the polarization dynamics) as a function of time delay  $\tau_{21}$  between the pump pulses. Measurements were performed, first, for  $E_1$  and  $E_2$  having the same linear (x) polarization state and, then, for  $E_1$  and  $E_2$  having the same (right) circular polarization state.

In Fig. 3(a), we show the total intensity  $S_0$  of the time-

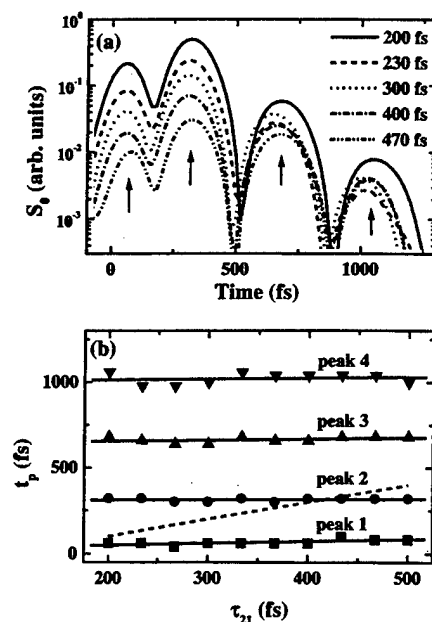


FIG. 3. Results of measurements to distinguish quantum beating from polarization interference using two linearly x-polarized incident pump pulses: (a) Time-resolved measurements of the total intensity  $S_0$  of the FWM intensity for selected time delays  $\tau_{21}$  between two incident pulses, and (b) the time  $t_p$  at which each peak [indicated by an arrow in (a)] occurs as a function of  $\tau_{21}$ , for a more complete set of time delays. The dotted line indicates a slope of unity.

resolved FWM signal for various time delays  $\tau_{21}$  between the pump and probe pulses when the sample was excited with two x-polarized pump pulses. The ellipticity angle and the orientation of the polarization ellipse were also time resolved. To within our experimental accuracy, the FWM signal was found to be linearly and x polarized for all times and all time delays. For this reason, we plot only the total intensity in Fig. 3(a). Clearly, oscillations at the hh-lh beat frequency are observed at each delay shown. In Fig. 3(b), we plot the position of each peak  $t_p$  in the time-resolved FWM signal [indicated by the arrows in Fig. 3(a)] as function of the time delay  $\tau_{21}$ , for a more complete set of time delays. Clearly, the slope is zero for each peak. Consequently, the oscillations shown in Fig. 3 behave as quantum beats and not polarization interference. This is exactly the behavior that we would have expected from a simple density matrix model for the  $2 \times 3$  system shown in Fig. 2 (without many-body effects) based on Eq. (3).

#### IV. A TEST FOR EXCITON-EXCITON CORRELATIONS

The results of performing the test to distinguish quantum beats from polarization interference when the sample is excited with two pulses that have the same (right) circular polarization are shown in Fig. 4. In Fig. 4(a), the results of measuring the time-resolved FWM signal for selected time delays  $\tau_{21}$  between the pump and probe pulses are shown. Again, the polarization state was also measured, and the FWM signal was found to be right circularly polarized for all times and all time delays. As for the linear excitation pulses [i.e., Fig. 3(a)], pronounced oscillations at lh-hh beat frequency are evident. In Fig. 4(b), the position of each peak in

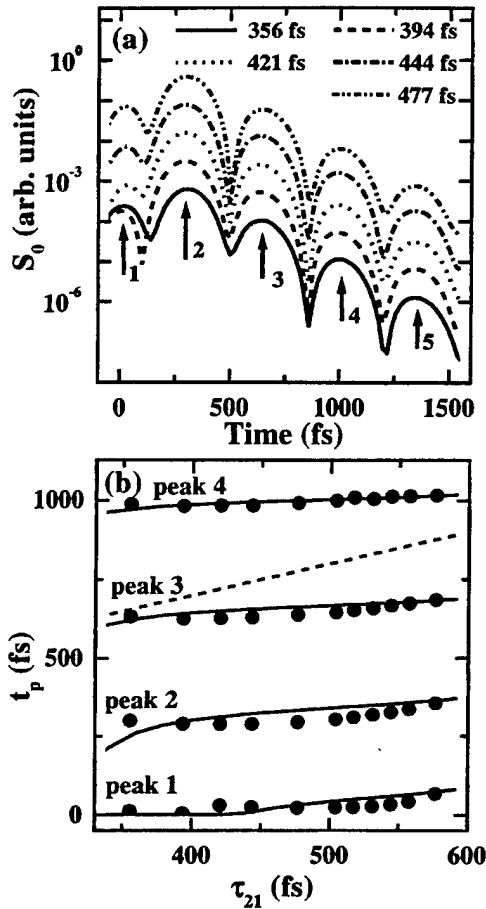


FIG. 4. Results of measurements to distinguish quantum beating from polarization interference using two right-circularly polarized pump pulses: (a) Time-resolved measurements of the total intensity  $S_0$  of the FWM intensity for selected time delays  $\tau_{21}$  between the two incident pulses in the range between 350 and 600 fs, and (b) the time  $t_p$  at which each peak [indicated by the first four arrows in (a)] occurs as a function of  $\tau_{21}$ , for a more complete set of time delays. The dotted line indicates a slope of unity, and the solid lines are the result of simulations based on Eq. (9).

the time-resolved FWM signal [indicated by the arrows in Fig. 4(a)] is plotted as function of the time delay  $\tau_{21}$ , again for a more complete set of delays. The slope of each curve is approximately zero, not unity. Consequently, the oscillations produced when the sample is excited by two right circularly polarized pulses satisfy the criterion for quantum beats, not polarization interference. Since quantum beats would not be expected for two independent three-level systems without many body effects [see Eq. (5)], this result suggests that the two excitonic systems are not independent, but are coupled and correlated. It should also be noted that the SBE, in their original form (i.e., in the Hartree-Fock limit, without EID or biexciton formation included), would also be expected to predict polarization interference, but no quantum beating, when two right circularly polarized pulses are used. Consequently, the observation of quantum-beat-like behavior suggests a correlation beyond the Hartree-Fock contribution. These measurements are consistent with other<sup>19,20,54</sup> recent observations.

## V. COUPLING BY EXCITATION-INDUCED-DEPHASING

The quantum-beating-like behavior shown in Fig. 4 requires the inclusion of a process that strongly couples the

two spin systems shown in Fig. 2. One such process, which has been invoked previously,<sup>32</sup> is EID. EID can be included in the SBE,<sup>33</sup> but analytical solutions to the full SBE are not possible, and in general, the SBE require lengthy numerical solution. The simplest approach is to solve the density matrix equations for the two three-level systems shown in Fig. 2 and to include EID phenomenologically by expanding the dephasing rate in a Taylor series and keeping the first two terms:

$$\gamma(n) = \gamma_0 + \frac{\partial \gamma}{\partial n} n = \gamma_0 + N \frac{\partial \gamma}{\partial n} (\rho_{ee}^+ + \rho_{ee}^-), \quad (8)$$

where  $\gamma_0$  is the low density dephasing rate at the operating lattice temperature and  $n = N(\rho_{ee}^+ + \rho_{ee}^-)$  is the total density of excited excitons, regardless of spin. Here,  $N$  denotes the total density of oscillators of each spin system and  $\rho_{ee}^+(\rho_{ee}^-)$  denotes the upper level population matrix element for the spin  $-\frac{1}{2}$  ( $+\frac{1}{2}$ ) system. Because it is the total population that determines the dephasing rate, this term provides a coupling between the two three-level systems.

One can readily obtain a closed form solution to these modified density matrix equations for right circular excitation pulses by making the same approximations that we have made throughout (namely, by assuming delta function time dependences for the excitation pulses and by assuming that the dephasing is much faster than the population decay). Under these circumstances, the FWM polarization that propagates in the  $2\mathbf{k}_2 - \mathbf{k}_1$  direction is found to be proportional to

$$\begin{aligned} \mathcal{P}_{\text{EID}} \propto & \Theta(t) \Theta(\tau_{21}) \mathcal{E}_2^* \mathcal{E}_1^* \exp[-\gamma(t + \tau_{21})] \\ & \times \left\{ [1 + A^2 \exp(-i\Omega(t - \tau_{21}))] + \left( \frac{\eta t}{2\hbar} \right) \right. \\ & \times [(1 + A \exp(i\Omega \tau_{21}))(1 + A \exp(-i\Omega t))] \left. \right\} \hat{\sigma}^+, \end{aligned} \quad (9)$$

where the parameter  $\eta \equiv 2N\hbar(\partial\gamma/\partial n)$ , which has units of energy, is the EID parameter that we have used in previous publications,<sup>23-27</sup> and it is a measure of the strength of the density dependence of the dephasing. Equation (9) basically consists of two terms (each enclosed in square brackets). The first term (in square brackets) has the same form as the FWM polarization that we have associated with polarization interference [see Eq. (5)], and the second term, which is multiplied by  $\eta t/2\hbar$ , has the same form as the FWM polarization that we have associated with quantum beats [see Eq. (2)].

There are two limits of immediate interest:  $\eta t/2\hbar \ll 1$  and  $\eta t/2\hbar \gg 1$ . When  $\eta t/2\hbar \ll 1$  for all times of interest, Eq. (9) reduces to the result that would be obtained for the two independent, uncoupled three-level systems shown in Fig. 2 [i.e., to Eq. (5)]. As we have already stated, in this case, the lh transition is excited in the system on the left, and the hh transition is excited in the system on the right. Under these conditions, the optically excited transitions share no common level, and there is no coupling between the excited states in the two independent systems. The latter conditions clearly correspond to polarization interference. In this limit, the detected intensity is given by Eq. (6) for polarization interference, and thus, there is a linear relationship between the peak

of one of the oscillations in time  $t_p$  and the time delay  $\tau_{21}$ , as predicted by Eq. (7). This limit ( $\eta=0$ ) is represented by the dotted line in Fig. 4(b).

By comparison, if  $\eta t/2\hbar \gg 1$ , the light is still directly coupled only to the lh transition on the left and the hh transition on the right in Fig. 2. That is, the optically-excited transitions still technically share no common level, but now the upper levels are strongly coupled through the density-dependent dephasing given by Eq. (8). In this limit, using Eq. (9), we find the total FWM intensity to be proportional to

$$S_0 \propto |\mathcal{P}_{\text{EID}}|^2 \propto \Theta(t) \Theta(\tau_{21}) I_2^2 I_1 (\eta t/2\hbar)^2 \exp[-2\gamma(t + \tau_{21})] \{1 + 2A^2 + A^4 + 2(A + A^3) \cos \Omega \tau_{21} + 2(A + A^3 + 2A^2 \cos \Omega \tau_{21}) \cos \Omega t\}. \quad (10)$$

Except for the multiplicative factor of  $(\eta t/2\hbar)^2$ , Eq. (10) is mathematically equivalent to Eq. (3). Thus, we see that in the strong coupling limit the effects of EID are mathematically equivalent to sharing a common level, even though there is clearly a physical difference. In this limit, as with Eq. (3), the slope of the  $t_p$  versus  $\tau_{21}$  curve is 0, which is identical to the slope exhibited by the data shown in Fig. 4. This is the type of behavior that previously has been attributed to quantum beating.

The solid curves in Fig. 4(b) are the results of simulations using the full FWM polarization given by Eq. (9) with  $\eta = 4$  meV and  $\Omega = 2\pi/340$  fs $^{-1}$ , and they demonstrate that this model produces qualitative and quantitative agreement with the data presented to this point. However, Eq. (9) predicts new features in the hh-lh oscillations that are not characteristic either of pure quantum beating or of polarization interference. For example, as we explained earlier, the first term in square brackets in Eq. (9) produces a response that is characteristic of polarization interference and the second term in square brackets (which is multiplied by  $\eta t/2\hbar$ ) produces a response that resembles quantum beating. Since the second term is proportional to time, it will be negligible for times  $t \ll 2\hbar/\eta$  and dominant for  $t \gg 2\hbar/\eta$ . In other words, for the parameters given here, Eq. (9) predicts a transition from polarization-interference-like behavior to quantum-beating-like behavior on a characteristic time scale of  $2\hbar/\eta \sim 330$  fs (for  $\eta = 4$  meV). It is very difficult to unambiguously distinguish a transition of this duration occurring near  $t=0$  because of the finite width of our pulses (which are not currently taken into account in our model).

Equation (9) also predicts a dynamic, periodic competition between the two types of oscillations as a function of time delay  $\tau_{21}$ , with a period equal to the lh-hh beat frequency. Inspection of Eq. (9) reveals that the “quantum-beating” term is not only multiplied by  $\eta t/2\hbar$ , but is proportional to  $[1 + A \exp(i\Omega \tau_{21})]$ . Consequently, the contribution of the term that we have associated with “quantum beating” will be periodically reduced with respect to the term that we have associated with “polarization interference”. A minimum in the “quantum beating” term will occur each time  $\tau_{21}$  is an odd multiple of  $\pi/\Omega$ . The consequences of this behavior are illustrated in Fig. 5, where the simulated time-resolved FWM signals [calculated using Eq. (9)] are shown for equally spaced time delays between 300 and 667 fs. Notice that for time delays  $\tau_{21}$  near 510 fs

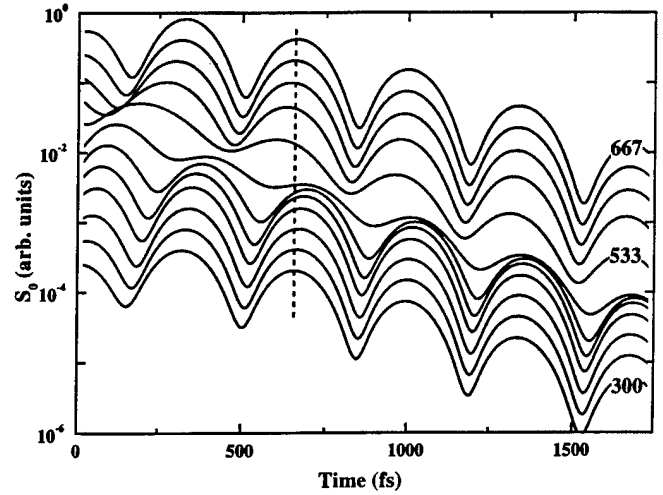


FIG. 5. Calculations of the total intensity  $S_0$  of the FWM intensity as a function of time for equally spaced time delays  $\tau_{21}$  between the two incident pulses in the range between 300 and 667 fs.

( $\sim 3\pi/\Omega$ ) the positions of the peaks in the FWM signal are shifted, the oscillations are distorted, and their amplitudes are dramatically reduced at early times  $t$ . At longer times  $t$  (as  $\eta t/2\hbar$  becomes larger and the “quantum beating” term increases in strength), the oscillations become stronger, their periods more regular, and the positions of the beat maxima more quantum-beat-like. Similar behavior is consistently observed in the data, as illustrated in Fig. 6.

Careful comparison of Figs. 5 and 6 shows that the minimum in the “quantum beating” contribution in the data occurs at a time delay that is shifted by  $\sim 140$  fs compared to the minimum in the simulations. We do not know the origin of this shift, and it is the subject of ongoing investigation; however, we speculate that it is a consequence of our assuming delta function excitation pulses. The actual excitation pulses are each  $\sim 150$  fs in duration, and the frequencies which are resonant with the hh exciton have been determined to have phases that are slightly different from those that are resonant with the lh. Consequently, with the exception of the

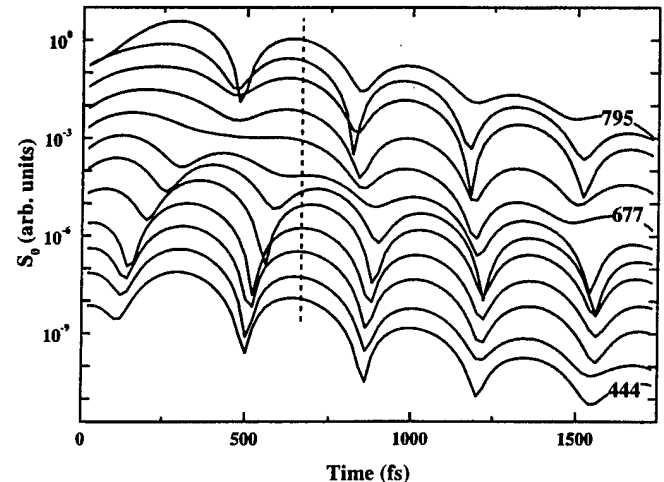


FIG. 6. Measurements of the total intensity  $S_0$  of the FWM intensity as a function of time for equally spaced time delays  $\tau_{21}$  between the two incident pulses in the range between 444 and 795 fs.



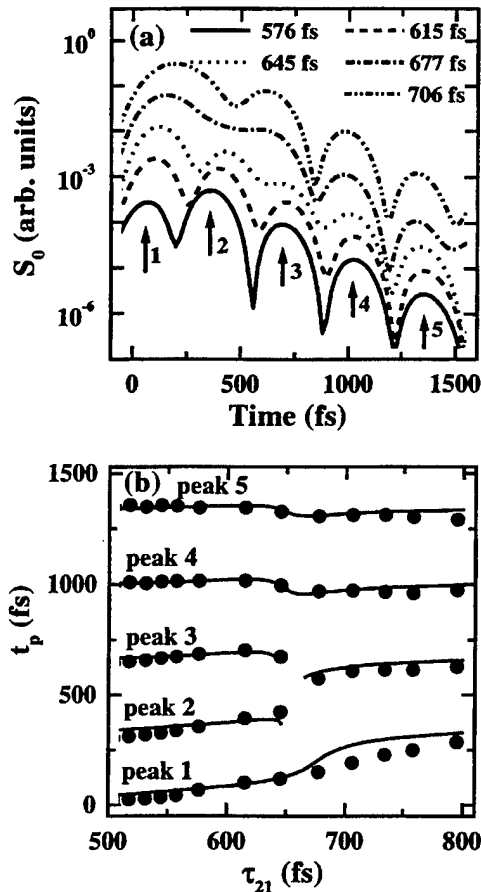


FIG. 7. (a) Time-resolved measurements of the total intensity  $S_0$  of the FWM intensity for selected time delays  $\tau_{21}$  between the two incident pulses in the range between 500 and 800 fs and (b) the time  $t_p$  at which each peak [indicated by the arrows in (a)] occurs as a function of  $\tau_{21}$ , for a more complete set of time delays. The solid lines are the result of simulations based on Eq. (9).

simulations shown in Fig. 5, the time delays for all simulations have been shifted by 140 fs to facilitate a direct comparison with the data.

The new features described above, which are not characteristic of quantum beating or polarization interference, and the excellent agreement between the data and the simulations based on Eq. (9) are also apparent if both data and simulation are plotted in the conventional format used to discriminate quantum beats from polarization interference (e.g., see Figs. 3 or 4). Figure 7 shows a plot of the temporal position of the peak in the lh-hh oscillations as a function of delay between the two pump pulses. This figure differs from Fig. 4 in that it focuses on the behavior at longer time delays in the vicinity of a minimum in the quantum beating term. Clearly, the data in this region can not be described by a straight line with slope of either 0 or 1 as required by quantum beating or polarization interference, respectively, acting individually. Simulations based on Eq. (10) (i.e., the solid lines in Fig. 7) do, however, produce good agreement with the data.

## VI. ESTIMATE OF THE COUPLING STRENGTH

We emphasize that this technique isolates, and is particularly sensitive to, the strength of the Coulomb-induced correlations, or coupling, between the excitons. We now illus-

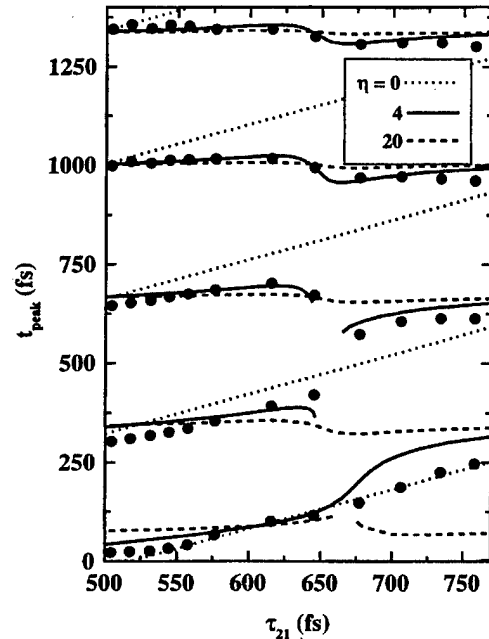


FIG. 8. Comparison between the measured (solid dots) and the simulated time  $t_p$  at which each peak in the lh-hh oscillations occurs as a function of  $\tau_{21}$  for three values of the EID parameter:  $\eta=0$  (dotted line), 4 (solid line), and 20 meV (dashed line).

trate that sensitivity by using the simple model that we have described in our previous work.<sup>24,25</sup> That model<sup>24</sup> phenomenologically includes EID, local field effects and biexciton formation. The local-field effects will not provide a resonant coupling between the two spin systems, and therefore, they can be neglected. Moreover, the technique described here prevents the formation of pure biexcitons involving either two hh excitons or two lh excitons of opposite spin by using two excitation pulses with the same circular polarizations. However, under these excitation conditions, mixed biexcitons can be formed from one hh exciton and one lh exciton having opposite spins. Mixed hh-lh biexcitons have been observed in ZnSe quantum wells, but their contribution to the FWM signal was found to be roughly an order of magnitude weaker than that of hh biexcitons.<sup>59</sup> We have examined our FWM spectra for evidence of mixed lh-hh biexciton formation when we excite with two right circularly polarized pulses, and we find no resolvable signal at the expected mixed biexciton frequency (to within our experimental accuracy under our excitation conditions). For these reasons, we neglect the contributions of mixed lh-hh biexcitons here. Consequently, within the context of this phenomenological model, only EID can provide the needed coupling. Therefore, when the sample is excited with two pulses having the same circular polarization, the model that we have used previously reduces to the one used in the previous section. Moreover, the features displayed in Figs. 4–7 allow a rough quantitative estimate of the strength of the EID coupling between the two spin systems, again, within the context of the model presented here.

Figure 8 illustrates the sensitivity of this technique to the EID parameter. This figure shows a comparison between the data and simulations using three values of the EID parameter:  $\eta=0$ , 4, and 20 meV. Notice that  $\eta=0$  produces reasonable agreement at early times  $t$ , when EID effects are

expected to be negligible (i.e.,  $t \ll 2\hbar/\eta$ ), for all time delays  $\tau_{21}$ , but this value produces poor agreement at later times (when  $t > 2\hbar/\eta$ ). By comparison,  $\eta = 20$  produces acceptable agreement with the data at later times when EID effects are expected to dominate, but poor agreement for earlier times. Of the three values shown here, only  $\eta = 4$  produces acceptable agreement at all times. The simulated solid curves shown in Figs. 4, 5, and 7 were all produced using this value for the EID parameter. From a comparison with the data presented in this work only, we estimate the EID parameter to be  $4 \pm 2$  meV.

Our principal point is not that EID is the only process that can produce the quantum-beating-like behavior shown in Figs. 4–8 (although we have shown this interpretation to be consistent with the simple phenomenological model which has been successful in accounting many other features in our FWM data<sup>24,25</sup>). A rigorous analysis should be based on a detailed microscopic theory. Once such a calculation is performed, the procedure described here can be used to evaluate the strength of the exciton-exciton correlations in that model in the same way that we have used it here to evaluate the EID parameter.

## VII. CONCLUSION

The data and calculations presented here demonstrate that, when excitation pulses with the same circular polarizations are used, the test that was originally designed to distinguish quantum beats from polarization interference becomes an effective test for Coulomb-induced excitonic correlations that go beyond the Hartree-Fock contributions (or, in terms of the phenomenological model used in this paper, beyond the local field effects).<sup>60</sup> Moreover, these correlations are in addition to biexcitonic effects, since biexcitonic contributions are found to be negligible when a single circular polarization is used for both pump pulses. In fact, the data presented in Figs. 4–8 suggest that these correlations are not only impor-

tant, but that they dominate the FWM response under these excitation conditions. Finally, the features observed here make it clear that the coupling between the spin systems is dynamic, rather than static. While hh-lh mixing of the valence band states (e.g., as the result of strain or quantum confinement) can conceptually provide a coupling between the two spin systems, such a mixing would produce a static coupling, and therefore, it can not explain the dynamic results discussed here.

A secondary point to be made concerning the results presented here is that the classification of lh-hh oscillations as quantum beats or polarization interference is problematic and, perhaps, overly simplistic. If one accepts the definition that oscillations arising from interference within the sample are quantum beats (and, conversely, that oscillations arising from interference at the detector are polarization interference) then, in this sense, the oscillations arising from the exciton-exciton correlations (Fig. 7) and those arising from a shared common level (Fig. 3) are both quantum beats. However, the beats arising from the exciton-exciton correlations are clearly fundamentally different from the beats arising from lh and hh transitions that share a common level. The coupling is dynamic in the case of the former, and the sharing is a static condition for the latter. Finally, it can be argued that the term “quantum beats” should be reserved for measuring oscillations that directly monitor the Raman coherence terms. In the latter sense, all of the phenomena that we have discussed here must be classified as polarization interference, since two-pulse self-diffraction FWM geometries do not monitor the Raman coherence directly (see Refs. 61 and 62 for a discussion of this latter point).

## ACKNOWLEDGMENTS

The authors gratefully acknowledge numerous insightful conversations with Rolf Binder. This research was supported in part by the National Science Foundation and the U.S. Army Research Office.

\*FAX: (319) 335-3462. Electronic address: art-smirl@uiowa.edu

<sup>1</sup> *Coherent Optical Interactions in Semiconductors*, edited by R. T. Phillips (Plenum, New York, 1994), and references therein.

<sup>2</sup> J. Shah, *Ultrafast Spectroscopy of Semiconductors and Nanostructures* (Springer-Verlag, Heidelberg, 1996), and references therein.

<sup>3</sup> L. Schultheis, M. D. Sturge, and J. Hegarty, *Appl. Phys. Lett.* **47**, 995 (1985).

<sup>4</sup> L. Schultheis, A. Honold, J. Kuhl, K. Köhler, and C. W. Tu, *Phys. Rev. B* **34**, 9027 (1986).

<sup>5</sup> L. Schultheis, J. Kuhl, A. Honold, and C. W. Tu, *Phys. Rev. Lett.* **57**, 1635 (1986).

<sup>6</sup> L. Schultheis, J. Kuhl, A. Honold, and C. W. Tu, *Phys. Rev. Lett.* **57**, 1797 (1986).

<sup>7</sup> K. Leo, M. Wegener, J. Shah, D. S. Chemla, E. O. Göbel, T. C. Damen, S. Schmitt-Rink, and W. Schäfer, *Phys. Rev. Lett.* **65**, 1340 (1990).

<sup>8</sup> S. T. Cundiff and D. G. Steel, *IEEE J. Quantum Electron.* **28**, 2423 (1992), and references therein.

<sup>9</sup> D. S. Kim, J. Shah, J. E. Cunningham, T. C. Damen, S. Schmitt-Rink, and W. Schäfer, *Phys. Rev. Lett.* **68**, 2838 (1992).

<sup>10</sup> D. S. Kim, J. Shah, T. C. Damen, W. Schäfer, F. Jahnke, S.

Schmitt-Rink, and K. Köhler, *Phys. Rev. Lett.* **69**, 2725 (1992).

<sup>11</sup> A. Lohner, K. Rick, P. Leisching, A. Leitenstorfer, T. Elsaesser, T. Kuhn, F. Rossi, and W. Stolz, *Phys. Rev. Lett.* **71**, 77 (1993).

<sup>12</sup> M. D. Webb, S. T. Cundiff, and D. G. Steel, *Phys. Rev. Lett.* **66**, 934 (1991).

<sup>13</sup> K. Leo, T. C. Damen, J. Shah, E. O. Göbel, and K. Köhler, *Appl. Phys. Lett.* **57**, 19 (1990).

<sup>14</sup> K. Leo, T. C. Damen, J. Shah, and K. Köhler, *Phys. Rev. B* **42**, 11 359 (1990).

<sup>15</sup> K. Leo, E. O. Göbel, T. C. Damen, J. Shah, S. Schmitt-Rink, W. Schäfer, J. F. Müller, K. Köhler, and P. Ganser, *Phys. Rev. B* **44**, 5726 (1991).

<sup>16</sup> E. O. Göbel, K. Leo, T. C. Damen, J. Shah, S. Schmitt-Rink, W. Schäfer, J. F. Müller, and K. Köhler, *Phys. Rev. Lett.* **64**, 1801 (1990).

<sup>17</sup> M. Koch, J. Feldmann, G. von Plessen, E. O. Göbel, P. Thomas, and K. Köhler, *Phys. Rev. Lett.* **69**, 3631 (1992).

<sup>18</sup> A. E. Paul, W. Sha, S. Patkar, and A. L. Smirl, *Phys. Rev. B* **51**, 4242 (1995).

<sup>19</sup> A. L. Smirl, X. Chen, and O. Buccafusca, *Opt. Lett.* **23**, 1120 (1998).

<sup>20</sup> A. L. Smirl, X. Chen, and O. Buccafusca, *IEEE J. Quantum Electron.* **35**, 523 (1999).

- <sup>21</sup>V. G. Lyssenko, J. Erland, I. Balslev, K.-H. Pantke, B. S. Razbirin, and J. M. Hvam, Phys. Rev. B **48**, 5720 (1993).
- <sup>22</sup>S. Schmitt-Rink, D. Binnhardt, V. Heuckeroth, P. Thomas, P. Haring, G. Maidorn, H. Bakker, K. Leo, D. S. Kim, J. Shah, and K. Köhler, Phys. Rev. B **46**, 10 460 (1992).
- <sup>23</sup>S. Patkar, A. E. Paul, W. Sha, J. A. Bolger, and A. L. Smirl, Phys. Rev. B **51**, 10 789 (1995).
- <sup>24</sup>A. E. Paul, J. A. Bolger, and A. L. Smirl, J. Opt. Soc. Am. B **13**, 1016 (1996).
- <sup>25</sup>J. A. Bolger, A. E. Paul, and A. L. Smirl, Phys. Rev. B **54**, 11 666 (1996).
- <sup>26</sup>A. L. Smirl, W. J. Walecki, X. Chen, and O. Buccafusca, Phys. Status Solidi B **204**, 16 (1997).
- <sup>27</sup>O. Buccafusca, X. Chen, W. J. Walecki, and A. L. Smirl, J. Opt. Soc. Am. B **15**, 1218 (1998).
- <sup>28</sup>S. Weiss, M.-A. Mycek, J.-Y. Bigot, S. Schmitt-Rink, and D. S. Chemla, Phys. Rev. Lett. **69**, 2685 (1992).
- <sup>29</sup>M. Wegener, D. S. Chemla, S. Schmitt-Rink, and W. Schäfer, Phys. Rev. A **42**, 5675 (1990).
- <sup>30</sup>S. Schmitt-Rink, S. Mukamel, K. Leo, J. Shah, and D. S. Chemla, Phys. Rev. A **44**, 2124 (1991).
- <sup>31</sup>W. Schäfer, F. Jahnke, and S. Schmitt-Rink, Phys. Rev. B **47**, 1217 (1993).
- <sup>32</sup>H. Wang, K. Ferrio, D. G. Steel, Y. Z. Hu, R. Binder, and S. W. Koch, Phys. Rev. Lett. **71**, 1261 (1993).
- <sup>33</sup>Y. Z. Hu, R. Binder, S. W. Koch, S. T. Cundiff, H. Wang, and D. G. Steel, Phys. Rev. B **49**, 14 382 (1994).
- <sup>34</sup>T. Rappen, U. G. Peter, M. Wegener, and W. Schäfer, Phys. Rev. B **49**, 10 774 (1994).
- <sup>35</sup>D. G. Steel, H. Wang, M. Jiang, K. Farrio, and S. T. Cundiff, in *Coherent Optical Interactions in Semiconductors*, edited by R. T. Phillips (Plenum, New York, 1994), pp. 157–179.
- <sup>36</sup>B. F. Feuerbacher, J. Kuhl, and K. Ploog, Phys. Rev. B **43**, 2439 (1991).
- <sup>37</sup>S. Bar-Ad and I. Bar-Joseph, Phys. Rev. Lett. **68**, 349 (1992).
- <sup>38</sup>H. H. Yaffe, Y. Prior, J. P. Harbison, and L. T. Florez, J. Opt. Soc. Am. B **10**, 578 (1993).
- <sup>39</sup>H. Wang, J. Shah, T. C. Damen, and L. N. Pfeiffer, Solid State Commun. **91**, 869 (1994).
- <sup>40</sup>T. Saiki, M. Kuwata-Gonokami, T. Matsusue, and H. Sakaki, Phys. Rev. B **49**, 7817 (1994).
- <sup>41</sup>E. J. Mayer, G. O. Smith, V. Heuckeroth, J. Kuhl, K. Bott, A. Schulze, T. Meier, D. Binnhardt, S. W. Koch, P. Thomas, R. Hey, and K. Ploog, Phys. Rev. B **50**, 14 730 (1994).
- <sup>42</sup>K.-H. Pantke, D. Oberhauser, V. G. Lyssenko, J. M. Hvam, and G. Weimann, Phys. Rev. B **47**, 2413 (1993).
- <sup>43</sup>K. Bott, O. Heller, D. Binnhardt, S. T. Cundiff, P. Thomas, E. J. Mayer, G. O. Smith, R. Eccleston, J. Kuhl, and K. Ploog, Phys. Rev. B **48**, 17 418 (1993).
- <sup>44</sup>W. Schäfer and J. Treusch, Z. Phys. B **63**, 407 (1986).
- <sup>45</sup>R. Zimmermann, *Many-Particle Theory of Highly Excited Semiconductors* (Teubner, Leipzig, 1988).
- <sup>46</sup>H. Haug and S. W. Koch, *Quantum Theory of the Optical and Electronic Properties of Semiconductors* (World Scientific, Singapore, 1993).
- <sup>47</sup>R. Binder and S. W. Koch, Prog. Quantum Electron. **19**, 307 (1995).
- <sup>48</sup>H. Haug and A. P. Jauho, *Quantum Kinetics in Transport and Optics of Semiconductors* (Springer, Berlin, 1996).
- <sup>49</sup>R. Zimmermann, K. Kilimann, W. D. Kraeft, D. Kremp, and G. Röpke, Phys. Status Solidi B **90**, 175 (1978).
- <sup>50</sup>W. Schäfer, K. H. Schuldt, and R. Binder, Phys. Status Solidi B **150**, 407 (1988).
- <sup>51</sup>C. Sieh, T. Meier, F. Jahnke, A. Knorr, S. W. Koch, P. Brick, M. Hübner, C. Ell, J. Prineas, G. Kitrova, and H. M. Gibbs, Phys. Rev. Lett. **82**, 3112 (1999).
- <sup>52</sup>V. M. Axt and A. Stahl, Z. Phys. B **93**, 195 (1994); **93**, 205 (1994).
- <sup>53</sup>M. Z. Maialle and L. J. Sham, Phys. Rev. Lett. **73**, 3310 (1994).
- <sup>54</sup>P. Kner, S. Bar-Ad, M. V. Marquezini, D. S. Chemla, and W. Schäfer, Phys. Rev. Lett. **78**, 1319 (1997).
- <sup>55</sup>W. J. Walecki, D. N. Fittinghoff, A. L. Smirl, and R. Trebino, Opt. Lett. **22**, 81 (1997).
- <sup>56</sup>K. W. DeLong, R. Trebino, J. Hunter, and W. E. White, J. Opt. Soc. Am. B **11**, 2206 (1994), and references therein.
- <sup>57</sup>L. Lepetit, G. Chériaux, and M. Joffe, J. Opt. Soc. Am. B **12**, 2467 (1995).
- <sup>58</sup>D. N. Fittinghoff, J. L. Bowie, J. N. Sweetser, R. T. Jennings, M. A. Krumbügel, K. W. DeLong, R. Trebino, and I. A. Walmsey, Opt. Lett. **21**, 884 (1996).
- <sup>59</sup>H. P. Wagner, W. Langbein, and J. M. Hvam, Phys. Rev. B **59**, 4584 (1999).
- <sup>60</sup>Th. Östreich, K. Schönhammer, and L. J. Sham, Phys. Rev. Lett. **74**, 4698 (1995).
- <sup>61</sup>K. B. Ferrio and D. G. Steel, Phys. Rev. Lett. **80**, 786 (1998).
- <sup>62</sup>M. Phillips and H. Wang, Solid State Commun. **111**, 317 (1999).

# Polarization Dynamics and Optical Selection Rules for Excitonic Transitions in Strained Quantum Wells

Scot A. Hawkins, Martin J. Stevens, and Arthur L. Smirl

*Laboratory for Photonics and Quantum Electronics*

*138 IATL, University of Iowa, Iowa City, Iowa 52242*

*Phone: 319-335-3460, FAX: 319-335-3462, art-smirl@uiowa.edu*

**Abstract:** Dual-beam spectral interferometric techniques are used to time-resolve the polarization state of the coherent emission from both intentionally and unintentionally strained GaAs/AlGaAs multiple quantum wells following irradiation with very weak femtosecond pulses. Any anisotropy in the in-plane strain is shown to result in dramatic oscillations in the intensity, the orientation, and the ellipticity of the coherent emission at the heavy-hole light-hole beat frequency. This behavior is shown to be the result of replacing the circularly polarized optical selection rules with elliptically polarized selection rules in the uniaxially strained sample. When only the heavy-hole transition is excited with linearly polarized light, these elliptical selection rules lead to a linearly polarized coherent emission that is rotated with respect to incident orientation. The degree of rotation of the coherent emission as a function of sample orientation is used to quantify the anisotropy in the strain. When the in-plane strain is uniform, no such rotation and no light-hole heavy-hole beats in the polarization state of the coherent emission are observed.

## 1. Introduction

Dephasing processes in semiconductors have been studied in detail in recent years.<sup>1</sup> The circularly polarized optical selection rules (CPOSr) for the heavy-hole (*hh*) and light-hole (*lh*) excitonic transitions have played an essential role in the interpretation of many of these experiments. In addition, it is often impossible to avoid introducing stress and strain into the samples used in these experiments during growth and fabrication.<sup>2</sup> For this reason, it is important to understand and to quantify the effects of stress and strain on the optical selection rules. Here, we describe our use of dual-beam spectral interferometric techniques to time resolve the polarization state of the coherent emission induced by a single ultrashort optical pulse in intentionally and unintentionally strained multiple quantum well (MQW) samples. From the dynamics of the polarization state, we determine whether the sample is uniformly or anisotropically strained in the plane of the wells. For the special case of a uniaxially-strained sample, we demonstrate that the polarization selection rules are elliptical, as expected, and we extract a numerical value for the difference in the strain tensor elements. That is, we quantify the strain.

## 2. Experimental Technique

The two samples used in this study are shown schematically in Fig. 1. The first sample (Fig. 1a) was prepared using a standard procedure that we (and others) routinely use to prepare our samples for four-wave-mixing (FWM) and other nonlinear optical studies.<sup>3</sup> In this case, no strain and no anisotropy were intentionally introduced. In the second sample (Fig. 1b), we intentionally introduced a uniaxial strain. Each sample was prepared from a separate piece of the

same wafer, which consists of ten periods of 14-nm-wide GaAs wells alternating with 17-nm-thick  $\text{Al}_{0.3}\text{Ga}_{0.7}\text{As}$  barriers grown on a (001)-oriented GaAs substrate. The first sample was glued to a BK7 glass window, the GaAs substrate was removed with a selective etch, and an antireflection coating was applied to the top surface. The second sample was processed in a similar manner, except that the sample was bonded to a *b*-cut  $\text{LiTaO}_3$  substrate with the *c*-axis in the plane of the sample along the [110] axis, as shown in Fig. 1b. Measurements (to be described below) were then performed on each sample at 80K. The thermal expansion coefficients<sup>4,5</sup> of GaAs, BK7 and  $\text{LiTaO}_3$  are shown in Table 1. The thermal expansion coefficients of GaAs and the amorphous BK7 glass are close, but not identical. Consequently, the sample in Fig. 1a will be strained, but the strain is expected to be uniform in the plane of the sample. By comparison, the sample in Fig. 1b will experience a net compressive uniaxial strain along the *a*-axis.<sup>6-8</sup>

The polarization state of the coherent emission induced in each of these samples by a single 172 fs pulse from a mode-locked Ti:sapphire laser was measured using a dual-beam spectral interferometer that we have described previously,<sup>3,9,10</sup> as indicated schematically in Fig. 2. For our purposes, we need only recall that this interferometer allows us to time resolve the amplitude, the phase, and the polarization state of the emitted signal. Also, for the measurements to be described in this paper, the incident pulse was always linearly and *x*-polarized, and the sample was rotated by an angle  $\delta$  with respect to the linear polarization of the incident field as shown in Fig. 2b. The notation that we use for the polarization ellipse of the emitted light is shown in Fig. 2c. Here,  $\theta_{\text{sig}}$  designates the orientation of the polarization ellipse and  $\epsilon$  denotes the ellipticity angle, which is determined by the ratio of the minor axis to major axis.

In general, the emission traveling in the direction of the incident pulse will consist of the transmitted portion of the incident pulse, the first-order coherent emission, and higher order contributions to the coherent emission. However, the excitation pulses used in the experiments to be reported here had a fluence of  $\sim 20 \text{ nJ/cm}^2$ , which would produce an estimated areal carrier density of  $\sim 10^8 \text{ cm}^{-2}$  (or  $\sim 10^{14} \text{ cm}^{-3}$ ). Consequently, the coherent emission is weak and is dominated by the first-order term. Unless otherwise stated, the laser was tuned so that both  $hh$  and  $lh$  excitonic transitions were excited.

For the measurements on the uniaxial sample, a second  $\text{LiTaO}_3$  window was attached to the first and rotated by  $90^\circ$ , so that the optical anisotropy from the first substrate would be compensated by the second. Nevertheless, a small residual anisotropy remained after the insertion of the second substrate. This remaining anisotropy was systematically removed by carefully measuring the Jones matrix<sup>11</sup> of the pair of substrates. The latter was accomplished by measuring the output polarizations after transmission through the pair of substrates for four known input polarizations. The Jones matrix was subsequently calculated from three of the known input polarizations and the corresponding measured output polarizations. As a check, the fourth input polarization was then calculated from the measured output polarization using the calculated matrix. Finally, to ensure consistency, this procedure was repeated for all combinations of the known input polarizations.

### 3. Results for the Uniaxial Sample

We discuss the results for the uniaxially strained sample first. The measured spectrum of the copolarized (with respect to the  $x$ -polarized incident field) component ( $I_x(\omega)$ ) of the emission is shown by the solid line in Fig. 3a, and the spectrum of the orthogonally polarized component

( $I_y(\omega)$ ) is shown in Fig. 3b. (The dashed lines are the results of simulations to be discussed below.) For these measurements, the sample was oriented such that the strain axis was at  $45^\circ$  with respect to the incident polarization (i.e.,  $\delta = -45^\circ$  in Fig. 2b). The spectrum of the copolarized signal is identical to that of the incident pulse, except for small dips located at the  $hh$  and  $lh$  resonances, indicating that the copolarized signal is dominated by the transmitted portion of the incident pulse. By contrast, the cross-polarized spectrum consists predominately of emission at the  $lh$  and  $hh$  exciton resonances. The very presence of a distinct cross polarized component to the signal indicates that the sample is anisotropic.<sup>2</sup>

Dual-beam spectral interferometry allows the measurement of the spectral phases as well as the spectral amplitudes (i.e., Fig. 3a and 3b) of the  $x$  and  $y$  components of the signal. The difference ( $\phi_x(\omega) - \phi_y(\omega)$ ) between the phases of the copolarized spectrum and the cross polarized spectrum is shown in Fig. 3c. The copolarized spectral phase,  $\phi_x(\omega)$ , is approximately constant; therefore, the structure evident in Fig. 3c is predominately associated with  $\phi_y(\omega)$ . Notice that the spectral phase difference has no significance, is difficult to obtain, and therefore, is not shown in spectral regions where there is no measurable contribution from either  $I_x(\omega)$  or  $I_y(\omega)$ .

The temporal signals that are obtained by inverse Fourier transformation of the spectral data in Fig. 3 (including the phase information) are shown in Fig. 4. The time resolved copolarized component of the signal (upper solid curve in Fig. 4a) is dominated at early times by a strong peak corresponding to the transmitted portion of the incident pulse. This initial peak is followed by beats associated with the polarization interference between the linear coherent emissions from the  $hh$  and  $lh$  excitons. By comparison, the cross polarized component of the signal (lower solid curve in Fig. 4a) is much weaker, and it exhibits polarization interference beats that are  $180^\circ$  out of phase with those for the parallel component. The temporal phase



difference ( $\phi_x(t) - \phi_y(t)$ ) between the copolarized and cross polarized fields is shown in Fig. 4b, and it too exhibits oscillations at the hh-lh beat frequency. Notice that we show the phase difference only for times after the transmitted pulse has passed. The transmitted portion of the incident pulse is linear and  $x$  polarized, and during the period that it is present, it so dominates the signal that it determines the polarization making the phase difference between it and the crossed component relatively irrelevant and difficult to determine.

It is interesting to note that the data shown in Fig. 3a and Fig. 3b could have been obtained by performing measurements of the  $x$  and  $y$  components of the signal with a spectrometer, and the upper and lower curves in Fig. 4a could have been obtained, for example, by performing a cross correlation measurement between the signal and a reference pulse in a second harmonic crystal. In fact, when Figs. 3a, 3b, and 4a are taken together, they provide similar information to that shown in Fig. 3 of Ref. [2]. The phase information shown in Fig. 3c and Fig. 4b, however, is not provided by these techniques. This information about the relative phases of the copolarized and cross-polarized components is essential if the vectorial dynamics of the coherent first-order emission are to be accurately determined. For example, if one were to assume that the phase difference between the  $x$  and  $y$  components of the field in Fig. 4 is zero, then one would conclude that the emission remains linearly polarized, but that the polarization direction varies in time. However, the time varying amplitudes and phases shown in Fig. 4 suggest a more complicated behavior.

The polarization dynamics are more evident if we plot the data of Fig. 4 in terms of the ellipticity angle  $\varepsilon$  and the azimuthal angle  $\theta_{\text{sig}}$  that determine the polarization ellipse, as we have done in Fig. 5. Clearly both parameters oscillate at the lh-hh beat frequency. The corresponding temporal behavior of the polarization ellipse for one beat period ( $\sim 265$  fs) is shown in Fig. 6 for

selected times. Notice that the orientation of the emission oscillates from  $\sim 0^\circ$  to  $\sim -45^\circ$  and back again each beat period and that the average orientation ( $\sim -25^\circ$ ) is rotated toward the axis of high compressive strain—that is, toward the  $a$ -axis. The ellipticity goes from linear to elliptical and then back to linear twice per beat period. Finally, the sense of rotation changes from clockwise (left circular) to counterclockwise (right circular) each period. This behavior can be understood in terms of the hh-lh mixing associated with the uniaxial strain as described in the next section.

#### 4. Theoretical Model

The effects of the strain can be readily taken into account by writing the Luttinger Hamiltonian for the valence bands for a compression along the  $[1\bar{1}0]$  direction (our  $a$ -axis) and a tension along  $[110]$  (our  $c$ -axis).<sup>6,8,12-14</sup> If the strain is treated as a small perturbation and the split off band is ignored, the strained Hamiltonian for the valence band can be shown to consist of a 4x4 matrix composed of two independent 2x2 matrices.<sup>6,8,12-14</sup> These matrices can be diagonalized to obtain new eigenenergies and eigenfunctions. It is straight forward to show that at the zone center the eigenfunctions of the strained Hamiltonian for the valence band are of the form:

$$|hh\rangle_{\pm} = a_1 \left| \frac{3}{2}, \pm \frac{3}{2} \right\rangle + a_2 \left| \frac{3}{2}, \mp \frac{1}{2} \right\rangle \quad (1)$$

$$|lh\rangle_{\pm} = -a_2 \left| \frac{3}{2}, \pm \frac{3}{2} \right\rangle + a_1 \left| \frac{3}{2}, \mp \frac{1}{2} \right\rangle, \quad (2)$$

where  $|3/2, \pm 3/2\rangle$  and  $|3/2, \pm 1/2\rangle$  denote the doubly degenerate  $hh$  and  $lh$  basis states of the unstrained Hamiltonian,

$$a_1 = \frac{1}{\sqrt{2}} \left( 1 + \sqrt{1 - R^2} \right)^{\frac{1}{2}} \quad (3)$$

and

$$a_2 = \frac{1}{\sqrt{2}} \left( 1 - \sqrt{1 - R^2} \right)^{\frac{1}{2}}, \quad (4)$$

and where for this strain configuration,  $R$  is defined as the ratio

$$R = \frac{d(\epsilon_a - \epsilon_c)}{\Delta}, \quad (5)$$

where  $\epsilon_a$  and  $\epsilon_c$  are the compressive and tensile strains along the  $a$  and  $c$  axes, respectively,  $d$  is the deformation potential appropriate for rhombohedral symmetry, and  $\Delta$  is the hh-lh hole splitting under these deformations. The conduction band states remain parabolic and are denoted here as

$$|e\rangle_{\pm} = \left| \frac{1}{2}, \pm \frac{1}{2} \right\rangle. \quad (6)$$

In the absence of strain or for a uniform in-plane strain, the valence-to-conduction band optical transitions can be shown to obey the CPOSR. For an interaction Hamiltonian of the form  $-\bar{\mu} \cdot \mathbf{E}$  (where  $\mathbf{E}$  denotes the incident field), the nonzero dipole matrix coupling elements are given by

$$\bar{\mu}_{eh}^{(+)} = {}_+ \langle e | \bar{\mu} | hh \rangle_+ = \left\langle \frac{1}{2}, \frac{1}{2} \left| \bar{\mu} \right| \frac{3}{2}, \frac{3}{2} \right\rangle = \mu_{eh}(\hat{\sigma}_-)^* \quad (7)$$

$$\bar{\mu}_{el}^{(+)} = {}_+ \langle e | \bar{\mu} | lh \rangle_+ = \left\langle \frac{1}{2}, \frac{1}{2} \left| \bar{\mu} \right| \frac{3}{2}, -\frac{1}{2} \right\rangle = \mu_{el}(\hat{\sigma}_+)^* \quad (8)$$

$$\bar{\mu}_{eh}^{(-)} = {}_- \langle e | \bar{\mu} | hh \rangle_- = \left\langle \frac{1}{2}, -\frac{1}{2} \left| \bar{\mu} \right| \frac{3}{2}, -\frac{3}{2} \right\rangle = \mu_{eh}(\hat{\sigma}_+)^* \quad (9)$$

$$\bar{\mu}_{el}^{(-)} = {}_- \langle e | \bar{\mu} | lh \rangle_- = \left\langle \frac{1}{2}, -\frac{1}{2} \left| \bar{\mu} \right| \frac{3}{2}, \frac{1}{2} \right\rangle = \mu_{el}(\hat{\sigma}_-)^*, \quad (10)$$

where  $\hat{\sigma}_+ = (\hat{a} + i\hat{c})/\sqrt{2}$  and  $\hat{\sigma}_- = (\hat{a} - i\hat{c})/\sqrt{2}$  are the unit vectors for right and left circularly polarized light, respectively, referenced to the strain axes and where  $\mu_{eh}$  and  $\mu_{el}$  are the  $hh$  and  $lh$  matrix elements for the unstrained system, respectively.

In the presence of an anisotropic in-plane strain, however, one can use Eq. (1) and (2) to show that the mixing of the  $lh$  and  $hh$  valence bands leads to elliptical coupling between the new eigenstates. In this case, the elliptically polarized optical selection rules (EPOSr) are given by

$$\bar{\mu}_{eh}^{(+)} = + \langle e | \bar{\mu} | hh \rangle_+ = \mu_{eh} \left[ a_1 (\hat{\sigma}_-)^* + \frac{a_2}{\sqrt{3}} (\hat{\sigma}_+)^* \right] \quad (11)$$

$$\bar{\mu}_{el}^{(+)} = + \langle e | \bar{\mu} | lh \rangle_+ = \mu_{el} \left[ -\sqrt{3} a_2 (\hat{\sigma}_-)^* + a_1 (\hat{\sigma}_+)^* \right] \quad (12)$$

$$\bar{\mu}_{eh}^{(-)} = - \langle e | \bar{\mu} | hh \rangle_- = \mu_{eh} \left[ a_1 (\hat{\sigma}_+)^* + \frac{a_2}{\sqrt{3}} (\hat{\sigma}_-)^* \right] \quad (13)$$

$$\bar{\mu}_{el}^{(-)} = - \langle e | \bar{\mu} | lh \rangle_- = \mu_{el} \left[ -\sqrt{3} a_2 (\hat{\sigma}_+)^* + a_1 (\hat{\sigma}_-)^* \right]. \quad (14)$$

Notice that in the absence of anisotropic strain,  $a_2=0$  and  $a_1=1$ , and the EPOSr reduce to the CPOSr given by Eq. (7)-Eq. (10). That is, the  $|hh\rangle_+$  valence state is coupled to the  $|e\rangle_-$  conduction state by right circularly polarized light, and the  $|lh\rangle_+$  valence state is coupled to the same  $|e\rangle_+$  conduction state by left circular light. By comparison, the  $|hh\rangle_-$  valence state is coupled to the  $|e\rangle_-$  conduction state by left circularly polarized light, and the  $|lh\rangle_-$  valence state is coupled to the  $|e\rangle_+$  conduction state by right circular light. In this case there is no preferred direction for absorption. In the presence of uniaxial strain, the  $lh$  and  $hh$  wavefunctions are mixed so that the selection rules become elliptical, with the major axis of the  $hh$  ellipse aligned along the compressive strain axis (i.e., parallel to  $\hat{a}$ ) and the  $lh$  perpendicular to this axis (i.e., parallel to  $\hat{c}$ ). In other words, the  $hh$  matrix element is increased along the compression axis and decreased along the tension axis. In contrast, the  $lh$  transition strength is increased along the tension axis

and decreased along the compression axis. Oscillator strength is conserved through  $|a_1|^2 + |a_2|^2 = 1$ .

When the incident radiation is resonant with the excitonic transitions, the linear absorption of this system is most easily calculated by representing the  $hh$  and  $lh$  excitonic transitions by two independent three level systems obeying the selection rules given by Eqs. (11)-(14) as depicted schematically in Fig. 7. A first-order perturbative solution to the density matrix equations for these two systems in response to a delta function excitation pulse gives

$$\begin{pmatrix} \mathcal{P}_{co} \\ \mathcal{P}_{cross} \end{pmatrix} \propto \left( \frac{i\mu_{eh}^2}{\hbar} \right) \mathcal{E} \theta(t) e^{-\gamma t} \left\{ \left[ (a_1^2 + a_2^2/3) + (a_2^2 + a_1^2/3) e^{-i\Omega t} \right] \begin{pmatrix} \hat{x} \\ 0\hat{y} \end{pmatrix} + \frac{2a_1a_2}{\sqrt{3}} [1 - e^{-i\Omega t}] \begin{pmatrix} \cos 2\delta \hat{x} \\ \sin 2\delta \hat{y} \end{pmatrix} \right\} \quad (15)$$

for the copolarized,  $\mathcal{P}_{co}$ , and cross polarized,  $\mathcal{P}_{cross}$ , components of the emission, where  $\gamma$  is the exciton dephasing rate (for the moment, assumed to be the same for both  $hh$  and  $lh$ ),  $\Omega$  is the  $hh$ - $lh$  splitting,  $\mathcal{E}$  is the incident field amplitude,  $\theta(t)$  is the Heaviside step function, and  $\delta$  is the angle between the compressive strain axis and the incident linear polarization. We will use this expression to guide our qualitative discussions in the following sections.

## 5. Extraction of Strain Parameters

The polarization state of the coherent emission as given by Eq. (15) clearly depends upon sample orientation, and we can use this orientational dependence to quantify the strain. For these measurements, the laser was tuned so that we excited only the  $hh$  transitions. Note that when only the  $hh$  excitons are excited, Eq. 15 is simplified by the elimination of all terms multiplied by  $\exp(-i\Omega t)$ :

$$\begin{pmatrix} \mathcal{P}_{co} \\ \mathcal{P}_{cross} \end{pmatrix} \propto \left( \frac{i\mu_{eh}^2}{\hbar} \right) \mathcal{E}\theta(t)e^{-\gamma} \left\{ (a_1^2 + a_2^2/3) \begin{pmatrix} \hat{x} \\ 0\hat{y} \end{pmatrix} + \frac{2a_1a_2}{\sqrt{3}} \begin{pmatrix} \cos 2\delta \hat{x} \\ \sin 2\delta \hat{y} \end{pmatrix} \right\}. \quad (16)$$

The *time-integrated* intensity and the *time-averaged* orientation and ellipticity of the emitted first-order field as a function of the orientation of the sample are shown in Fig. 8 when only the *hh* is excited. These time-averaged parameters were obtained by gating the time-resolved emission to remove the contributions of the transmitted pulse in the following way. We first time resolved the *x* and *y* components of the intensity and the phase, as described in our discussions surrounding Fig. 3 and Fig. 4. For convenience, we then expressed this data in terms of the time resolved Stokes parameters,<sup>11</sup> and we numerically integrated the time-resolved Stokes parameters beginning at a time of roughly 400 fs after the pump pulse. Finally, we converted the time-integrated Stokes parameters to time averaged values for the ellipticity and the orientation. This procedure was repeated for each sample orientation. In this way, we were able to eliminate the effects of the transmitted pump pulse (and the reflection from the second substrate that we describe below) and were able to average over the first-order emission only.

Several features in Fig. 8 are worth noting. First, in agreement with Eq. 16, the emission is in general rotated, but linearly polarized (i.e.,  $\varepsilon \approx 0$ ) for all sample orientations. The total emission is strongest when the incident polarization is parallel to the compressive strain axis ( $\delta=0$ ), and it decreases with angle until the polarization is along the tensile strain axes ( $\delta=90^\circ$ ). When the incident polarization is along one of these axes, there is no cross polarized component, and the emission is *x*-polarized. However, when the incident polarization is not oriented along either of these axes, the emission is rotated towards the compressive strain axis.

The dashed curves in Fig. 8 are the results of simulations based on Eq. (16) and on the elliptical selection rules given by Eqs. (11)-(14). From such fits, we are able to extract a value of

$a_2=0.353\pm0.004$ . Using this value for  $a_2$  in Eq. (4) and Eq. (5), we can estimate the net compressive strain to be  $\epsilon_a-\epsilon_c=-2.3\times10^{-3}$ . In making this estimate, we have used the measured hh-lh splitting of  $\Delta=15.6$  meV and taken  $d=-4.55$  eV.<sup>15</sup>

Numerical simulations using finite pulses (172 fs, full width at half maximum of the intensity), the elliptical selection rules given by Eq. (11)-(14), and  $a_2=0.353$  are shown by the dashed curves in Figs. 3-6. For these simulations, we assumed that the pulses were tuned 8.1 meV above the hh transition, in agreement with the experimental detuning. Clearly, all of the key features in the data are accurately reproduced by these simulations. One exception is the disagreement between simulation and experiment near 260 fs, which is particularly evident in Fig. 4. The anomalous experimental behavior at this time has been identified as a reflection from the interface between the crossed LiTaO<sub>3</sub> windows, and it has the same polarization as the incident pulse. This reflection makes it difficult to extract the correct intensity and phase of the co-polarized emission in this temporal region. One final remark concerning the simulations is that, in order to correctly account for the decay of the oscillations in  $\epsilon$  and  $\theta_{\text{sig}}$  (see Fig. 5), it was necessary to take the dephasing rate for the  $lh$  to be slightly larger than the  $hh$ . We offer no justification for this ansatz.

## 6. Results for the Uniformly Strained Sample

Finally, in Fig. 9a, we show the emission that is copolarized and cross polarized to the incident field as a function of time for the conventionally-prepared sample mounted on the amorphous glass substrate when both  $hh$  and  $lh$  are excited. The spectra for the parallel and orthogonal intensities are also shown (Fig. 9b). As in Fig. 4, the copolarized component of the time-resolved signal is dominated by a peak corresponding to the transmitted portion of the

incident pulse, and this peak is followed by beats associated with the polarization interference between the linear coherent emission from the  $hh$  and  $lh$  excitons. In contrast to the uniaxial measurements, however, the orthogonal signal and spectrum are in every respect identical to the parallel signals, except that they are reduced in magnitude by  $4 \times 10^{-6}$ , which is equal to the measured leakage of our analyzer. Thus, to within the accuracy of our measurements the light from this sample is linearly and  $x$ -polarized. This result is independent of sample orientation. This confirms the validity of the CPOSR and confirms that the processing used to mount the sample has introduced no measurable anisotropy.

## 7. Summary and Conclusions

Time resolving the polarization state of the coherent emission induced by weak ultrashort pulses from these two MQW samples has allowed us to characterize the in-plane anisotropic strain present in the samples. Our intentionally uniaxially-strained sample, mounted on  $\text{LiTaO}_3$ , shows clear evidence of anisotropy. From measurements of the time-integrated polarization state of the  $hh$  emission as a function of sample orientation, the  $hh$ - $lh$  valence-band mixing parameters have been determined. By comparison, our conventional sample mounted on BK7 glass, shows no sign of anisotropic strain, validating the use of the circular polarization optical selection rules in describing the coherent emission from this sample. Finally, as a note of caution, it should be pointed out that, in contrast to our results using amorphous substrates and our mounting procedures, another group<sup>2</sup> has investigated samples glued to sapphire substrates and has found evidence of a small, but detectable, strain-induced anisotropy. While these effects<sup>2</sup> were small, nevertheless, the validity of the CPOSR may depend upon the manner in which the sample is prepared and mounted and upon the sensitivity of the measurements to any anisotropy present.



## 8. Acknowledgements

The authors gratefully acknowledge numerous insightful conversations with Rolf Binder and Eric Gansen. This research was supported in part by the U. S. Army Research Office and the Office of Naval Research.

## References

1. J. Shah, *Ultrafast Spectroscopy of Semiconductors and Semiconductor Nanostructures*, Second Edition, Springer-Verlag, New York, 1999, and references therein.
2. N. H. Bonadeo, D. G. Steel, and R. Merlin, *Phys. Rev. B* **60** 8970 (1999).
3. A. L. Smirl, in *Ultrafast Phenomena in Semiconductors*, edited by K.-T. Tsen (Springer-Verlag, New York, 2001), pp. 443-507 and references therein.
4. Y. Lu, H. C. Kuo, et al., *Mat. Res. Soc. Symp. Proc.* **300**, 537 (1993).
5. Melles Griot Catalog 2000.
6. H. Shen, M. Wraback, J. Pamulapati, P. G. Newman, M. Dutta, Y. Lu and H. C. Kuo, *Phys. Rev. B* **47**, 13933 (1993).
7. M. F. Huang, E. Garmire, A. Partovi and M. Hong, *Appl. Phys. Lett.* **66**, 736 (1995).
8. M.-F. Huang, E. Garmire, Y.-K. Kuo, *Jpn. J. Appl. Phys.* **39**, 1776 (2000).
9. W. J. Walecki, D. N. Fittinghoff, A. L. Smirl, R. Trebino, *Opt. Lett.* **22**, 81 (1997).
10. A. L. Smirl, X. Chen, O. Buccafusca, *IEEE J. Quantum Electron.* **35**, 523 (1999).

11. R. M. A. Azzam and N. M. Bashara, *Ellipsometry and polarized light* (North-Holland, Amsterdam, 1977), Chap. 3.
12. F. H. Pollak, in *Strained-Layer Superlattices: Physics, Semiconductors and Semimetals* Vol. 32, edited by T. T. Pearsall (Academic, New York, 1990), pp.17-53.
13. F. H. Pollak and M. Cardona, *Phys. Rev.* 172, 816 (1968).
14. R. Binder, *Phys. Rev. Lett.* **78**, 4466 (1997).
15. S. Adachi, *J. Appl. Phys.* **53**, 8775 (1985).

**Table 1.** The thermal expansion coefficients of the sample and windows at room temperature.

Material	Thermal Expansion Coefficient $\times 10^{-6}/^{\circ}\text{C}$	Reference
GaAs	6.15	[4]
BK7 glass	7.1	[5]
LiTaO <sub>3</sub> (along a)	16.2	[4]
LiTaO <sub>3</sub> (along c)	4.1	[4]

**Figure Captions:**

Fig. 1. Schematic drawing of (a) the uniformly strained and (b) the uniaxially strained samples.

Fig 2. (a) The experimental geometry for time-resolving the polarization state of transmitted and coherently emitted light using dual-beam spectral interferometry. Schematic drawings showing (b) the orientation of the sample relative to the incident  $x$ -polarized radiation and (c) the notation used to describe the polarization ellipse associated with the transmitted and emitted radiation.

Fig. 3. The spectrally-resolved emission from the uniaxially strained sample when the sample was rotated to  $\delta=-45^\circ$  and when both the  $hh$  and  $lh$  excitonic transitions were excited: (a) the  $x$  component,  $I_x(\omega)$ , and (b) the  $y$  component,  $I_y(\omega)$ , of the intensity (in arbitrary units) and (c) the spectral phase difference  $\phi_x(\omega)-\phi_y(\omega)$  (in degrees) between the  $x$  and  $y$  components of the field. Notice that the  $y$  component of the intensity has been multiplied by a factor of 82 for comparison on the same scale as the  $x$  component. The solid lines are data, and the dashed curves are the results of simulations described in the text.

Fig. 4. The temporally-resolved emission from the uniaxially strained sample when the sample was rotated to  $\delta=-45^\circ$  and when both the  $hh$  and  $lh$  excitonic transitions were excited: (a) the  $x$  component,  $I_x(t)$ , and the  $y$  component,  $I_y(t)$ , of the intensity (upper and lower curves, respectively, in arbitrary units) and (b) the temporal phase difference  $\phi_x(t)-\phi_y(t)$  (in degrees) between the  $x$  and  $y$  components of the field. The solid lines are data, and the dashed curves are the results of simulations described in the text.

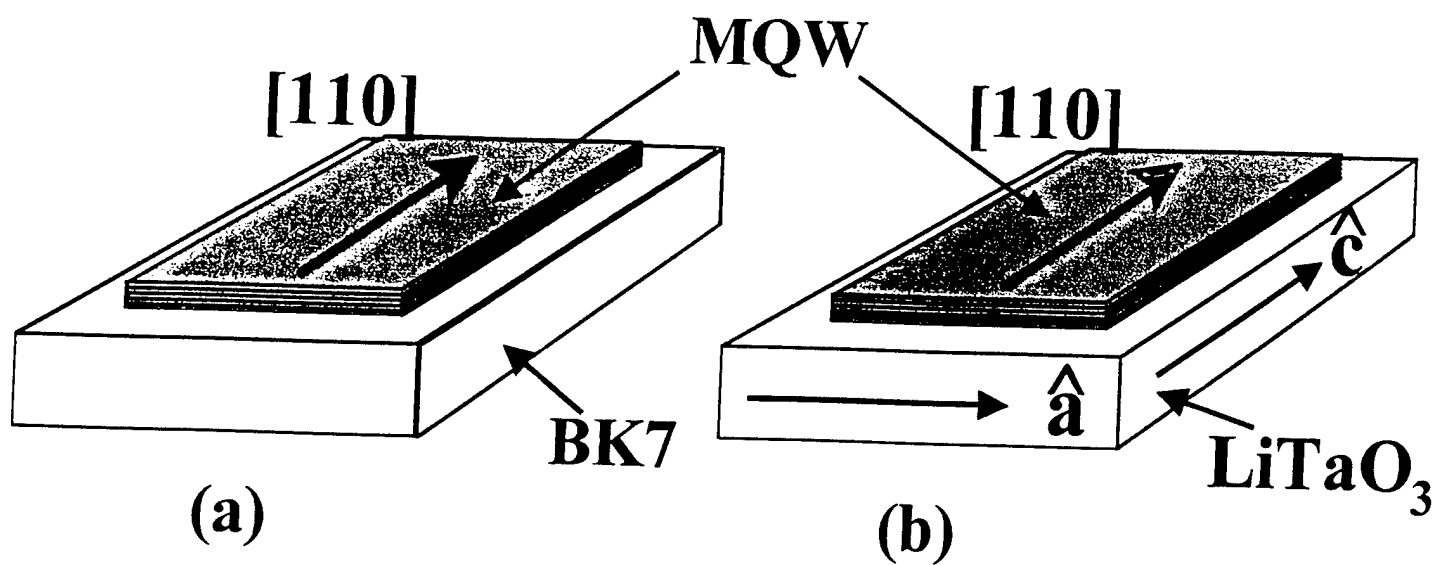
Fig. 5. The time-resolved polarization state for the emission from the uniaxially strained sample when the sample was rotated to  $\delta = -45^\circ$  and when both the  $hh$  and  $lh$  excitonic transitions were excited: (a) the orientation of the polarization ellipse  $\theta_{sig}(t)$  and (b) its ellipticity  $\varepsilon(t)$  in degrees. The solid lines are data, and the dashed curves are the results of simulations described in the text.

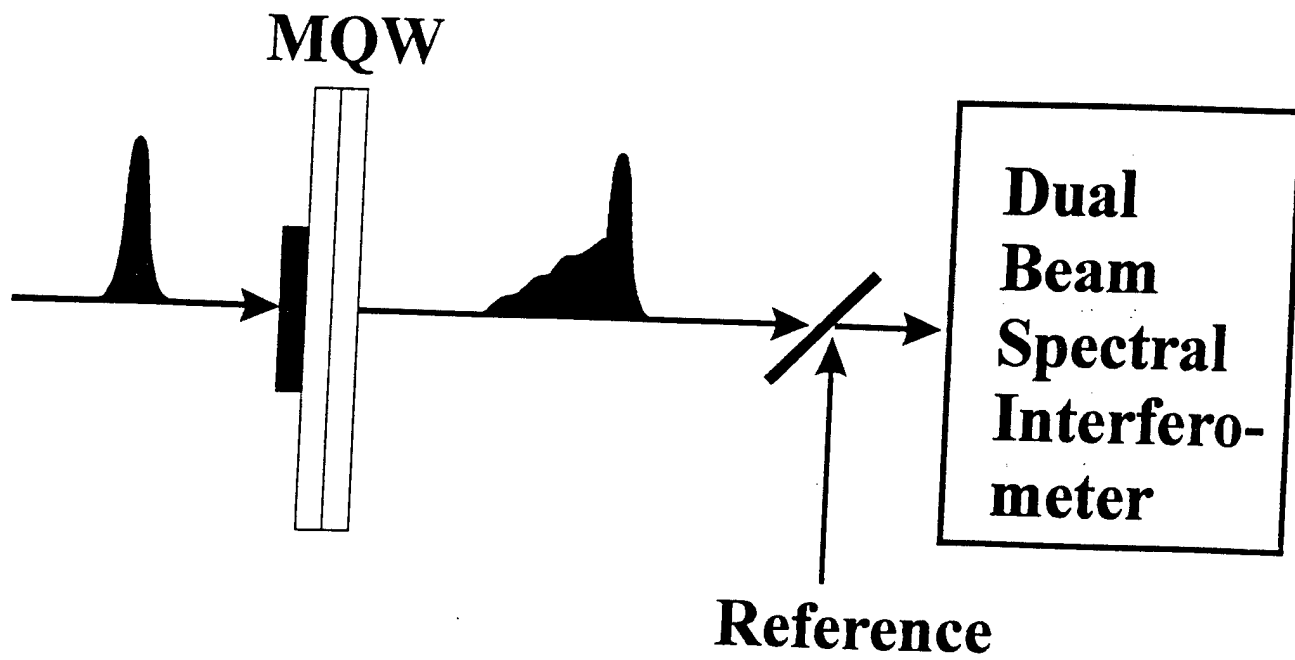
Fig. 6. Sketches of the polarization ellipse at selected times during a single oscillation period corresponding to the data in Fig. 5.

Fig. 7. The energy level diagram used to model the  $hh$  and  $lh$  excitonic transitions. The matrix elements and eigenstates are given in the text.

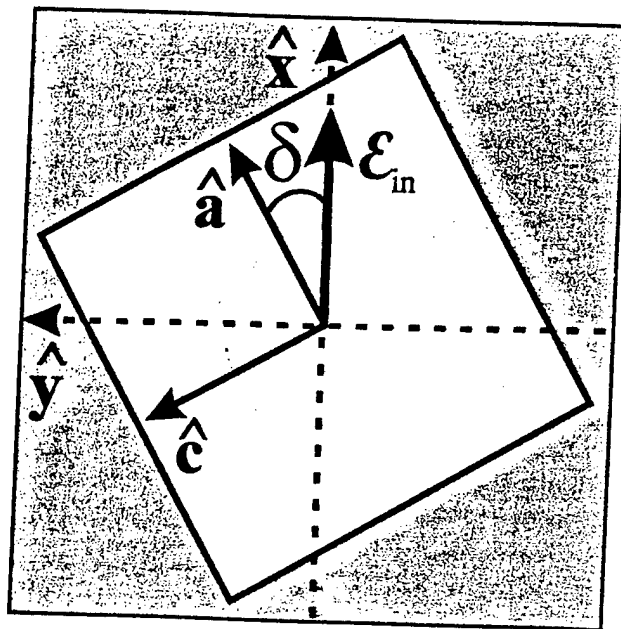
Fig. 8. The gated, time-averaged polarization state for the emission from the uniaxially strained sample as a function of sample orientation when only the  $hh$  excitonic transition was excited: (a) the total intensity (in arbitrary, but relative units), (b) the orientation of the polarization ellipse  $\theta_{sig}$ , and (c) the ellipticity angle  $\varepsilon$ . The solid lines are data, and the dashed curves are the results of simulations described in the text.

Fig. 9. The (a) temporally-resolved and (b) spectrally-resolved  $x$  component (solid) and  $y$  component (dashed) of the emitted intensity from the uniformly strained sample when both the  $hh$  and  $lh$  excitonic transitions were excited. Notice that the  $y$  component of the intensity has been multiplied by a factor of  $2.5 \times 10^5$  for comparison on the same scale as the  $x$  component. This result was independent of sample orientation.

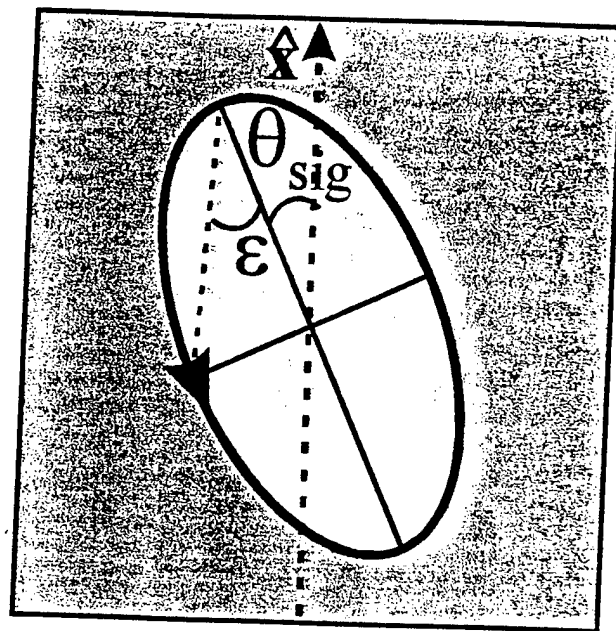




(a)

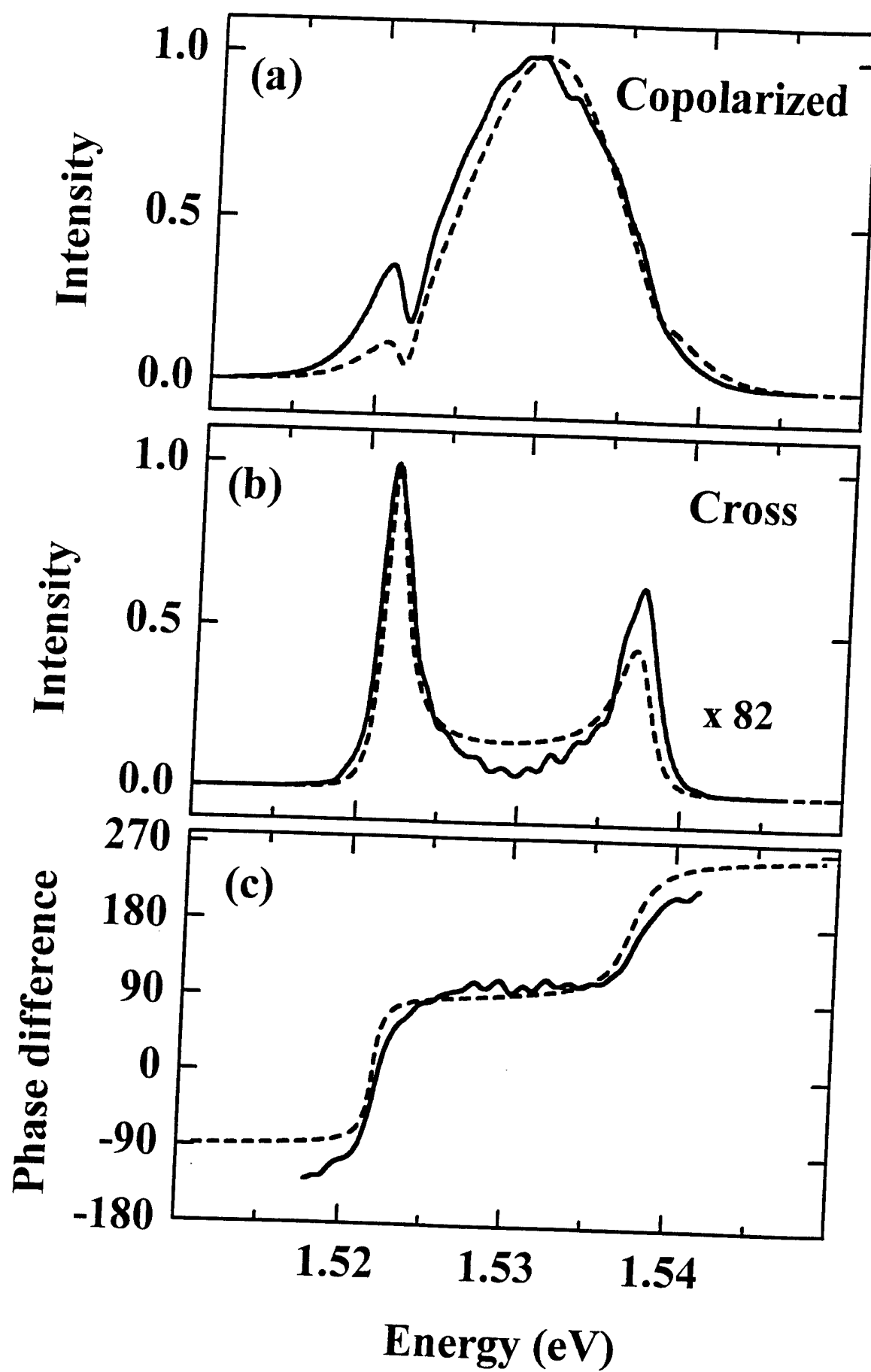


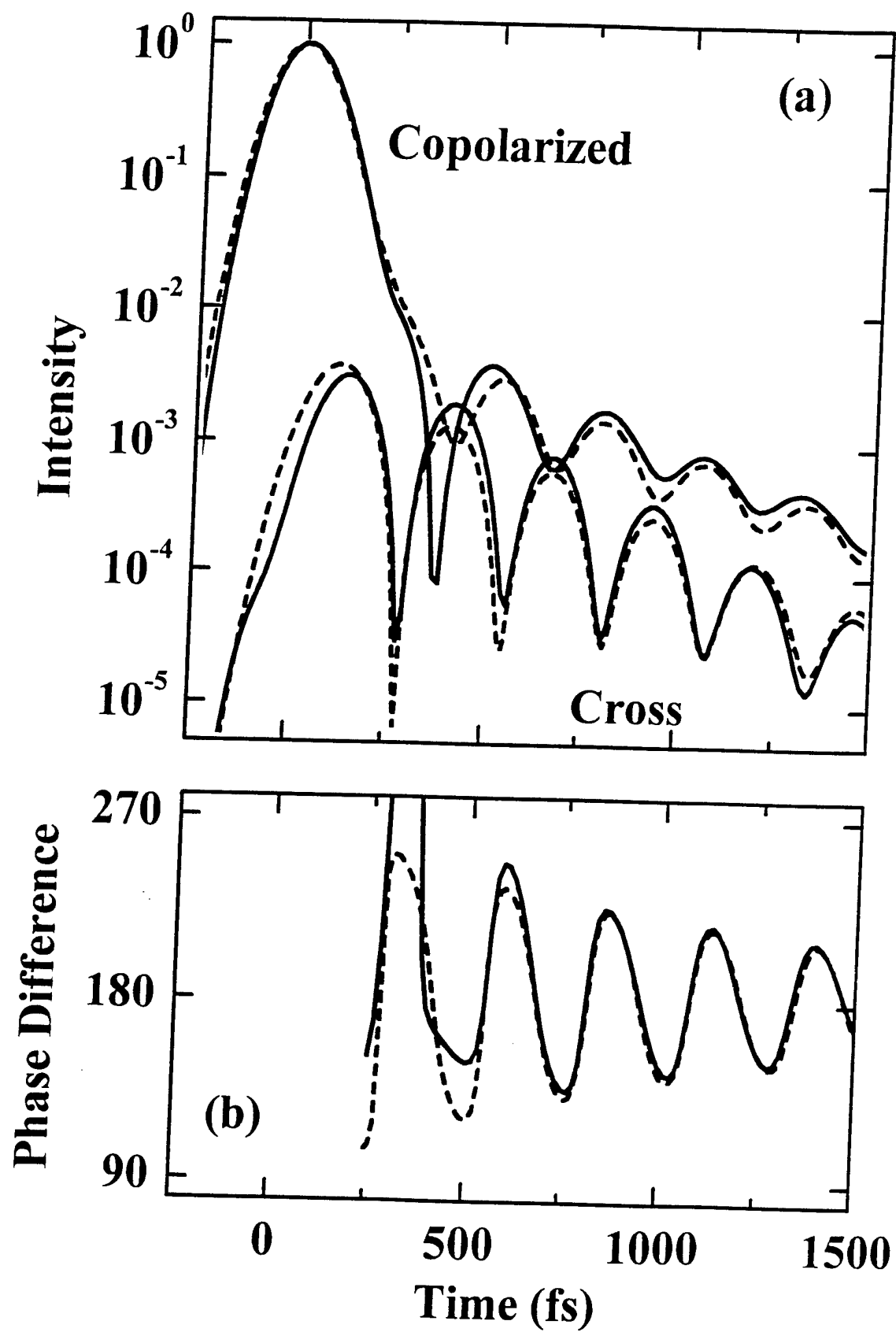
(b)

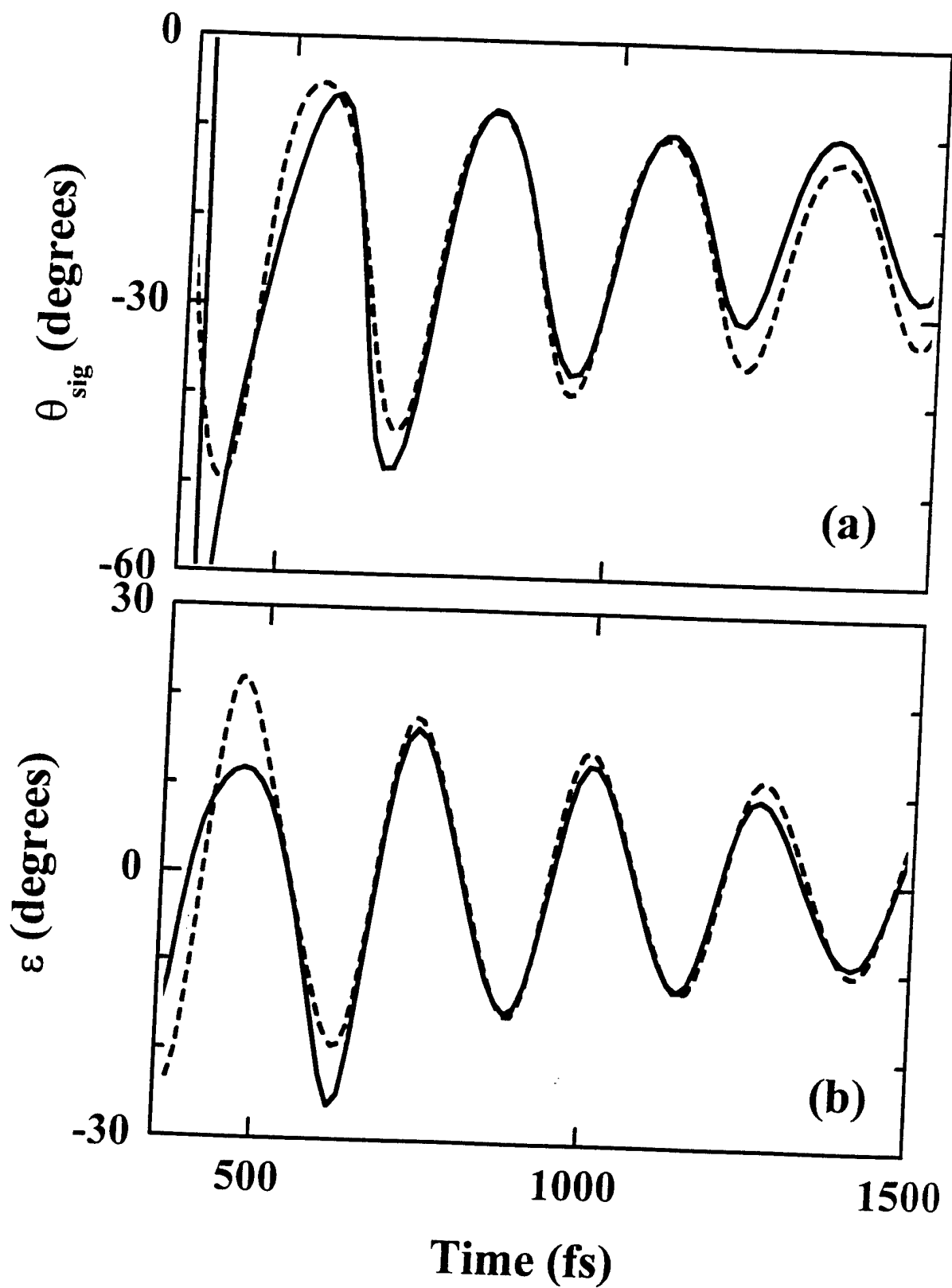


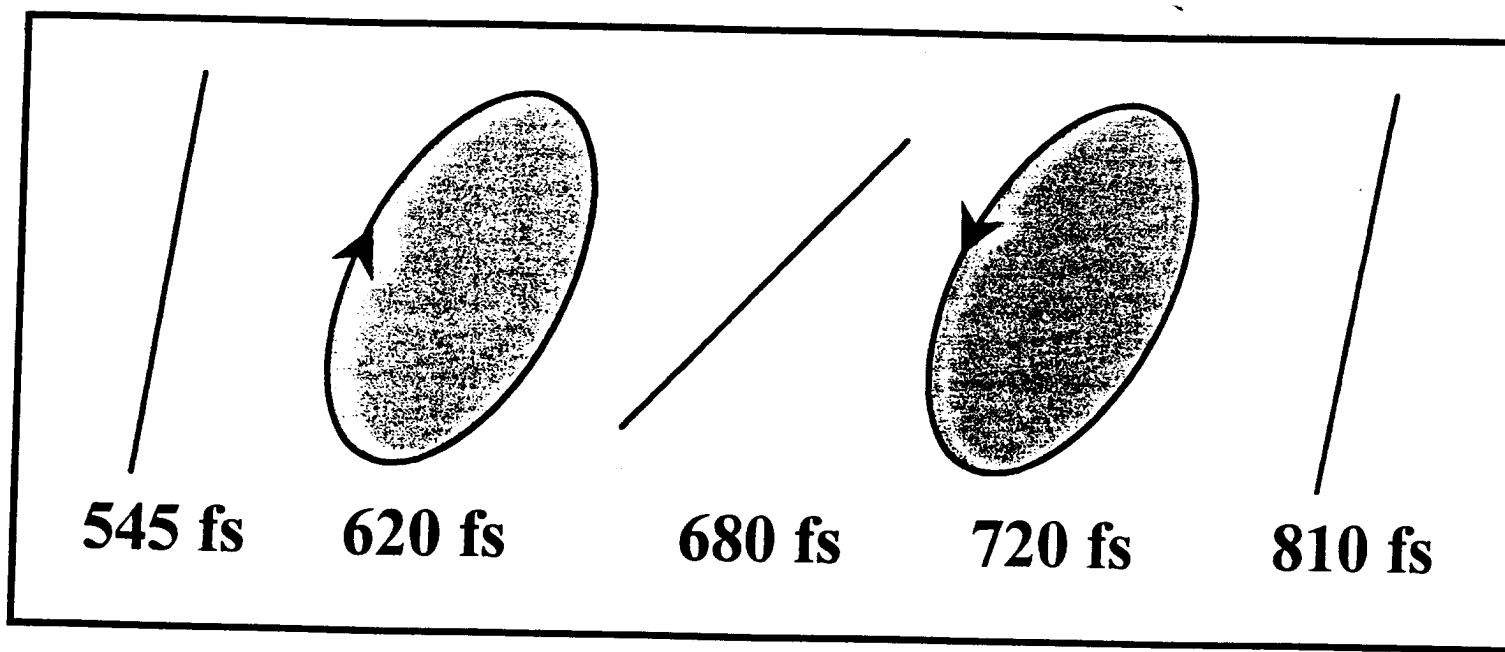
(c)

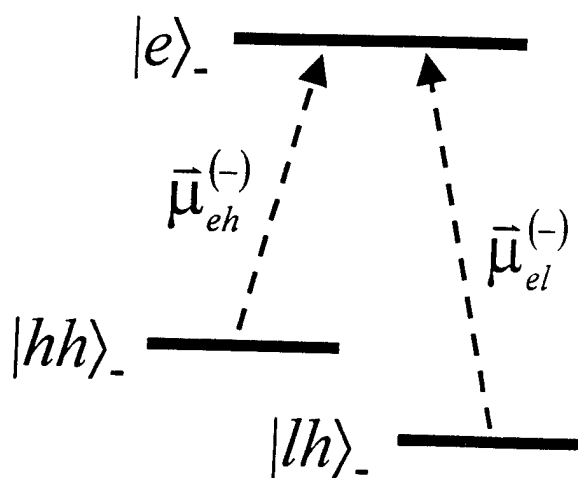
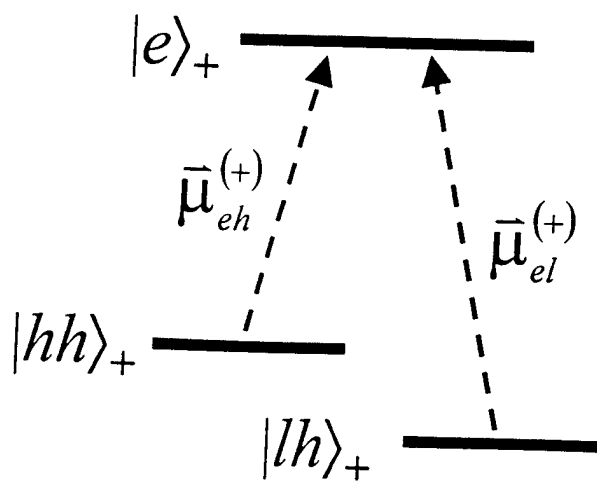


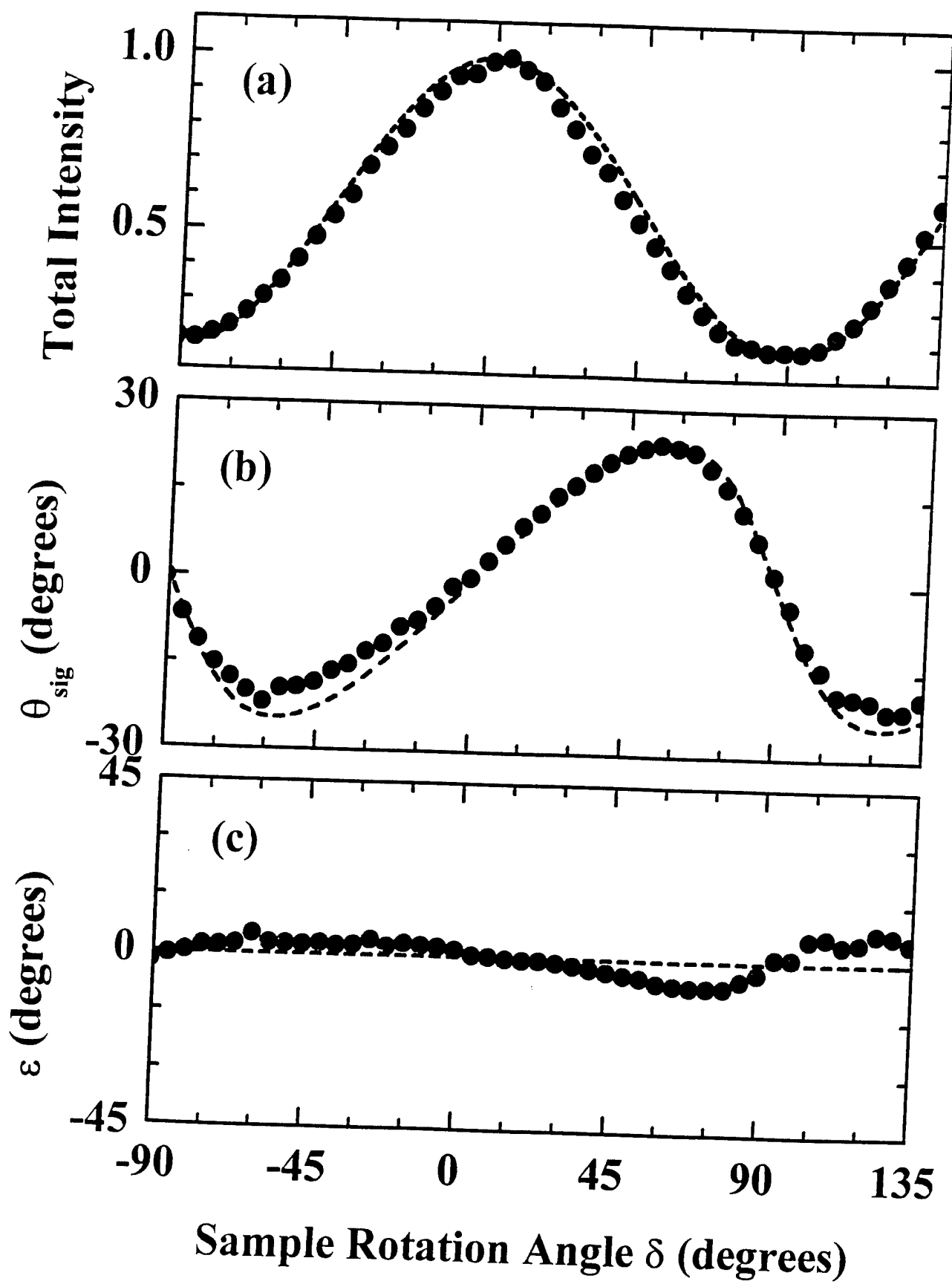


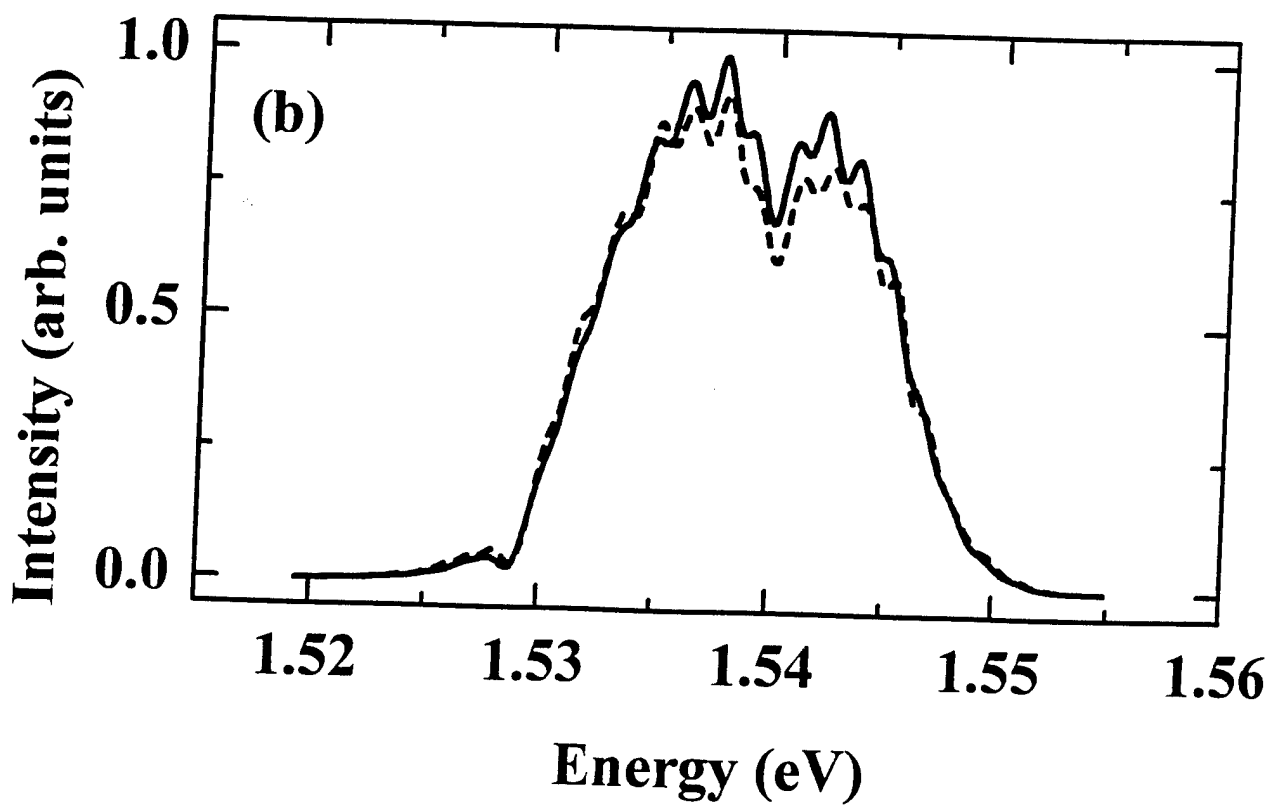
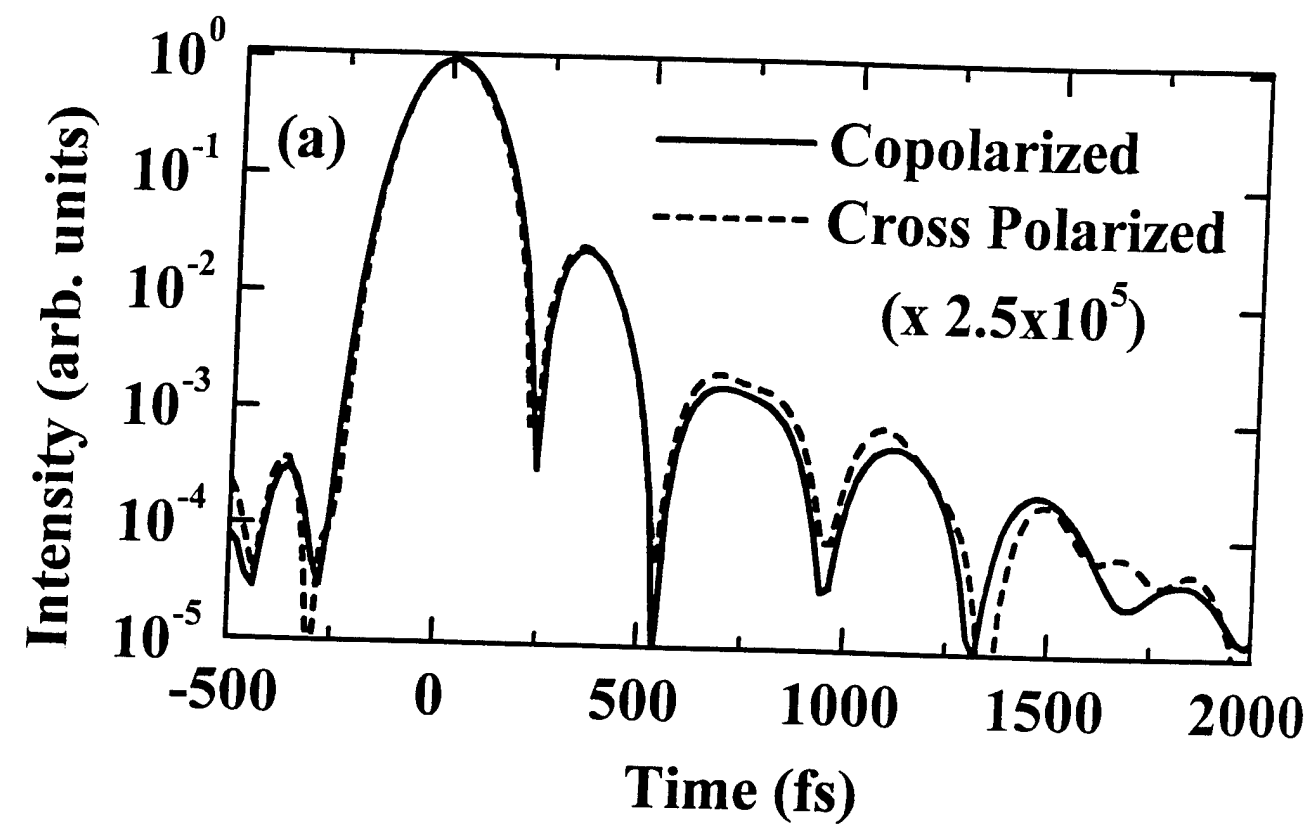












# Differential measurements of dipole and Raman coherences and of exciton-exciton interactions in quantum wells

Martin J. Stevens, Eric J. Gansen, Scot A. Hawkins, K. Jarasiunas, and Arthur L. Smirl  
*Laboratory for Photonics & Quantum Electronics, 138 IATL, University of Iowa, Iowa City,  
Iowa 52242*

*Phone: 319-335-3460, FAX: 319-335-3462, art-smirl@uiowa.edu*

**D. G. Steel**

*H. M. Randall Laboratory of Physics, University of Michigan, Ann Arbor, Michigan  
Phone: 734-764-4469, FAX: 734-763-9694, dst@eecs.umich.edu*

**Abstract:** Quantum beats involving the light-hole and heavy-hole excitons in GaAs quantum wells are studied using both conventional and novel temporally-gated differential detection techniques. The contributions of the conduction-to-valence band coherence are separated from those of the intervalence band coherence, and the contributions of the cumulative exciton-exciton correlations are identified by monitoring the signal in the unconventional probe direction and by taking advantage of the polarization selection rules for the excitonic transitions.



## I. INTRODUCTION

When excitons of different energies are excited in semiconductors and multiple quantum wells (MQWs), the coherent superposition of electronic states produces oscillations (or quantum beats) in the third-order nonlinear optical emission. Such beats have been observed, for example, between light-hole (*lh*) and heavy-hole (*hh*) excitons.<sup>1-8</sup> In order for quantum beats (as opposed to polarization interference) to be produced, the *hh* and *lh* excitons must be coupled in some way. If the two excited oscillators share a common energy level, then that level can provide the necessary coupling. However, recent experimental and theoretical work has demonstrated that the *lh-hh* excitonic coupling necessary for *lh-hh* quantum beating also can be produced by the many-body Coulomb interactions between excitons.<sup>9-11</sup> As we will discuss below, some of these Coulomb correlations (e.g. biexciton formation<sup>12-19</sup>) are established on a time scale that is rapid compared to the pulsewidths used here and can be regarded as instantaneous. By comparison, others [e.g. excitation-induced dephasing (EID)<sup>20-23</sup>] are initially weak, but they continue to act and to build-up over time; hence, they can be regarded as cumulative.

In this work, we investigate these *hh* and *lh* correlations by using a novel temporally-gated differential technique in concert with a conventional technique to measure the time-integrated quantum beats (TI-QBs) in the ultrafast coherent third-order emission from excitons in GaAs/AlGaAs quantum wells. We demonstrate that, when the emitted signal is measured in the probe direction, the conventional technique approximately samples the third-order nonlinear polarization at its initial value (for optically thin samples), and as a consequence, tends to suppress the contributions of the *cumulative* many-body correlations to the emission. By contrast, the *gated* differential technique (described below) yields a signal that integrates over the emission time of the third-order nonlinear polarization, and therefore, this signal is dominated by these cumulative correlations between *hh* and *lh* excitons.

We then show that these two complementary techniques can be used together with the polarization selection rules for the *hh* and *lh* excitonic transitions to isolate the contributions of the higher-order cumulative coupling between the excitons and to separately measure the conduction-to-valence band (interband) coherence and the coherence between the *hh* and *lh* valence bands (intervalence band coherence). These correlations go beyond those provided local field corrections (LFC) or by the Semiconductor Bloch Equations in the Hartree-Fock approximation, and they can not be attributed to biexciton formation. Consequently, these results provide further evidence<sup>9,24-28</sup> of the contributions of cumulative four-particle (in the  $\chi^{(3)}$  limit<sup>29,30</sup>) correlations to the coherent response.

## II. DIFFERENTIAL MEASUREMENT TECHNIQUES

Both geometries for measuring the time-integrated differential signal are shown in Fig. 1 and are essentially identical to that used for simple pump-and-probe experiments. In each case, a  $\sim 150$  fs pulse from a mode-locked Ti:sapphire laser (not shown) is divided into two parts: a pumping pulse (with field  $\mathcal{E}_1$  and propagation wavevector  $\mathbf{k}_1$ ) and a weaker probing pulse (with field  $\mathcal{E}_2$  and wavevector  $\mathbf{k}_2$ ). The two pulses are spatially overlapped in the sample with a variable time delay  $\tau_{21} = t_2 - t_1$  between them.

Each of the two types of measurements to be described here was performed on a separate sample prepared from a single multiple quantum well (MQW) wafer. This is the same wafer that was used in many of our previous studies.<sup>6-8,10,31-35</sup> That wafer consists of 10 periods of 14-nm-wide GaAs wells separated by 17-nm-wide  $\text{Al}_{0.3}\text{Ga}_{0.7}\text{As}$  barriers. Each sample was processed by mounting it onto a glass flat, by removing the substrate with a selective etch to permit transmission measurements, and by applying an antireflection coating to the exposed semiconductor-air interface to reduce Fabry-Perot effects. The measurements reported here were performed at 80 K to ensure that the exciton was homogeneously broadened. At this temperature, the  $hh$  exciton for each sample has a linewidth of  $\sim 1.3$  meV. The splitting between the  $hh$  and  $lh$  excitons is 11.3 meV for one sample, and 12.1 meV for the other. All of the conventional measurements (Fig. 1a) were performed with the 11.3 meV sample, and the gated measurements (Fig. 1b) with the 12.1 meV sample. This difference in the  $hh$ - $lh$  splittings is the only measurable distinction between the two samples that we have observed, and it is most likely the result of differing uniform in-plane strains introduced when the samples are cooled. This strain is caused by the differing thermal expansion coefficients of the materials that form the semiconductor-glass interfaces. It should be emphasized that neither sample exhibits any measurable in-plane anisotropy in its linear or nonlinear optical properties. Therefore, we conclude that the strain introduced by mounting and cooling is uniform in the plane of the wells. For all measurements, the spectrum of the 150 fs pulses was tuned so that both  $hh$  and  $lh$  excitonic transitions were excited, as shown in Fig. 1c, and at the fluence used here ( $1 \mu\text{J}/\text{cm}^2$ ), we estimate the  $hh$  areal density to be  $\sim 4 \times 10^9 \text{ cm}^{-2}$  (corresponding to  $\sim 3 \times 10^{15} \text{ cm}^{-3}$ ).

The conventional differential signal ( $DS$ ) is obtained by subtracting the time-integrated signal without the pump present from the signal with the pump present at each time delay. As shown in Fig. 1a, this difference is usually obtained by modulating each of the incident beams with a mechanical chopper and by synchronously detecting the signal in the  $\mathbf{k}_2$ -direction as a function of time delay at the difference frequency using a lock-in amplifier. In this case, in the weak saturation limit, the  $DS$  is proportional to:

$$DS \cong DS_1 + DS_2 = \left( \frac{c\epsilon_0}{2} \right) \left\{ \int_{-\infty}^{+\infty} dt (\mathcal{E}_2^*(t) \cdot \mathcal{E}^{(3)}(\mathbf{k}_2, \tau_{21}, t) + c.c.) + \int_{-\infty}^{+\infty} dt (\mathcal{E}^{(1)*}(\mathbf{k}_2, t) \cdot \mathcal{E}^{(3)}(\mathbf{k}_2, \tau_{21}, t) + c.c.) \right\} \quad (1)$$

where  $c$  and  $\epsilon_0$  are the speed of light and the dielectric constant, respectively, and where  $\mathcal{E}^{(1)}(\mathbf{k}_2)$ , and  $\mathcal{E}^{(3)}(\mathbf{k}_2)$  are the slowly varying envelopes of the first-order and third-order fields traveling in the  $\mathbf{k}_2$ -direction, respectively. For an optically-thin sample, these fields are related to the corresponding first-order and third-order polarizations by  $\mathcal{E}^{(1)}(\mathbf{k}_2) \cong (ikl/2\epsilon_0)\mathcal{P}^{(1)}(\mathbf{k}_2)$  and  $\mathcal{E}^{(3)}(\mathbf{k}_2) \cong (ikl/2\epsilon_0)\mathcal{P}^{(3)}(\mathbf{k}_2)$ , where  $k$  and  $l$  are the magnitude of the propagation vector and the thickness of the MQW's, respectively. Finally,  $\mathcal{E}_2$  is the envelope of the probe field. (We emphasize that in writing Eq. (1) we have assumed that the effects of phase-space filling are small (i.e.  $\mathcal{P}^{(1)} \gg \mathcal{P}^{(3)}$ ). If this is not the case, then terms of the order  $\mathcal{P}^{(1)}\mathcal{P}^{(5)}$  and  $|\mathcal{P}^{(3)}|^2$  must be taken into account.)

The first term  $DS_1$  integrates over the product of the transmitted probe,  $\mathcal{E}_2$ , and the third order polarization,  $\mathcal{P}^{(3)}$ , and the second term,  $DS_2$  integrates over the product of the first-order polarization  $\mathcal{P}^{(1)}$  and the third-order polarization  $\mathcal{P}^{(3)}$ . If the probe is short compared to all other time scales of interest (i.e., it acts as a delta function in Eq. (1)), the first term essentially samples the third-order polarization  $\mathcal{P}^{(3)}$  at  $t=0$ . By contrast, the second term integrates over the third-

order coherent emission. In addition, for optically thin samples,  $\mathcal{E}_2$  will be much larger than  $\mathcal{E}^{(1)}$ , and hence, the first term will dominate the second in conventional DS measurements under these conditions.

The first term in Eq. (1) can be eliminated, allowing the measurement of the weaker second term by using a gated version of differential spectroscopy conceptually illustrated in Fig. 1b. Initially, the probe signals (with and without the pump present) are independently time resolved for each time delay. We used dual-beam spectral interferometric techniques, which completely determine the amplitude, phase and vectorial dynamics of the coherent emission and which we have described previously,<sup>7,8,10,34-36</sup> but any technique that time-resolves the intensity will suffice for the measurements described here. Next, the time-resolved intensity without the pump is subtracted from the intensity with the pump, and the difference is integrated beginning at a time *shortly after* the end of the probe in order to eliminate the first term in Eq. (1):

$$TGDS \cong \left( \frac{c\mathcal{E}_0}{2} \right) \left\{ \int_{-\tau}^{+\infty} dt \left( \mathcal{E}^{(1)*}(\mathbf{k}_2, t) \cdot \mathcal{E}^{(3)}(\mathbf{k}_2, \tau_{21}, t) + c.c. \right) \right\} \cong DS_2 \quad (2)$$

where  $\tau$  is the full-width at half-maximum of the probe pulse. Thus, the temporally-gated differential signal (*TGDS*) tends to integrate the third-order emission.

This gating process is illustrated in Fig. 2. Figure 2 shows the time-resolved signal emitted in the  $\mathbf{k}_2$  direction with the pump present (lower curve) and without the pump present (upper curve) for a single fixed time delay ( $\tau_{21}=0$ ) as extracted from our spectral interferometric measurements. The shaded area indicates the difference between the two curves. To obtain the *TGDS*, we integrate this difference beginning at a time immediately after the probe has passed. This eliminates the first term in the conventional signal. This procedure must be repeated for each time delay. The main point is that (for an optically-thin sample) the conventional technique, which is dominated by the first term in Eq. (1), allows us to obtain a signal that is proportional to the initial value of the third order polarization, while the gated technique yields a signal that is proportional to the integral over the third-order polarization.

In principle, both differential signals can be obtained from the same set of time-resolved measurements (e.g. those in Fig. 2) by integrating from  $-\infty$  to  $+\infty$  to obtain the conventional *DS* and from  $-\tau$  to  $+\infty$  to obtain the *TGDS*. First, consider the feasibility of obtaining the *DS* from such measurements. As we have already discussed, even though the conventional *DS* integrates the difference in the signals (with and without the pump) over all times, nevertheless, it is dominated by the integral over the time that the probe  $\mathcal{E}_2$  is present in the MQWs (i.e., by the first term in Eq. (1)). Specifically, for  $\tau_{21}=0$ , the *DS* is dominated by the integral of the difference in the two curves shown in Fig 2 over the range of roughly  $t \approx -\tau$  to  $t \approx +\tau$ . In this range, the magnitudes of the signal with the pump and the signal without the pump are approximately equal and large, and the difference between these two signals is a small fraction of either signal ( $\ll 1\%$ ). It is well known that a change of much less than 1 part in 100 is difficult to reliably measure using a single-shot technique, such as spectral interferometry. Extensive signal averaging is needed, and for that reason, we chose to use the synchronous homodyne detection scheme shown in Fig. 1a. In addition, the latter scheme has the advantage of automatically performing the temporal integration.

By comparison, the *TGDS* (for  $\tau_{21}=0$ ) is obtained by integrating the difference in the two curves in Fig. 2 over the range  $t > -\tau$  (i.e. over all time after the probe pulse has exited the

sample). In this range, the magnitudes of both signals are much smaller (notice the log scale), but the difference is now comparable to the larger of the two signals (i.e., the signal without the pump). That is, the fractional change in the signal with and without the pump pulse is large. In this regime, a single-shot technique (such as spectral interferometry) is appropriate. In principle, the *TGDS* also can be obtained by temporally resolving the signal in Fig. 1a (with and without the pump) by cross correlating it with a reference pulse (e.g., by using upconversion in a nonlinear crystal) and, subsequently, by subtracting the result with and without the pump pulse and integrating the difference over the range  $-\tau$  to  $+\infty$ . This procedure would, however, require tedious cross correlation scans of a second delay stage for each fixed time delay  $\tau_{21}$  between the pump and probe pulses. For the latter reason, we chose to use spectral interferometry for the *TGDS* measurements.

### III. EXCITON-EXCITON CORRELATIONS

Figure 3 illustrates that indeed these two techniques produce very different results. The conventional ungated *DS* measurements are shown in Fig. 3a, and the *TGDS* measurements in Fig. 3b. In each case, the pump and probe pulses had the same circular polarization (SCP). Notice that the conventional *DS* exhibits a "coherent dip" when the pulses overlap, but there is no evidence of TI-QB's. In contrast, the *TGDS* measurements exhibit TI-QB's at both positive and negative delays.

The results shown in Fig. 3 can be understood qualitatively and discussed most simply by representing the *lh* and *hh* excitonic transitions by two three-level systems--one for each spin state--with the optical selection rules shown in Fig. 4. For pump and probe pulses with the same right circular ( $\sigma^+$ ) polarizations, only the *hh* transition on the left (in Fig. 4) and the *lh* transition on the right will be directly excited. In the absence of any interactions between the two excitonic systems, the two excited oscillators do not share a common level and are not coupled. Therefore, no TI-QB's would be expected. On the other hand, if the two three-level systems interact through, for example, Coulomb scattering processes, then the two excitonic systems will be coupled, and TI-QB's may be observed in the coherent emission. Consequently, regardless of the model invoked to discuss them, the gated (*TGDS*) results shown in Fig. 3b provide direct evidence for the importance of exciton-exciton interactions, since without these four-particle correlations no TI-QB's would be expected. In addition, these results demonstrate that the *TGDS* (which tends to integrate over the third-order coherent emission) is particularly sensitive to these correlations.

By contrast, the conventional ungated *DS* measurements performed under identical excitation conditions (Fig. 3a) exhibit no TI-QB's, which indicates that this technique is insensitive to the coupling between the two excitonic spin systems. Since this technique tends to sample the third-order emission at  $t=0$ , the absence of TI-QBs suggests that the exciton-exciton interactions responsible for the coupling in Fig. 3b have a finite build-up time and that they are initially weak or nonexistent. This capability of the conventional ungated *DS* technique to minimize the exciton-exciton correlations can be used to isolate the intervalence coherence, as we discuss in the next section.

The qualitative discussions of the previous two paragraphs can be put on a more quantitative (yet intuitive) basis by using the simple phenomenological model that we have described in our previous work.<sup>32,33,37</sup> In this model, again for simplicity, the *lh* and *hh* excitonic

transitions are represented by two three-level systems--one for each spin state--with the optical selection rules shown in Fig. 4. A density-dependence to the dephasing (or EID),<sup>20-23</sup> local field corrections (LFC),<sup>3,38-41</sup> and biexciton formation<sup>12-19</sup> are then included phenomenologically. The EID is incorporated by expanding the dephasing rate in a Taylor series and by retaining the first two terms:

$$\gamma(n) \cong \gamma_0 + \frac{\partial \gamma}{\partial n} n = \gamma_0 + N \frac{\partial \gamma}{\partial n} (\rho_{ee1} + \rho_{ee2}) = \gamma_0 + \frac{\eta}{2\hbar} (\rho_{ee1} + \rho_{ee2}), \quad (3)$$

where  $\gamma_0$  is the low density dephasing rate at the operating lattice temperature and  $n=N(\rho_{ee1}+\rho_{ee2})$  is the total density of excited excitons. Here,  $N$  denotes the total density of oscillators of each spin system and  $\rho_{ee1}$  ( $\rho_{ee2}$ ) denotes the upper level population matrix element for the spin -1/2 (+1/2) system. The parameter  $\eta \equiv 2N\hbar(\partial\gamma/\partial n)$ , which has units of energy, is the EID parameter that we have used in previous publications,<sup>10,31-35</sup> and it is a measure of the strength of the density dependence of the dephasing. Because it is the total population that determines the dephasing rate, EID provides a coupling between the two three-level systems. However, this coupling is not instantaneous, but cumulative. In fact, within the context of the approximations given here, the EID has a characteristic build-up time of  $2\hbar/\eta \sim 330$  fs (for  $\eta=4$  meV, a value used in previous work). Finally, notice that EID is an example of a four-particle interaction (i.e., two electrons and two holes).

Local field corrections (LFC) are included phenomenologically by adding a term proportional to the total material polarization to the incident field:

$$\mathbf{E}_{local} = \mathbf{E} + L\mathbf{P}, \quad (4)$$

where  $\mathbf{P}$  is the total material polarization,  $\mathbf{E}$  is the total incident field, and  $L$  the a local field parameter. As previously stated, for pump and probe pulses with the same right circularly polarizations, only the  $hh$  transition on the left (in Fig. 4) and the  $lh$  transition on the right will be directly excited. The local-field produced by the oscillator on the left will be right circularly polarized and will be emitted at the  $hh$  frequency. Consequently, this local field will not couple to the  $hh$  transition on the right because it has the incorrect polarization and will only weakly couple to the  $lh$  transition on the right because it is not resonant with that transition. For these reasons, LFC will not provide a significant coupling between the two spin systems. Consequently, we omit it from our discussions here. Nevertheless, we have included it in simulations (which are not shown), and it does not change the substance of our conclusions.

Finally, biexciton formation is included in our phenomenological model as described in Ref. 32, 33 and 37. Excitation with two right circularly polarized pulses precludes the formation of pure biexcitons consisting either of two  $hh$  excitons or of two  $lh$  excitons of opposite spins. However, under these same excitation conditions, mixed biexcitons can be formed from one  $hh$  exciton and one  $lh$  exciton having opposite spins. Mixed  $hh$ - $lh$  biexcitons have been observed in ZnSe quantum wells, but their contribution to the FWM signal was found to be roughly an order of magnitude weaker than that of  $hh$  biexcitons.<sup>42</sup> More recently, evidence of mixed  $hh$ - $lh$  biexciton formation also has been reported in the spectra from GaAs quantum wells.<sup>43</sup> We have examined our FWM spectra for evidence of mixed  $lh$ - $hh$  biexciton formation when we excite with two right circularly polarized pulses, and we find no resolvable signal at the expected mixed biexciton frequency (to within our experimental accuracy under our excitation conditions).

While we do not preclude possible contributions from mixed  $hh-lh$  biexcitons, we neglect their contributions here.

One advantage of this simple model is that one can readily solve the density matrix equations to obtain closed form solutions by assuming delta function time dependences for the excitation pulses. For example, when the system shown in Fig. 4 is excited by right circular excitation pulses and when the density matrix equations are modified to include EID, the first-order field that propagates in the  $k_2$  direction is found to be:

$$\mathcal{E}^{(1)} \cong \left( \frac{ikl}{2\epsilon_0} \right) \mathcal{P}^{(1)}(k_2, t) = -\Theta(t) \alpha_0 l \gamma \mathbf{a}_2 \exp(-\gamma t) (1 + A \exp(-i\Omega t)), \quad (5)$$

and the third-order field has the form:

$$\mathcal{E}^{(3)} \cong \left( \frac{ikl}{2\epsilon_0} \right) \mathcal{P}^{(3)}(k_2, \tau_{21}, t) = \mathcal{E}_{no}^{(3)} + \mathcal{E}_{EID}^{(3)}, \quad (6)$$

where the induced-field without many-body effects is:

$$\begin{aligned} \mathcal{E}_{no}^{(3)} \cong \alpha_0 l \gamma \left( \frac{F_1}{F_s} \right) \mathbf{a}_2 \exp(-\gamma t) \{ & \Theta(t) \Theta(\tau_{21}) [2(1 + A^2 \exp(-i\Omega t))] \\ & + \Theta(t + \tau_{21}) \Theta(-\tau_{21}) [(1 + A^2 \exp(-i\Omega t))] \} \end{aligned} \quad (7)$$

and the contribution from EID is:

$$\begin{aligned} \mathcal{E}_{EID}^{(3)} \cong \alpha_0 l \gamma \left( \frac{F_1}{F_s} \right) \mathbf{a}_2 \exp(-\gamma t) \left( \frac{\eta}{2\hbar} \right) \\ \{ & \Theta(t) \Theta(\tau_{21}) t [(1 + A)(1 + A \exp(-i\Omega t)) + \exp(-2\gamma\tau_{21})(1 + A \exp(i\Omega\tau_{21}))(1 + A \exp(-i\Omega(t + \tau_{21})))] \\ & \Theta(t + \tau_{21}) \Theta(-\tau_{21}) (t + \tau_{21}) [(1 + A)(1 + A \exp(-i\Omega t)) + (1 + A \exp(i\Omega\tau_{21}))(1 + A \exp(-i\Omega(t + \tau_{21})))] \} \end{aligned} \quad (8)$$

Here  $\Theta$  denotes the Heaviside step function,  $\gamma$  is the dipole dephasing rate,  $\hbar\Omega$  is the difference between the  $hh$  and  $lh$  energies, and  $A$  is a phenomenological constant that reflects the relative strength of the  $lh$  FWM emission. In our case,  $A$  is the product of the square of the ratio of the  $lh$  and  $hh$  optical transition matrix elements ( $\sim 1/3$ ) and a spectral weighting factor ( $\sim 2$ ) to account for the detuning of the excitation wavelength with respect to the  $hh$  and  $lh$  excitons, as shown schematically in Fig. 1c. Furthermore, we have assumed that the pump is much larger than the probe ( $\mathcal{E}_1 \gg \mathcal{E}_2$ ) and that the dephasing is much faster than the population decay. Also,  $\alpha_0 \equiv \mu^2 N k / 2 \hbar \epsilon_0 \gamma$  is the steady-state linear absorption coefficient for the field;  $F_s \equiv \hbar^2 \epsilon_0 c / \mu^2 \tau_1$  is the saturation fluence, where  $\mu$  is the heavy-hole dipole matrix element and  $\tau_1$  is the width of the intensity envelope of the Gaussian shaped pump and probe pulses, as defined by  $\text{Gaus}(t/\tau_1) = \exp[-\pi(t/\tau_1)^2]$ ; and where  $F_1$  denotes the fluence of the  $k_1$  pulse. Finally, the vector  $\mathbf{a}_2$  is the amplitude

of the delta-function probe pulse:  $\mathcal{E}_2(t)=\mathcal{A}_2\delta(t)$ . In terms of experimentally measured parameters,  $\mathcal{A}_2=(4\tau_1 F_2/c\epsilon_0)^{1/2}$ , where  $F_2$  is the fluence of the  $\mathbf{k}_2$  pulse.

As indicated in Eq. (6), the third-order emission in the  $\mathbf{k}_2$  direction can be written as the sum of two terms. If there is no coupling between the two three-level systems shown in Fig. 4 (i.e.,  $\eta=0$ ), then the third-order field is given by the first term:  $\mathcal{E}_{no}^{(3)}$ . As we have already stated, for the case of right circularly polarized pump and probe pulses, the  $hh$  transition is excited in one system, and the  $lh$  transition is excited in the other. Consequently,  $\mathcal{E}_{no}^{(3)}$  describes the emission from two independent oscillators. Under these circumstances, we would expect to observe  $lh$ - $hh$  beating due to polarization interference in the time-resolved measurements, but no TI-QBs. These expectations are confirmed by the simulations for  $\eta=0$  shown by the dotted lines in Fig. 5. Notice that, in the absence of exciton-exciton coupling, no TI-QB's are expected in either the  $DS$  or the  $TGDS$  measurements, which directly contradicts the  $TGDS$  measurements shown in Fig. 3b.

With exciton-exciton coupling included, there are two limits of immediate interest:  $\eta t/2\hbar \ll 1$  and  $\eta t/2\hbar \gg 1$ . When  $\eta t/2\hbar \ll 1$ , the emission (Eq. (6)) again is dominated by  $\mathcal{E}_{no}^{(3)}$ , and therefore, its behavior is identical to that described in the previous paragraph. That is, the emission at early times behaves as though it were coming from two uncoupled oscillators. This is the temporal regime that is sampled by the conventional ungated  $DS$  measurements (when optically thin samples and pulses short compared to  $2\hbar/\eta$  are used). Consequently, even in the presence of EID, one would expect to observe no TI-QBs in the  $DS$  measurements (as indicated by the solid line in Fig. 5a, in agreement with the measurements shown in Fig. 3a. [Note: Careful inspection of the solid line in Fig. 5a will reveal very faint beats. These are the remnants of the weaker contributions from the  $DS_2$  terms (see Eq. (1)) which tend to integrate over the third-order emission.]

By comparison, when  $\eta t/2\hbar \gg 1$ , the emission is dominated by the second term in Eq. (6):  $\mathcal{E}_{EID}^{(3)}$ . In this limit, the light is still directly coupled only to the  $hh$  transition on the left and the  $lh$  transition on the right in Fig. 4. That is, the optically-excited transitions still technically share no common level, but now they are strongly coupled through the density-dependent dephasing given by Eq. (3), allowing the emission to exhibit quantum-beat-like behavior. For this reason, TI-QBs are expected in the  $TGDS$  signal (which integrates over the third-order emission) as indicated by the solid line in Fig. 5b, in agreement with the measurements shown in Fig. 3b. Notice that these TI-QBs decay in a time determined by the radiative dipole dephasing rate  $\gamma$ , which is associated with the decay of the radiative interband dipole density matrix elements  $\rho_{e-hh}$  and  $\rho_{e-lh}$ . Consequently, these measurements not only provide evidence of exciton-exciton correlations, but they provide a direct measurement of the dipole dephasing rate.

It should be pointed out that we<sup>10</sup> and others<sup>9,11</sup> have independently observed  $hh$ - $lh$  quantum-beat-like behavior in the third-order emission in the  $2\mathbf{k}_2$ - $\mathbf{k}_1$  FWM direction using pump and probe pulses with the same circular polarizations. As we have discussed here,  $lh$ - $hh$  quantum beats are forbidden for these excitation conditions if one considers only the polarization selection rules indicated in Fig. 4. Consequently, such studies<sup>9-11</sup> also provide direct experimental evidence for  $\sigma^+ hh$  exciton and  $\sigma^+ lh$  exciton correlations. In addition, one of these studies<sup>10</sup> demonstrated that this coupling was cumulative in nature. Specifically, the  $hh$ - $lh$  coupling was shown to be initially weak and to increase in strength, until the coupled behavior dominated the third-order response -- consistent with our observations here.

#### IV. RAMAN COHERENCE

The situation is slightly more complicated when the system shown in Fig. 4 is excited by pump and probe pulses having the same linear polarizations (SLP). In this case, both  $hh$  and  $lh$  transitions in each spin system are excited, and two types of coherences are produced. One is associated with the *interband* density matrix elements  $\rho_{e-hh}$  and  $\rho_{e-lh}$ , and it decays with the *dipole* dephasing rate  $\gamma$  (where we have assumed that  $\gamma_{e-hh} = \gamma_{e-lh} = \gamma$ ). A dipole coherence is also produced with circular polarizations and was discussed and measured in the previous section. The second coherence is that associated with the *intervalence band* matrix element  $\rho_{hh-lh}$ , which decays at a rate  $\gamma_{hh-lh}$ . The latter has also been referred to as Raman coherence.<sup>44</sup>

Also, under linear excitation conditions, two types of couplings are produced. The first is the coupling associated with the exciton-exciton interactions discussed in the previous section (and represented in our model by EID). As discussed in Sec. III, in the  $\chi^{(3)}$  regime, these interactions occur at a constant rate (e.g.,  $\eta/2\hbar$  for EID) and are considered cumulative because the third-order emission associated with this coupling is initially zero, and it requires a finite time to build up (see Eq. 8). The other coupling is associated with the shared level between the  $hh$  and  $lh$  transitions for each spin system. The latter is present for all times and, therefore, is regarded as static.

The *DS* and *TGDS* measurements using  $x$ -polarized pump and probe pulses are shown in Fig. 6. For the ungated *DS* measurements (Fig. 6a), notice that TI-QBs are observed for positive delays, but no beats are observed at negative delays. The results at positive delays can be understood by recalling that the *DS* technique minimizes the influence of the cumulative exciton-exciton coupling by sampling the third-order response at  $t=0$  (for delta function pump and probe). Consequently, the TI-QBs in Fig. 6a cannot be associated with the cumulative coupling associated with exciton-exciton interactions such as EID, but can only be attributed to the static coupling associated with the shared level. As we will discuss below, these oscillations decay in the Raman coherence time  $\gamma_{hh-lh}^{-1}$ . No significant TI-QBs are observed in the *DS* at negative delays because the *DS<sub>i</sub>* term does not contribute when the probe arrives before the pump. (Note: the jumps near zero delay that are visible in Fig. 6a are not reproducible. They vary in phase and amplitude from measurement to measurement. We believe that they are associated with the interference between pump and probe scattered light near zero delay. The oscillations that we have identified with TI-QBs are reproducible.)

By comparison, the *TGDS* exhibits TI-QB's at both positive and negative delays for SLP. There are at least two possible contributions to the beats in the *TGDS* seen at positive delays. As we will discuss more quantitatively below, the shared level between  $lh$  and  $hh$  oscillators (see Fig. 4) will result in TI-QB's that decay with the Raman dephasing rate  $\gamma_{hh,lh}$ , even in the absence of excitonic interactions. In addition, if interactions between the  $lh$  and  $hh$  excitons are included, beats will also be produced that decay in a time determined by the dipole dephasing rate  $\gamma$ . Consequently, the *TGDS* measurements with SLP contain contributions from both  $\gamma_{hh,lh}$  and  $\gamma$ , while the *DS* measurements do not. For negative delays, the time ordering of the fields is such that the decay of the TI-QBs is determined solely by the dipole dephasing rate.

The density matrix equations for the system shown in Fig. 4 also can be readily solved for  $x$ -polarized pump and probe pulses (under the same assumptions as for SCP). In this case,



the first-order coherent emission,  $\mathcal{E}^{(1)}$  has the same form as Eq. (5), except that the emitted light is now  $x$ -polarized rather than circularly polarized. The third-order emission has the form:

$$\mathcal{E}^{(3)} \cong \frac{1}{2}\mathcal{E}_{no}^{(3)} + \mathcal{E}_{EID}^{(3)} + \mathcal{E}_{SL}^{(3)} \quad (9)$$

where  $\mathcal{E}_{no}^{(3)}$  and  $\mathcal{E}_{EID}^{(3)}$  have the same form as Eq. (7) and Eq. (8), respectively, except that the emitted light is now  $x$ -polarized. The additional term in the third-order emission that arises from the shared level,  $\mathcal{E}_{SL}^{(3)}$ , is given by:

$$\begin{aligned} \mathcal{E}_{SL}^{(3)} \cong & \alpha_0 l \gamma \left( \frac{F_1}{F_s} \right) a_2 \exp(-\gamma t) \left( \frac{A}{4} \right) \\ & \{ 2\Theta(t)\Theta(\tau_{21})[(1 + \exp(-i\Omega t)) + \exp(-\gamma_{hh-lh}\tau_{21})(\exp(i\Omega\tau_{21}) + \exp(-i\Omega(t + \tau_{21})))] \\ & + \Theta(t + \tau_{21})\Theta(-\tau_{21})[(1 + \exp(-i\Omega t)) + (\exp(i\Omega\tau_{21}) + \exp(-i\Omega(t + \tau_{21})))] \} \end{aligned} \quad (10)$$

The most notable feature of this equation is that it contains a term that will produce TI-QBs that decay at a Raman dephasing rate  $\gamma_{hh-lh}$ . This Raman coherence only contributes at positive delays. By contrast, the EID term,  $\mathcal{E}_{EID}^{(3)}$ , produces TI-QBs both at positive and at negative delays.

The simulations corresponding to the *DS* and *TGDS* measurements with and without Raman coherence included are shown in Fig. 7. Notice that TI-QBs are observed in the *TGDS* for this polarization configuration with or without the inclusion of the Raman coherence (Fig. 7b). The TI-QBs are slightly stronger with Raman coherence included because the common level and the coupling from EID both contribute to the TI-QBs. In the latter case, the decay of the TI-QBs at positive delays is determined by  $\gamma$  and  $\gamma_{hh-lh}$ . Without the Raman coherence, only the *hh*-exciton-*lh*-exciton interactions provide the coupling that produces the beats.

By comparison, no TI-QBs are expected in the *DS* with the Raman coherence turned off—even though EID is included (Fig. 7a). However, with Raman coherence included, TI-QBs are expected because of the static coupling provided by the common level—in agreement with the measurements shown in Fig. 6a. This confirms that the *DS* technique has eliminated the cumulative many-body effects by sampling at  $t=0$  and that the *hh-lh* beats in Fig. 6a are associated with the Raman coherence. Ferrio and Steel<sup>44</sup> have previously reported measurements of Raman quantum beats in GaAs at 5 K similar to those shown in Fig. 6a. However, they performed only the *DS* measurements, not the *TGDS* measurements, and, to our knowledge, did not explore the polarization dependence of the signal. In addition, they attributed the observed Raman coherence to a static interaction between *lh* and *hh* excitons, while we attribute them to a common level shared by the two excitons. Again, faint beats can be seen in the simulations of Fig. 7a even when the Raman coherence is turned off. As before, these are the contributions of the weaker  $DS_2$  term. It should be emphasized that if care is not taken to use optically thin samples this signal can actually become comparable to (or dominate) the  $DS_1$  term and complicate the interpretation of the measurements.

Finally, it should be noted that the *DS* shown in Fig. 6a produces a negative jump in going from negative to positive delays, while the corresponding simulations in Fig. 7a produce a positive step (ignoring the region near 0 delay). This apparent discrepancy is an artifact of having used delta function pulses (which have an infinite bandwidth) in the simulations. The magnitude and the sign of this step are a sensitive function of the bandwidth and the detuning of the pulses in both the experiments and in the simulations. Similar comments apply to Fig. 3a and Fig. 5a.

## V. SUMMARY and CONCLUSIONS

In summary, we have contrasted two different techniques for measuring the differential probe signal. These two techniques are complementary in the sense that the ungated *DS* tends to sample the third-order polarization  $\mathcal{P}^{(3)}$  and emission  $\mathcal{E}^{(3)}$  at  $t=0$ , while the *TGDS* integrates over the emission time for  $\mathcal{P}^{(3)}$ . When the pump and probe pulses have the same circular polarizations, the ungated *DS* technique minimizes the cumulative exciton-exciton interactions (represented here by EID) and the polarization selection rules preclude any shared level between the hh and lh excitons (thus, turning off the Raman coherence). In this case, we expect (and we observe) no TI-QBs. By contrast, for the *TGDS* using the same circular polarizations, the polarization selection rules eliminate the common level, thereby turning off the Raman coherence, but the technique emphasizes the EID: TI-QBs are observed which can only be attributed to four-particle *hh-lh* exciton-exciton correlations, and the decay of these TI-QBs is determined by the interband dipole dephasing rate  $\gamma$ .

By comparison, when the pump and probe pulses have the same linear polarizations, the *TGDS* signal is complicated both by the presence of exciton-exciton Coulomb correlations (which decay at a rate determined by  $\gamma$ ) and by the coupling associated with the shared level (which decays at  $\gamma_{hh-lh}$ ). The ungated *DS* technique, however, minimizes the contributions of EID and allows the measurement of the Raman dephasing rate  $\gamma_{hh-lh}$ .

We also emphasize that we have made our measurements in the  $\mathbf{k}_2$  direction rather than the more conventional  $2\mathbf{k}_2-\mathbf{k}_1$  direction. Monitoring the signal in the  $\mathbf{k}_2$ -direction is dramatically different from monitoring the four wave mixing signal in the  $2\mathbf{k}_2-\mathbf{k}_1$  direction. One obvious difference is that the transmitted probe  $\mathcal{E}_2$  and the first-order emission from  $\mathcal{P}^{(1)}(\mathbf{k}_2)$  travel in the  $\mathbf{k}_2$  direction, but not in the  $2\mathbf{k}_2-\mathbf{k}_1$  direction. Consequently, there will be no detection terms corresponding to  $DS_1$  or  $DS_2$  in the  $2\mathbf{k}_2-\mathbf{k}_1$  direction. In fact, the time integrated signal in the  $2\mathbf{k}_2-\mathbf{k}_1$  direction will simply be proportional to the integral of  $|\mathcal{P}^{(3)}(2\mathbf{k}_2-\mathbf{k}_1)|^2$ .

The third-order polarization emitted in the  $\mathbf{k}_2$  direction,  $\mathcal{P}^{(3)}(\mathbf{k}_2)$ , is also fundamentally different from the polarization propagating in the  $2\mathbf{k}_2-\mathbf{k}_1$  direction,  $\mathcal{P}^{(3)}(2\mathbf{k}_2-\mathbf{k}_1)$ . For example, it has been shown<sup>44,45</sup> that the TI-QBs in the  $2\mathbf{k}_2-\mathbf{k}_1$  direction decay with a rate determined by the radiative dipole dephasing rates  $\gamma_{e-lh}$  and  $\gamma_{e-hh}$  and that the time ordering of the fields is such that these beats are inherently insensitive to the decay of the nonradiative Raman coherence. Therefore, the  $2\mathbf{k}_2-\mathbf{k}_1$  direction provides no access to the decay of the Raman coherence. By comparison, in the  $\mathbf{k}_2$ -direction, either a common level or static interactions between the hh and lh excitons can be shown to produce TI-QBs that decay with the Raman dephasing rate  $\gamma_{lh,hh}$ .

Finally, we note that all of the simulations presented here use a phenomenological model and assume delta-function-width pulses, but Rolf Binder at the University of Arizona has

performed microscopic simulations of our experiments in the  $\chi^{(3)}$  limit<sup>29,30</sup> using the dynamics controlled truncation scheme.<sup>9,30,46</sup> Those calculations<sup>47</sup> will be discussed elsewhere.

## VI. ACKNOWLEDGEMENTS

The authors gratefully acknowledge numerous insightful conversations with Rolf Binder. This research was supported in part by the U. S. Army Research Office and the Office of Naval Research.

## REFERENCES

1. K. Leo, T. C. Damen, J. Shah, E. O. Göbel, and K. Köhler, *Appl. Phys. Lett.* **57**, 19 (1990).
2. K. Leo, T. C. Damen, J. Shah, and K. Köhler, *Phys. Rev. B* **42**, 11359 (1990).
3. K. Leo, E. O. Göbel, T. C. Damen, J. Shah, S. Schmitt-Rink, W. Schäfer, J. F. Müller, K. Köhler, and P. Ganser, *Phys. Rev. B* **44**, 5726 (1991).
4. E. O. Göbel, K. Leo, T. C. Damen, J. Shah, S. Schmitt-Rink, W. Schäfer, J. F. Müller, and K. Köhler, *Phys. Rev. Lett.* **64**, 1801 (1990).
5. M. Koch, J. Feldmann, G. von Plessen, E. O. Göbel, P. Thomas, and K. Köhler, *Phys. Rev. Lett.* **69**, 3631 (1992).
6. A. E. Paul, W. Sha, S. Patkar, and A. L. Smirl, *Phys. Rev. B* **51**, 4242 (1995).
7. A. L. Smirl, X. Chen, and O. Buccafusca, *Opt. Lett.* **23**, 1120 (1998).
8. A. L. Smirl, X. Chen, and O. Buccafusca, *IEEE J. Quantum Electron.* **35**, 523 (1998).
9. P. Kner, S. Bar-Ad, M. V. Marquezini, D. S. Chemla, and W. Schäfer, *Phys. Rev. Lett.* **78**, 1319 (1997).
10. A. L. Smirl, M. J. Stevens, X. Chen, and O. Buccafusca, *Phys. Rev. B* **60**, 8267 (1999).
11. M. Phillips and H. Wang, *Solid State Commun.* **11**, 317 (1999).
12. B. F. Feuerbacher, J. Kuhl, and K. Ploog, *Phys. Rev. B* **43**, 2439 (1991).
13. S. Bar-Ad and I. Bar-Joseph, *Phys. Rev. Lett.* **68**, 349 (1992).
14. H. H. Yaffe, Y. Prior, J. P. Harbison, and L. T. Florez, *J. Opt. Soc. Am. B* **10**, 578 (1993).
15. H. Wang, J. Shah, T. C. Damen, L. N. Pfeiffer, *Solid Stat. Comm.* **91**, 869 (1994).
16. T. Saiki, M. Kuwata-Gonokami, T. Matsusue, H. Sakaki, *Phys. Rev. B* **49**, 7817 (1994).
17. E. J. Mayer, G. O. Smith, V. Heuckeroth, J. Kuhl, K. Bott, A. Schulze, T. Meier, D. Bennhardt, S. W. Koch, P. Thomas, R. Hey, and K. Ploog, *Phys. Rev. B* **50**, 14730 (1994).
18. K.-H. Pantke, D. Oberhauser, V. G. Lyssenko, J. M. Hvam, and G. Weimann, *Phys. Rev. B* **47**, 2413 (1993).
19. K. Bott, O. Heller, D. Bennhardt, S. T. Cundiff, P. Thomas, E. J. Mayer, G. O. Smith, R. Eccleston, J. Kuhl, and K. Ploog, *Phys. Rev. B* **48**, 17418 (1993).
20. H. Wang, K. Ferrio, D. G. Steel, Y. Z. Hu, R. Binder, and S. W. Koch, *Phys. Rev. Lett.* **71**, 1261 (1993).
21. Y. Z. Hu, R. Binder, S. W. Koch, S. T. Cundiff, H. Wang, and D. G. Steel, *Phys. Rev. B* **49**, 14382 (1994).
22. T. Rappen, U. G. Peter, M. Wegener, and W. Schäfer, *Phys. Rev. B* **49**, 10774 (1994).
23. D. G. Steel, H. Wang, M. Jiang, K. Farrio, and S. T. Cundiff, in *Coherent Optical Interactions in Semiconductors*, edited by R. T. Phillips (Plenum, New York, 1994), pp. 157-179.
24. W. Schäfer, D. S. Kim, J. Shah, T. C. Damen, J. E. Cunningham, K. W. Goosen, L. N. Pfeiffer, and K. Köhler, *Phys. Rev. B* **53**, 16429 (1996).
25. P. Kner, W. Schäfer, R. Lövenich, and D. S. Chemla, *Phys. Rev. Lett.* **81**, 5386 (1998).
26. C. Sieh, T. Meier, F. Jahnke, A. Knorr, S. W. Koch, P. Brick, M. Hübner, C. Ell, J. Prineas, G. Khitrova, and H. M. Gibbs, *Phys. Rev. Lett.* **82**, 3112 (1999).
27. C. Sieh, T. Meier, A. Knorr, F. Jahnke, P. Thomas, and S. W. Koch, *Europ. Phys. J B* **11**, 407 (1999).
28. S. Weiser, T. Meier, J. Möbius, A. Euteneuer, E. J. Mayer, W. Stolz, M. Hofmann, W. W. Rühle, P. Thomas, and S. W. Koch, *Phys. Rev. B* **61**, 13088 (2000).

29. M. Lindberg, Y. Z. Hu, R. Binder, and S. W. Koch, *Phys. Rev. B* **50**, 18060 (1994).
30. V. M Axt and A. Stahl, *Z. Phys. B* **93**, 195 (1994); *ibid*, 205 (1994).
31. S. Patkar, A. E. Paul, W. Sha, J. A. Bolger, and A. L. Smirl, *Phys. Rev. B* **51**, 10789 (1995).
32. A. E. Paul, J. A. Bolger, and A. L. Smirl, *J. Opt. Soc. Am. B* **13**, 1016 (1996).
33. J. A. Bolger, A. E. Paul, and A. L. Smirl, *Phys. Rev. B* **54**, 11666 (1996).
34. A. L. Smirl, W. J. Walecki, X. Chen, and O. Buccafusca, *Phys. Stat. Sol. (B)* **204**, 16 (1997).
35. O. Buccafusca, X. Chen, W. J. Walecki, and A. L. Smirl, *J. Opt. Soc. Am. B* **15**, 1218 (1998).
36. W. J. Walecki, D. N. Fittinghoff, A. L. Smirl, and R. Trebino, *Opt. Lett.* **22**, 81 (1997).
37. A. L. Smirl: in *Semiconductor Quantum Optoelectronics: From Quantum Physics to Smart Devices*, edited by A. Miller, M. Ebrahimzadeh and D. M. Finlayson (Institute of Physics Publishing, London 1999), pp. 25-94.
38. K. Leo, M. Wegener, J. Shah, D. S. Chemla, E. O. Göbel, T. C. Damen, S. Schmitt-Rink, and W. Schäfer, *Phys. Rev. Lett.* **65**, 1340 (1990).
39. S. Weiss, M.-A. Mycek, J.-Y. Bigot, S. Schmitt-Rink, and D. S. Chemla, *Phys. Rev. Lett.* **69**, 2685 (1992).
40. M. Wegener, D. S. Chemla, S. Schmitt-Rink, and W. Schäfer, *Phys. Rev. A* **42**, 5675 (1990).
41. S. Schmitt-Rink, S. Mukamel, K. Leo, J. Shah, and D. S. Chemla, *Phys. Rev. A* **44**, 2124 (1991).
42. H. P. Wagner, W. Langbein and J. M. Hvam, *Phys. Rev. B* **59**, 4584 (1999).
43. T. Meier, S. W. Koch, M. Phillips and H. Wang, *Phys. Rev. B*, to be published (2000).
44. K. B. Ferrio and D. G. Steel, *Phys. Rev. Lett.* **80**, 786 (1998).
45. S. Schmitt-Rink, D. Bennhardt, V. Heuckeroth, P. Thomas, P. Haring, G. Maidorn, H. Bakker, K. Leo, D. S. Kim, J. Shah, and K. Köhler, *Phys. Rev. B* **46**, 10460 (1992).
46. M. Z. Maialle and L. J. Sham, *Phys. Rev. Lett.* **73**, 3310 (1994).
47. R. Binder, University of Arizona, Private communication, (2000).

## FIGURE CAPTIONS

Fig. 1. Schematic geometry for the measurement of (a) the conventional temporally-integrated differential signal (DS) and (b) the temporally-gated differential signal (TGDS), where (c) shows the position of the laser spectrum with respect to the  $hh$  and  $lh$  excitonic absorption lines and where  $C_1$  and  $C_2$  denote mechanical choppers.

Fig. 2. The time-resolved coherent emission in the  $k_2$  direction with the pump (bottom) and without the pump (top) for a fixed time delay of  $\tau_{21}=0$ . The shaded area indicates the time-resolved differential signal.

Fig. 3. Measurements of (a) the ungated differential signal (DS) and (b) the temporally-gated differential signal (TGDS) using pump and probe pulses with the same circular polarizations (SCP).

Fig. 4. Optical selection rules for the  $lh$  and  $hh$  transitions.

Fig. 5 Phenomenological simulations of (a) the ungated differential signal (DS) and (b) the temporally-gated differential signal (TGDS) using pump and probe pulses with the same circular polarizations (SCP). The solid lines are simulations that include EID, and the dashed lines do not.

Fig. 6. Measurements of (a) the ungated differential signal (DS) and (b) the temporally-gated differential signal (TGDS) using pump and probe pulses with the same linear polarizations (SLP).

Fig. 7 Phenomenological simulations of (a) the ungated differential signal (DS) and (b) the temporally-gated differential signal (TGDS) using pump and probe pulses with the same linear polarizations (SLP). The solid lines are simulations that include the Raman coherence, and the dashed lines do not. Both include EID.

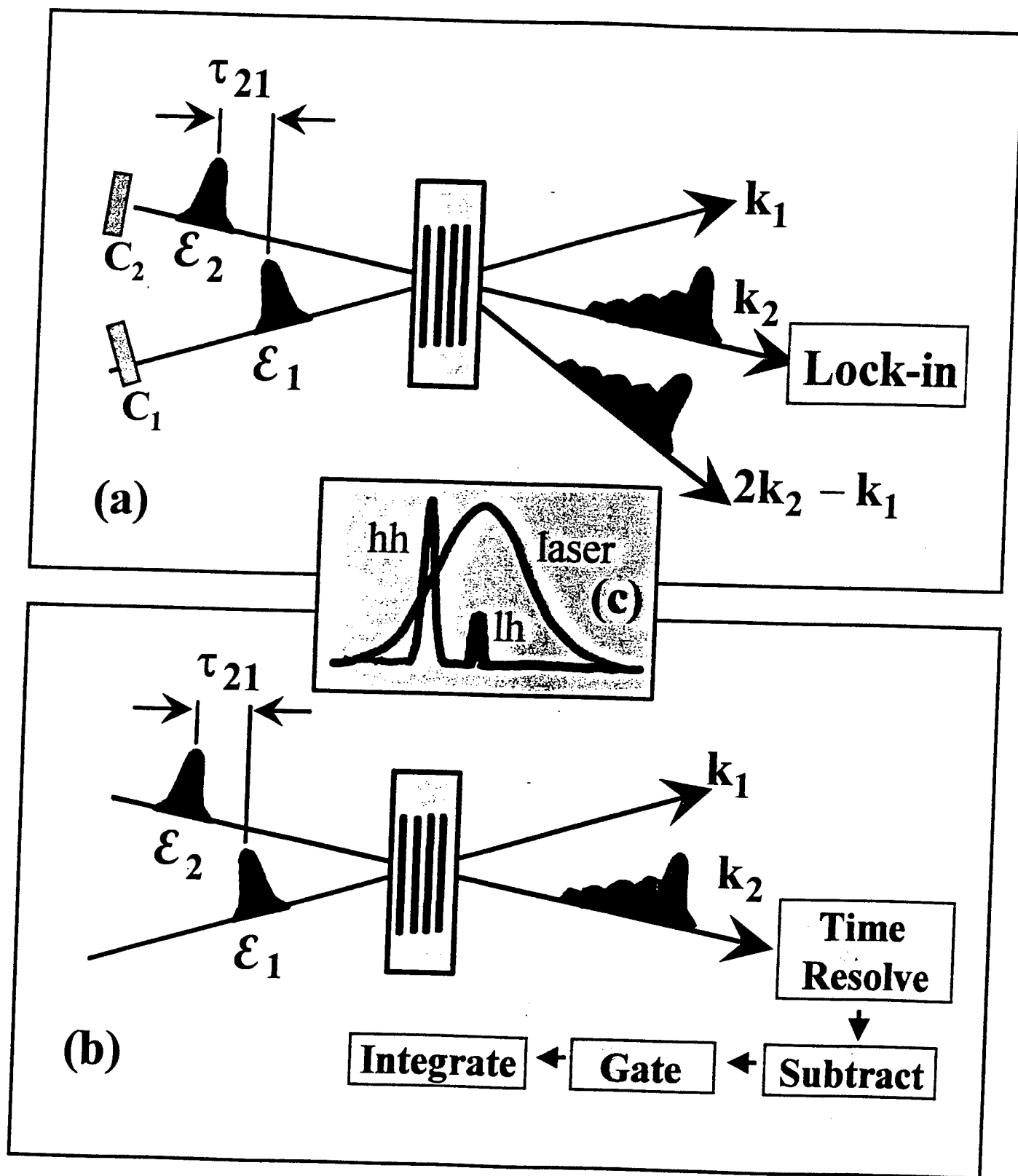


Figure 1, Stevens et al.

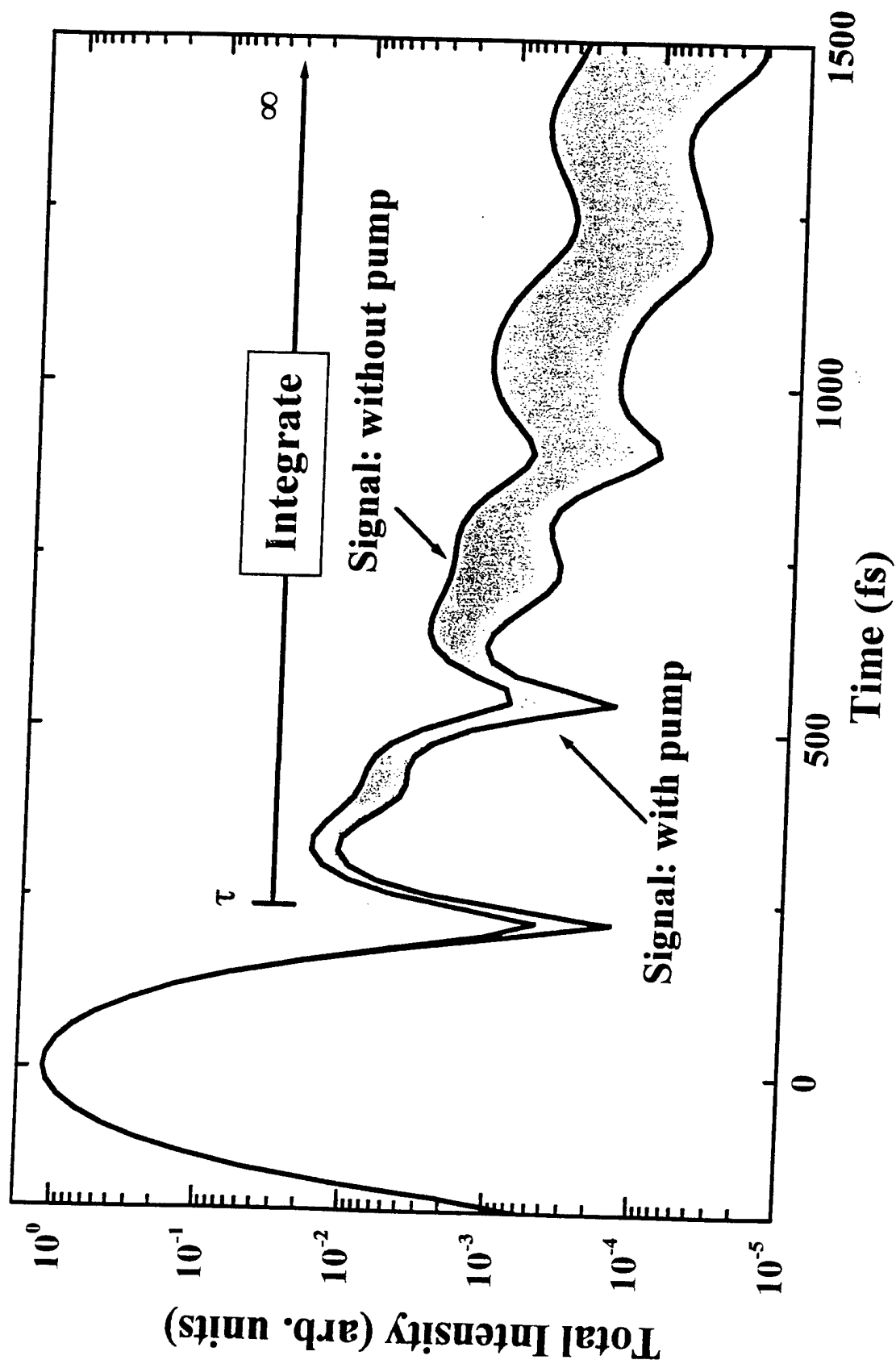


Figure 2, Stevens et al.



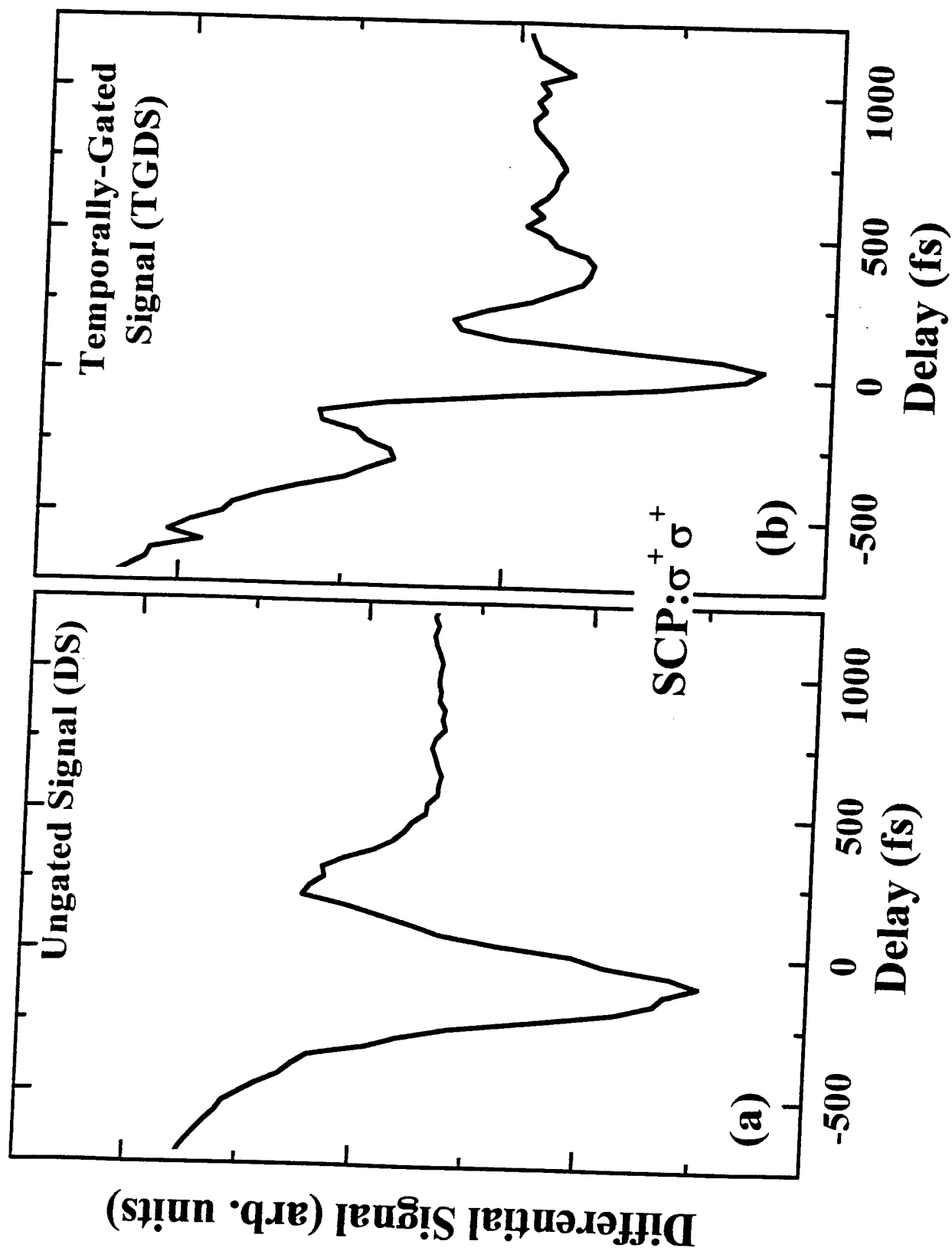
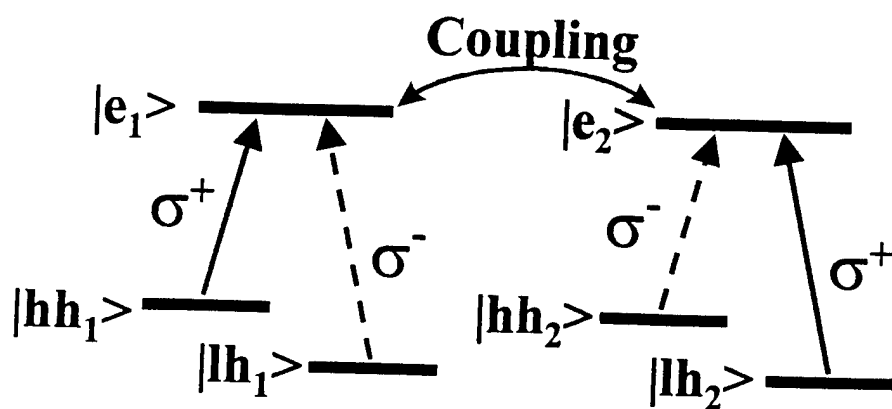
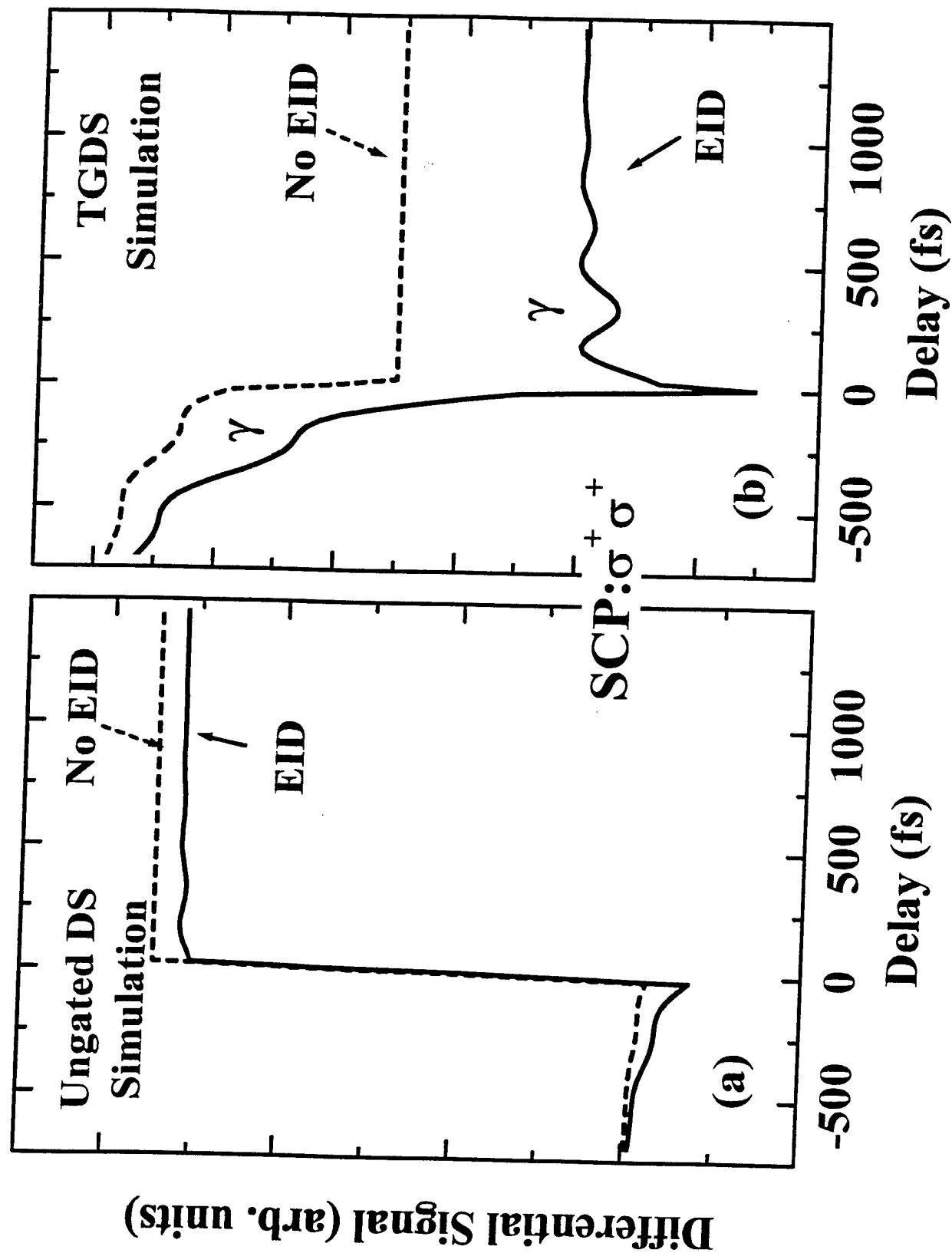
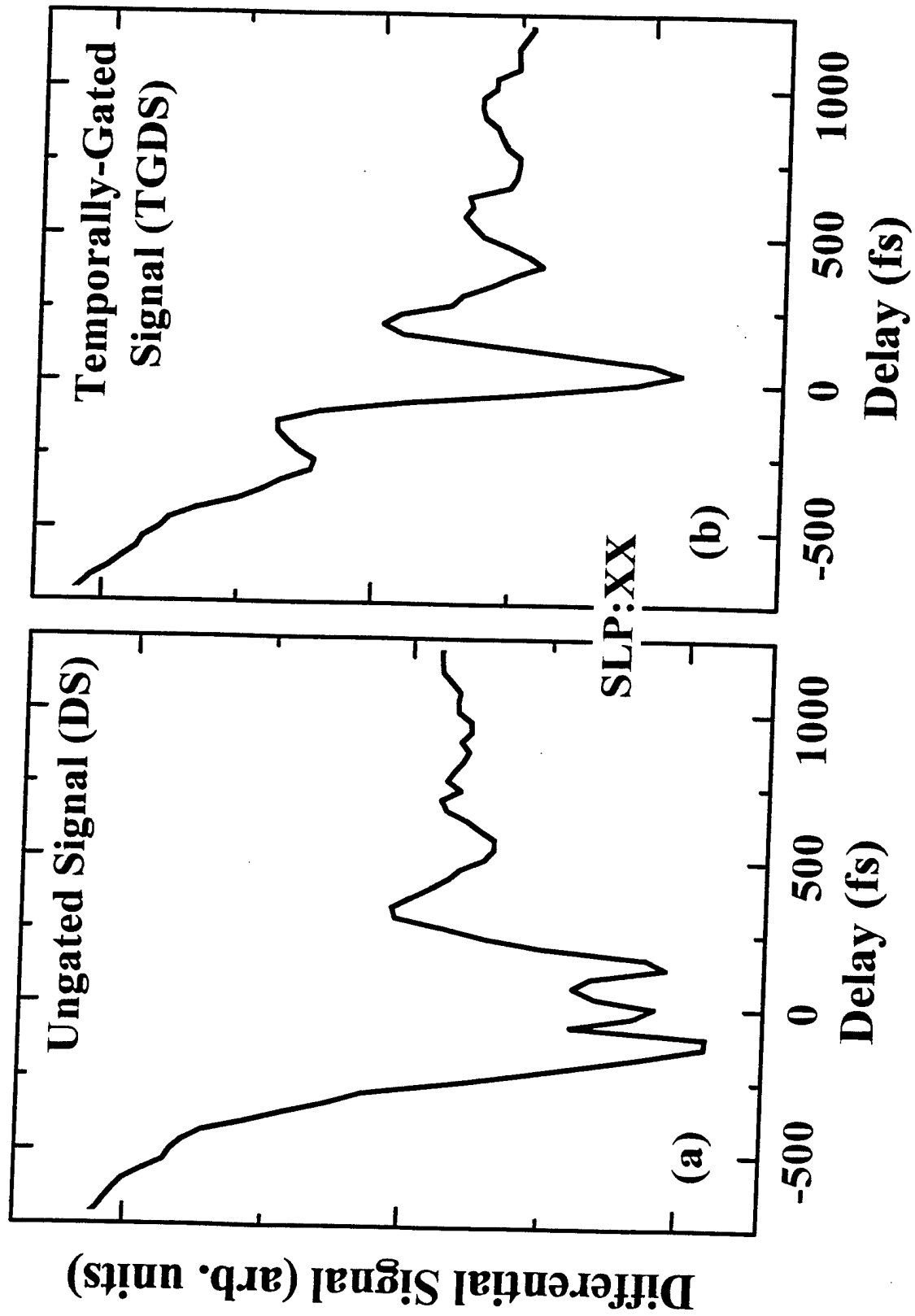


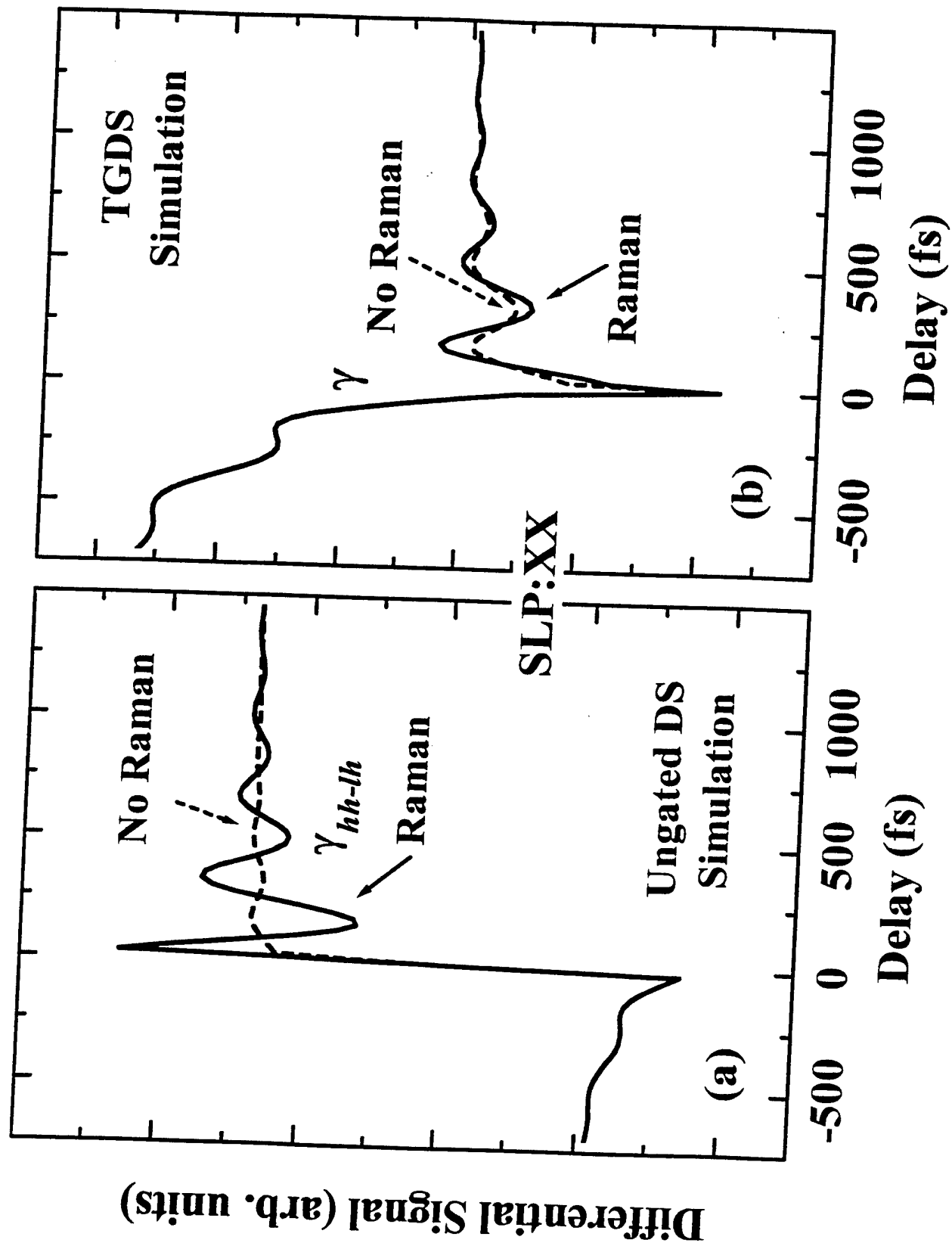
Figure 3, Stevens et al.



Stevens et al., Figure 4







## **Polarization Dynamics of the Nonlinear Coherent Emission from Uniaxially-Strained Quantum Wells**

Arthur L. Smirl, X. Chen, Martin J. Stevens and O. Buccafusca

*Laboratory for Photonics and Quantum Electronics, 138 IATL, University of Iowa, Iowa City, IA 52242*

*Phone: (319) 335-3460 Fax: (319) 335-3462 E-mail: art-smirl@uiowa.edu*

R. Binder and I. Rumyantsev

*Optical Sciences Center, University of Arizona, Tucson, AZ 85721*

*Phone: (520) 621-2892 Fax: (520) 621-6778 E-mail: binder@argonaut.opt-sci.arizona.edu*

Here, we measure the dynamics of the *polarization state* of the coherent nonlinear emission from a uniaxially-strained GaAs-AlGaAs quantum well, and we show that the vectorial dynamics of the nonlinear signal are determined both by the intrinsic static anisotropy associated with the strain-induced valence band mixing and by the induced dynamic anisotropy associated with many body processes.

## Polarization Dynamics of the Nonlinear Coherent Emission from Uniaxially-Strained Quantum Wells

Arthur L. Smirl, X. Chen, Martin J. Stevens and O. Buccafusca

*Laboratory for Photonics and Quantum Electronics, 138 IATL, University of Iowa, Iowa City, IA 52242*

*Phone: (319) 335-3460 Fax: (319) 335-3462 E-mail: art-smirl@uiowa.edu*

R. Binder and I. Romyantsev

*Optical Sciences Center, University of Arizona, Tucson, AZ 85721*

*Phone: (520) 621-2892 Fax: (520) 621-6778 E-mail: binder@argonaut.opt-sci.arizona.edu*

Conventional nonlinear techniques, such as four-wave-mixing (FWM), have provided considerable information about the spectral and temporal *amplitudes* of ultrafast coherent radiation emitted by semiconductors and multiple quantum wells (MQW's), but they typically provide no information about the temporal or spectral *phases* of the nonlinear signal. In addition, conventional techniques have been used to address the dependence of the magnitude of the FWM signal (or its spectrum) on the relative polarizations of the incident pulses, but there have been few attempts to measure the polarization state of the FWM signal itself.

Recently, however, we have used direct time-resolved ellipsometric<sup>1,2</sup> and spectrally-resolved interferometric techniques<sup>3,4</sup> to characterize the *amplitude*, *phase* and *polarization state* of the weak coherent nonlinear FWM emission from GaAs/AlGaAs MQW's. From these studies, a self consistent picture of the temporal dynamics of the amplitude, phase and polarization state of the nonlinear signal is obtained that delineates the roles of many body effects, such as local field corrections, excitation-induced dephasing and biexcitons, in determining the excitonic dynamics. Such studies have established the sensitivity of polarization-based nonlinear techniques for studying many body and biexcitonic processes. Most recently, we also have reported the observation of dramatic time-resolved light-hole-heavy-hole quantum beats in each of the parameters that describes the polarization state of the nonlinear signal. For example, during each beat period (in the strong quantum beat regime), the ellipticity is found to oscillate twice between linear and almost circular polarization, the orientation of the polarization ellipse rotates through a complete 180°, and the sense of rotation changes from left to right circular polarization.

To date, however, our experiments have been performed in conventional [001]-oriented unstrained GaAs/AlGaAs MQW's. MQW structures grown along the [001]-direction possess no intrinsic in-plane anisotropy in their linear absorptive or refractive properties. Even though quantum confinement breaks the symmetry along the growth direction, the in-plane linear optical properties remain isotropic. It has been shown<sup>5</sup>, however, that the application of a uniaxial stress in the plane of the wells will reduce the in-plane symmetry by mixing the heavy-hole and light-hole valence band states to produce large linear and nonlinear optical anisotropies. Here, we describe the first measurements of the dynamics of the *amplitude*, *phase* and *polarization state* of the coherent nonlinear emission from an anisotropic uniaxially-strained GaAs-AlGaAs MQW. We use time-resolved polarimetry to identify and to study two different links between the macroscopic changes in the vectorial nature of the emitted nonlinear signal and the microscopic materials processes. One source of the polarization changes is the anisotropy in the bandstructure introduced by the noncubic uniaxial strain. The other is the microscopic dynamics of many body processes.

In our experiments, we divide each ~150 fs pulse from our laser into three parts. Two of the pulses with wavevectors  $\mathbf{k}_1$  and  $\mathbf{k}_2$  are used to produce the third-order FWM signal in the direction  $2\mathbf{k}_2 - \mathbf{k}_1$  in the usual manner. We then use a dual-channel spectral interferometric technique (which has been described elsewhere<sup>3</sup>) to obtain the spectral amplitudes and phases of the x- and y-components of the nonlinear FWM signal. The temporal amplitude and the temporal phase of each component is then obtained by inverse Fourier transformation. Using this technique, we have time-resolved the amplitude,

phase and polarization state of the nonlinear FWM emission as the polarization states of the two incident pulses and the sample orientation were systematically varied.

The sample used in this study consists of 10 periods of ~14-nm-wide GaAs wells alternating with 17-nm-thick  $\text{Al}_{0.3}\text{Ga}_{0.7}\text{As}$  barriers. The uniaxial in-plane strain was obtained following growth by bonding the MQW structure to a transparent uniaxial lithium tantalate ( $\text{LiTaO}_3$ ) substrate and subsequently removing the semiconductor substrate on which the sample was grown by selective etching. The  $\text{LiTaO}_3$  substrate was cut such that the thermal expansion coefficient along one direction approximately matched that of the MQW, but along the orthogonal direction it did not. A thermally-induced uniaxial strain was then obtained by operating the device at a temperature (~100 K) different from the bonding temperature (~300 K). The linear absorption coefficient for light polarized along the strained axis is measured to be more than twice that for light polarized along the unstrained axis (when the wavelength is tuned to the peak of the exciton).

Typical measurements of the parameters that directly determine the time-resolved polarization state of the FWM emission from the uniaxially-strained MQW are shown in Fig. 1 and Fig. 2 for selected angles  $\theta_{12}$  between the two linearly polarized input pulses. For the measurements shown in Fig. 1, the sample was oriented so that the strong absorption axis (denoted by the vector  $\hat{a}$  in the inset) was aligned parallel to the fixed polarization of the  $E_2$ -pulse, while for Fig. 2, the sample was rotated by  $90^\circ$  so that  $\hat{a}$  was orthogonal to the  $E_2$ -polarization.

Notice that both the ellipticity and the

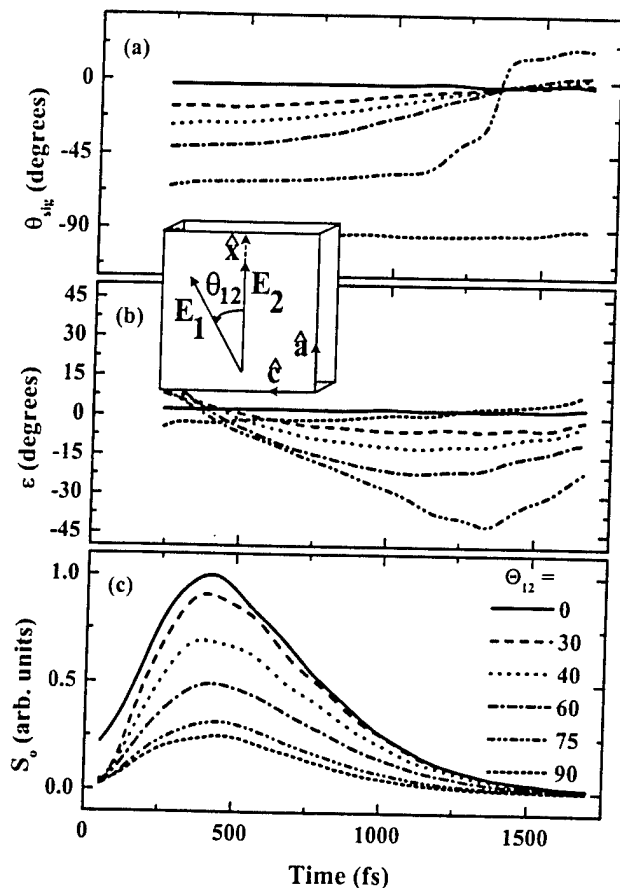


Fig. 1. The azimuthal angle  $\theta_{\text{sig}}$ , ellipticity angle  $\epsilon$ , and the total intensity  $S_0$  as a function of time for selected angles  $\theta_{12}$  between the input polarizations. The inset shows the sample orientation and the polarizations of the incident fields.

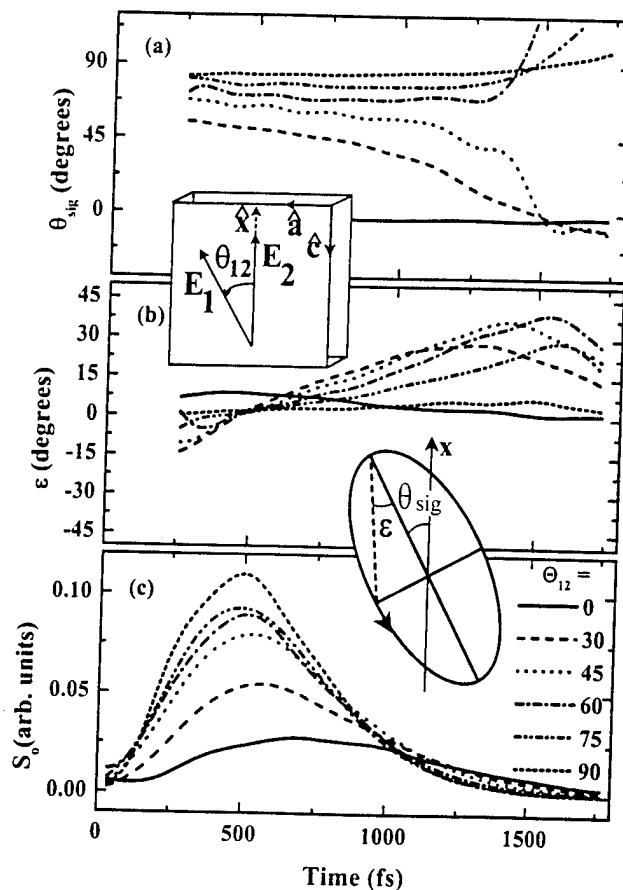


Fig. 2. The same measurements as in Fig. 1 except that the sample has been rotated by  $90^\circ$  as shown in the inset. The second inset indicates the notation used to specify the polarization ellipse for the emitted FWM signal.  
 orientation of the polarization ellipse vary



substantially with time in both figures. This is in contrast to what one would expect for either an isotropic or anisotropic sample in the absence of many body effects. The polarization of the FWM emission from a sample that is *isotropic* is expected to vary with input polarization, but is expected to be linearly polarized with an orientation that is constant in time (without the inclusion of many body effects). By comparison, for a sample with an intrinsic static *anisotropy* (for example, as the result of uniaxial strain), the orientation  $\theta_{\text{sig}}$  of the polarization ellipse and the ellipticity angle  $\varepsilon$  are expected to vary with the sample orientation and input polarization; however, for a fixed sample orientation and for fixed input polarizations, the orientation of the ellipse and the ellipticity are expected to remain constant in time. Consequently, the time-varying ellipticity and orientation shown in Figs. 1 and 2 indicate the presence of a dynamic induced anisotropy. In fact, they are definitive signatures of many body effects and indicate that such must be taken into account.

The dramatic influences of the intrinsic static (strain-induced) anisotropy are also apparent in these figures. For the sample orientation of Fig. 1, when  $E_1$  is rotated counter-clockwise to a positive angle  $\theta_{12}$  with respect to  $E_2$ , notice that the FWM polarization is initially oriented at a negative angle, then it proceeds to rotate counter-clockwise towards more positive angles. For this sample orientation (Fig. 1), the magnitude of the ellipticity increases then decreases with time, but is always negative (corresponding to a clockwise, or left circular, rotation). When the sample is rotated by  $90^\circ$ , these features are reversed. Namely, the orientation of the polarization begins at positive angles then rotates to more negative angles, and the ellipticity is positive (right circular).

The influence of the static anisotropy is also apparent in the temporal evolution of the total intensity  $S_0$  (which reflects the effective density-of-states seen by the two pulses). When the strong absorption axis is oriented parallel to the fixed  $E_2$ -polarization (Fig. 1), the nonlinear FWM intensity is largest when the two input polarizations are parallel and the smallest when they are orthogonal. When the sample is rotated so that the weak axis is parallel to  $E_2$  (Fig. 2),  $S_0$  is largest when the two input polarizations are orthogonal and smallest when they are parallel. By comparison, when the measurements are repeated in an identical unstrained control sample, the maximum value for  $S_0$  is independent of sample orientation and is roughly independent of the angle between the linear input polarizations.

Taken together, Figs. 1 and 2 illustrate that the vectorial dynamics are determined by (and therefore contain information about) both intrinsic static and induced dynamic anisotropies. In order to interpret the experimental results further, we have extended the phenomenological model described in Ref. 2 to include anisotropic optical matrix elements which correspond to the strain in our sample. This model reproduces many of the qualitative features displayed by the data. We anticipate that further refinements in the model will allow a more detailed analysis of the many body effects underlying the vectorial dynamics. Finally, we emphasize that a knowledge of the temporal phases of both the x and y components of the radiation are necessary for determining the vectorial dynamics (i.e., the polarization state) and that this information is not provided by conventional techniques.

1. J. A. Bolger, A. E. Paul, and A. L. Smirl, Phys. Rev. B **54**, 11666 (1996).
2. A. E. Paul, J. A. Bolger and A. L. Smirl, J. Opt. Soc. Am. B **13**, 1016 (1996).
3. W. J. Walecki, D. N. Fittinghoff, A. L. Smirl, and R. Trebino, Opt. Lett. **22**, 81 (1997).
4. O. Buccafusca, X. Chen, W. J. Walecki, and A. L. Smirl, to be published in J. Opt. Soc. Am. B (1998).
5. H. Shen, M. Wraback, J. Pamulapati, P. G. Newman, M. Dutta, Y. Lu and H. C. Kuo, Phys. Rev. **47**, 13933 (1993).